

Prediction of the effective thermal conductivity of porous building blocks based on their pore structure

Wouter Van De Walle

Supervisor:
Prof. dr. ir. Hans Janssen

Dissertation presented in partial fulfilment of the requirements for the degree of Doctor of Engineering Science (PhD): Civil Engineering

September 2019

PREDICTION OF THE EFFECTIVE THERMAL CONDUCTIVITY OF POROUS BUILDING BLOCKS BASED ON THEIR PORE STRUCTURE

Wouter VAN DE WALLE

Supervisor:
Prof. H. Janssen

Members of the Examination
Committee:
Prof. P. Sas
Prof. H. van Lenthe
Prof. C. Glorieux
Prof. B. Nait-Ali
Prof. P. Talukdar
Dr. E. Vereecken

Dissertation presented in
partial fulfilment of the
requirements for the degree of
Doctor of Engineering Science
(PhD): Civil Engineering

September 2019

© 2019 Wouter Van De Walle
Uitgegeven in eigen beheer, Wouter Van De Walle, Leuven

Alle rechten voorbehouden. Niets uit deze uitgave mag worden vermenigvuldigd en/of openbaar gemaakt worden door middel van druk, fotokopie, microfilm, elektronisch of op welke andere wijze ook zonder voorafgaandelijke schriftelijke toestemming van de uitgever.

All rights reserved. No part of the publication may be reproduced in any form by print, photoprint, microfilm, electronic or any other means without written permission from the publisher.

Acknowledgements

If I have seen further it is by standing on the shoulders of giants.

Isaac Newton

Isaac Newton allegedly once wrote the above quote in a communication with Robert Hooke, expressing how much of what we achieve in our endeavours is only possible because of the people and the context around us. And I wholeheartedly support this claim: although it is my name on the front of this work, it is by no means only ‘my’ efforts that made this work possible.

Hans, I have had the enormous pleasure of you promoting my work, first during my master’s thesis, and subsequently during all those years preparing the doctoral thesis. Already 8 years ago, you ignited a spark in me during your *Building Physics* course, marking the first time I got deeply interested in a topic. So when you asked whether I was interested in a PhD with you, it didn’t take me long to decide. During the past 5 years, I could bother you anytime with any question or doubt, which you always responded with enthusiasm and an open mind. Even when parts of my work needed a lot of improvement, you were always generously providing concrete help on how to go forward and never stopped expressing your belief in me. All the while, you were equally understanding for those moments my life besides the PhD required more attention. Your accessibility, scientific reasoning and work ethics are exemplary of what scientific research and promotorship could and should be. Looking back at it, I simply cannot thank you enough for all the things you taught me.

My gratitude also goes to all the members of the Examination Committee, for revising the thesis and improving the quality of the work and text at hand. Special thanks to Evy and Harry, who embarked already at the beginning of this journey as part of my supervisory committee and who provided feedback as my work was progressing. Thank you for your ever-friendly guidance. Evy, I need to thank you furthermore for all the help you provided in the lab, the papers you sent me, the meetings with Hans you joined, and for involving me in some other projects that broadened my horizon. Christ, I would like to thank you additionally for the help on the very nice conference we attended together, and for the trip through the landscape of Utah you invited me to.

Most of the work presented in this thesis took place in office 04.09, where I started 5 years ago together with Michiel and Fabio. It has been my honour to share not alone this office with you, but all those moments of hardship when results didn't make sense, of victory when you could explain them, and of stress when paper and presentation deadlines neared. In between, there was always room (in our not so roomy office) to discuss various topics, ranging from bicycle aerodynamics over porous materials to cavity ventilation (there must be some joint application out there), on Inter Milan vs Juventus, politics and economics, coffee and food. Of course, also a large thanks to Geert and Twan, who both spent several years in our office as postdocs and who were always very kind in providing help and motivating us.

I've had the joy that our office is part of the *Building Physics Section*, where professors pursue high scientific standards, but at the same time create a warm and motivating environment. Dirk and Staf, thank you for the genuine interest in my work and in me as a person, the nice talks and discussion at the coffee table or over lunch, and the fun teambuilding activities you organised for the section. Furthermore, you somehow manage to hire wonderful people whom I've had the privilege to call my colleagues. An-Heleen, Jo-Hendrik and Astrid, thank you for all the exercise and P&O sessions we guided together. I've found these sessions always very pleasant, being a break from the daily simulation work. Jelena and Islah, thank you so much for helping me get through my first conference (where I got horribly sick). Steven, for your kind help and experience in pore structure characterization, which was an enormous improvement for my work. Christina and Juliana, for all those highly interesting discussions you so often started over lunch on so many topics like politics, social (in)justice, economics, art ..., showing how there are so many other interesting things besides the PhD. A very special thanks also to the technical personnel. Patricia, Wim, Esther, Jimmy, Gerda, Paul, Tom, Jan, Bernd, Eli: needless to say it is your skilful work that made a lot of the things accomplished in this thesis possible. But even more than that, I highly appreciate your friendliness and how you are always open for a little chat or advice on the other aspects of life. And of course, a very large thank you to all other colleagues: Ina, Evi, Michele, Ando, Chi, Tianfeng, Jonathan, Vincent, Vasilis, Glenn, Ruben, Marieline, Wout, Jelle, Arrash, Jason ... it is the daily contact with you at the coffee machine, the breaks, the lunches, the Kubb and ping pong games, the trying-to-follow-Hans-on-a-bike-excursions that made sure I kept enjoying coming to the office, even when PhD results seemed grim.

Outside the work environment, I have always had the privilege to have some very dear friends around. Some of you I now don't see as often as before, partially due to my time investment in this PhD, but I hope you realize how much I appreciate our gatherings, even if it's only a few times a year, and hope we can keep doing it for many years to come. Although I consider myself as having a lot of dear friends, I want to specifically thank Ward, Lander, Laurent and Jonas, whom I have known for more than a decade and with whom I have shared wonderful moments that shaped me a lot to the person I am today. I can always count on you for a talk, even if it is about unhappy things, and I cherish your presence enormously.

I really need to thank my family, for the support and love they provided during the past (almost) 28 years. Robin, Dorine, Steven, Stijn and Stan, I grew up with you as my beloved siblings, and all the joys and fights that come along with that. Although every one of us goes his/her own path, we always kept a very good bond; meeting with all of you, no matter where, always feels like coming home. Mom and dad, for all those years raising me to the person I am today. Now that I have two daughters myself, I even more realise how much I owe to your patience, your continuous believe in me and the relentless efforts you put without ever being thanked for.

Evelien, my last words go out to you. I don't know how I will ever be able to make up for all the support and love I received the past 13 years. Both of us changed a lot during those defining years of early adolescence. All the while, you were there for me, that someone I could always go to and be myself with. It feels like our roots got more and more intertwined along the way, and if I didn't fall down during this phd, it is because of you holding me up. Thank you also for all the love and efforts you put in our two daughters, Auke and Line, when I was again overly busy. Holding the three of you at the end of the day means the world to me.

Wouter Van De Walle

Leuven, September 9 2019.

Abstract

Porous building blocks are increasingly gaining interest, thanks to their suitable compromise of structural and thermal properties, and their potential as high-end solution for upcycling waste materials. Having a low thermal conductivity is one of their key performance indicators with respect to their market viability. The present work studies the relation between the pore structure and the effective thermal conductivity of these materials. A numerical framework is implemented to simulate the heat transfer at the pore scale, in order to predict the macroscopic effective thermal conductivity. Simulations are performed on 3D voxel images of the pore structure acquired via micro computed tomography or virtual generation techniques. The thesis first focusses on conventional building blocks with granular and cellular pore structure types, and characteristic pore sizes in the micrometre and millimetre range. A comparison with measurements on real materials validates the framework's performance. Subsequently, the model is applied to perform a parameter study on the impact of several pore scale parameters. In the second part of the thesis, the framework is extended towards materials with pore sizes down to the nanometre scale. To account for the Knudsen effect on gaseous conduction a novel simplified method is presented, based on the equivalence with thermal radiation. The model's performance is verified using experimental findings on nanocellular foams provided in the literature, showing good agreement. The parameter study on conventional porous building blocks is finally extended to investigate the potential benefits of such novel pore structures on the resulting effective thermal conductivity.

Samenvatting

Poreuze bouwblokken krijgen steeds meer belangstelling dankzij hun praktische combinatie van structurele en thermische eigenschappen. Bovendien bieden ze een opportuniteit als hoogwaardige oplossing voor het upcyclen van afvalstromen. Om hun marktpotentieel te verhogen is een verdere verlaging nodig van hun warmtegeleidingscoëfficiënt. Dit proefschrift bestudeert de relatie tussen hun poriënstructuur en hun effectieve warmtegeleidingscoëfficiënt. Een numeriek framework wordt geïmplementeerd om de warmtestromen die plaatsvinden op de porieschaal te simuleren, met als opzet de voorspelling van hun macroscopische warmtegeleidingscoëfficiënt. Simulaties worden uitgevoerd op 3D voxelbeelden van de poriënstructuur die bekomen wordt via microtomografie of virtuele generatie technieken. Het proefschrift richt zich in eerste instantie op conventionele bouwblokken met granulaire en cellulaire poriënstructuurtypes, en karakteristieke poriegroottes in het micrometer- en millimeterbereik. Het model wordt gevalideerd aan de hand van experimentele metingen op verschillende poreuze materialen. Vervolgens wordt het model toegepast om een parameterstudie uit te voeren naar de impact van verschillende parameters op de poriënschaal. In het tweede deel van het proefschrift wordt het model uitgebreid naar materialen met poriëndiameters tot op de nanometerschaal. Om rekening te houden met het Knudsen effect op de warmtegeleiding doorheen het gas wordt een nieuwe vereenvoudigde methode uitgewerkt, gebaseerd op de equivalentie met thermische straling. De prestaties van het model worden gevalideerd aan de hand van experimentele bevindingen op nanocellulaire schuimen in de literatuur en tonen een goede overeenkomst. De parameterstudie op conventionele poreuze bouwblokken wordt uiteindelijk uitgebreid om de potentiële voordelen van dergelijke nieuwe poriënstructuren op de resulterende effectieve warmtegeleidingscoëfficiënt te onderzoeken.

Table of Contents

CHAPTER 1 INTRODUCTION	1
1.1. BACKGROUND & PROBLEM STATEMENT	1
1.2. RESEARCH QUESTIONS & OBJECTIVES	6
 <u>PART I - PREDICTING THE ETC OF CONVENTIONAL POROUS BUILDING BLOCKS</u>	
CHAPTER 2 PREDICTION OF THE EFFECTIVE THERMAL CONDUCTIVITY: STATE-OF-THE-ART	13
2.1. INTRODUCTION.....	13
2.2. ANALYTICAL PREDICTION OF THE ETC.....	14
2.3. NUMERICAL PREDICTION OF THE ETC.....	23
2.4. IMPACT OF PORE SCALE PARAMETERS ON ETC	29
2.5. CONCLUSIONS	31
CHAPTER 3 IMPLEMENTATION OF THE MICROSCALE MODEL FRAMEWORK	33
3.1. INTRODUCTION.....	33
3.2. IMPLEMENTED FRAMEWORK OVERVIEW	34
3.3. THERMAL CONDUCTION	42
3.4. THERMAL RADIATION	45
3.5. THERMAL CONVECTION.....	62
3.6. VERIFICATION OF IMPLEMENTED PHYSICAL MODELS	63
3.7. CONCLUSIONS	76
CHAPTER 4 VALIDATION OF THE MICROSCALE MODEL FRAMEWORK	77
4.1. INTRODUCTION.....	77
4.2. THE HEAT FLOW METER	78
4.3. MATERIALS & METHODS	89
4.4. SINTERED GLASS FILTER	93
4.5. REAPOR POROUS BLOCK	97
4.6. CELLULAR GLASS PERINSUL S.....	103
4.7. CONCLUSIONS	107

CHAPTER 5 PARAMETER STUDIES TOWARDS OPTIMAL PORE STRUCTURES.....	109
5.1. INTRODUCTION.....	109
5.2. EXPLORATORY PARAMETER STUDY.....	110
5.3. DETAILED PARAMETER STUDY.....	123
5.4. CONCLUSIONS.....	129

PART II - NANOSCALE EFFECTS ON THE ETC OF POROUS BUILDING MATERIALS

INTRODUCTION TO PART II.....	133
-------------------------------------	------------

CHAPTER 6 STATE-OF-THE-ART ON MODELLING OF HEAT TRANSFER IN NANOPOROUS AND LOW-GAS-PRESSURE MATERIAL.....	137
--	------------

6.1. INTRODUCTION.....	137
6.2. GASEOUS CONDUCTION.....	138
6.3. SOLID CONDUCTION.....	146
6.4. PORE SCALE RADIATION.....	155
6.5. CONCLUSIONS.....	160

CHAPTER 7 IMPLEMENTATION AND VALIDATION OF THE MODEL FRAMEWORK FOR PORE SCALE HEAT TRANSFER WITH NANOSCALE EFFECTS.....	163
--	------------

7.1. INTRODUCTION.....	163
7.2. EXPANSION OF THE MODEL FRAMEWORK.....	164
7.3. VALIDATION OF MODEL FRAMEWORK.....	179
7.4. CONCLUSIONS.....	189

CHAPTER 8 PARAMETER STUDIES TOWARDS OPTIMAL PORE STRUCTURES FOR POROUS BUILDING BLOCKS WITH NANOSCALE FEATURES.....	191
--	------------

8.1. INTRODUCTION.....	191
8.2. EXPLORATORY PARAMETER STUDY.....	192
8.3. DETAILED PARAMETER STUDY.....	201
8.4. CONCLUSIONS.....	208

CHAPTER 9 CONCLUSIONS & FUTURE WORK.....	209
---	------------

9.1. CONCLUSIONS.....	209
9.2. FUTURE WORK.....	213

**APPENDIX A ANALYTICAL MODEL FOR MACROSCOPIC RADIATIVE CONDUCTIVITY
CONSIDERING TRANSMISSION AND INTERFERENCE..... 217**

A.1. INTRODUCTION 217

A.2. MODEL OVERVIEW 217

CURRICULUM VITAE..... 225

BIBLIOGRAPHY..... 227

Nomenclature

Greek

ϕ	Porosity	-
λ	Thermal conductivity	W/mK
λ_{eff}	Effective thermal conductivity	W/mK
$\lambda_{mat(rix)}$	Thermal conductivity of the matrix	W/mK
λ_{pore}	Thermal conductivity of the pore space	W/mK
λ_{gas}	Thermal conductivity of the gas	W/mK
$\lambda_{rad,pore}$	Pore scale equivalent radiative conductivity	W/mK
$\lambda_{cond,macro}$	Effective conductive conductivity	W/mK
$\lambda_{rad,macro}$	Effective radiative conductivity	W/mK
γ	Pore shape factor	-
γ_{heat}	Specific heat ratio	-
σ_{SB}	Stefan-Boltzmann constant	W/m ² K ⁴
ϵ	Emissivity	-
λ_{wave}	Radiation wavelength	m
β_{ext}	Extinction coefficient (for radiation energy)	1/m
$\rho_{material}$	Mass density of material	kg/m ³
ρ	Reflectivity	-
τ	Transmissivity	-
η	Dynamic viscosity	Pa.s
ω	Circular frequency	rad/s
Ω	Solid angle	Sr
μ_{λ}	Spectral absorption coefficient	1/m
$\sigma_{s,\lambda}$	Spectral scattering coefficient	1/m
Φ	Scattering phase function	-
β_{kag}	Coefficient for molecule-wall collision energy transfer efficiency	-
$n + ik$	Complex refractive index, where real part n is refractive index and imaginary part κ is the absorption coefficient	-

Roman

f_s	Strut factor	-
d_{sample}	Sample thickness	m
$d_{pore,mean}$	Mean pore diameter	m
$d_{i,mean}$	Mean distance between opposing pore walls in direction 'i'	m
d_{wall}	Pore wall thickness	m
T	Temperature	K
d_{wall}	Pore wall thickness	m
q	Heat flux	W/m ²
A	Area	m ²
V	Volume	m ³
i'_λ	Spectral radiation intensity	W/(m ² .Sr.wavelength)
I_{tot}	Total radiation intensity	W/(m ² .Sr)
$I_{hem.,tot}$	Hemispherical total radiation flux	W/m ²
$S_{f,i}$	Directional slenderness factor for a pore, in direction 'i'	-
C_i	Radiation factor for a pore, in direction 'i'	-
Gr	Grashof number	-
g	Gravitational acceleration constant	m/s ²
R	Thermal resistance	m ² K/W
$R_{specific,gas}$	Specific gas constant	J/kgK
m	Mass	kg
$v_{norm,factor}$	Variance normalised by the square of the average pore diameter	-
c_V	Specific heat at constant volume	J/kgK
v_{avg}	Average speed	m/s
L_{MFP}	Mean free path	m
$L_{MFP,eff}$	Effective mean free path	m
$L_{MFP,bdy}$	Boundary mean free path	m
p	Pressure	Pa
Kn	Knudsen number	-
k_B	Boltzmann constant	m ² kg/s ² K
a	Thermal accommodation coefficient	-

Acronyms and abbreviations

ETC	Effective Thermal Conductivity	W/mK
RP	Reduction Potential	-
RJF	Rejoin factor	-
μ CT	Micro Computed Tomography	
DSMC	Direct Simulation Monte Carlo	
RTMC	Ray Tracing Monte Carlo	
SC	Simple Cubic	
BCC	Body Centred Cubic	
FCC	Face Centred Cubic	
FVM	Finite Volume Method	
FEM	Finite Element Method	
DOM	Discrete Ordinates Method	
HFM	Heat Flow Meter	
GHP	Guarded Hot Plate	
Hfs	Heat flux sensor	
RBI	Random Bubble Insertion	
WSB	Watershed Based	

Introduction

1.1. BACKGROUND & PROBLEM STATEMENT	1
1.2. RESEARCH QUESTIONS & OBJECTIVES	6

1.1. Background & Problem Statement

1.1.1. General background

The built environment is one of the primary consumers of both energy and material resources in the EU. Space heating alone accounts for almost 20 % of the EU's total energy use (EEA 2017; Pardo et al. 2012). At the same time, about 25 % of extracted raw materials are consumed by the construction industry (Eurostat 2016) and about 30 % of the waste streams in the EU originate from the construction and demolition of buildings (Herczeg et al. 2014; Monier et al. 2017). Hence, several European regulations target the reduction of dwelling energy use and the recycling of building construction waste. For example, new buildings need to have envelope components with very low thermal transmittance, and 70 % of the generated construction waste is to be recycled by 2020. These regulations pose serious challenges to the building and construction industry, and have so fostered research for materials with improved insulating properties as well as for recycling waste via construction materials.

One of the suggested strategies to further reduce the construction-related resource depletion is the production of insulating porous building blocks from available waste materials. These porous building blocks combine load-bearing and insulating properties, making them suited to replace structural wall or floor elements or to provide solutions for thermal bridges. Well-known commercial variants like cellular concrete or cellular glass typically come as large brick elements, usually available in different thicknesses, sizes and densities. Their insulating properties also reduce the needed thermal insulation thickness to comply with the increasingly stringent energy regulations and the often associated loss of useful floor area. Porous building blocks can therefore provide an interesting alternative in the design process for reducing energy needs, but at the same time also by providing a valuable alternative for

waste materials (Barbuta et al. 2015). Indeed, earlier research efforts have focussed on producing such blocks partially or fully based on recycled materials. Arcaro et al. (2016) for example presented several blocks made from recycled bottle glass, using banana leaves residue as a foaming agent. Varying the production parameters, different blocks with thermal conductivities between 0.06 and 0.15 W/mK were obtained. Ngouloure et al. (2015), for example, describe the utilization of waste rice husk ash as a sustainable replacement of metakaolin in the production process of porous building blocks with a thermal conductivity of 0.15 W/mK. Other authors have described similar efforts, recycling metal slag waste, industry waste cinders, sewage sludge etc., in porous blocks with low ETC, i.e. (Drochytka et al. 2013; Kriskova et al. 2015; Raut and Gomez 2016; Z. Zhang et al. 2014). A further increase of their insulating property is needed though to advance their market viability and boost their application.

1.1.2. Typical properties of porous building blocks

Porous building blocks find frequent application in the construction of dwellings and other buildings that require an adequate thermal resistance of the outer envelope. Commercial variants are available with a range of different properties, depending on the foreseen application. The two most common types of blocks nowadays are cellular concrete (i.e. by Xella or Cellumat) and cellular glass (i.e. by Foamglas). Their ETC is in the range of 0.04 W/mK – 0.17 W/mK and depends strongly on the mass density (or porosity). As illustration, the ETC of some commercially available materials are shown in Figure 1.1 as a function of their density. For comparison, also shown are the properties of two typical insulation materials (PUR foam and mineral wool (Recticel 2019; Rockwool 2019)) and two innovative materials (aerogel and vacuum insulation (Schiavoni et al. 2016)). Cellular glass has a lower range of ETC than most cellular concretes, but is only meant as a solution for construction details (the base of a wall) or as a floor element. The cellular concretes with higher densities find application as wall elements.

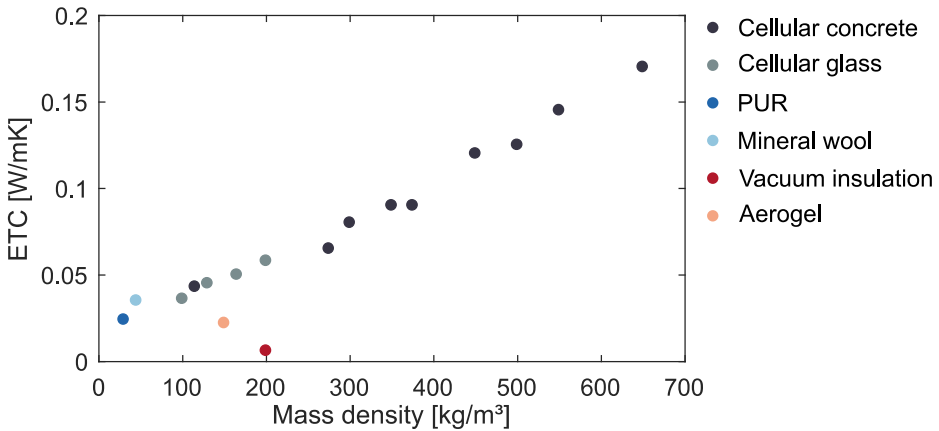


Figure 1.1: ETC of typical porous building blocks and insulation materials as a function of their mass density.

These porous building blocks typically have a cellular pore structure because of the good mechanical and thermal performance (Ashby and Medalist 1983): the cellular matrix ensures a redistribution of the mechanical load while the air-filled pores reduce the heat flow through the material. For illustrative purposes, some pore structures of typical blocks are shown in Figure 1.2a&b. They show indeed the typical cellular pore structure of such materials. For reasons of comparison, the pore structure of a polymer foam and a mineral wool are also shown in Figure 1.2c&d.

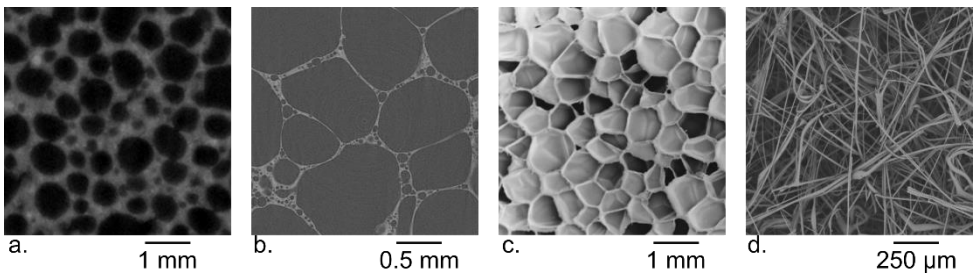


Figure 1.2: View on the pore structure of a cellular concrete (a), a cellular glass (b), a polyolefin foam (c) (Almanza et al. 2001) and a stone wool (d) (Chapelle 2016).

1.1.3. Optimising insulation properties

The effective thermal conductivity (ETC) of porous materials is closely related to their pore structure properties. Indeed, the total heat flow through a porous material originates in fact from the complex interaction of several heat transfer mechanisms occurring at the pore scale, illustrated conceptually in Figure 1.3. As shown, there is thermal conduction through the solid matrix and the gaseous phase due to the local temperature gradients. Besides, thermal

radiation transfers heat from one surface to (and even partially through) another surface. Finally, thermally induced movement of air can cause thermal convection, increasing the transfer of heat in the gas space. From this microscopic perspective, it can be easily appreciated that the pore scale properties like porosity, pore size etc. will affect these different mechanisms and hence also the macroscopic ETC. For example, classic insulation materials like mineral wools or polymer foams have very high porosities to reduce the conduction of heat through the matrix. Similarly, a relatively small pore size is often targeted to reduce potential thermal convection and thermal radiation in the pores. Other parameters like matrix connectivity, pore shape etc. have also been shown to directly influence the material's ETC.

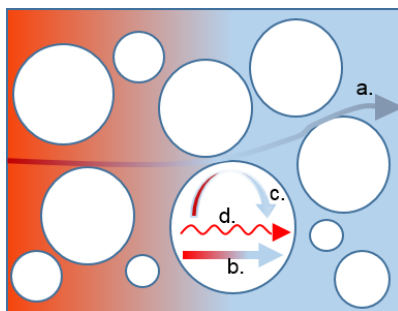


Figure 1.3: conceptual overview of heat transfer mechanisms at the pore scale in a cellular material: (a) solid heat conduction, (b) gaseous heat conduction, (c) thermal convection and (d) thermal radiation.

Tweaking the pore structure, insulation materials have been produced with ETC's on the order of the thermal conductivity of air (~ 0.025 W/mK at room temperature), see Figure 1.1. However, in the search for even better performing materials, new innovative strategies have recently been proposed to alter the pore scale behaviour and reduce the ETC of porous materials below the thermal conductivity of still air (B. P. Jelle, Gustavsen, and Baetens 2010; Schiavoni et al. 2016; Cuce et al. 2014). Promising results have been obtained by lowering the gas pressure in the pores and/or by reducing the pore size to the nanoscale (Berge and Johansson 2012; Baetens, Jelle, Thue, et al. 2010; Bjørn Petter Jelle, Baetens, and Gustavsen 2011; S. Liu, Duvigneau, and Vancso 2015). Such measures have been shown to decrease the conductivity of the gas in the pores significantly, leading to a ballistic type of conduction. Some examples are vacuum insulation panels or aerogels, reaching extremely low ETC's between 0.004 W/mK and 0.02 W/mK thanks to their advanced pore structures (Figure 1.1).

Optimizing the pore structure can hence result in a desirable reduction of the ETC. Nowadays, material pore structures can be reasonably controlled by changing the production parameters

(chemical constituents, temperature, ...) i.e. (Denissen, Kriskova, and Pontikes 2019; Medri and Ruffini 2012; Kamseu et al. 2015). Recently, techniques to design the material pore structure at the pore scale are put forward, leading to so-called architected cellular materials (Schaedler and Carter 2016; Kaur, Han, and Kim 2016). This then leads to the question on which pore structure is the optimal one regarding the ETC. Indeed, while the impact of specific parameters is often known, the combined effect of different parameters is still not completely understood. Certainly for porous building blocks, where desired structural performance can for example limit the maximum porosity, it is often not known what other strategies are most beneficial to reduce the ETC.

Reducing the ETC of a porous building block is frequently performed by experimental trials: several block prototypes are produced and their resultant conductivity is measured. This trial-and-error process is extremely expensive in both time and cost, and neither does it deliver insight in the individual influences of specific parameters. Moreover, it is inherently limited to already-existing materials and production techniques. Concurrently, several analytical and numerical modelling attempts have been performed to predict the ETC of porous materials based on selected pore scale parameters. She et al. (2014, 2018), for example, developed a numerical model to simulate the heat transfer through virtual representations of the pore structure of cellular concrete samples. Their simulations indicated that adjusting the pore shape can reduce the ETC significantly. Placido et al. (2005) simulated the conductive and radiative heat transfer through a unit cell representation of an EPS foams, showing the optimum porosity and average pore size that should be strived for. Coquard and Baillis (2009), as a last example, simulated the heat transfer through the pore structure of several actual and virtual ceramic and polymeric foam pore structures. Their results showed for example that open-celled foams generally have lower ETC's than closed-celled foams.

These and other examples found in literature (see Chapter 2) indicate the potential of such numerical strategies for studying the impact of the pore structure on the ETC. However, their conclusions are typically derived for specific types of porous materials (polymer foams, ...) in a limited range of varying pore scale parameters, leaving uncertainty on their applicability for porous building blocks. Furthermore, validation and application of developed models on the broad range of pore structures encountered in typical porous building blocks still remains a daunting task. This hinders the development and optimization of new, improved porous building blocks and the re-utilization of waste products.

1.1.4. Problem statement

Optimizing the pore structure shows great promise for reducing the ETC of waste-based porous building blocks and foster their application. However, the combined impact of the pore structure parameters is not fully understood yet. Similarly, the development of super-insulation materials like aerogels has raised the question on the potential of pore structures with nanoscale features for porous building blocks. Numerical prediction strategies have shown to be of great help in such optimization efforts, but have focussed so far on other types of materials and pore structures, clouding the applicability of their conclusions for porous building blocks. A thorough investigation on the impact of these and other pore structure parameters on the ETC of porous building blocks is needed.

1.2. Research Questions & Objectives

The main research question towards which the work in this thesis is oriented can be stated as '*How do the pore scale parameters affect the ETC of porous building blocks?*'. Several sub-questions emanating from this main question can be formulated:

- Which heat transfer mechanisms contribute to the ETC and how to model them?
- Which parameters should be tackled first given a certain pore structure?
- What is the potential of new strategies like vacuum and nanoscale pore sizes for porous building blocks?

1.2.1. Objectives

The general aim of this thesis is to study the impact of the pore structure on the ETC of porous building blocks. This thesis will focus on the development of a numerical model to predict the ETC based on the pore structure. Several objectives are put forward:

Objective 1: Development of a numerical model.

So far, optimization of the porous materials' ETC is often performed experimentally by trial-and-error, or by simplified analytical correlations. Numerical prediction strategies, on the other hand, have been shown very promising for the accurate characterization of the relation between the pore scale parameters and the material's ETC (see also Chapter 2). Therefore, a new numerical framework will be implemented in this work to predict the ETC based on pore scale heat transfer simulations. Furthermore, all relevant heat transfer mechanisms need to be included together with the impact of nanoscale features on these heat transfer mechanisms, to allow for a consistent assessment of all relevant pore scale parameters. Lastly, the model

needs to be able to predict the ETC for the wide variety of pore structures retrieved in typical porous building blocks

Objective 2: Validation of the numerical model

Previous developments of numerical model frameworks often lack a thorough validation with experimental measurements, certainly over the wide spectrum of possible pore structures. Nonetheless, such validation is necessary to allow employing the model in future optimization studies. Therefore, the numerical framework developed in this thesis will be validated on different experimentally characterized materials having different types of pore structures.

Objective 3: Identify pathways towards optimal pore structures

The (combined) impact of the pore scale parameters on the ETC over the whole range of potential values is still unclear. The developed and validated model is envisioned to be used in a wide parameter study to highlight potential optimization routes towards better performing porous building blocks. Parameters with the most important contribution are identified together with their quantitative potential for reducing the ETC.

These objectives accord to the different chapters in the thesis, as will be clear from the outline described in Section 1.2.3.

1.2.2. Scope limitation

Although during this work efforts have been made to develop the model as generally as possible, some limitations for its applicability were set. First of all the thesis only tackles the **effective thermal conductivity of porous building blocks in dry conditions**. This simplifies the modelling and simulation work and moreover agrees with the usual practice of certifying the materials in dry conditions. The impact of the pore structure on other parameters like structural strength, specific heat, ... is beyond the scope of this work.

Secondly, the thesis focusses on **two-phase materials with a cellular pore structure**: gas-filled cavities enclosed in a solid material matrix. Such pore structures are known to provide an excellent combination of structural and thermal performance up to high porosities (Ashby 1983). Additionally, the pore cells in the studied materials should be closed or only connected via relatively smaller cells, excluding highly open-porous structures, like metallic foams used as heat exchangers. Application of the model for other types of pore structures (like in mineral wools) or composite types of materials (like those with inclusion of low-conducting spheres

in materials) is neither covered, although the present work can certainly serve as inspiration for pore scale modelling on such microstructures.

Lastly, the model is developed for predicting the ETC of porous building blocks in their **typical temperature range** of application, roughly -10 °C till 50 °C. Other studies in literature focus on materials for high-temperature applications like ovens or fire-resistant insulations.

1.2.3. Thesis outline

As was already mentioned in the introduction, innovative strategies are being developed to reduce the ETC of porous building materials: inclusion of nano-sized pores and reduction of the pore gas pressure. These measures affect the way heat is transferred, and require a different physical modelling strategy compared to the traditional materials with pore sizes in or larger than the micrometre range. Therefore, this thesis is divided in two main parts: the first part targets more traditional building blocks and the impact of their pore structure on the ETC. In the second part, the study is expanded to incorporate the new type of physics associated with superinsulating materials.

Part I: Predicting the ETC of conventional porous building blocks

The first part focusses on traditional porous building blocks with pore sizes above a few μm in diameter and atmospheric gas pressure in the pores. This includes typical commercial blocks like cellular glass, most of the waste-based blocks and porous materials where abstraction can be made of the nano-pores present in the solid matrix, as is for example the case for cellular concrete.

Chapter 2 starts with a literature survey of previous and current modelling efforts of the ETC of porous materials. This survey serves as inspiration for the development of a new numerical framework in Chapter 3. The framework workflow is discussed, and the implemented models of the different heat transfer physics are presented. The chapter concludes with a verification exercise. Chapter 4 tackles the validation of the model with real materials: their experimentally measured ETC is compared with the ETC predicted by the modelling framework, starting from micro-CT images of the materials' pore structures. The last chapter of Part I, Chapter 5, finally predicts the ETC of a wide range of generated pore structures to study the influence of several pore scale and physical parameters.

Part II: Nanoscale effects on the ETC of porous building materials

The second part of the thesis expands on the work performed in Part I to study the potential benefits of innovative strategies on the ETC of porous building blocks. The effect of nano-sized pores and low-gas-pressures inside the pores, both called 'nanoscale effects', is emphasised.

Chapter 6 introduces the fundamental aspects of the heat transfer physics at the nanoscale and provides a literature survey of modelling efforts to account for such effects on the ETC of porous materials. Subsequently, Chapter 7 presents the expansion of the model framework to account for the changing physics at the occurrence of nanoscale effects. The influence on each single heat transfer mechanism is elaborated and appropriate modelling strategies are proposed. The performance of the framework is validated by comparing predictions of the ETC of nanocellular foams with experimental measurements. Chapter 8, finally, applies the model to study the potential of such nanoscale effects for reducing the ETC, by studying their impact on several generated pore structures.

Part I

-

Predicting the ETC of conventional
porous building blocks

Chapter 2

Prediction of the effective thermal conductivity: state-of-the-art

2.1. INTRODUCTION	13
2.2. ANALYTICAL PREDICTION OF THE ETC.....	14
2.3. NUMERICAL PREDICTION OF THE ETC.....	23
2.4. IMPACT OF PORE SCALE PARAMETERS ON ETC.....	29
2.5. CONCLUSIONS	31

2.1. Introduction

Identifying and quantifying the impact of pore scale parameters on the ETC will facilitate and accelerate the optimization of insulating materials by material producers. To that end, several experimental studies have been reported (Laurent 1991; Goual, Bali, and Quéneudec 1999; Nait-Ali et al. 2006; Aurangzeb, Khan, and Maqsood 2007; Nait-Ali et al. 2007; Solórzano et al. 2008; R. Coquard, Rochais, and Baillis 2009; Xu et al. 2012; Smith et al. 2013; Baghban, Hovde, and Jacobsen 2013; R. J. Z. Zhang, Liu, and Wang 2013; Bourret et al. 2014; Kamseu et al. 2015; Batool and Bindiganavile 2017; Jin et al. 2017). In these, the pore scale properties and the ETC's are measured for a range of actual materials, and results are discussed based on observed correlations. While such experimental investigations provide interesting insights on the combined impact of pore scale properties, a detailed investigation of the isolated influence of specific parameters is very challenging. Moreover, the preparation of and the experimentation on porous material samples is often expensive both in terms of time and cost. The inherent limitation to already-existing materials finally results in insufficient versatility to study and design new porous materials.

Therefore, several other studies have attempted to provide analytical and numerical pathways to investigate the relation between pore scale properties and ETC. Such prediction models can help in explaining the thermal behaviour of existing porous materials and facilitate designing new porous materials before their actual production. A review of several prediction modelling strategies is detailed in this chapter. Due to the large volume of existing literature, this review cannot be exhaustive, and thus largely aims at surveying previous and current developments. On the other hand, as the specific literature on prediction models for porous building blocks is relatively scarce, studies performed on other types of materials (mainly foams) are included. The chapter first discusses some often-cited analytical models, and then presents a selection of numerical modelling efforts. Other reviews on these two topics can be found for example in (Öchsner et al., 2008; Öchsner & Murch, 2010; Randrianalisoa & Baillis, 2014). A concluding section summarizes some general trends observed in literature on the effect of the pore structure on the resulting ETC.

2.2. Analytical prediction of the ETC

Numerous analytical ETC prediction equations have been developed in literature, relating the ETC to pore scale properties like the matrix conductivity, gaseous conductivity, porosity etc. These equations are typically derived via simplification of the pore structure to a set of unit cells and/or by simplification of the local heat flow patterns, to come to the required analytical solution. Excellent overviews can be found in (Progelhof et al., 1976; Collishaw and Evans, 1994; Singh, 2008). In the following, some selected analytical models are discussed. First, models that exclusively predict the conductive part of the ETC are highlighted, followed by approaches to incorporate thermal radiation. Natural convection, as will be discussed later on, is deemed negligible for pore sizes below a few millimetres in radius.

2.2.1. Analytical models for thermal conduction

Two simple but often discussed models are the series and parallel models attributed to Wiener (1904). The matrix space and pore space are simplified to two continuous slabs with relative volumes related to the porosity. The heat transfer through both phases is then modelled with series or parallel thermal resistances, allowing to deduce Eq. (2.1) & (2.2):

$$\lambda_{eff,series} = \left(\frac{1 - \phi}{\lambda_{matrix}} + \frac{\phi}{\lambda_{pore}} \right)^{-1} \quad (2.1)$$

$$\lambda_{eff,parallel} = (1 - \phi) * \lambda_{matrix} + \phi * \lambda_{pore} \quad (2.2)$$

Here, λ_{matrix} and λ_{pore} [W/mK] represent the conductivity of the matrix phase and the pore phase and ϕ [-] the porosity. These two models provide the absolute lower and upper bound for a porous material's ETC at a certain porosity when only thermal conduction is considered. More strict bounds for macroscopically homogeneous and isotropic materials were proposed by Hashin & Shtrikman (1962), see Eq. (2.3) & (2.4), based on the variational principle. Although derived in a different manner, Maxwell (1873) previously obtained these same equations for dilute concentrations of spheres in a continuous medium. These spheres can be either gas-filled pores in a solid matrix (cellular-like, upper bound) or solid particles in a continuous gas phase (granular-like, lower bound). The isotropic H-S bounds always fall within the series and parallel limits, which are in fact extreme cases of anisotropic pore structures.

$$\lambda_{eff,H-S,upper} = \lambda_{Maxwell,1} = \lambda_{matrix} + \frac{3 * \lambda_{matrix} * (\lambda_{pore} - \lambda_{mat}) * \phi}{3 * \lambda_{matrix} + (\lambda_{pore} - \lambda_{mat}) * (1 - \phi)} \quad (2.3)$$

$$\lambda_{eff,H-S,lower} = \lambda_{Maxwell,2} = \lambda_{pore} + \frac{3 * \lambda_{pore} * (\lambda_{mat} - \lambda_{pore}) * (1 - \phi)}{3 * \lambda_{pore} + (\lambda_{mat} - \lambda_{pore}) * \phi} \quad (2.4)$$

Bruggeman (1935) generalized Maxwell's first equation to agree better for higher concentrations of spherical inclusions in a solid matrix, see its implicit form in Eq. (2.5). The model also predicts values in between the isotropic H-S bounds, and typically agrees better with cellular materials at high porosities.

$$\left(\frac{\lambda_{pore} - \lambda_{eff,Bruggeman}}{\lambda_{pore} - \lambda_{matrix}} \right) * \left(\frac{\lambda_{matrix}}{\lambda_{eff,Bruggeman}} \right)^{\frac{1}{3}} = 1 - \phi \quad (2.5)$$

Landauer (1952) proposed an equation known as the 'effective medium theory' (emt) model, assuming the pore structure is a random distribution of both phases, see Eq. (2.6), which again yields values in between the isotropic H-S bounds.

$$\lambda_{eff,EMT} = \frac{1}{4} * \left[\lambda_{pore}(3\phi - 1) + \lambda_{matrix}(2 - 3\phi) + \sqrt{\left(\lambda_{pore}(3\phi - 1) + \lambda_{matrix}(2 - 3\phi) \right)^2 + 8\lambda_{pore}\lambda_{matrix}} \right] \quad (2.6)$$

Since the assumed pore structure is neither granular or cellular, Carson et al. (2005) used the emt model to divide the region in between both H-S bounds into a cellular and granular region: granular (isotropic) materials have thermal conductivities between the lower bound

and the emt model, while cellular (isotropic) materials have thermal conductivities between the emt model and the upper bound. They also presented a number of measurements on both types of materials indeed confirming both regions. Hence, granular materials will always have lower thermal conductivities than cellular materials at similar porosities and matrix conductivities, although it needs to be noted that granular materials lose their structural integrity at very high porosities.

Models taking into account other pore structure parameters than just the porosity have been derived as well. Glicksman & Torpey (1989), for example, proposed a model for the conductive ETC of a porous foam structure. Modelling the pore structure as a regular array of cubic cells, they derived an upper and a lower bound. Since the difference between both bounds is rather small at high porosities, they continued only with the upper bound. They performed a similar analysis for the case where the solid matrix is comprised in the cell struts instead of in the cell walls. Both results were combined to come to Eq. (2.7), where f_s [-] represents the fraction of the solid material comprised in the struts ($0 < f_s < 1$). Ahern et al. (2005) derived a similar equation as Glicksman & Torpey (1989), similarly applying the strut factor f_s , but with a better prediction at low and medium porosities, see Eq. (2.8) & (2.9). Both equations predict that a higher concentration of solid material in the struts leads to lower thermal conductivities, an effect that was later confirmed by Coquard & Baillis (2009) by numerical simulation.

$$\lambda_{eff,Glicksman} = \left(\frac{2 - f_s}{3}\right) * (1 - \phi) * \lambda_{matrix} + \phi * \lambda_{pore} \quad (2.7)$$

$$\lambda_{eff,Ahern} = \lambda_{pore} + (\lambda_{matrix} - \lambda_{pore}) * (1 - \phi) * \beta \quad (2.8)$$

$$\beta = (1 - f_s) * \frac{2}{3} * \left(1 + \frac{\lambda_{pore}}{2 * \lambda_{matrix}}\right) + f_s * \frac{1}{3} * \left(1 + \frac{4 * \lambda_{pore}}{\lambda_{pore} + \lambda_{matrix}}\right) \quad (2.9)$$

Bauer (1993) proposed a model similar to Bruggeman (1935) but accounting for non-spherical pore shapes. For materials consisting of randomly-oriented pores with equal shapes, Eq. (2.10) is obtained, showing the ETC as an implicit function of porosity and a pore shape factor γ_{Bauer} [-]. For spherical pores, this shape factor is equal to 1, implying that the equation then reduces to Bruggeman's equation (Eq. (2.5)). For other shapes, Yang et al. (2013) proposed to use the pore sphericity (the ratio of pore surface area to surface area of spherical pore with equal volume) as shape factor in Bauer's equation. Another possibility is to use the shape factor as a calibration coefficient fitting the model to experimental or numerical measurements on a certain material.

$$\left(\frac{\lambda_{pore} - \lambda_{eff,Bauer}}{\lambda_{pore} - \lambda_{matrix}}\right) * \left(\frac{\lambda_{matrix}}{\lambda_{eff,Bauer}}\right)^{1 - \frac{2}{3 * \gamma_{Bauer}}} = 1 - \phi \quad (2.10)$$

Kaddouri et al. (2016) recently proposed an equation for 2D materials with randomly oriented elliptically shaped pores, based on a set of numerical simulations with different porosities and matrix conductivities. Based on the outcomes, an expression expanding the Maxwell equation with a term dependent amongst others on the shape factor $\gamma_{Kaddouri}$ [-] is put forward, see Eq. (2.11), with the ratio of the shortest axis to the longest axis of the ellipse as shape factor.

$$\lambda_{eff} = \lambda_{Maxwell,1} + \ln(\gamma_{Kaddouri}) * 0.7 * \lambda_{matrix} * \phi * (\phi^2 - 2 * \phi + 1) \quad (2.11)$$

Other authors proposed models with calibration factors not connected to any physical property, but only serving to improve the agreement between model and measurements. Asaad (1955), for example, expanded Wiener's geometric mean model with a calibration factor based on ETC measurements on rocks. Li et al. (2011) proposed an expansion of the Cheng-Vachon equation with a calibration factor for ETC prediction of cellular concrete materials. Bhattacharya et al. (2002), Jagiwanram & Singh (2004) and Singh & Kasana (2004) all proposed equations with calibration factors for highly porous foams. Sugawara & Yoshizawa (1962), Aurangzeb et al. (2006), Pande et al. (1984) and Kunii & Smith (1960) did the same for granular materials. Such calibrated models allow to accurately predict the ETC of materials with similar pore structure and physical properties as the materials used to obtain the calibration factors, their limited applicability range and their need for an 'unphysical' calibration factor constitute on the other hand also their major weakness.

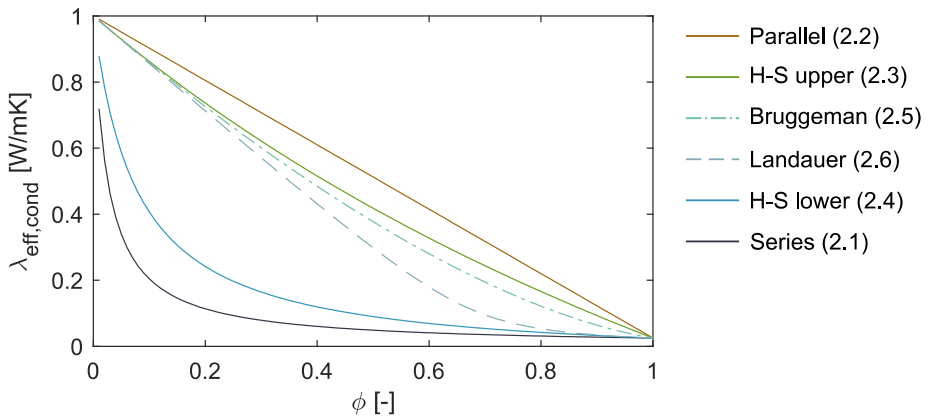


Figure 2.1: Predicted ETC as a function of porosity by selected analytical models for a solid conductivity of 1 W/mK and a gaseous conductivity of 0.025 W/mK.

Figure 2.1 demonstrates the predicted ETC as a function of porosity using the presented analytical models that only require the porosity as pore structure input. A solid and gaseous conductivity of 1 W/mK respectively 0.025 W/mK are assumed for the calculation. As is obvious from the graph, there is a large spread in predicted results.

2.2.2. Analytical models for thermal radiation

Although often neglected by authors due to its complexity, thermal radiation can play an important role in the total heat transfer depending on the pore structure and temperature (Solórzano et al. 2009). Two general approaches appear in literature: calculating a macroscopic radiative conductivity or calculating a local radiative conductivity.

Macroscopic radiative conductivity

The impact of thermal radiation on the ETC is often accounted for by adding a macroscopic radiative conductivity $\lambda_{rad,macro}$ [W/mK] to the macroscopic conductive conductivity $\lambda_{cond,macro}$ [W/mK] (Eq. (2.12)), the latter usually obtained with one of the analytical models discussed above.

$$\lambda_{eff} = \lambda_{cond,macro} + \lambda_{rad,macro} \quad (2.12)$$

Several methods to calculate this macroscopic radiative conductivity have been proposed in literature. Batty et al. (1984) for example simplified the pore structure to a set of N equidistant, opaque, parallel plates. Thermal radiation through the material is then modelled as a sequence of surface-to-surface processes, leading to Eq. (2.13).

$$\lambda_{rad,macro,Batty} = \frac{4 * \sigma_{SB} * T_{avg}^3 * d_{sample}}{N * \frac{2 - \epsilon}{\epsilon}} \cong \frac{4 * \sigma_{SB} * T_{avg}^3 * d_{pore,mean}}{\frac{2}{\epsilon} - 1} \quad (2.13)$$

Eq. (2.13) relates the macroscale radiative conductivity to the average temperature T_{avg} [K], the Stefan-Boltzmann constant σ_{SB} [W/m²K⁴], the material emissivity ϵ [–] and the sample thickness d_{sample} [m]. For high-porosity materials consisting of relatively equal pore sizes, the equation can be expressed as a function of the mean pore size $d_{pore,mean}$ [m] by equalizing this pore size to d_{sample}/N , yielding the second equality in Eq. (2.13). For highly-porous polymeric foams, the amount of radiation transmitted through a cell wall might become non-negligible though, invalidating Batty's model. Hence, Williams & Aldao (1983) proposed a model similarly based on parallel plates but now considering the transmitted part of the radiation. It calculates the radiative conductivity as a function of, among others, the net

fraction of radiation transmitted by one such plate (T_N [-]). The equations as presented by Solórzano et al. (2009) are shown in Eq. (2.14) & (2.15):

$$\lambda_{rad,macro,W\&A} = \frac{4 * \sigma_{SB} * T_{avg}^3 * d_{sample}}{1 + \frac{d_{sample}}{d_{pore,mean}} * \left(\frac{1}{T_N} - 1\right)} \quad (2.14)$$

$$T_N = \frac{1 - \rho}{1 - \rho * \tau} * \left(\frac{(1 - \rho) * \tau}{1 + \rho * \tau} + \frac{1 - \tau}{2}\right) \quad (2.15)$$

Here, ρ [-] is the infrared reflectivity of the solid-gas interfaces at normal incidence ($\theta_i = 0^\circ$) given by Eq. (2.16) as a function of the real part of the complex refractive index $n + i\kappa$ [-] of the solid material. The factor τ [-] is the transmissivity given in Eq. (2.17) as a function of the imaginary part of the complex refractive index $n + i\kappa$, the membrane thickness d_{wall} [m] and the wavelength λ_{wave} [m]. For thermal radiation at room temperature, it is reasonable to set the wavelength to 10 μm (at which there is the peak emission intensity).

$$\rho = \left(\frac{n - 1}{n + 1}\right)^2 \quad (2.16)$$

$$\tau = \exp\left(-\frac{4 * \pi * \kappa}{\lambda_{wave}} * d_{wall}\right) \quad (2.17)$$

Another often applied methodology is the Rosseland diffusion approximation. It calculates the macroscale radiative conductivity from the mean extinction coefficient $\beta_{ext,mean}$ [1/m] using Eq. (2.18) (the ‘mean’ refers to it being averaged over all wavelengths, the extinction coefficient is a parameter that also exist as a spectral radiative property). This approach is derived for optically thick materials with an isotropic intensity inside the material (Siegel & Howell, 1981), although corrections can be made to account for non-isotropic scattering (Glicksman, Schuetz, and Sinofsky 1987; Baillis, Coquard, and Moura 2015).

$$\lambda_{rad,macro,Rosseland} = \frac{16}{3} * \frac{\sigma_{SB} * T_{avg}^3}{\beta_{ext,mean}} \quad (2.18)$$

Physically, the extinction coefficient represents the inverse of the mean free path a photon will travel inside the medium before being either absorbed or scattered. The mean extinction coefficient can be measured but several authors have also presented correlations or models to calculate this factor. For example, Hsu & Howell (1992) present a function for this coefficient for open-celled reticulated ceramic foams based on experimental measurements, see Eq. (2.19). Glicksman & Torpey (1989) provided a similar formula for polymeric foams where the

cell walls are assumed to be transparent and all radiation extinction is due to the struts, see Eq. (2.20). The formulae again depend on the mean pore diameter, and on the mass density ratio of the porous material to the solid phase, which can be converted to the porosity ϕ .

$$\beta_{ext,mean} = \frac{3}{d_{pore,mean}} * (1 - \phi) \quad (2.19)$$

$$\beta_{ext,mean} = 3.68 * \frac{\sqrt{\frac{\rho_{sample}}{\rho_{solid}}}}{d_{pore,mean}} = \frac{3.68}{d_{pore,mean}} * \sqrt{1 - \phi} \quad (2.20)$$

Figure 2.2 shows the effective radiative conductivity predicted by three analytical models as a function of porosity (for a pore size of 1 mm) and as a function of pore size (for a porosity of 0.9). It is clear that all three models predict very different results owing to their different derivation and intended pore structure application.

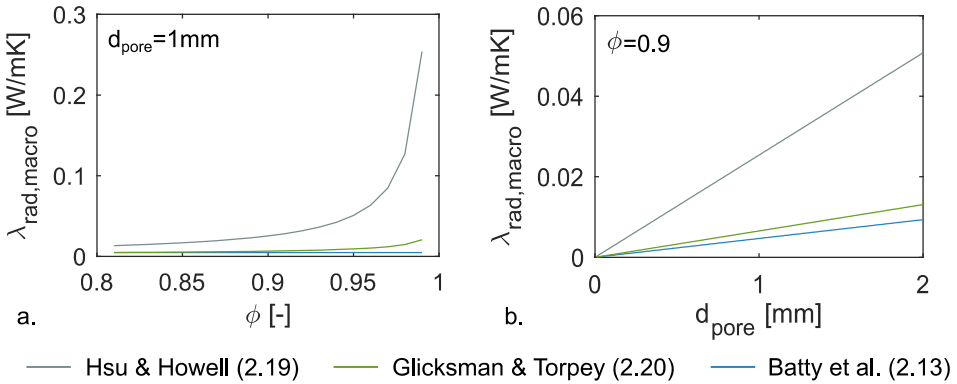


Figure 2.2: Predicted effective radiative conductivity as a function of porosity (a) and as a function of pore size (b). An average temperature of 20 °C is assumed for both cases. For case (a), the pore size is assumed to be 1 mm, while for case (b) the porosity is assumed to be 0.9.

A more elaborate procedure for calculating the mean extinction coefficient has been proposed by Placido et al. (2005) for insulation foams, taking into account the distribution of the solid material over the struts and cell walls using the strut factor f_s and the complex refractive index of the polymer. The calculation procedure is based on the independent scattering theory, and assumes a random orientation of the matrix components and no correlations of the extinction properties of each matrix component, so that the contributions of different components can be summed together. Similar approaches were developed for polymeric foams (Arduini-Schuster et al., 2015; Coquard et al., 2009; Kaemmerlen et al., 2010; Kuhn et al., 1992) and for open-celled metallic foams (Loretz, Maire, and Baillis 2008). The averaged pore structure

characteristics required in such models (cell wall thickness, strut size & shape, ...) can be obtained either from an ideal representation of the sample with unit cells or through microstructural analysis using SEM or μ CT scanning.

Coquard et al. (2010) introduced a number of correlations for the mean extinction coefficient derived from numerical simulations. Simulation results were obtained by solving the radiative transfer equation with the discrete ordinates method inside a unit cell pore structure. Several types of unit cells were tested, leading to a number of different correlations. Patel et al. (2018) recently also presented correlations for calculating the macroscale radiative conductivity of open-celled tetrakaidehedra pore structures. Based on numerical results obtained with a detailed modelling strategy developed by Talukdar et al. (2013), one of the correlations was presented as a form of the Rosseland approximation, with the extinction coefficient dependent on parameters as average temperature, pore size and porosity. The needed averaged pore structure characteristics can again be obtained from μ CT scanning or other characterization methods.

To avoid use of averaged pore scale parameters (cell size, wall thickness, ...), several numerical models have been developed to predict the mean extinction coefficient based on the detailed pore structure of a material. This is explored further in the section on numerical modelling. Although the mean extinction coefficient is hence not derived analytically, it can still be used in the Rosseland diffusion equation to calculate the macroscopic radiative conductivity.

Local radiative conductivity

A different analytical approach to account for thermal radiation was proposed by Loeb (1954), who suggested to calculate a local radiative conductivity in the pores instead of a macroscopic radiative conductivity for the whole material. He assumed that the radiative heat transfer takes place as a surface-to-surface process, implying that the solid phase is perfectly opaque. The radiative conductivity in each single pore is calculated with Eq. (2.21) based on the pore diameter d_{pore} [m], average temperature T_{avg} [K], Stefan-Boltzmann constant σ_{SB} [W/m^2K^4], material emissivity ϵ [-] and a shape factor γ_{Loeb} [-] to account for the pore shape. Considering the gas inside the pores as non-participating, radiative heat transfer occurs simultaneously with and parallel to gaseous heat conduction. The obtained radiative conductivity can thus simply be added to the gaseous conductivity, resulting in the total conductivity of the pore (Eq. (2.22)).

$$\lambda_{rad,pore,Loeb} = 4 * \epsilon * \sigma_{SB} * T_{avg,pore}^3 * d_{pore} * \gamma_{Loeb} \quad (2.21)$$

$$\lambda_{pore} = \lambda_{gas} + \lambda_{rad,pore,Loeb} \quad (2.22)$$

Loeb proposed a shape factor for circular and spherical pores as summarized in Table 2.1. Bakker et al. (1995) further investigated Loeb's method, by refining the shape factor for circular and spherical pores. Furthermore, he also calculated the shape factor for elliptical (2D) and oblate ellipsoidal (3D) pores. As the pore diameter is not clearly defined anymore for ellipse-shaped cavities, the parameter d_{pore} was defined as the maximum width of the pore (in the direction of the heat transfer).

Table 2.1: summary of shape factors proposed by Loeb (1954) and Bakker et al. (1995).

Pore Type	Loeb (1954)	Bakker et al. (1995)
Circular pore (2D)	$\pi/4 = 0.79$	0.55
Spherical pore (3D)	$2/3 = 0.67$	0.45
Elliptical (2D)	/	$0.55 - \pi/4$
Oblate ellipsoid (3D)	/	$0.45 - 0.56$

Later on, Fitzgerald and Strieder (1998) expanded the study, proposing an analytical formula to calculate the radiative conductivity in prolate and oblate ellipsoid shaped cavities/pores with variational theory. Application of these formulas requires the fitting of ellipsoids in every pore to subtract this information, which can be quite cumbersome certainly for real materials with irregular pore shapes.

For application in an analytical context, the pore diameter in Loeb's model is usually taken as the average pore diameter. Summation with the gaseous conductivity then provides an equivalent pore conductivity that can be used in the earlier discussed analytical models instead of the gas conductivity. This methodology has been applied several times in literature, i.e. in (Do, Bentz, and Stutzman 2007; Wan et al. 2011; Pennec et al. 2013). Calculating a proper radiative conductivity in every pore depending on the true local characteristics requires a numerical approach to predict the ETC, as will be discussed further on.

2.3. Numerical prediction of the ETC

Analytical models require an averaging of pore structure parameters and/or a simplification of the heat flows to obtain the desired analytical expressions. Several authors hence proposed numerical modelling strategies to allow for a full consideration of the pore structure and heat transfer mechanisms. The available models can be distinguished firstly according to the way they represent the pore structure geometry, and secondly along the numerical techniques applied to simulate the local heat transfer mechanisms. This section first investigates different techniques for pore structure representation and subsequently discusses numerical simulation techniques used to model the heat transfer. Due to the relatively limited availability of studies on porous building blocks, some results on other types of materials (i.e. foams) are included.

2.3.1. Pore structure representation

Regarding the geometry, pore structures are modelled via either unit cell approaches, virtual generation techniques or actual material images. Unit cell models, similar to some analytical models, simplify the pore structure to a regular periodic structure of cells. They provide a more exact solution of the local heat transfer though via the numerical solution. Some examples are described in literature for an open-celled metal foam (Schmierer and Razani 2006; Öchsner et al. 2009; R Coquard, Rochais, and Baillis 2010), a graphite foam (Druma, Alam, and Druma 2004; Chai et al. 2017), and polymeric foams (R. Coquard and Baillis 2009; Mendes, Ray, and Trimis 2013). Unit cell based models again present the disadvantage of very simplified representations of the pore structure with averaged pore structure parameters. Results are hence not directly applicable to real porous materials with randomly varying pore structures.

Therefore virtual generation techniques have been introduced, generating pore structures that mimic the irregular nature of porous materials. Several algorithms have been presented in literature to create different material types, different porosity ranges etc. Being conceptually and computationally more simple, several authors have presented such algorithms for 2D pore structures. Kaddouri et al. (2016) for example generated structures with randomly oriented but equally sized elliptically shaped pores to study the ETC of 2D composites. By varying the aspect ratio of the pores over different samples, they predicted a reducing ETC with higher aspect ratio (i.e. more elongated ellipses). She et al. (2018) also generated several 2D structures with randomly oriented pores to study the ETC of cellular concrete. They impose a certain pore size distribution and used different types of pore shapes (like triangles, squares, hexahedra etc.). Their simulation results showed for example a minimum ETC for triangular shaped pores. Lu & Chen (1999) aimed to study the ETC of aluminium foams and used a

different type of generation based on the Voronoi technique. By varying the generation parameters, they created 2D foam-like structures with different cell size distributions, matrix randomness and other geometric imperfections. A high degree of randomness and geometric imperfections was shown to reduce the resulting ETC. Solórzano et al. (2009) later on applied a similar technique to show that an increasing matrix tortuosity reduces the ETC. Other investigations employing generation techniques for 2D pore structure can be found in literature (M. Wang, Wang, Pan, and Chen 2007; Askari, Taheri, and Hejazi 2015). Although these models provide interesting insights on the effect of some parameters on the ETC, they tend to underestimate the actual ETC due to their neglect of heat flow via the third dimension (Van De Walle & Janssen, 2016; M Wang et al., 2007). This implies that their predictions are again not directly comparable to measurements, complicating the validation of the models. Given the increasing availability of computational resources, several studies have hence also presented 3D modelling techniques.

Nait-Ali et al. (2007) for example presented simulations performed on structures generated to represent highly porous ceramics. Starting from a lattice of all solid cubes, random cubes are designated as pores. They generated samples with either a monomodal or a bimodal pore size distribution, and demonstrated that the monomodal pore structures have a lower ETC. Ji et al. (2014) employed a similar approach to study the ETC of foamed concrete and lightweight concrete. She et al. (2014) describe a random sphere insertion (RSI) algorithm to represent the pore structures of foamed and cellular concretes. The algorithm generates spherical pores at random locations in a cubic sample with a random diameter according to a certain distribution and a controlled degree of overlap. Dyck & Straatman (2015) generated similar structures to study carbon foams. Their algorithm furthermore allows to create a random structure which is spatially periodic. Randrianalisoa et al. (2013) discuss a Voronoi method to mimic closed-cell polymer foams and open-cell ceramic and metallic foams by randomly perturbing a set of nodes placed on a regular grid. They studied for example the effect of matrix randomness on the ETC. Later on, Randrianalisoa et al. (2015) presented a Laguerre-Voronoi technique able to obtain foam-like structures with more controlled pore size distributions and studied among others the influence of the strut cross-section on the ETC. Wang et al. (2007) presented an original method called the Quartet Structure Generation Set (QSGS) to generate both granular and cellular porous media. The algorithm generates discrete images of voxels (or pixels in 2D) by randomly locating starting nodes and subsequently randomly growing these nodes in all directions until a set porosity is reached. Anisotropic materials can be generated as well by

specifying direction-dependent growth probabilities. Wang & Pan (2008) presented a similar discrete image generation method to create highly open-celled carbon and polyurethane foam structures. Nodes are randomly inserted and connected with neighbouring nodes by randomly growing 'fibers', resulting in a 3D net-like structure. Chen et al. (2015) presented a method to generate granular pore structures mimicking asphalt concrete. A randomly generated polygon with controlled aspect ratio is extruded in the third dimension and placed under a random angle as an aggregate in the asphalt volume. A similar procedure adds gas-filled pores as well in the volume. The algorithm was used in a multiscale hierarchical approach to study the effect of the aggregate aspect ratio and angle and the effect of graphite fillers on the ETC. Pennec et al. (2013) presented a methodology based on the discrete element method to generate granular structure with different degrees of compaction. The method was applied to study the ETC of bio-aggregates materials for building insulation. Gaiselmann et al. (2014) detailed an approach for generating fiber- and granular-like pore structures. Nodes are randomly inserted following a Poisson process and are connected with straight lines using a modified version of the relative neighbourhood graph able to create anisotropic materials. The lines are subsequently dilated with random radii allowing structures with very different geometrical properties. Based on a large set of generated samples, they showed that the porosity and the matrix tortuosity and constrictivity are the most influential parameters concerning the ETC.

Summarizing, simulations on virtually generated pore structures facilitate parameter studies on the impact of selected pore scale parameters. To generate strongly realistic pore structures, detailed knowledge of the pore structure is necessary, like porosity, pore size, pore topology, matrix shape etc. Such characterization can for example be done using imaging techniques like microscopy or μ CT scanning, resulting in an image of the material's pore structure. Along with the improvement of imaging techniques, some authors have thus proposed to use the detailed image of the pore structure directly as the input for a heat transfer model. Such image-based modelling alleviates the uncertainty on the similarity between the generated and real pore structure and allows to compare simulations directly with measurements on the same material. Attempts on 2D images of the pore structure again tend to underestimate the actual ETC though (Bakker 1997; Altun, Boke, and Alanyali 2011; Y.-H. Dong et al. 2012). Simulations on 3D images have been performed as well. Throughout literature, μ CT is clearly the most applied technique to obtain a 3D image of the pore structure as input for pore scale heat transfer simulations. Saadatfar et al. (2004) for example studied the ETC of several polyurethane foams with porosities between 45 % and 75 %, based on μ CT scans of their pore

structure. Results showed a consistent decrease of ETC with increasing porosity and fall in between both H-S bounds. Coquard & Baillis (2009) examined the conductive heat transfer in closed-cell PVC and XPS foams and open-cell metallic foams based on μ CT scans, showing a good agreement with analytical models and with simulations on idealized pore structures. Mendes et al. (2014) compared simulations of an open-cell metal foam directly with measurements over a large temperature range. The image-based model provided very good agreement. Other examples in literature can be found for different types of polymeric foams (Mendes, Talukdar, et al. 2014; Vignoles and Ortona 2016), ceramic foams (Ackermann et al. 2014; Jörg Petrasch et al. 2008; Haussener et al. 2009) and metallic foams (Fiedler et al. 2009; F. Wang and Li 2017).

2.3.2. Heat flow mechanisms modelling

At room temperature, heat is transferred mainly through the material via conduction through the matrix and the gas (Solórzano et al. 2009). For the pore structures considered in this part, having characteristic pore sizes above $1\ \mu\text{m}$, the local conduction in both phases (matrix and pores) can still be described by Fourier's heat law. Popular numerical solution methods solving this partial differential equation are the finite volume or the finite element method, both well-established and widely available in commercial as well as open source packages. Typically local conductivities are designated to the respective material phases and local thermal equilibrium is assumed at the phase boundaries. Examples can be found in literature (Jörg Petrasch et al. 2008; Wei et al. 2014; Talukdar et al. 2013; Ferkl, Pokorný, and Kosek 2014). The discretization of the domain in small elements has been carried out by both regular and unstructured grids, both attaining good results. Both methods are extensively covered in handbooks and no further discussion is provided here. Other methods have been proposed as well, for example the Lattice Boltzmann method using regular discretization grids (M. Wang and Pan 2008), or a random walker method using thermal resistor networks to represent the pore structure (F. Wang and Li 2017). For pore structures with pore sizes spanning multiple scales, the Multiscale Finite Elements technique has been applied as well (H. W. Zhang, Zhou, and Zheng 2011).

Apart from conduction, heat can transport through the pore structure via convection and radiation. Regarding natural convection, it is generally acknowledged in literature that the influence on the total heat transfer is negligible for pore structures with pore size dimensions of less than 2-4 mm (Sanjaya 2011; Clyne et al. 2006). The contribution of thermal radiation, on the other hand, is highly dependent on the pore structure (primarily the porosity and pore

size) and the temperature the material is subjected to. For medium to high porosities ($< 90\%$) and around room temperature, its contribution is often estimated to be moderate (Solórzano et al. 2009; Vignoles and Ortona 2016). Hence, many studies neglected this heat transfer mechanism due to its modelling complexity and computational cost. In foams with extremely high porosities, it can play an important role in the heat transfer through the material though, even at room temperature (Baillis et al. 2013). Most studies concerning the thermal radiation inside porous materials are hence focussed on highly porous polymeric, ceramic or metallic foam materials, which, together with their potential application in high-temperature applications, pushed the development of detailed predictive models. Good reviews of some models have been published (Baillis and Sacadura 2000; Dombrovsky and Baillis 2010; Baillis et al. 2013; Randrianalisoa and Baillis 2014; Cunsolo et al. 2016; Cunsolo, Baillis, and Bianco 2019). A short overview of some modelling strategies is given in the next paragraphs.

An often applied strategy for the integration of radiation is to use the Rosseland approximation (Eq. (2.18)) to calculate a macroscopic radiative conductivity, which is added to the macroscopic conductive conductivity (Eq. (2.12)). The required mean extinction coefficient can be calculated analytically as described before, but also numerical models have been proposed to better take into account the irregular pore structure of typical materials. For example, several ray tracing monte carlo algorithms (RTMC) have been developed. Such models generate rays at random locations on the pore surface and follow their path until they are extinct. Petrasch et al. (2007), Haussener et al. (2009) and Parthasarathy et al. (2012) for example used this strategy to study the radiative properties of reticulated ceramics, and Dyck & Straatman (2016) for graphitic foams. All these studies assumed an opaque solid material. Randrianalisoa & Baillis (2010) on the other hand developed a ray-tracing model to account for the semi-transparent solid phase. The methodology was later expanded to study the macroscale radiation properties of closed-cell polymeric foams characterized by μ CT scanning (Coquard et al., 2010) as well as virtually generated foams (Rémi Coquard, Randrianalisoa, and Baillis 2013).

The separate calculation of a radiative and conductive conductivity neglects the interaction of the local coupling between these two flow mechanisms. This can induce some errors in the derivation of the ETC, as was studied by Mendes et al. (2014). Therefore, several authors presented strategies to model the total heat transfer through a porous material considering the local coupling between conduction and radiation. The local radiative heat flux is then often

obtained by solving the radiative transfer equation (RTE). Two main strategies are available to deal with the combined conduction and radiation: the homogeneous phase approach (HPA) and the multiphase approach (MPA). In the HPA, conductive and radiative properties are first homogenized separately over the whole pore structure. Subsequently, the coupled conduction and radiation is simulated based on a homogeneous sample with the homogenized properties. Coquard & Baillis (2006) for example used this approach to model the heat transfer through expanded polystyrene foams: radiative properties were calculated with independent scattering theory and the conductive conductivity with analytical equations using a detailed geometrical representation of the two-scale pore structure. Subsequently, a finite volume in combination with a discrete ordinates method was used to model the heat transfer knowing the previously derived effective conductive and radiative properties. Mendes, Skibina, et al. (2014) used the HPA to study the ETC of metal foams at high temperatures. The radiative properties and effective conductivity are each derived based on the μ CT scans of the sample. In the last step, the coupled heat transfer was simulated by the finite volume method in combination with the discrete transfer method on a homogeneous sample.

The multiphase approach (MPA), on the other hand, does not involve such homogenization and solves the coupled equations in both the matrix phase and the pore space considering the respective local conductive and radiative properties. For 2D samples, Lu & Chen (1999) for example used the view factor method to model the radiative heat exchange between the opaque pore cell walls. For 3D samples, this strategy would necessitate unreasonable amounts of computational power though. Therefore, Talukdar et al. (2013) for example developed a blocked-off-region approach for porous materials consisting of an opaque solid phase, based on the finite volume method. Conductive heat flow was modelled with Fourier's law while radiative heat transfer in the pore space was quantified with the RTE. The model was later used to investigate the radiative properties of unit cell and real open cell foams (Patel and Talukdar 2016, 2018), and to obtain analytical correlations for the radiative conductivity (Patel et al. 2018). Other applications of the MPA can be found in literature for polymeric foams (Ferkl, Pokorný, and Kosek 2014) or open-cell foams with opaque matrix (Vignoles 2016; Vignoles and Ortona 2016). A comparison of the HPA and MPA can be found as well (Jörg Petrasch, Haussener, and Lipinski 2011; Mendes, Talukdar, et al. 2014; R. Coquard, Baillis, and Randrianalisoa 2011; Cunsolo, Baillis, and Bianco 2019)

Lastly, some authors have applied Loeb's method (1954) to account for thermal radiation in their numerical model. As discussed earlier, this method consists of calculating a local

radiative conductivity in every pore based on the local dimensions. This equivalent radiative conductivity is then summed with the gaseous conductivity in the respective pore. This provides a computationally less complex way of modelling thermal radiation while still respecting the local coupling with thermal conduction. As such, it can also be considered as a MPA method, though simplified to a conduction-only problem. As discussed previously, the approach assumes opaque cell walls, meaning it cannot be applied in cases where transmission through the cell walls is playing an important role (i.e. in high porosity polymer foams). Examples can be found in (Bentz 2006; Pennec et al. 2013).

2.4. Impact of pore scale parameters on ETC

Porous building blocks based on waste materials need a reduced ETC to promote their application potential. Based on studies performed with previously presented modelling strategies, some general effects of the pore structure on the ETC can be distilled. Furthermore, some experimental studies investigated the effect of some pore scale properties as well. A short summary on the effect of some pore structure parameters described in literature is presented here.

Porosity: all models agree on the porosity as a very important parameter. The ETC as expected decreases with increasing porosity due to the lower thermal conductivity of the pore space gas compared to the matrix conductivity (Laurent 1991; Bracconi et al. 2018). However, at the same time the amount of radiative heat transfer through the material increases, which might cause the ETC to start increasing again at certain high porosities, depending on the matrix material and the pore size. At room temperature, authors reported such transition points around and above 95 % porosity (R. J. Z. Zhang, Liu, and Wang 2013; Placido, Arduini-Schuster, and Kuhn 2005; Ferkl, Pokorný, and Kosek 2014).

Average pore size: the effect of the average pore size is on the contrary less clear. Regarding thermal conduction through the material, the pore size theoretically has no impact. To avoid an increasing ETC by natural convection, pore sizes should however remain below 2 to 4 mm (Sanjaya 2011; Clyne et al. 2006). At smaller pore sizes, solely the radiative transfer through the material is influenced. With reducing the pore size, the ETC typically decreases due to the reduced mean free path of the photons between pore surfaces (Almanza et al. 2001). However, below a certain pore size, the amount of thermal radiation going directly through a cell wall – whose thickness reduces as well – may become important, depending on the porosity and the matrix' physical properties (Placido, Arduini-Schuster, and Kuhn 2005; R. Coquard and Baillis

2006; G. Wang, Zhao, Wang, et al. 2017). Thus, the ETC can increase again with further reduction of the pore size, depending strongly on the material's properties (G. Wang, Wang, et al. 2017; G. Wang et al. 2018).

Pore size distribution: Nait-Ali et al. (2007) demonstrated that a monomodal distribution performs better than a bimodal distribution for ceramics with cubically shaped pores. Pia & Sanna (2014) similarly obtained such conclusions for pore structures generated using fractals: a narrower distribution reduces the ETC. Xu et al. (2012) made a similar conclusion, noticing a reducing ETC with a more compact distribution. Randrianalisoa et al. (2013) on the other hand obtained a reduced ETC with a wider distribution. She et al. (2018), then, found that the distribution has a negligible influence on the ETC, based on 2D structures. In short, the effect of the pore size distribution is not well understood and results seem somewhat contradictory, though this is probably at least partially explained by the different types of materials studied.

Pore shape: Bauer's model using the sphericity as shape factor indicates that non-spherical pores with higher aspect ratios reduce the ETC (Eq. (2.10)). Ordonez-Miranda et al. (2012) used a modified Bruggeman's model showing the same results and showing that randomly-oriented 'pancake-shaped' pores reduce the ETC more effectively than 'cigar-shaped' pores. Kaddouri et al. (2016) recently also showed that a higher aspect ratio for elliptically shaped pores in 2D reduces the ETC. She et al. (2018) also obtained this reducing influence of an increasing aspect ratio on the ETC. They equally showed that, in case the elliptic pores are aligned, the ETC is anisotropic and largest in the direction of the largest axis. Furthermore, they showed that triangular pores perform even better than elliptic pores, which was explained by the increasing matrix tortuosity.

Matrix structure: regarding the matrix structure, an increasing tortuosity expectedly reduces the ETC (She et al. 2018; Gaiselmann et al. 2014). Although it is not clear whether this differs from the tortuosity, Lu & Chen (1999) argue that a certain 'randomness' of the matrix structure reduces the ETC as well. As indicated by Glicksman's model (Eq. (2.7)), a higher concentration of matrix material in the struts versus the walls also decreases the ETC. This was confirmed by Coquad & Baillis (2009). Ultimately, the matrix constrictivity has also been put forward as an important factor influencing the ETC: representing the ratio of highest area to lowest area, an increasing constrictivity was shown to reduce the ETC by Gaiselmann et al. (2014). Randrianalisoa et al. (2015) also demonstrated a significant reduction when struts have a non-uniform cross-section, Bracconi et al. (2018) came to similar conclusions.

Summarizing, to obtain low ETC, literature points in the direction of high porosities combined with a small pore size, although for both properties there exist optimal combinations of values, depending on other properties such as matrix conductivity as well. The effect of the pore size distribution is still contested and certainly merits further research. Regarding the pore shape, higher aspect ratios seem to reduce the ETC. This is probably also related to an increasing matrix tortuosity, which together with the matrix constrictivity are put forward as most influential. Combined impact of all mentioned parameters is still unclear though, certainly for porous building blocks for which required mechanical properties can impose certain limits on the parameters. A better knowledge of the impact of the parameters over different ranges can hence provide useful insights in further optimization efforts.

2.5. Conclusions

This chapter provided a survey of previous modelling efforts described in literature to predict the ETC of porous materials. Some analytical expressions were discussed relating the ETC to the phases' conductivities and the porosity and – for more advanced models – the pore size or pore shape. The contribution of thermal radiation has also been considered analytically, either via a macroscopic or a local radiative conductivity. Analytical models are based on simplified pore structures though and require averaged characteristics as input. Their application for true optimization is thus very limited. Numerical modelling on the other hand seems very promising to more accurately consider the local pore structure parameters. Both detailed imaging and virtual generation of the pore structure have been proposed to represent the pore scale geometry, providing the opportunity to study the ETC of actual materials and to virtually design materials. Most studies have focussed on high-porosity foams while only a limited amount of studies have targeted – moreover very specific types of – porous building blocks. Furthermore, some studies have neglected certain heat transfer mechanisms leaving doubt on the applicability of the conclusions for the diverse range of pore structure properties present in porous building blocks.

The last section of this chapter introduced the current knowledge on the impact of the pore structure parameters on the ETC. Although some general trends on their separate impact have been discussed in literature, their combined impact is still unclear though, clouding the current optimal pathway to further reduce the ETC. A better knowledge of the impact of the parameters over different ranges is hence needed for further optimization efforts.

Implementation of the microscale model framework¹

3.1. INTRODUCTION	33
3.2. IMPLEMENTED FRAMEWORK OVERVIEW	34
3.3. THERMAL CONDUCTION	42
3.4. THERMAL RADIATION	45
3.5. THERMAL CONVECTION	62
3.6. VERIFICATION OF IMPLEMENTED PHYSICAL MODELS	63
3.7. CONCLUSIONS	76

3.1. Introduction

The literature reviewed in the previous chapter indicates the advantages of using numerical pore scale simulations to investigate the impact of the pore scale parameters on the macroscale effective thermal conductivity (ETC). Such strategy alleviates the need for averaging pore characteristics and reduces the applicability uncertainty typically associated with correlations derived on a specific type of pore structure. Hence, in this chapter a numerical model framework is presented and implemented to perform pore scale heat transfer simulations. Based on the literature on numerical modelling detailed in Chapter 2, a number of requirements for an accurate and versatile performance of the model can be distinguished:

- **3D model:** as stated by several authors (i.e. Dong et al., 2012; Wang et al., 2007; Wei et al., 2013), numerical simulations performed on 2D representations of the pore structure result in a consistent underestimation of the ETC due to the neglecting of heat transfer paths around the heat blocking pores in the third dimension. Although

¹ Parts of this chapter have been published in Van De Walle et al., 2018, *Constr. Build. Mater.* 182,427-440

such simulations can still be used to study the relative effect of some parameters, a good agreement with experimentally measured samples requires the simulations to be performed on a full 3D representation of the pore structure.

- **Image-based approach:** direct comparison of the obtained ETC with experimental measurements requires the simulated pore structure to closely resemble the real pore structure. An image-based approach allows simulations on images obtained by μ CT scanning of the material. Furthermore, several generation algorithms can also easily generate a 3D image format of a virtual structure. Hence, such image-based approach has the most application potential.
- **Account for relevant physics:** several models presented in the literature review either neglect gaseous conduction or thermal radiation, assuming their contribution to the total ETC is negligible (i.e. She et al., 2014). However, their contribution depends strongly on the pore structure parameters like porosity, pore size etc. and the physical parameters like solid conductivity, emissivity etc. Therefore, to not a-priori confine the model's applicability range, all relevant physics should be accounted for.

The here presented numerical framework is implemented to conform to all these requirements. The different steps of the model are presented in the next section. Subsequently, the implementation of the physical models for the respective heat transfer mechanisms are detailed in the three following sections. The model framework is finally verified with reference solutions obtained from literature and via simulations performed with other modelling strategies.

3.2. Implemented framework overview

To quantify the effective thermal conductivity of porous building materials, a novel numerical model framework is implemented, simulating the heat transfer through the material at the pore scale. The framework consists of three main steps, as shown in Figure 3.1:

- 1) **Obtaining the geometry:** to accurately study the influence of local pore scale characteristics, a 3D representation of the actual pore structure should be obtained, avoiding the need of averaging pore scale parameters like pore shape, size and distribution in the volume. As input for the framework, the structure should be represented by a 3D, cubic image consisting of voxels.

- 2) **Creating a finite element mesh:** a tetrahedral finite element mesh is constructed based on the 3D image of the pore structure. Both the matrix phase and pore space are meshed. This mesh serves as input for the numerical simulation in the next step.

- 3) **Performing the thermal simulation:** a stationary thermal simulation of the local heat transfer is performed by applying a constant temperature difference across the sample. The resulting heat fluxes allow to deduce an effective thermal conductivity for the studied sample.

The entire framework is controlled via a set of MATLAB routines allowing an easy automatization and parametrization. All three steps are discussed in more detail below.

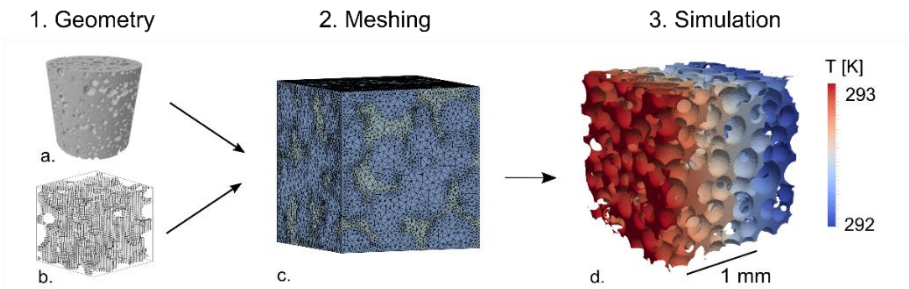


Figure 3.1: Overview of the model workflow: (a) micro-CT image as input; (b) virtually generated image as input; (c) finite element mesh; (d) temperature profile after simulation.

3.2.1. Pore structure geometry image

An adequate representation of the material's microstructure is primordial to accurately capture the influence of the microstructural features – like the material porosity, matrix connectivity, ... – on the effective thermal conductivity. To alleviate the known underestimation by simulations based on 2D models and to allow for an easy and versatile modelling of both virtually generated and real structures, a 3D volumetric voxel image is adopted here to represent the microstructure. Similarly to 2D pixel images, voxel images consist of cubical elements organized in a regular 3D grid, where the intensity value of each voxel depicts the material phase located at that specific position. The total amount of voxels and the side length of one voxel is called the image size and the voxel size, respectively. The term resolution refers to the amount of voxels per length unit.

The discussed 3D images are generally acquired via one of two methods: through microscale scanning techniques for real materials, or through microstructure generation algorithms for virtual materials.

μ CT scanning of real materials²

Performing simulations on real materials enables a direct comparison of the model with experimental measurements of the thermal conductivity and microstructural features. Micro-CT scanning is a commonly used technique to characterize the microstructure of porous materials, measuring the X-ray penetration of the sample at different sample rotation angles and reconstructing the obtained 2D projections into a 3D voxel image (Herman 2009; Wevers et al. 2018). Typically, the smallest voxel size attainable with these systems is about $1\ \mu\text{m}$, while the maximum image size is around 1000^3 voxels. Major advancements throughout the past decennia have furthermore significantly reduced the amount of scanning inaccuracies and artefacts, allowing an adequate and detailed characterization of the microstructure.

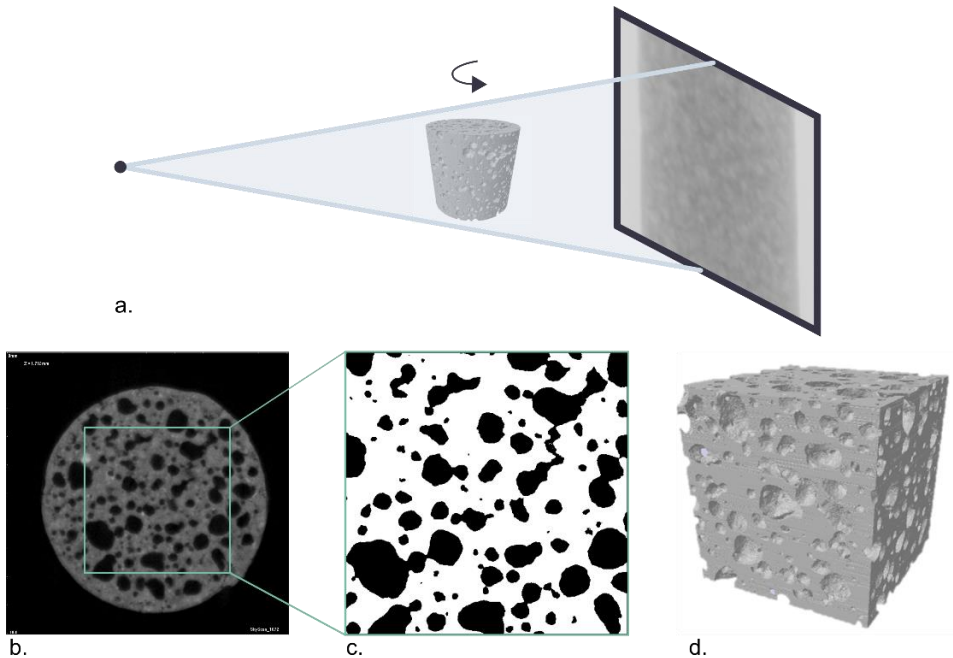


Figure 3.2: demonstration of process to obtain 3D image matrix of a Xella C5/650 cellular concrete block: μ CT-scanning of a cylindrical sample results in projection images (a), which are subsequently reconstructed to slices (b). A segmentation procedure is performed on part of the scan to differentiate the pores and the matrix phase (c), resulting in a 3D image matrix (d).

² Most CT images in this work are acquired and segmented by dr. ir. Steven Claes.

After scanning, the resulting projection images are reconstructed by dedicated software to a 3D image volume consisting of horizontal slices. The resulting 3D image is a grayscale image, with the voxel intensity values having a distribution of grayscale values. To use the image for simulation, the pore space and matrix need to be clearly differentiated, a process referred to as image segmentation. For more details, the reader is referred to more specialized literature (Claes 2015; Wirjadi 2007). A demonstration of the whole process on a cellular concrete sample is shown in Figure 3.2.

Generation of virtual materials

Performing simulations on virtual materials facilitates the study of specific microscale features and the evaluation of newly designed microstructures. The voxel image format is also adopted here, allowing a deterministic or stochastic generation of pore structures. Examples of deterministic generation are unit-cell-like materials like honeycomb structures or spheres organized on a regular lattice. Stochastic generation algorithms, on the other hand, can be used to generate a wide variation of pore structures, mimicking the typically stochastic nature encountered in real porous materials. The algorithm by She et al. (2014) (further on called the Random Bubble Insertion method, RBI), for example, inserts spherical pores at random locations inside a cubic medium. The pores' diameters can be randomly assigned according to a statistical distribution (i.e. lognormal). An example is shown in Figure 3.3a&b, showing a slice through the material and a 3D render of the matrix structure. Randrianalisoa et al. (2013), as another example, describe a technique based on the Voronoi algorithm (further on called the Voronoi technique). The algorithm divides the cubic volume in pore cells based on initially placed seeds, resulting in a foam-like pore structure. An example is shown in Figure 3.3c&d. Other recent examples can be found a.o. in (Gaiselmann et al. 2014; M. Wang, Wang, Pan, and Chen 2007; Dyck and Straatman 2015).

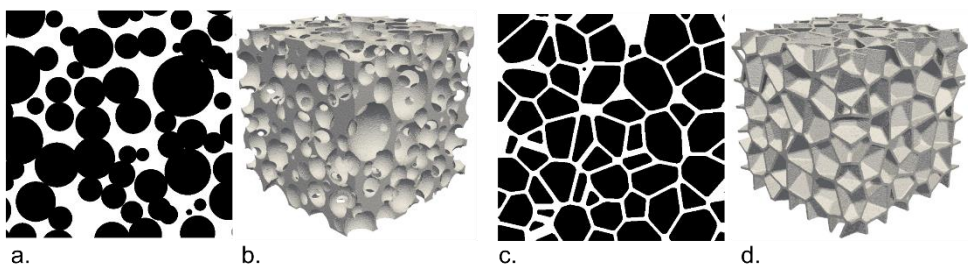


Figure 3.3: Slice and 3D render of sample generated by the Random Bubble Insertion (a&b) and by the Voronoi (c&d) technique. The white space in the slices marks the matrix phase, the black space marks the pore space.

3.2.2. Numerical discretization

Several numerical techniques exist to solve the heat transfer equations in a complex geometry like the intended pore structure. Well-known examples are the control volume method, finite element method, finite difference method, lattice Boltzmann method, etc. Due to the existing expertise with the finite element (FE) method in the Building Physics Section of the KU Leuven, the choice is made to use this technique. Although the FE method is not locally conservative, it has been shown to obtain very good results of the total heat flow and temperature distribution. As such, it has become a well-established technique for solving heat transfer problems and is supported by many simulation packages. The technique requires the domain to be divided into small elements of finite size, where every element has a number of nodes. During the simulation, the temperature is calculated at every node, while inside every element the temperature field is approximated by a polynomial interpolation between its nodes.

The FE method is a very versatile method, allowing to use several different types of interpolation functions, with higher order polynomials, and different types of finite elements for the numerical discretization of the domain. Here, the choice is made to use tetrahedral elements for the numerical discretization. This type of elements is supported by many simulation packages and permits the approximation of complex-shaped geometries with curved edges. Furthermore, tetrahedral elements allow a locally varying mesh size, which can be beneficial to reduce the computational cost. Nonetheless, other techniques might be equally suitable but have not been tested in this work.

Meshing procedure

Building a tetrahedral mesh from a geometry represented by a voxel image is a non-trivial task. Indeed, boundaries between two phases (i.e. the surface of a pore) appear as very crenelated surfaces. It is usually not desired to follow this staircase-like geometry very strictly, since it is not representative for the actual pore surface, and furthermore would lead to excessively small finite elements and huge computational demands. In the last decade, a lot of interest has been shown in such image-based meshing strategies (Young et al. 2008), with several commercial codes starting to offer this possibility (Simpleware, Mimics, Avizo, ...). Different types of meshing algorithms have been developed and applied for such meshing, like advancing front techniques, octree-based models and Delaunay triangulation techniques.

Here, the choice is made to use the open-source code `iso2mesh` for creating the tetrahedral finite element mesh. Implemented as a toolbox for Matlab, it offers a number of scripts to handle and prepare the 3D image matrix for the meshing procedure (Q. Fang and Boas 2009). The actual meshing is performed by a c++ code based on the functions provided by the CGAL library (v4.6.3). The meshing algorithm is based on the Delaunay refinement technique (Boltcheva et al. 2009; Alliez et al. 2015). An initial set of points (or vertices) is sampled on the domain boundaries and serves to calculate a first tetrahedral mesh based on the Delaunay triangulation algorithm: every resulting tetrahedral element will have a circumscribing sphere that does not contain any other vertex except for the vertices constituting the concerning tetrahedron. Subsequently, the triangulation is refined by adding additional vertices at specific locations until a set of preset meshing criteria are met. Lastly, an optimization procedure is executed to remove bad tetrahedra (called ‘slivers’) that still survived the Delaunay refinement. The whole procedure was completely implemented in the CGAL library and the `iso2mesh` toolbox, requiring the user only to specify the meshing criteria. Tetrahedral meshes obtained by such Delaunay refinement techniques usually consist of relatively qualitative elements (Shewchuk 2003). Furthermore, depending on the chosen criteria, it allows to naturally smooth out the jagged interfaces existing between the pores and the matrix in the voxel image.

Two problems can arise though when creating a tetrahedral mesh using the previously described method. The first is that the algorithm does not inherently respect 1D (lines) and 0D (points) features present in the voxel image. To improve the approximation of the edges of the cubic sample, we extend the existing procedure with an edge-point-insertion algorithm. The algorithm will place, before the actual Delaunay triangulation, vertices along the edges of the cubic sample at a specified equidistant interval. These vertices will be used in the subsequent mesh refinement, ensuring an improved approximation of the straight cube edges. The other problem is that very small subdomains, like small pores, can be overlooked by the meshing algorithm because of its semi-random nature. Indeed, the material phase associated with each tetrahedron is defined based on the location of the centre of its circumscribing sphere. Since the meshing algorithm first creates a coarse tetrahedral mesh, it is quite likely that by coincidence some small pores don’t contain any such sphere centre, and hence no tetrahedron is associated with that pore. Even in the refinement stage of the meshing algorithm, it can happen that still no such sphere centre falls into the overlooked small pores. Hence, the respective pores do not appear in the resulting mesh. Imposing a smaller mesh size

for the respective pore will only help if a tetrahedron falls by coincidence in this subdomain. To solve this known issue³, we implement a seeding algorithm that locates 4 vertices forming a tetrahedron in every subdomain. This will guide the Delaunay triangulation and help to not overlook certain very small pores.

Meshing parameters

During the Delaunay refinement, the algorithm will continue refining the mesh until a certain set of criteria is met. These criteria govern respectively the surface elements (triangles) and volume elements (tetrahedra). In this work, the two most important parameters that have been altered to construct the meshes are the parameters governing the resulting size of the mesh. These are the maximum radius of the triangle's surface Delaunay ball (for surface elements), and the maximum radius of the tetrahedron circumscribing sphere (for volume elements). This last value can be defined separately per material label, allowing to create a mesh with locally smaller mesh elements. The lower bound for the angles of the triangular elements, and the maximum ratio between the tetrahedron circumscribing sphere's radius and its shortest edge are kept the same as proposed standardly by iso2mesh (30° and 3 respectively). The maximum distance between the surface elements and the actual surface is also kept at the standard value of 0.5 voxel side length, which naturally leads to a smoothing of the jagged interfaces present in the 3D voxel image.

3.2.3. Simulation

In the last step, simulation of the local heat transfer is performed based on the finite element mesh constructed before. All relevant heat transfer mechanisms are modelled as conductive transfer mechanisms, by specifying a constant thermal conductivity for the concerning domains. Hence, the thermal simulation reduces to solving the Fourier equation for stationary heat conduction in every element. A temperature difference of 1 K is applied across the cubic sample in the x-direction by specifying a constant temperature on both opposing sides of the sample. The other 4 sides are set to adiabatic conditions, which can be interpreted as if a geometric symmetry exists in the pore structure along these sides. More details on how the respective heat transfer mechanisms are modelled are given in Section 3.3 till 3.5.

Both COMSOL Multiphysics and Elmer have been used to perform the simulations. COMSOL Multiphysics is a commercial software package offering an already implemented toolchain for

³ See for example discussion online (last consulted on 04/05/2019): <http://cgal-discuss.949826.n4.nabble.com/make-mesh-3-sub-domain-not-meshed-td4655774.html#a4655820>

operation directly from Matlab. Elmer on the other hand is an open-source package specially designed for large-scale parallel computing and is available on the High Performance Computing supercomputer of the KU Leuven. A toolchain to operate the software directly from Matlab is implemented in this work. Inter-comparison of results obtained with both software packages indicate the accurate performance of both packages.

After simulation, the local temperature field and heat fluxes are obtained. Based on the heat fluxes, the ETC can be obtained by assuming that a similar total heat flux should flow through the sample when considering it as a homogeneous material with such ETC. Rewriting the Fourier equation for such a homogeneous sample leads to the expression shown in Eq. (3.1), where $\bar{q}_x [W/m^2]$ is the one-dimensional heat flux in the direction of the applied temperature difference through such a homogeneous sample. $T_{hot}[K]$ and $T_{cold}[K]$ are the temperatures applied on both sides of the sample and $d_{sample}[m]$ is the sample thickness.

$$\lambda_{eff} = \frac{\bar{q}_x * d_{sample}}{(T_{hot} - T_{cold})} \quad (3.1)$$

The equivalent homogeneous heat flux \bar{q}_x can be calculated from the simulation results in two ways: either as a surface-averaged value on one of the constant temperature boundaries of the real sample (Eq. (3.2)), or, as proposed by Chen et al. (2015), as a volumetric-averaged value over all tetrahedral elements in the simulated sample (Eq. (3.3)). This latter approach has the advantage of results being integrated over a larger domain, meaning local numerical deviations will less influence the calculated ETC. Hence, this approach is followed throughout the rest of the work.

$$\bar{q}_x = \frac{\int_{A_{bdy}} q_x * dA}{\int_{A_{bdy}} dA} = \frac{\int_{A_{bdy}} q_x * dA}{d_{sample}^2} \quad (3.2)$$

$$\bar{q}_x = \frac{\int_{V_{sample}} q_x * dV}{\int_{V_{sample}} dV} = \frac{\int_{V_{sample}} q_x * dV}{d_{sample}^3} \quad (3.3)$$

3.2.4. Remarks

As a final note on the model framework, it needs to be stressed that the proposed framework is just one of the many possibilities for such pore-scale simulations. Apart from the mentioned advantages, it is quite likely that other modelling strategies have certain benefits as well. However, the aim of this work was never to create the single most optimally functioning

framework: it is a proof-of-concept framework to investigate the merit of pore-scale based simulation and quantify the impact of certain pore scale parameters on the ETC. Several measures to improve the efficiency of the current framework are indeed still possible, but are out of scope for this current work. For example, regarding the meshing part of the framework, it is envisioned that the continuous improvements of mesh generation algorithms probably facilitate the creation of meshes with improved quality and at higher computational speed thanks to, for example, parallel meshing algorithms. Likewise, several scripts needed during the pre-processing of the 3D image are implemented for robust functioning, and have not yet been optimized for speed.

3.3. Thermal Conduction

At room temperatures, heat is transported mainly in the form of solid or gas conduction through the material (Solórzano et al. 2009). In the presented model framework, local conduction through the solid matrix and through the pore gas is modelled with Fourier's conduction law, by specifying the respective thermal conductivities of the concerning phases. The following sections provide a short discussion on the actual mechanisms behind such conduction processes and the characteristic lengths below which the conduction law is not valid anymore. More in-depth discussion is reserved for Part II of this thesis.

3.3.1. Solid heat conduction

Although solid heat conduction is often modelled as a diffusive process using Fourier's conduction law and a material-dependent thermal conductivity λ_{solid} , the actual physics behind this process are much more sophisticated. Indeed, Fourier's conduction law is in fact an empirical law, using the thermal conductivity as, even for perfectly solid elements of one single material, a macroscopic parameter averaging the microscopic behaviour. Research on the actual physics of heat conduction has evolved rapidly since the introduction of microscopic elements like micro-electronic chips, for which the microscopic behaviour of heat conduction is more notable and Fourier's conduction law loses its validity.

For non-electrically conducting materials, heat conduction occurs via atoms oscillating around their position. Atoms at higher temperature will vibrate more intensely, transferring energy to their neighbouring atoms through their connecting bonds. Several mathematical models have already been proposed to describe the resulting conduction and macroscopic thermal conductivity based on the microscopic behaviour, Debye's model and Einstein's model being two of the most famous (Z. M. Zhang 2007; Cahill and Pohl 1989). Such models

allow to explain and study the effect of the domain's size and temperature on the macroscopic thermal conductivity of the solid material. Indeed, for a certain material with certain atomic structure, both parameters can have a large influence on the ease of solid conduction through the material.

The size of the domain influences the extent to which vibration waves of collectively oscillating atoms can travel through the medium. A reducing domain size will reduce the possible distance such energy waves can travel, reducing the ease of conduction and accordingly the macroscopic conductivity. The domain size below which such effects become important depends largely on the type of atomic structure (crystalline, poly-crystalline, amorphous), local impurities and sample temperature. For materials typically found in the building industry (polymers, silicates, ...), there is hardly any effect noticeable around room temperature in domains with a characteristic size above hundreds of nanometres (see Part II). Pore structures considered in this first part of the thesis all have characteristic dimensions in the order of μm and above, meaning no such reducing effect is expected here. Together with the fact that detailed modelling strategies like molecular dynamics are computationally very intensive on a full complex 3D pore structure, the solid conduction process is modelled using Fourier's conduction law.

The local temperature influences the material's specific heat capacity and the amount of vibration waves, which in turn affects the thermal conductivity: depending on the atomic structure, the thermal conductivity can increase or decrease strongly with increasing temperature. However, for the limited temperature range building materials are typically exposed to (roughly $-10\text{ }^{\circ}\text{C}$ to $40\text{ }^{\circ}\text{C}$), the effect on the solid conductivity is quite small. Hence, this temperature-dependence is not considered in this work and the solid thermal conductivity is simply considered as an a-priori set constant parameter. Needed values can be retrieved in specialized literature or determined experimentally (i.e. Fiala et al., 2018; Horai and Simmons, 1969). Some exemplary values are shown in Table 3.1 illustrating the order of magnitude; exact values can vary because of chemical properties, mass density, etc.

Table 3.1: Exemplary values of solid thermal conductivity at room temperature of some typical materials used for porous building materials.

Material	λ [W/mK]	Source
PMMA polymer	0.2	(Childs, Ericks, and Powell 1973)
PU polymer	0.21	(Nielsen et al. 2000)
Glass	1.06	(Choudhary and Potter 2005)
Cement mortar (dried)	1.1	(Siwińska and Garbalińska 2011)

3.3.2. Gaseous heat conduction

Gaseous heat conduction in macroscale applications is also usually modelled using Fourier's conduction law with a gaseous thermal conductivity. Microscopically, the physics behind gaseous heat conduction are again much more sophisticated, and different from solid conduction as well. Gaseous conduction originates from the microscopic movement of gas molecules. Each molecule has a certain amount of energy, with molecules in zones of higher temperature on average in possession of more energy. Moving around in random directions, energy is transported over small distances and partially exchanged with other molecules via collisions. This, on average, causes heat to flow from the warmer side of the gas to the colder side. Macroscopically, this translates to a diffusive process that can be described with a gaseous conductivity.

The gaseous conductivity depends mainly on the type of gas and the gas temperature. Different types of gas molecules with different weight or atomic structure can have different modes of energy storage (like kinetic energy, rotational energy, internal vibrational energy, ...), leading to different thermal conductivities. Temperature, on the other hand, will increase the amount of energy per molecule and their speed, hence also increasing the energy transported and as a result also the macroscopic thermal conductivity. For most gases, the thermal conductivity is well detailed in literature as a function of temperature (NIST 2018). For a selected range of gases, the thermal conductivity is shown in Figure 3.4 as a function of temperature.

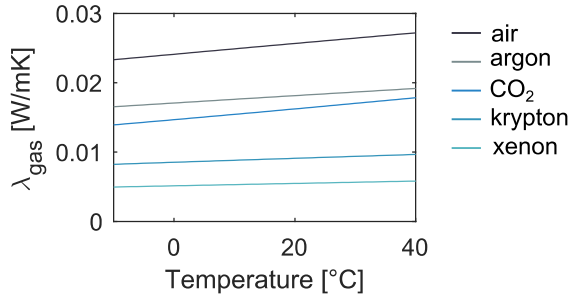


Figure 3.4: gaseous thermal conductivity of some common gases as a function of temperature.

The gaseous thermal conductivity also depends on the domain size and, in case of entrapment in a cavity, on the gas pressure. Indeed, when the domain size reduces to the order of the gas molecules' mean free path, their energy is transported literally less far. As a consequence, the gaseous conductivity reduces as well. For air, such effects set in at pore sizes below a few hundreds of nanometres. A similar effect occurs when the gas pressure is reduced for gas entrapped in a cavity: reducing the pressure induces an increasing mean free path, meaning gas molecules sooner 'feel' the effect of the cavity. Several formalisms exist in literature to model the microscopic behaviour and interaction of the gas molecules, allowing to explain such reducing effects (see Part II). In this part, focus is placed on materials with pore sizes well above 1 μm and at atmospheric gas pressure, meaning no such nanoscale effects will occur. The gaseous conductivity is set to its value retrieved in literature for the concerning temperature. Given the small temperature difference of 1 K applied across the sample, a constant value instead of a temperature-dependent value is used, reducing computation complexity without significant effects on the accuracy.

3.4. Thermal Radiation

The contribution of thermal radiation to the ETC of porous materials depends on a large range of parameters. It is generally acknowledged that in materials at room temperature and with low to medium porosity, thermal radiation plays a negligible role (Solórzano et al. 2009). However, in materials with extremely high porosities like insulation foams, it can contribute considerably to the total amount of heat transferred through the material, certainly in case of transparent cell walls (Baillis et al. 2013; Placido, Arduini-Schuster, and Kuhn 2005; Glicksman, Schuetz, and Sinofsky 1987). For materials with medium to high porosities, its contribution is less clear and it's often not taken into account in models of such porous building materials. To be able to quantify the contribution, a simplified modelling strategy is

introduced in this section. First, a short background on the origin of thermal radiation is given. Subsequently, the implementation and expansion of a simplified method is detailed.

3.4.1. Background on thermal radiation

Thermal radiation refers to electromagnetic radiation generated due to the internal thermal state of the material's molecules. All molecules with a temperature higher than 0 Kelvin will emit electromagnetic waves carrying energy (or heat) in a certain direction. The maximum amount of emitted energy per surface area and per time is predicted by Stefan-Boltzmann law, and is according to Planck's law distributed over a spectrum of wave frequencies or wavelengths. Roughly, electromagnetic waves considered as thermal radiation have wavelengths in the range between 0.1 μm and 1000 μm , the distribution depending on the temperature of the emitting body and its material properties. When encountering other molecules along the way, waves can be absorbed as thermal energy or scattered in a different direction. The emission of thermal radiation by a certain material and the interaction of thermal radiation incident on a material not only depends on the material properties, but also on the direction of the radiation compared to the material and the wavelength of the thermal radiation.

The propagation of electromagnetic waves is described by Maxwell's four equations. However, for most thermal applications, the full consideration of the system's electromagnetic behaviour would be unreasonably demanding regarding computational cost. Furthermore, one is often only interested in the resulting flow of energy intensities. Such flow of radiative intensity can be modelled using the radiative transfer equation (RTE). The (quasi-stationary version of this) equation describes the change in spectral radiation energy intensity i'_λ [$W/(m^2 \cdot sr \cdot \text{wavelength})$] at position S along the direction \hat{s} in the solid angle $d\omega$ for waves of wavelength λ . The intensity can decrease due to absorption by the local molecules or scattering of the waves in a different direction, and can increase due to emission by the local molecules and scattering of radiation from other directions into the concerning direction (Siegel and Howell 1981). These four effects also return in the right-hand-side of the radiative transfer equation:

$$\begin{aligned} \frac{di'_\lambda}{dS} = & -\mu_\lambda * i'_\lambda(S) - \sigma_{s,\lambda} * i'_\lambda(S) + \mu_\lambda * i'_{\lambda b}(S) \\ & + \frac{\sigma_{s,\lambda}}{4\pi} * \int_{\omega_i=0}^{4\pi} i'_\lambda(S, \Omega_i) * \Phi(\lambda, \Omega, \Omega_i) * d\Omega_i \end{aligned} \quad (3.4)$$

Hence, the radiation intensity depends on the (possibly location dependent) spectral absorption coefficient μ_λ [1/m], spectral scattering coefficient $\sigma_{s,\lambda}$ [1/m], spectral blackbody intensity $i'_{\lambda b}$ [W/m^3Sr] and scattering phase function Φ [–]. Integration over the different wavelengths allows to obtain the local total radiation intensity at every location in the considered volume. The local net radiative heat flux through a certain surface dA is then given by the integration over all directions of the product of the local total intensities and the surface normal \hat{n} .

$$q_{r,\hat{n}} = \int_{\omega=0}^{4\pi} i' * \hat{s} * \hat{n} * d\Omega \quad (3.5)$$

A simplification often made to avoid solving this rather complex integro-differential equation is considering the radiating bodies as optically thick or ‘opaque’ to thermal radiation. Indeed, the relatively high absorption coefficient of most common materials leads to the thermal radiation actually penetrating the body being completely absorbed in the surface layer of a few micron thick. Concurrently, the interaction with typical gases like air is limited in enclosures of limited size (below kilometre scale). Both effects permit the approximation of thermal radiation as a surface-to-surface process, neglecting the interaction with the gas between the bodies and assuming the emission and absorption of radiation by the bodies happening directly at their surfaces. For every surface, an emissivity, absorptivity and reflectivity can be defined. These surface parameters can be calculated based on the optical properties of the material. In case of bodies being optically thin, a transmissivity can be defined accounting for the portion of radiation transmitted through the material. All these coefficients can be defined as dependent on the concerning wavelength and wave direction relative to the surface’s orientation. Values averaged over all directions are called hemispherical spectral coefficients, while averaged values over all directions and wavelengths are called hemispherical total coefficients. Regarding the reflectivity, incident radiation waves can be reflected in a diffuse way or specular way, or something in between. This depends on the type of material and the surface properties like roughness. The complex volumetric process of thermal radiation is hence reduced to a surface-to-surface problem in this formalism, which is more easily solved. Nonetheless, simulating the thermal radiation with the surface-to-surface paradigm inside the pore space is still a daunting task, due to its complex pore surface shape requiring a fine numerical discretization. To avoid the associated enormous computational cost, a simplified modelling strategy based on Loeb’s original model (Loeb 1954) will be presented in the next section.

3.4.2. Thermal radiation in pores: Loeb's method

Chapter 2 discussed several modelling strategies presented in literature to simulate the radiative heat transfer through a porous material. These range from simple analytical models based on averaged characteristics, to complex numerical models taking into account the interaction of the rays with and in the solid matrix. It is expected that in the porous building blocks studied in Part I, thermal radiation has a secondary influence due to the relatively low temperatures and porosities of the envisioned materials. Therefore, the choice is made in Part I to adopt and improve the model by Loeb (1954). As was already discussed in the previous chapter, he proposed a method to simplify thermal radiation as a conductive process inside the pores. This offers the advantage of a local coupling between thermal radiation and thermal conduction, while being computationally less demanding than more advanced techniques discussed in literature. Loeb's equation for the local radiative conductivity in every pore is repeated here in Eq. (3.6), with σ_{SB} [$W/(m^2K^4)$] the Stefan-Boltzmann constant, ϵ [-] the emissivity, T_{avg} [K] the average temperature inside the pore, d_{pore} [m] the diameter of the pore and γ_{pore} [-] a shape factor. This conductivity should subsequently be added to the local gaseous conductivity in every pore, as is shown in Eq. (3.7).

$$\lambda_{rad,pore} = 4 * \epsilon * \sigma_{SB} * T_{avg,pore}^3 * d_{pore} * \gamma_{pore} \quad (3.6)$$

$$\lambda_{pore} = \lambda_{gas} + \lambda_{rad,pore} \quad (3.7)$$

The shape factor γ_{pore} depends on the pore shape and was defined by Loeb (1954) and later refined by Bakker et al. (1995) as shown in Table 3.2. Shape factors have so far only been defined for simple pore shapes, and they differ between different authors. Therefore, in the next sections a numerical study will be performed to allow calculating the shape factor for a wider variety of pore shapes.

Table 3.2: summary of shape factors proposed by Loeb (1954) and Bakker et al. (1995)

Pore type	Loeb (1954)	Bakker et al. (1995)
Circular pore (2D)	0.79	0.55
Spherical pore (3D)	0.67	0.45
Elliptical (2D)	/	$0.55 - \pi/4$
Oblate ellipsoid (3D)	/	0.45 - 0.56

Although not really mentioned so far, there is an important assumption in Loeb's method that delimits its applicability for studying the thermal radiation in porous materials. The method is based on the surface-to-surface modelling paradigm and hence assumes opaque cell walls. Since pore walls can be relatively thin (depending on the porosity and pore size), this assumption is not obvious: the thin pore walls may cause partial transmission of radiation through them, which would increase the total thermal radiation through the material. The relative amount of radiation intensity transmitted through a pore wall with thickness d_{wall} [m] can be estimated using Bouguer's law in Eq. (3.8), where μ [1/m] is the solid's total (=integrated over the spectrum) absorption coefficient and I_0 [$W/(m^2 sr)$] and I_t are the total radiation intensity incident on and transmitted through the cell wall (De Micco and Aldao 2006).

$$I_t = I_0 * e^{-\mu * d_{wall}} \quad (3.8)$$

The absorption coefficient depends on the type of material, but for most non-metallic solids it is on the order of 10^4 1/m to 10^6 1/m (i.e. De Micco and Aldao, 2005; Sahba and Rockett, 1992). For both values, the transmittance calculated with Bouguer's law is shown in Figure 3.5a as a function of the cell wall thickness. A different view on the relation is provided in Figure 3.5b, where the minimum cell wall thickness to have a transmittance below 10 % is shown as a function of the absorption coefficient. From an engineering point of view, we assume that less than 10 % transmittance will not affect the results to a significant extent. For the remainder of Part I, we will assume the absorption coefficient to be relatively high, allowing to neglect the transmitting part of the radiation and use Loeb's method. The effect of transmission of radiation will be covered in Part II.

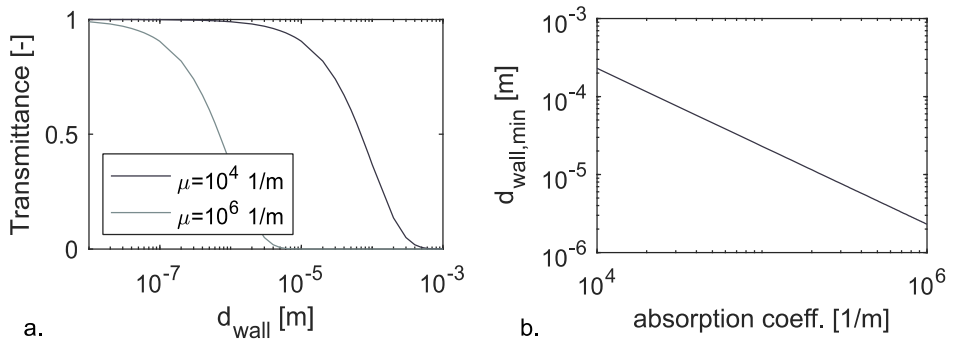


Figure 3.5: transmittance through 1 cell wall as a function of cell wall thickness for an absorption coefficient of 10^4 1/m and 10^6 1/m (a). Needed minimum cell wall thickness to have less than 10 % transmittance as a function of the absorption coefficient (b).

3.4.3. Expansion of Loeb's method to randomly orientated ellipsoidal pores

In this work, Loeb's model is studied and expanded to allow for application in cellular materials. For granular materials, it is assumed that thermal radiation has a negligible influence due to their relatively lower porosity. We focus on ellipsoid-like shaped pores of random orientation: indeed, pores in real materials are rarely exactly spherical, as instead they approach more an ellipsoid shape. Also, two overlapping pores can often be approximated as forming one ellipsoid. In this section, a comprehensive study is performed to assess the influence of the pore size, shape and wall emissivity on the radiative heat transfer in the pores. First, numerical simulations are performed studying radiative heat transfer in single, isolated pores. Based on these simulation results, an analytical formula is proposed linking the radiative conductivity to the aforementioned parameters, similar to but more versatile than Loeb's original formula. The methodology is first demonstrated on 2D pores and subsequently expanded to 3D pores.

2D pores

First, the radiation in one single, isolated pore is studied to derive a correlation linking the local radiative conductivity to the pore parameters. Elliptically shaped pores are employed to mimic the random nature of pore shapes and orientations. As shown in Figure 3.6, such a pore is defined by its long axis length a [m], short axis length b [m] and inclination angle α [°].

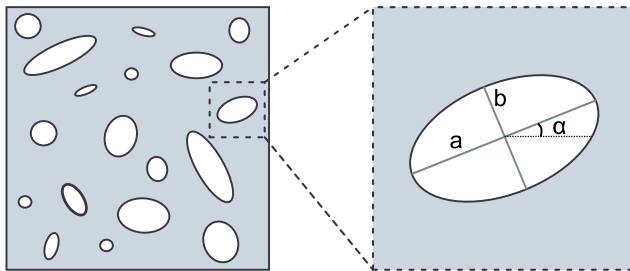


Figure 3.6: one isolated elliptic pore inside a porous medium is simulated.

Simulation setup

Radiative heat transfer through a single pore is studied by applying a temperature difference across the square domain enclosing this one pore (Figure 3.6 right). The length of the main axes (a & b) is varied, as well as the angle of inclination, obtaining a wide range of possible

pores. Parameters are detailed in Table 3.3. Furthermore, each configuration is resimulated using different emissivities and average temperatures as detailed also in Table 3.3.

Table 3.3: Summary of parameters varied during the thermal radiation simulation in a 2D elliptic pore.

Parameter	Values
Long axis length a [mm]	0.1 – 0.25 – 0.5 – 0.75 – 1 – 1.5 – 2
Ratio short axis to long axis b/a [-]	0.33 – 0.5 – 0.75 – 1
Inclination angle α [°]	0 – 18 – 36 – 54 – 72 – 90
Emissivity ϵ [-]	0.1 – 0.3 – 0.5 – 0.7 – 0.9
Average temperature [K]	273 – 283 – 293 – 303 – 313

The thermal conductivity of the matrix and the pore space are set to 1 W/mK respectively 0.025 W/mK , while the length l_x of the square matrix is always made 20 % larger than the long axis length of the ellipses. Tests with other matrix conductivities ($\lambda_{mat} = 0.5\text{ W/mK}$ or 2 W/mK) and other square sizes indicated a very low dependence of the radiative conductivity on these parameters.

Heat transfer simulations are performed in the numerical package COMSOL Multiphysics, modelling surface-to-surface thermal radiation using the view factor method. The effective conductivity of each configuration is determined, once incorporating thermal radiation and once without. The difference between both is the macroscopic radiative contribution to the sample's ETC (not to be confused with the pore's radiative conductivity). Subsequently, a search algorithm performs a series of simulations to determine the pore's radiative conductivity such that the error on the total radiative contribution is smaller than 1 %, as expressed in Eq. (3.9).

$$\left| 1 - \frac{\lambda_{eff,with\ radiative\ conductivity} - \lambda_{eff,without\ radiation}}{\lambda_{eff,with\ view\ factor\ radiation} - \lambda_{eff,without\ radiation}} \right| < 0.01 \quad (3.9)$$

Simulation results

A different radiative conductivity $\lambda_{rad,pore}$ is obtained for every configuration depending on the pore size, shape, orientation, wall emissivity and average temperature. Configurations where the resulting local radiative conductivity was less than 1 % of the gaseous conductivity of 0.025 W/mK are not further considered in the analysis since they are deemed inaccurate.

The third power dependence of the temperature as indicated in Loeb's original formula is clearly retrieved in the results, as shown for two pores in Figure 3.7a. However, Loeb's pore diameter d_{pore} is less well defined for inclined elliptic shaped pores, and even more so for irregularly shaped pores occurring in real porous materials. Instead, the mean distance $d_{i,mean}$ is introduced here, being the average distance between the opposing pore walls in the direction of the general heat flow ('i'). This parameter is easily calculated in 2D pixel images or 3D voxel images as discussed further on. Figure 3.7b reveals a linear dependence of the radiative conductivity as a function of the pore's mean distance for two different pore shapes and orientations and a wall emissivity of 0.9 and a temperature of 293 K.

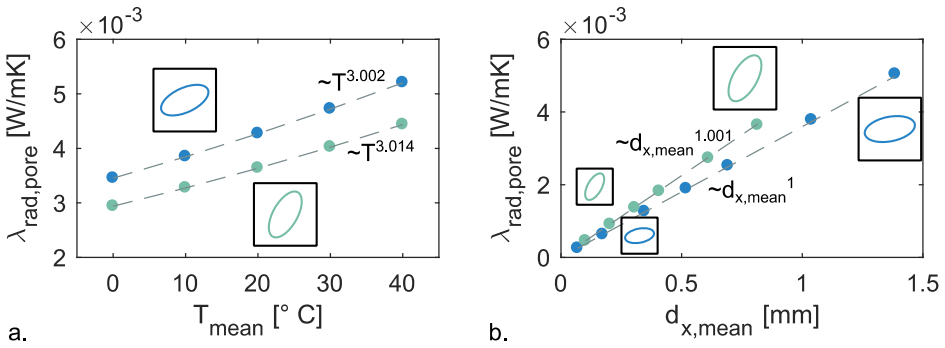


Figure 3.7: variation of local radiative conductivity as a function of temperature for two different pores (a); variation of local radiative conductivity as a function of the mean distance for two different pores (b). The sketched squares with pores experience a heat flow generally from left to right.

Subsequently, the influence of the wall emissivity is studied. Contrary to Loeb's original formula, the emissivity has no linear influence on the radiative conductivity. Furthermore, results indicate that its influence depends on the pore shape (defined later on). This was already suggested by earlier results by Fitzgerald and Strieder (1998). Therefore, a radiation factor $C(\epsilon, shape)$ is introduced, capturing the combined influence of both variables. The adapted version of Loeb's original formula for the pore's radiative conductivity hence becomes:

$$\lambda_{rad,pore,i} = 4 * \sigma_{SB} * T_{avg,pore}^3 * d_{i,mean} * C(\epsilon, shape) \quad (3.10)$$

A new factor is introduced to represent the shape of the pore, defined as the 'directional slenderness factor' $S_{f,i}$. This factor is defined as the ratio of the mean height of the pore (perpendicular to direction 'i') to the mean distance of the pore (parallel to direction 'i'), and is again easily calculated for every pore based on its digital image as will be discussed later. Notice that the pore's slenderness depends on the general direction of the heat flow, thus

accounting for possible anisotropy effects. By definition, the slenderness factor of a circular pore equals 1.

$$S_{f,x} = d_{y,mean}/d_{x,mean} \quad (3.11)$$

The radiation factor $C_i(\epsilon, S_{f,i})$ represents by definition the radiative conductivity normalized by the factor $4 * \sigma_{SB} * T_{avg,pore}^3 * d_{i,mean}$. This ratio is shown for all simulation results as a function of the emissivity and the slenderness factor in Figure 3.8. As can be seen, the slenderness factor captures the influence of the pore shape on the radiative conductivity very well. The factor $C_i(\epsilon, S_{f,i})$ for 2D pores can now be approximated analytically as a function of both parameters by fitting the results shown in Figure 3.8. The analytical approximation is given in Eq. (3.12) and plotted in Figure 3.9.

$$C_{i,2D}(\epsilon, S_{f,i}) = \left(\frac{0.475 + 2.1403 * S_{f,i}}{0.3855 + 2.3045 * S_{f,i} - 0.003 * S_{f,i}^2} \right)^{8.1445 - 14.8995 * \epsilon} * (0.6726 * \epsilon)^{0.9415} \quad (3.12)$$

Hence, we obtain the following expression, Eq. (3.13), replacing Loeb's original formula. Summarizing, it enables calculating the direction dependent radiative conductivity in a certain cellular pore, taking into account the temperature, pore size and combined influence of emissivity and pore shape. It alleviates the a-priori definition of a constant shape factor γ_{pore} or any other parameter.

$$\lambda_{rad,pore,i} = 4 * \sigma * T_{avg,pore}^3 * d_{i,mean} * C_{i,2D}(\epsilon, S_{f,i}) \quad (3.13)$$

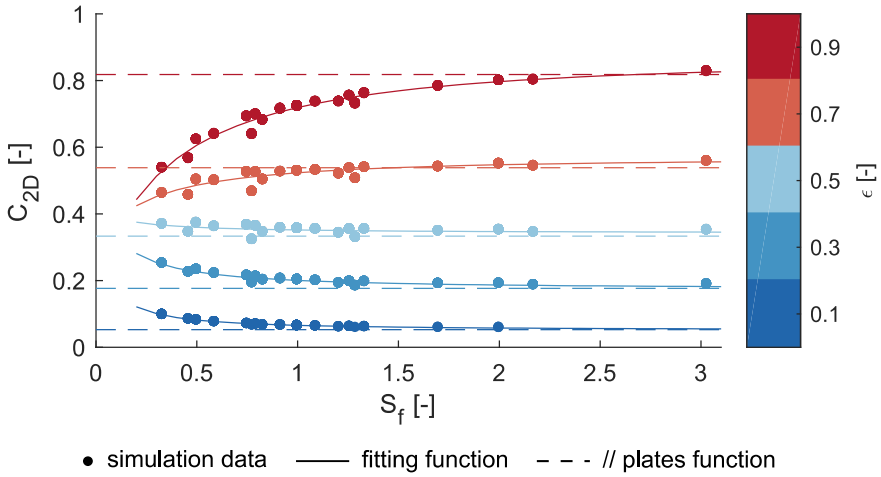


Figure 3.8: simulation data obtained for C_{2D} as function of slenderness factor and emissivity. Also shown is the analytical fitting function at the respective emissivity and the limiting formula for C_{2D} in the case of thermal radiation between parallel plates.

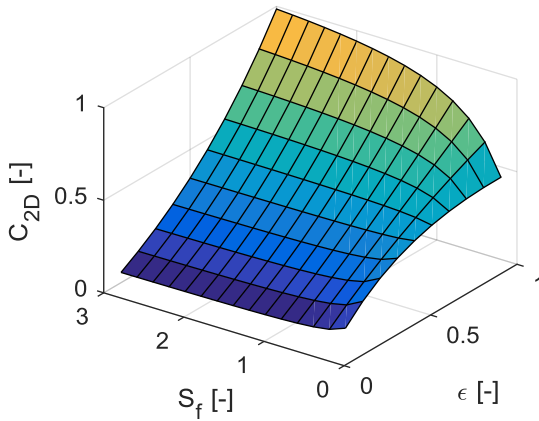


Figure 3.9: fitting function for C_{2D} as a function of the slenderness factor and the emissivity.

Figure 3.10 shows the analytically calculated factor $C_{i,2D}$ versus its original simulated result. The trendline through the results indicates a good fit of the analytical equation. The relative deviation between the analytical and numerical results are mostly below 3 %, as can be seen in Figure 3.10.

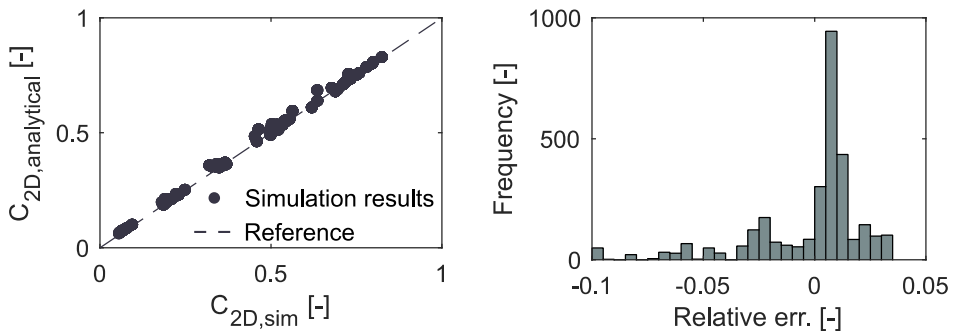


Figure 3.10: C_{2D} calculated with new analytical model vs simulated C_{2D} showing the goodness of fit (left); histogram of relative deviations between analytically calculated and simulated C_{2D} factors (right).

Discussion on obtained correlation

As can be seen in Eq. (3.13), the local radiative conductivity depends on 4 major factors. Expectedly, temperature has a very important influence, with increasing temperatures leading to increasing thermal radiation in the pores. Similarly, the average distance between the opposing walls has a direct influence. Bigger pores allow the photons to travel a longer distance before being reflected or absorbed, explaining the increase of radiation with increasing mean distance. Finally, the factor C_i combines the influence of the emissivity and the pore shape. Expectedly, radiation increases with increasing emissivity. However, the increase depends strongly on the pore shape, becoming more influential in pores with a high slenderness factor. Likewise, the effect of the pore shape depends on the emissivity. At high emissivity (>0.5), the radiative conductivity will increase when the slenderness factor increases. This is because the pore shape approaches a configuration of two parallel plates, where photons emitted in any direction by the hot plate can all reach the other plate, instead of being prematurely extinct by the ‘side walls’. At low emissivity (<0.5), the high reflectivity of the walls will cause a larger portion of the photons hitting the side walls being scattered forward. Hence the ‘extinction effect’ of the side walls is lower for low emissivity (or high reflectivity) pore surfaces. On the contrary, it seems even that at reducing slenderness, the C factor and thus (for equal mean distance) the radiative conductivity increases. Closer examination shows that this is due to how the pores block the conductive heat transfer through the matrix. Indeed, in the two extreme cases, a matrix containing a pore with a very high slenderness factor will resemble more closely the plates/resistances in series configuration (Figure 3.11 right), while a pore with a very low slenderness factor will resemble more closely the resistances in parallel configuration (Figure 3.11 left). To compensate a same

amount of radiative heat flux by additional gaseous conduction, the gaseous thermal conductivity in the parallel configuration should be increased relatively stronger.

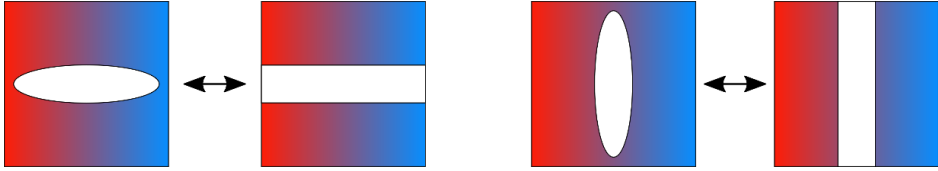


Figure 3.11: Pores with a low slenderness factor (left) resemble more closely the parallel configuration model, while pores with a high slenderness factor (right) resemble more closely the serial configuration model

As a limiting case, with increasing slenderness factor the pore shape approaches two plates parallel to each other with radiative heat transfer perpendicular to the plates. An exact analytical formulation hence exists as a limit value for the radiation factor $C_{i,2D}$, shown in Eq. (3.14).

$$C_{2D, //} = \frac{\epsilon}{2 - \epsilon} \quad (3.14)$$

This limit is also shown in Figure 3.8 for the different emissivities, agreeing very well with results at a slenderness factor of 3. Since the analytical formulation for $C_{i,2D}$ given in Eq. (3.12) before is fitted on simulation results for pores with slenderness factor up till 3, this limit is set as value for all directional slenderness factors larger than 3.

3D pores

The methodology explained for the 2D case is applied to expand Loeb's model for a wider range of cellular pores in 3D. Thermal radiation is studied in several individual/isolated ellipsoid-shaped pores with varying sizes, shapes, orientations and wall emissivities. An analytical formula similar to the formula for 2D pores is deduced, linking the pore's radiative conductivity to several geometrical and physical parameters.

Simulation setup

Ellipsoid-shaped pores are used to mimic the typical pore shapes found in cellular materials. Similar to elliptic shapes, such 3D pores are defined by the length of their primary axes, a , b and c . Their orientation is changed by the zenith and azimuth angle and a rotation around the third primary z -axis. Simulations in 2D already confirmed the linear dependence between the radiative conductivity and the pore size (the parameter $d_{x,mean}$). To reduce the needed computation time, the length of the long axis a is kept constant. All other 5 parameters are

varied to obtain a large range of pore shapes and orientations (Table 3.4). Five different emissivities are studied as well. The temperature is not varied this time, again because 2D simulations confirmed the third power dependence of temperature proposed by Loeb.

Table 3.4: summary of parameters varied during the thermal radiation simulations in one 3D pore.

Parameter	Values
Long axis length a [mm]	2
Ratio short axis to long axis b/a [-]	0.33 - 0.5 - 0.75 - 1
Ratio short axis to long axis c/a [-]	0.33 - 0.5 - 0.75 - 1
Zenith angle θ [°]	0 - 30 - 60 - 90
Azimuth angle ϕ [°]	0 - 30 - 60 - 90
Rotation angle z_{rot} [°]	0 - 30 - 60 - 90
Emissivity ϵ [-]	0.1 - 0.3 - 0.5 - 0.7 - 0.9
Average temperature [K]	293

The thermal conductivity of the matrix and the pore space are set to 1 W/mK respectively 0.025 W/mK , while the length l_x of the square matrix is always kept 50 % longer than the ellipsoid's longest axis length. The simulation setup and derivation of the radiative conductivity is otherwise similar to the simulations performed in the 2D case.

Simulation results

The resulting radiative conductivities are again approximated using the adapted version of Loeb's formula proposed for the 2D pores in the previous section (Eq. (3.15)). Again, the same parameters return: the mean temperature T , the mean distance $d_{x,mean}$ between the opposing pore walls and a factor C_i taking into account the dependence on the emissivity ϵ and a direction-dependent pore shape. The pore shape is again approximated by its slenderness factor, which is (similar as the 2D version) defined in Eq. (3.16).

$$\lambda_{rad,pore,x} = 4 * \sigma_{SB} * T_{avg,pore}^3 * d_{x,mean} * C_{x,3D}(\epsilon, S_{f,x}) \quad (3.15)$$

$$S_{f,x,3D} = \frac{d_{z,mean} * d_{y,mean}}{d_{x,mean}^2} \quad (3.16)$$

A correlation for the factor $C_{x,3D}$ in 3D is again determined based on the simulation results, see Eq. (3.17). The simulation results for $C_{x,3D}$ are shown in Figure 3.12, the analytical fitting function in Figure 3.13.

$$C_{x,3D}(\epsilon, S_{f,x}) = \left(\frac{0.6615 + 2.4642 * S_{f,x}}{0.3526 + 2.8103 * S_{f,x} + 0.0189 * S_f^2} \right)^{1.673 - 3.5092 * \epsilon} * (0.7051 * \epsilon)^{0.9604} \quad (3.17)$$

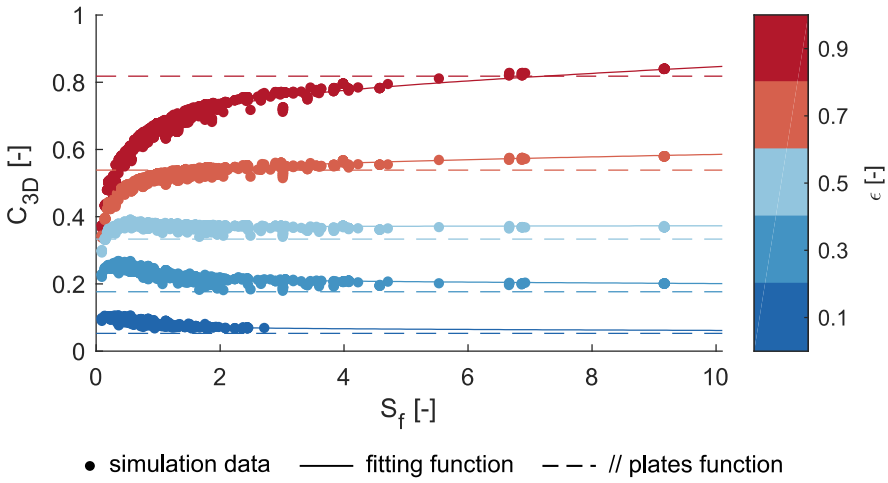


Figure 3.12: simulation data obtained for C_{3D} as function of slenderness factor and emissivity. Also shown is the analytical fitting function at the respective emissivity and the limiting formula for C_{3D} in the case of thermal radiation between parallel plates.

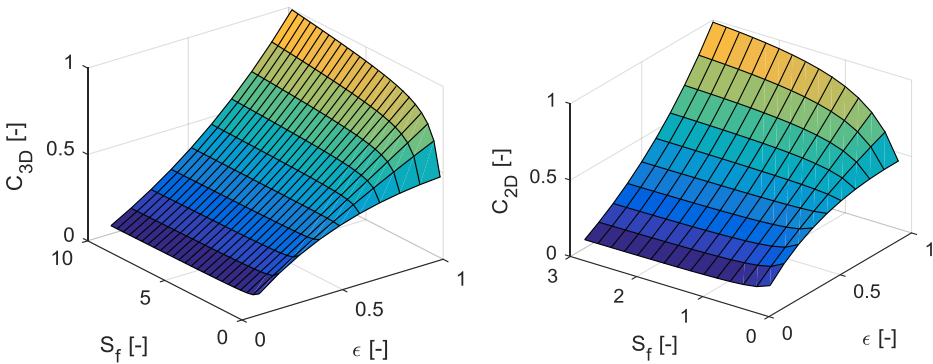


Figure 3.13: fitting function for C_{3D} (left) as a function of the slenderness factor S_f and the emissivity ϵ . The same is repeated here for the 2D case (right) for reasons of comparison.

The goodness of fit of the analytical approximation for the 3D case is demonstrated in Figure 3.14. For most configurations a relative deviation below 5 % between the analytical approximation and the numerical result is obtained, which is slightly higher than for the 2D case.

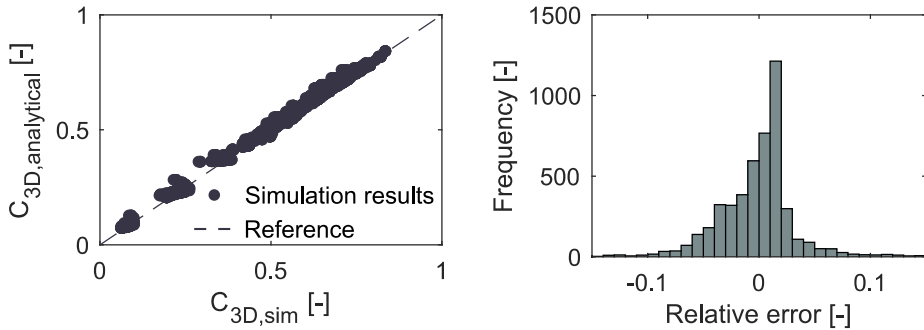


Figure 3.14: C_{3D} calculated with new analytical model vs simulated C_{3D} showing the goodness of fit (left); histogram of relative deviations between analytically calculated and simulated C_{3D} factors (right).

Discussion on obtained correlation

Again, the same effects as discussed in 2D appear for the local radiative conductivity in 3D. At increasing temperature and increasing mean pore distance, the local radiative conductivity will increase as well because of the larger amount of photons being generated and the longer distance they travel before interacting with the pore surface. The emissivity has a similar expected effect, with increasing values increasing the radiative conductivity. The relative increase depends on the pore shape, with a larger effect of the emissivity at pores with higher slenderness factor. The effect of the pore shape is again two-fold: at increasing slenderness factor, the opposing pore walls can more easily radiate towards one another, which increases the radiative conductivity at high emissivities. However, at low emissivities the blockage effect of the pore becomes more important explaining the increase of the radiative conductivity for a decreasing slenderness factor. Lastly, in case of very low slenderness factors (<0.2), the radiation factor $C_{x,3D}$ seems to decrease again regardless of the emissivity. This effect is not well taken into account by the analytical approximation for emissivities below 0.3 as can be seen in Figure 3.13. Applying the correlation for such cases is expected to lead to an overestimation of the thermal radiation contribution.

Compared to the original Loeb method, the new correlations for the 2D and 3D case allow to much better take into account the effect of the pore shape (and the combined effect with the

emissivity). Indeed, for an emissivity of 0.9, the radiation factor varies easily between 0.5 and 0.8 as can be seen in Figure 3.12. The original method on the other hand employs a fixed-value shape factor, meaning that significant discrepancies would occur in the case of pores with small/large slenderness factors. At lower emissivity, the difference between the new method and the original method will be smaller, due to the relatively lower effect of the pore shape as is obvious from Figure 3.12. Lastly, the original method's formula depends on the pore diameter, which is an undefined quantity in non-spherical pores. The new method alleviates this issue by employing the mean distance between the opposing pore walls.

Implementation in model framework

To apply the developed correlations for thermal radiation in the framework, several preprocessing steps are needed. First of all, the pore space needs to be divided into separate pores. Indeed, in high porosity materials, a large part of the pores are often interconnected via smaller connection zones. When the opening width of the connection between two pores is relatively small, thermal radiation travelling from one to the other can effectively be neglected. Hence, the 2 pores should be separated and a different radiative conductivity for both should be calculated. The splitting of the pores is executed according to the distance transform and watershed procedure described in Morpho+ (Brabant et al. 2011). This procedure splits all the pores at their narrowest point, resulting in a set of completely disconnected pores. This is demonstrated on the image obtained through μ CT scanning shown in Figure 3.15a. The pore space (in white) is divided into separate zones resulting in an image matrix as shown in Figure 3.15b with a different label for each separated pore.

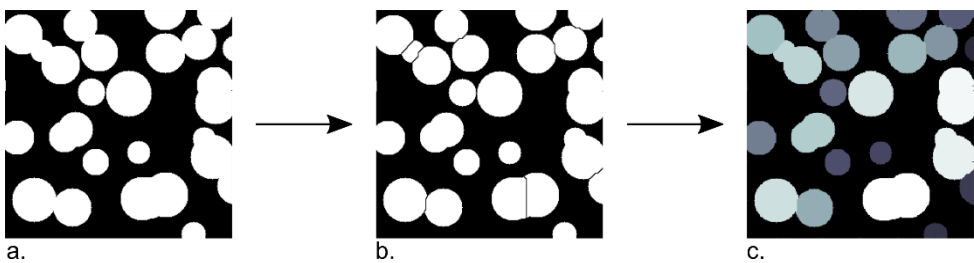


Figure 3.15: The pore space (colour white) in the original image (a) is split in separate pores (b). Subsequently, pores are labelled and are – depending on the rejoin factor (here set to 0.5) – rejoining to form one pore cluster (c).

However, when pores were originally connected via a relatively large opening width, splitting them is not desirable since a non-negligible part of the thermal radiation travels between both pores. Furthermore, the watershed procedure sometimes tends to cause splitting in the middle

of 1 pore, which is also not desirable. Therefore, the rejoining procedure described in Morpho+ is also implemented to rejoin mistakenly split pores and connected pores that share a relatively large opening window. This procedure first calculates the radii of the maximum inscribed balls of 2 originally connected but now split pore zones. Subsequently, the largest of both radii is compared to the radius of the maximum inscribed circle in the connection zone between both pores. If the ratio of these radii is larger than a set value (the rejoin factor RJF), the pores are rejoined:

$$\frac{r_{\text{inscribed circle of connection}}}{\max(r_{\text{inscribed balls of pores}})} > RJF \quad (3.18)$$

If the rejoin factor is set to 0, all separated pores will be rejoined, nullifying the whole splitting procedure. If set to 1, no zones will be rejoined. The binary image matrix is thus transformed to an image matrix consisting of separately labelled pores. The result of this last step is illustrated in Figure 3.15c for an RJF of 0.5, where some of the separated pore zones have been rejoined.

Subsequently, the directional slenderness factor needs to be calculated for every pore cluster. The mean distance in every direction is determined by calculating for every pore the number of ‘needles’ needed to stitch all voxels inside the concerning pore cluster in that direction. Figure 3.16 shows such needles for the horizontal direction in a 2D pore as example. The pore volume is then divided by this number of needles to obtain the mean distance. The directional slenderness factor is then calculated by Eq. (3.11) for 2D pores and Eq. (3.16) for 3D pores, and is then used to calculate the pore cluster’s radiative conductivity using Eq. (3.13), respectively (3.15). The emissivity is specified by the user. The pore’s average temperature is approximated as the sample’s average temperature. Since there is only 1 Kelvin temperature difference across the whole simulated sample, the resulting deviation is expectedly negligible.

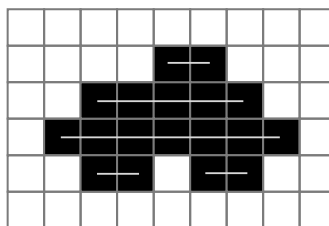


Figure 3.16: The pore (in black) consists of 18 voxels and there are 5 needles in the horizontal direction of the pore, leading to a mean horizontal distance of $18/5=3.6$ voxels.

3.5. Thermal Convection

Natural convection refers to buoyancy driven movement of air: hotter air will rise relative to colder air due to its lower density, which can lead to enhanced heat transfer through the gas. As mentioned in the literature review, it is often assumed that natural convection has a negligible contribution to a porous material's ETC. Although relatively little studies enter the subject, some authors have estimated its importance for heat transfer in the gas confined in the pores using the Grashof number Gr [–], Eq. (3.19), which expresses the ratio between the buoyant and viscous forces in the gas.

$$Gr = \frac{g * \Delta T * L^3 * \rho^2}{T * \eta^2} \quad (3.19)$$

Here, g [m/s^2] is the gravity acceleration constant, ΔT [K] is the temperature difference between opposing pore surfaces, ρ [kg/m^3] is the mass density of the gas, T [K] is the average temperature of the gas, η [$Pa * s$] is the dynamic viscosity of the gas and L [m] is a characteristic length (i.e. the pore size). When the Grashof number is smaller than 1000, natural convection has a negligible contribution to the gaseous heat transfer compared to the gas conduction. For air at room temperature and atmospheric pressure, this is the case for a characteristic length (i.e. the pore size) smaller than about 10 mm (Clyne et al. 2006). A numerical computational fluid dynamics (CFD) study by Sanjaya (2011) confirms this order of magnitude for the pore size, showing that natural convection has a negligible effect in spherical pores with diameters below 6-8 mm. Of course, for porous materials with a highly interconnected pore space (like for example mineral wools or open celled metal foams), the length scale in the Grashof number corresponds more closely to the total material thickness instead of the pore size, which can induce a non-negligible contribution in large-thickness situations. However, such materials are not considered in this study. Porous materials where forced convection plays an important role (for example in heat exchangers) are not considered either. Hence, for the remainder of this study, the contribution of convective heat transfer to the total heat transfer is neglected.

3.6. Verification of implemented physical models

To be able to study the impact of different microstructural properties on the ETC, the model needs to attain a certain accuracy level for a wide range of possible pore structures. The framework's ETC prediction capability is compared in this section with reference solutions obtained with other models for several pore structures. First, the conduction-only performance is verified, followed by a verification exercise for the thermal radiation implementation.

3.6.1. Verification of thermal conduction implementation

The whole model framework is applied on three unit-cell reference microstructures with varying porosities and composition, verifying the numerical results with existing reference results. Subsequently, the influence of the voxel size and mesh size settings on the predicted thermal conductivity is tested using the same reference structures, further investigating the model's numerical performance.

Verification of accuracy

The model's accuracy is verified using 3 different virtual periodic microstructures, consisting of equal-sized spherical inclusions organized in a continuous phase: the simple cubic (SC), the body-centred cubic (BCC) and the face-centred cubic (FCC) structure. The SC system contains a spherical inclusion on every corner of a cubic unit cell, while the BCC and FCC structures extend the SC system with a spherical inclusion in the middle of the cube or in the middle of every face of the cube, respectively. The cubic elemental lattice of all 3 systems is shown in Figure 3.17 for the case where the spheres touch. Both cellular and granular materials can be represented using these structures, considering the spheres as a gaseous phase embedded in a solid matrix (cellular) or as solid particles with gas around them (granular). The sample porosity, defined as the volume ratio of the low-conducting phase to the high-conducting phase, is varied from 10 to 90 % by adapting the sphere's diameter, yielding both structures with overlapping and non-overlapping spherical inclusions. Although this means that at high porosities granular materials lose their structural integrity, results are shown to widen the conclusions.

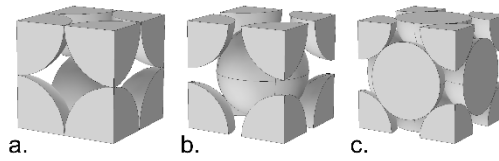


Figure 3.17: Unit cell examples of the three studied elementary arrangements of spheres in a regular lattice. Simple cubic (a), body-centered cubic (b) and face-centered cubic (c). The spheres are either designated as the high-conducting phase (granular configuration) or as the low-conducting phase (cellular configuration).

The model framework introduced in the previous sections is applied to calculate the ETC of the different virtual microstructure systems. The voxel images are generated using a voxel size of $1/200$ of the sphere diameter; the mesh's triangle and tetrahedron radius parameters are set to $1/50$ of the sphere diameter. The thermal conductivities of the conducting and insulating phase are set to respectively 1 W/mK and 0.01 W/mK , resulting in a conductivity ratio of 100. The inclusions and the matrix are consecutively designated as the conducting phase or insulating phase, simulating the heat transfer through granular and cellular materials. Results are shown in Figure 3.18a-c for all three packing types as a function of porosity. As expected, the thermal conductivity decreases with increasing porosity for both cellular and granular materials. For the granular case, the conductivity exhibits a steep drop until the packing porosity of the respective structure is reached, above which the spheres become non-touching, hence impeding a direct heat flow path through the high-conducting phase. For the cellular material, the continuous conducting phase is never fully interrupted, hence no such steep drops can be observed.

The obtained conductivities are compared with analytical reference solutions found in literature to assess the model's accuracy (McKenzie, McPhedran, and Derrick 1978; Cheng and Torquato 1997). However, since these reference models are not defined for the whole porosity range, they are extended with numerical simulations performed in COMSOL using the software's proprietary geometry and meshing functionalities instead of the image-based approach implemented in the framework. The numerical reference results show very good agreement with the analytical solutions in their applicable porosity range. The relative error between the model framework and the reference model is calculated and depicted on the right axis of the graphs in Figure 3.18a-c. For the granular configuration, the largest deviations are observed around the packing porosity of the respective structure, where the spheres are just (or just not) overlapping. This can be explained by the voxel-based representation of the geometry, inherently resulting in a discretization error. In small, high-conducting regions, this effect is more distinct due to the absolute nature of this discretization error, as is particularly

the case at the packing porosity where an infinitely small contact surface is formed between the spheres. For the cellular configuration, deviations are generally slightly increasing with increasing porosity. Again, at higher porosities the continuous conducting phase becomes relatively smaller, hence leading to increasingly relevant discretization errors. An appropriate voxel resolution should therefore be chosen considering the relative size of the conducting phase, as will be further elaborated in the next section.

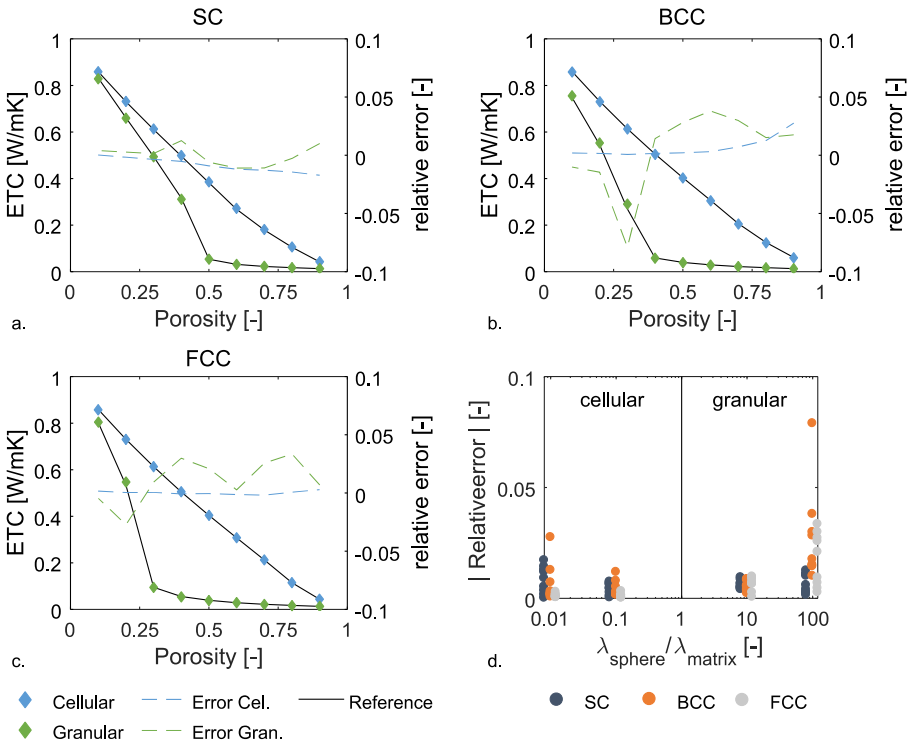


Figure 3.18: Simulation results and relative errors for the cellular and granular SC (a), BCC (b) and FCC (c) configuration, for a matrix-sphere conductivity ratio of 100 (0.01 for granular config.). Results are compared with the reference solution obtained in COMSOL Multiphysics for the same configurations. Graph (d) shows the relative errors for all three arrangements as a function of the sphere-matrix conductivity ratio. Results for the SC and FCC configuration are shown at a slightly different conductivity ratio for clarity.

The influence of the ratio of both material phases' thermal conductivity on the model's performance is studied by repeating the same simulations, changing the insulating phase's thermal conductivity from 0.01 W/mK to 0.1 W/mK, hence resulting in a conductivity ratio of 10 instead of 100 (or 0.1 instead of 0.01 for the granular configuration). The relative errors with the reference model are presented for all porosities in Figure 3.18d as a function of the sphere-

matrix thermal conductivity ratio. As expected, the deviations decrease when the conductivity ratio approaches 1, since the effect of the geometrical discretization error diminishes.

Grid and mesh sensitivity

The numerical performance of the model is mainly affected by the two discretization parameters: the voxel size of the 3D image and the mesh size of the finite element mesh. Indeed, a fine resolution is needed to correctly represent the microstructural geometry, while an adequate mesh size ensures a satisfactory structural conformity of the microstructure and a reasonable approximation of the temperature and the heat flow distribution. The influence of both parameters on the accuracy of the predicted ETC is investigated using the 3 regular lattice structures mentioned previously. Four different voxel sizes, varying from 1/25 to 1/200 of the sphere diameter, are tested to build the 3D images. For the mesh size, the radius of the surface faces Delaunay balls and the tetrahedra-circumscribing balls is varied from 1/10 to 1/50 of the spherical inclusions' diameter. The thermal conductivity ratio is set to 100 and 0.01 to obtain cellular and granular arrangements respectively. The deviations between the numerical reference model and the model framework simulations are shown in Figure 3.19.

As expected, a finer voxel size (or higher resolution) and a smaller mesh size (or higher mesh density) generally lead to increased accuracies. For cellular materials, the error generally increases with increasing porosity, meaning a finer voxel grid and mesh size should be used to obtain accurate results for high-porosity samples. As already stated in the previous section, this is due to the discretization error of the conducting matrix induced by the voxel-based representation, which becomes more pronounced for thin microstructural features. For the granular materials, the error increases till the packing porosity where the conducting particles just overlap, after which the error generally decreases with increasing porosity. This is again explained by the discretization error in the representation of the microstructures: the contact zones between the particles become gradually smaller at increasing porosity till the packing porosity, after which they don't touch anymore. In conclusion, the attained accuracy varies appreciably with the type of structure (cellular or granular), the configuration of the matrix (SC, BCC and FCC), and the concerning porosity, making it difficult to formulate universal guidelines for choosing optimal discretization parameters. Cellular materials with high porosities or granular materials with small contact surfaces between the particles generally demand a finer discretization to obtain a certain accuracy. However, the selection of the discretization settings should be performed with caution and a convergence analysis should be performed if possible. Finally, as indicated in Figure 3.18d, it is expected that these effects

depend strongly on the phases' thermal conductivity ratios, generally requiring less fine voxel and mesh sizes with decreasing matrix-fluid conductivity ratios.

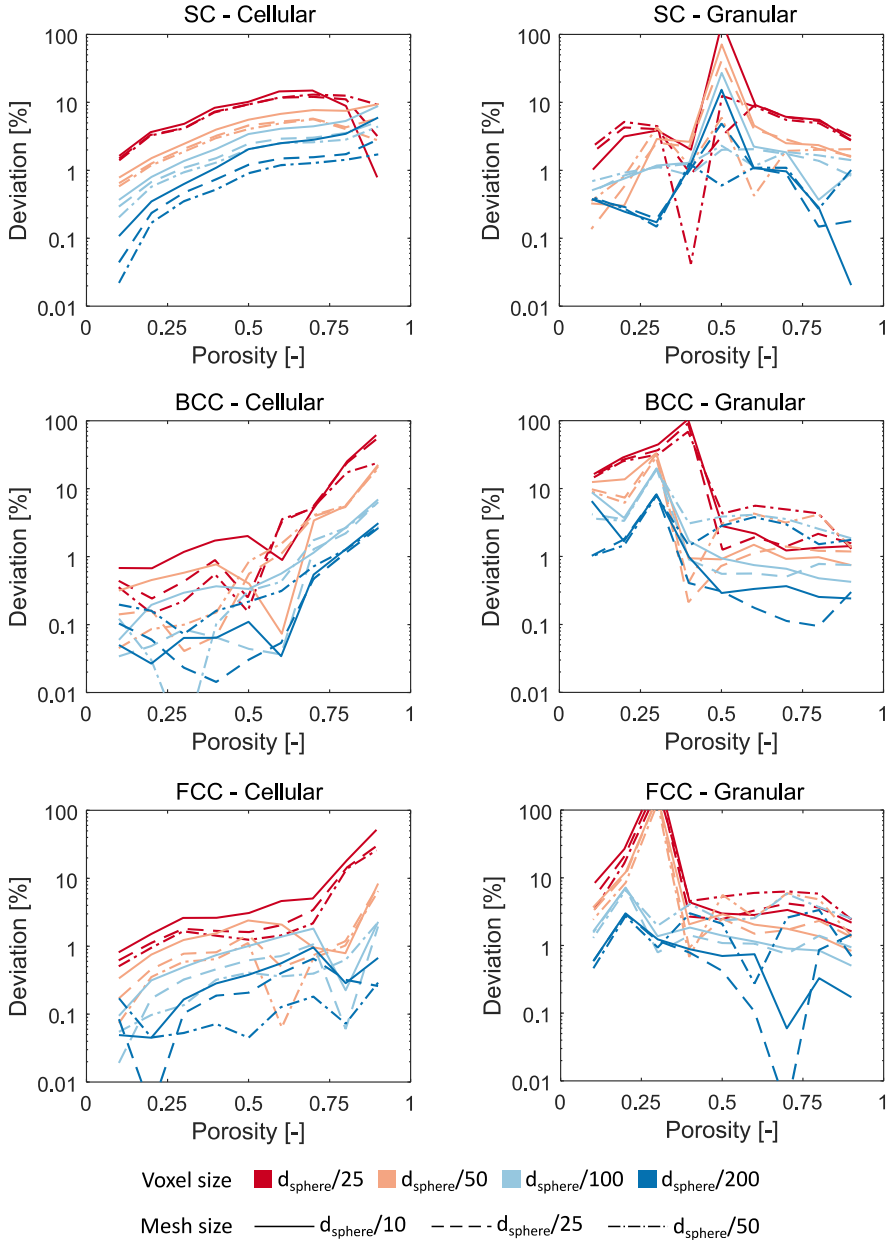


Figure 3.19: Influence of discretization parameters on the accuracy of the model framework for three regular structures as a function of the porosity. The accuracy is again assessed by comparison with the numerical reference model. A thermal conductivity ratio of 100 (0.01 for granular config.) is employed. A finer voxel size and mesh size clearly lead to generally improved accuracies.

3.6.2. Verification of thermal radiation implementation

The correlations for the approximation of thermal radiation as a conductive process in every pore have been derived based on configurations containing only one pore. In real porous materials, the vicinity of other pores might influence the temperature field around the concerning pore and consequently also the radiative heat flow inside the pore. Therefore, in this part, the calculation procedure is compared to other procedures when simulating samples containing several pores, at different porosities and pore shapes.

2D samples

The expanded Loeb model is first tested on 2D samples. Three different pore structure types are used to test the accuracy of the analytical correlation: two different types of virtually generated structures and one type of structure obtained through μ CT scanning. The effective total and radiative conductivity of every sample is predicted first using the model framework and the expanded Loeb model and subsequently using the view factor simulation method serving as the reference method.

Preparation of samples

Three different types of pore structures are used as input for the model: two types of virtually generated pore structures, and one type based on a μ CT scan of a Multipor porous building block. The first employed virtual generation method is the RBI method generating circular pores at random locations and with lognormal distributed pore diameters (She, Zhang, and Jones 2014). 14 samples with side length of 1 cm and porosities between 10 % and 70 % are generated. The maximum overlap ratio of two adjacent pores is set to 0.2, to allow partially connected pores but avoiding highly open-porous samples. Samples with higher porosities could not be achieved with the applied maximum overlap ratio. The mean and variance of the lognormal distribution are set to 1.1 mm and 0.072 mm² respectively to obtain a distribution of pore diameters roughly between 0.5 mm and 2 mm. An exemplary sample is shown in Figure 3.20a.

The other employed generation method is the Voronoi technique, which partitions the sample in separate Voronoi cells based on an initial seeding procedure (Randrianalisoa, Coquard, and Baillis 2013). 9 samples with porosities between 10 % and 90 % are generated with a sample length around 1 cm. The perturbation factor is set to 0.2. Only closed-cell samples are generated. An exemplary sample is shown in Figure 3.20b, showing a more foam-like pore structure with distinctive features compared to the RBI algorithm.

A final type of samples are based on a real pore structure to complement the virtually generated types of samples. Multipor by Xella, a commercial type of cellular concrete, is chosen because of its high (macro-)porosity and relatively large pore cells. A cylinder of diameter 7.5 mm is extracted from the material and scanned using the Skyscan 1172 μ CT scanner apparatus. The pixel side length of the resulting slices is 14.9 μ m. During segmentation, all microporosity is ignored and designated as matrix material to obtain a pore structure with a monomodal pore size distribution. Simulation results are hence only meant to study the accuracy of the thermal radiation implementation and should not be compared to experimental data on real Multipor samples. For simulations, a region of 4.5 mm x 4.5 mm is extracted from five different binary slices, resulting in five 2D samples. An example of one of the samples is shown in Figure 3.20c.

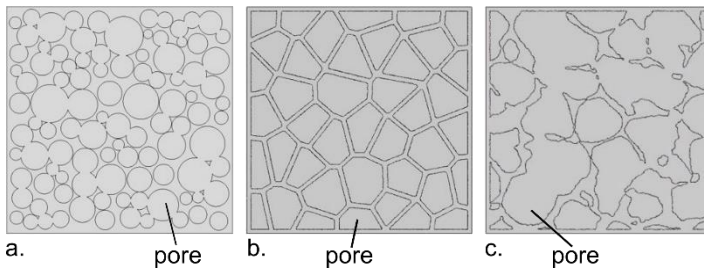


Figure 3.20: from left to right: a sample generated with the RBI technique, with the Voronoi technique and a slice obtained through μ CT scanning from a Multipor sample.

Simulation setup

Thermal simulations largely follow the same methodology for all three types of samples. The pore clusters present in the Multipor samples and virtually generated samples are first split using the divide-and-rejoin algorithm described in section 3.4.3. Rejoin-factors between 0 and 1 were tested on a few RBI-generated virtual samples, with a factor of 0.4 leading to the best results. The same rejoin-factor was also applied on the Multipor samples. Meshing is performed directly in COMSOL for the RBI-generated samples while the voxel-images obtained through Voronoi generation and μ CT scanning are meshed using the adapted iso2mesh code presented in the beginning of this chapter. Mesh refinement analysis was performed on all three sample types until no significant further improvement was observed. Subsequently, all thermal simulations are performed in COMSOL Multiphysics. Boundary temperatures of 293.65 K and 292.65 K are applied at opposing boundaries of the square sample while the other two boundaries are set to adiabatic conditions. Matrix and gaseous thermal conductivity are set to 1 W/mK respectively 0.025 W/mK. The thermal transport

through each sample is simulated three times. First, no thermal radiation is modelled to obtain the purely conductive effective conductivity $\lambda_{eff,cond}$. Subsequently, the presented simplified strategy with the expanded Loeb model is applied to account for thermal radiation, obtaining the effective conductivity with simplified radiation $\lambda_{eff,with\ simple\ rad}$. Finally, every sample is simulated a third time with thermal radiation modelled through the view factor method, resulting in the effective conductivity with detailed radiation $\lambda_{eff,with\ detailed\ rad}$. The resolution of the hemicube method to calculate the view factors in COMSOL is refined until no meaningful change is observed in the resulting conductivity. All simulations are performed with a pore wall emissivity once of 0.9 and once of 0.5.

Results & discussion

Results of the thermal simulations on all three sample types are shown in Figure 3.21a&b. The samples' effective radiative conductivity (Figure 3.21a) shows an expected increase with increasing sample porosity, since thermal radiation is here modelled as a process happening exclusively inside the pore space. Combined with a decreasing conduction-only conductivity at increasing porosities, this also leads to a strong increase in the relative contribution of thermal radiation to the total heat transfer (Figure 3.21b). As expected, a higher wall emissivity also leads to a higher importance of thermal radiation. Differences between the types of samples regarding their radiative conductivity and contribution to the total conductivity are entirely due to their different type of microstructure. For example, at equal porosity, the radiative conductivity is generally higher in the RBI generated samples than in the Voronoi generated samples. Apart from the influence of the pore size, this is partially explained by the generally higher matrix conduction occurring in Voronoi based samples due to their well-connected matrix (Van De Walle and Janssen 2019a). Relatively less heat will hence make its way through the pores leading to less contribution of thermal radiation.

The accuracy of the simplified strategy to approximate the radiative contribution is shown as an absolute and relative deviation in Figure 3.21c&d. For an emissivity of 0.9, the relative error stays below 5 % for porosities up till 50 % and increases from there on till 15 %. In general, the relative error is lower for the simulations performed on the RBI generated samples. This is probably the result of the pore structure's similarity to the elliptical pores used to deduce the simplified radiative methodology. At an emissivity of 0.5, the relative error goes up to 20 % and is generally higher than in simulations with an emissivity of 0.9. The absolute error is for both emissivities well below 10^{-3} W/mK though.

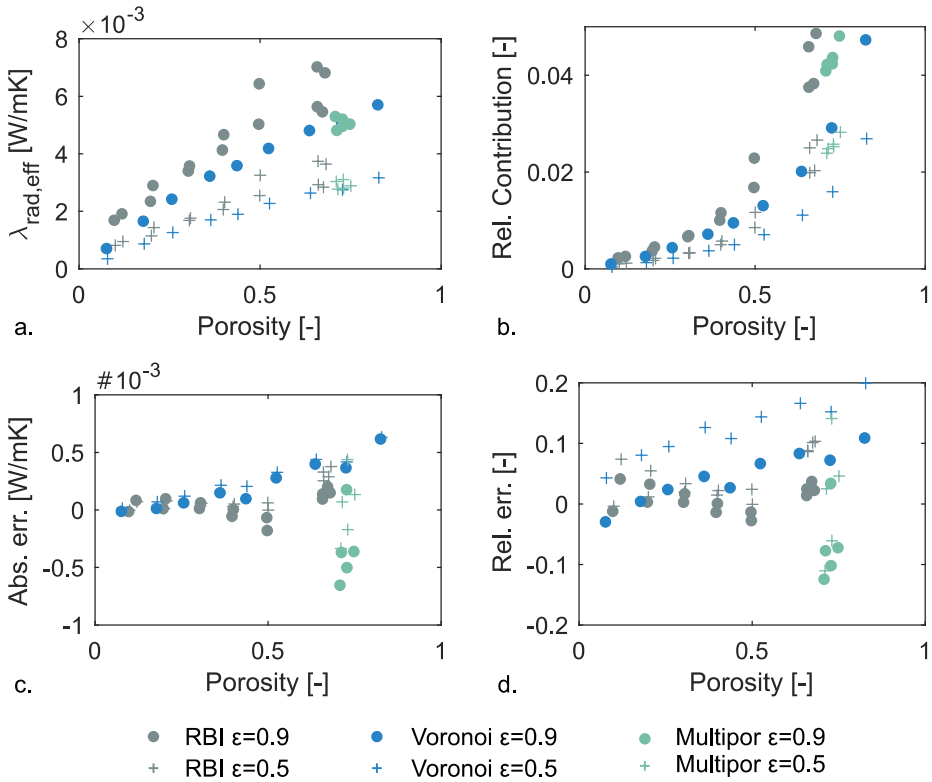


Figure 3.21: (a) effective radiative conductivity for every simulated sample as a function of porosity. (b) relative contribution of thermal radiation to total effective conductivity. (c) error on predicted effective radiative conductivity by expanded Loeb method compared to full simulation with view factors method. (d) relative error on effective radiative conductivity by expanded Loeb method compared to full simulation with view factors.

Concluding, the simplified method predicts reasonably well the radiative contribution to the total heat transport. At higher porosities, the method becomes less accurate, with deviations on the predicted radiation contribution up to 15 % or 20 % depending on the emissivity. However, taking into account the reduced importance of thermal radiation at reduced emissivities, the method performs adequately well to study the impact of thermal radiation on the total heat transport in 2D porous building blocks.

3D sample

Performing a comparison of the expanded Loeb model with the view factor simulation technique for a 3D sample, similarly as was done in 2D, is computationally extremely demanding: the irregular nature of the pore structure complicates the calculation of the view factors. Furthermore, the stiffness matrix created to solve the heat transfer problem with finite

elements becomes much harder to solve because of the inclusion of many terms outside of the diagonal due to the thermal radiation. Therefore, the newly implemented radiation calculation procedure is compared with a different numerical strategy: the Ray Tracing Monte Carlo (RTMC) technique developed by the group of D. Baillis, as already shortly discussed in Chapter 2.

Sample

The verification exercise is performed on a 3D sample generated by the Voronoi technique (Randrianalisoa, Coquard, and Baillis 2013), see previous section for explanation. 91 seeds are inserted on a body centred cubic lattice and are displaced randomly with a perturbation factor of 0.2. The cell wall thickness is increased to obtain a sample of 87.8 % porosity. The image is discretized with 500^3 voxels and the voxel size of the resulting 3D image is rescaled to $18 \mu\text{m}$. The sample side length is hence 9 mm, leading to pores with a diameter between 2 to 3 mm. A slice through the pore structure and a 3D view of the pore structure is show in Figure 3.22.

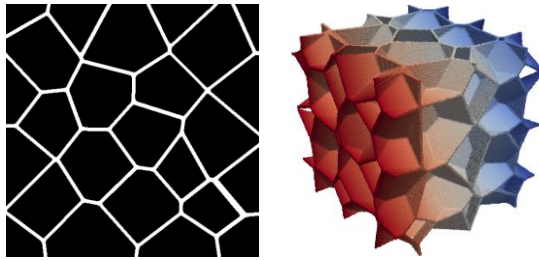


Figure 3.22: slice through simulated 3D sample (left) and 3D render of the matrix of the simulated sample (right).

Simulation setup

Simulations are performed using the model framework with the expanded Loeb radiation approximation described in this work, and by Zi Kang Low of the research group of prof. D. Baillis with the Modélia® by EC2-Modélisation software.

The simulations performed by the developed framework are performed with a matrix thermal conductivity of 0.5 W/mK and a gaseous conductivity of 0.025 W/mK . Temperatures of the opposing boundaries are set to 293.65 K respectively 292.65 K , while the other boundaries are adiabatic. The simulation is performed first without accounting for thermal radiation, leading to the conductive conductivity λ_{cond} . Subsequently, thermal radiation is accounted for via the expanded Loeb method, with an emissivity of 0.9. However, some of the pores lying at the boundary have a smaller size in the sample than their actual size (roughly only $\frac{1}{2}$, $\frac{1}{4}$ or $\frac{1}{8}$).

Therefore, the simulation accounting for thermal radiation is performed twice: once with the values obtained directly from the image, and once correcting for the small-sized pores by setting the local radiative conductivity of all pores to the one calculated in the largest pore. This adaptation is justified by the relatively monomodal pore size distribution typically obtained in samples generated with a low perturbation factor of 0.2 (Randrianalisoa, Coquard, and Baillis 2013).

Simulations performed by Zi Kang Low with the Modélia® by EC2-Modélisation software are based on the homogeneous phase approach. Radiative properties of the material (extinction coefficient, scattering coefficient etc.) are first calculated by performing an RTMC procedure inside the pore space. Subsequently, the finite volume method and discrete ordinates method (FVM-DOM) are used to solve the combined conduction-radiation problem described by Fourier's conduction law and the radiative transfer equation, leading eventually to the effective conductivity λ_{eff} . Zi Kang Low also calculated the macroscale radiative conductivity with the Rosseland approximation, using the radiative properties earlier determined by the RTMC procedure to allow a broader comparison.

Results & discussion

The resulting conductivities of the sample calculated by all simulations are summarized in Table 3.5. Also shown are the values obtained by Zi Kang Low using the full model (RTMC + FVM-DOM) but corrected for the derivation of the radiative properties on a shell mesh representation of the sample. Indeed, in the shell mesh, the pores will be larger than they really are, leading to an overestimation of the photons' travelled path lengths. Zi Kang Low proposed a correction for this effect by calculating the length overestimation for photons incident at 45 ° and correcting the previously obtained mean free paths by this length. The results are also shown in Table 3.5 (RTMC+FVM-DOM corrected) and are considered as the reference values. Hence, all other simulation results are compared to these values, percentages in brackets showing the relative deviation.

Table 3.5: Summary of calculated ETC and radiative conductivities calculated on a 3D sample by the expanded Loeb method and the FVM-DOM method implemented in Modélia.

$\lambda \left[\frac{mW}{mK} \right]$	RTMC + FVM-DOM	RTMC + FVM + Rosseland	RTMC + FVM- DOM (corrected)	FEM + Loeb expanded	FEM + Loeb expanded (corrected)
λ_{cond}	65.70	65.70	65.70	66.3 (+0.9%)	66.3 (+0.9%)
$\lambda_{rad,macro}$	11.46 (+13.7%)	11.45 (+13.6%)	10.08	5.2 (-48.4%)	6.6 (-34.5%)
λ_{eff}	77.16 (+1.8%)	77.15 (+1.8%)	75.78	71.5 (-5.7%)	72.9 (-3.8%)

As can be seen, the conduction-only conductivities of both methods (model framework and the shell mesh simulation) agree very well, with less than 1 % deviation. Also the total effective thermal conductivity values are reasonably close, with deviations in the order of 5 %. This deviation is hence almost completely due to the deviating macroscale radiative conductivities. Without correcting for the unphysically small pores at the sides of the sample, the expanded Loeb method predicts a radiative conductivity that shows a deviation with the corrected RTMC + FVM-DOM method of about 48 %. With correction for the small pores, this reduces to 35 %.

This relatively large underestimation by the expanded Loeb model is so far not completely understood. One possible explanation is the fact that the expanded Loeb model is derived for spherical and ellipsoid pore shapes, while the studied sample consists of relatively flat cell walls organized in some sort of Kelvin cell like geometry. However, this was also the case for the Voronoi-based samples studied in the 2D verification exercise, and there a overestimation of 15 % was obtained instead of the 35 % underestimation seen in 3D. The same can be said about the effect of the high porosity of the sample compared to the one of the single pore samples used to derive the expanded Loeb model, causing in 2D case also an overestimation instead of an underestimation. Another explanation could be the relatively small sample size, inducing a difference in both methods since both methods handle the adiabatic boundaries differently.

The most probable explanation is the different formalism between both models regarding the simulation of thermal radiation. The expanded Loeb model is derived for isolated pores with the assumption of thermal radiation as a surface-to-surface process. The RTMC + FVM-DOM procedure on the other hand is developed for extremely high porosity foams considering the

medium as a homogeneous semi-transparent medium, with radiation rays being emitted, absorbed or scattered at any location in the sample. The latter modelling strategy has indeed shown good agreement for high porosity foams with a semi-transparent solid phase. In case of decreasing porosities, the approach of homogeneous equivalent radiative properties becomes more questionable though, certainly for a very absorbing solid matrix. Indeed, rays travelling inside the solid matrix will behave differently than the rays travelling inside the pore space. With decreasing porosity, the homogeneous phase assumption will become less suitable. Although a porosity range between 80 % and 100 % is sometimes stated as the applicability range, there are currently no application examples of this strategy for closed cell foams with opaque cell walls. More research is hence needed to clearly quantify the validity of both the expanded Loeb method and the RTMC + FVM-DOM approaches at different porosities, for opaque vs transparent cell walls, diffuse and specular reflection, etc.

Concluding, it remains difficult to make any decisive conclusion on the accuracy of the expanded Loeb model for 3D samples. The discrepancy with the RTMC + FVM-DOM approach suggest that it is certainly not applicable for the case of very high porosity foams, especially when having semi-transparent solid phase. However, for porous building blocks where the assumption of diffuse surface-to-surface radiation is valid, the expanded Loeb model should be able to give a good estimate of the contribution of thermal radiation, certainly for medium to high porosities as was already indicated by the 2D verification exercise. The actual radiative conductivity will have a value probably somewhere in between both extremes obtained by both modelling formalisms. Lastly, the presented model framework is focussed on obtaining the total effective thermal conductivity. Comparison of both models on the studied Voronoi sample shows a very good agreement with less than 5 % difference, even when including thermal radiation in a different manner. Not accounting for thermal radiation at all, on the other hand would lead to an underestimation of more than 10 %. Hence, using the expanded Loeb method for the thermal radiation calculation at least improves the calculation of the total ETC.

3.7. Conclusions

This chapter discussed the implementation of a pore scale numerical model framework to simulate the heat transfer through the pore structure. An image-based modelling strategy is employed, using voxel images to represent the pore structure and finite elements to simulate the heat transfer. Solid and gaseous conduction are modelled using Fourier's conduction law, assigning the respective conductivities to the matrix phase and pore space. Thermal radiation is also modelled as a conductive process inside the pore space using an improved version of Loeb's method derived in this chapter. An analytical model to calculate an equivalent radiative conductivity for every pore is derived based on an extensive set of numerical simulations in 2D and 3D pores with different sizes, shapes, orientations and emissivities. As such, thermal radiation is accounted for locally based on the pore size, its directional shape factor and its wall emissivity. Thermal convection, finally, was discussed to be negligible and is thus not considered in the model.

The framework was verified with other numerical simulation strategies. The predicted conduction-only ETC agrees very well with analytical and simulation results on regular arrays of spherical pores. The thermal radiation calculation methodology was confronted with view factor simulations on several types of 2D pore structures, showing deviations below 1 mW/mK and below 20 % of the radiation contribution. In 3D, simulations on a virtually generated pore structure were compared with calculations performed by another laboratory using a different simulation method. A discrepancy of about 35 % on the predicted contribution of radiation was obtained, which is significantly larger than for the 2D cases. The cause for this large discrepancy is so far not fully understood, but is at least partially explained by the different formalisms used in both methods. The conduction-only conductivities agreed very well though, with only 1 % difference. Concluding, the different verification exercises indicate that the model framework was correctly implemented and is able to simulate the heat transfer through the pore structure. In cases where thermal radiation is not the major mode of heat transport through the material, the implemented methodology should suffice to properly account for it.

Chapter 4

Validation of the microscale model framework⁴

4.1. INTRODUCTION	77
4.2. THE HEAT FLOW METER.....	78
4.3. MATERIALS & METHODS	89
4.4. SINTERED GLASS FILTER	93
4.5. REAPOR POROUS BLOCK.....	97
4.6. CELLULAR GLASS PERINSUL S	103
4.7. CONCLUSIONS	107

4.1. Introduction

The previous chapter presented a novel numerical framework to predict the ETC of porous building blocks based on their pore structure. The verification of the model with other numerical models on some simple pore structures demonstrated the correct implementation of the workflow and physical models. However, real materials have much more complex pore structures, and other physical phenomena not implemented in the model could be occurring in reality. Therefore, the framework's performance to predict the ETC of three different porous materials is studied in this chapter (sintered glass filter, acoustic absorber, and cellular glass), in order to validate the simulation model.

Such validation of the model requires experimental measurements of the ETC of these porous materials. As small samples are envisioned for the validation exercise, first the implementation of a small Heat Flow Meter measurement setup is discussed. Subsequently, the three different

⁴ Parts of this chapter are published in Van De Walle et al., 2018, *Constr. Build. Mater.* 182, 427-440, or are submitted as part of a chapter in the book 'The Art of Measuring in Thermal Sciences, Meyer & de Paepe (eds.), 2019'.

porous materials are described, followed by their experimental and numerical characterization and the confrontation between both.

4.2. The Heat Flow Meter

An accurate characterization of the materials' ETC's is primordial for this validation exercise. Several techniques exist to measure the ETC of a material, which can be roughly classified as either stationary or transient. Stationary techniques, on the one hand, try to achieve a thermal equilibrium inside the setup and the sample, after which the ETC is determined. Examples are the Guarded Hot Plate technique and the Heat Flow Meter. Transient techniques, on the other hand, typically induce a sudden temperature change in the sample (which firstly is at thermal equilibrium). Measuring the evolution of temperature distribution and/or power dissipation over time then allows to determine the ETC. Some examples are the Hot Wire method, Hot Disk method, Hot Ball method and Laser Flash method (Yüksel 2016; Kubičár et al. 2010; Gustafsson 1991). Since there is no need to reach equilibrium, transient techniques typically yield results in the order of minutes, while stationary techniques may take several hours. On the other hand, stationary methods are considered as more reliable and accurate, due to their extensive research history and operation record and their intuitive functioning (Salmon and Tye 2001; Bomberg and Solvason 1985). In conjunction with the lab's existing knowledge in stationary measurements on building materials using a Heat Flow Meter (HFM), the choice was made to use this technique for the experimental characterization.

The HFMs available in the Building Physics Section of KU Leuven have a surface size of 30 x 30 cm² and 60 x 60 cm² respectively, hence requiring large samples for optimal results. However, working with smaller samples can have several advantages: it allows performing the measurement on several subsamples of a bigger sample, enlarging the dataset and providing an idea on the variation, it facilitates measurements in special conditions (e.g. at moisture saturation), and it allows for faster operation as less material is to achieve the thermal equilibrium. Finally, some samples (like material prototypes) are only available in small sample sizes. Therefore, a new HFM is implemented, with a surface size of 10 x 10 cm². As the literature focusses on the implementation of HFMs of 30 x 30 cm² or larger, a thorough study is needed to allow construction and operation of an accurate apparatus.

The next sections describe the principles, design and implementation of a small HFM, which is constructed as part of this PhD. Numerical simulations are performed to investigate the impact of several parameters on the accuracy. Lastly, the set-up is calibrated with a reference

sample, and its performance is compared with other measurement techniques on the same samples.

4.2.1. Heat Flow Meter Principle

The HFM’s measurement procedure involves placing a flat sample between two isothermal plates kept at a different temperature. When steady conditions are attained, the resulting heat flow through the sample is measured by one or several heat flux sensors. A conceptual sketch of the principle is shown in Figure 4.1. Assuming a one-dimensional temperature gradient in the sample, the thermal conductivity can be derived using the 1D version of Fourier’s conduction equation, rewritten in Eq. (4.1) to isolate the sample’s thermal conductivity on the left side. Here, $q [W/m^2]$ is the heat flux through the material, $T_{hot} - T_{cold} [K]$ the applied temperature difference across the sample and $d_{sample} [m]$ the sample’s thickness.

$$\lambda_{sample} = q * \frac{d_{sample}}{T_{hot} - T_{cold}} \tag{4.1}$$

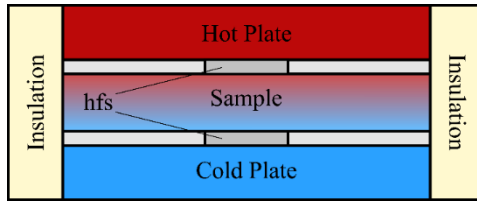


Figure 4.1: Conceptual sketch of Heat Flow Meter showing the sample sandwiched between two isothermal plates at different temperature and the heat flux sensors measuring the heat flux through the sample.

4.2.2. Design of a small Heat Flow Meter

Since literature focusses on larger HFMs, numerical simulations are performed to quantify the effect of certain design choices (e.g. the location of sensors, materials used for construction, edge insulation thickness, etc.) on the theoretical accuracy of such a small set-up. Jointly, the influences of the sample properties and the mean sample temperature on the resulting accuracy are investigated as well. In conclusion, the set-up’s performance is studied in a calibration exercise and a round robin test.

General design

At the core, a HFM apparatus consists of two plate ensembles clamping a sample in between. For simplicity and versatility of the set-up, both plate ensembles are typically designed exactly the same. Figure 4.2 shows a technical sketch of one of the plates. A thermoelectric element

(c) is used to heat or cool the thermal block (b) and contact plate (a) to a specified temperature, while a heat sink with ventilator (d) provides the heat exchange with the environment. The contact plate and thermal block are made as a solid part of aluminium, its high conductivity effectively spreading and homogenizing the temperature front induced by the thermoelectric element. Additionally, the thermal block serves to increase the physical distance between the contact plate and the heat sink and supporting plate (e), minimizing their thermal influence. The space in between both plates and around the contact plate is filled with thermal insulation (f). The whole plate ensemble is bound together with 4 screws made from plastic (g) so as to again minimize the thermal influence of the support plate on the contact plate. Four steel threaded rods (h) are used to support both plate ensembles. Eight bolts (i) per ensemble allow positioning the plates carefully at a certain distance from each other (important when measuring compressible materials like glass wool), or pressing the plates firmly together to reduce contact resistances. Moreover, the parallelism between the plates can be easily verified and adjusted if needed.

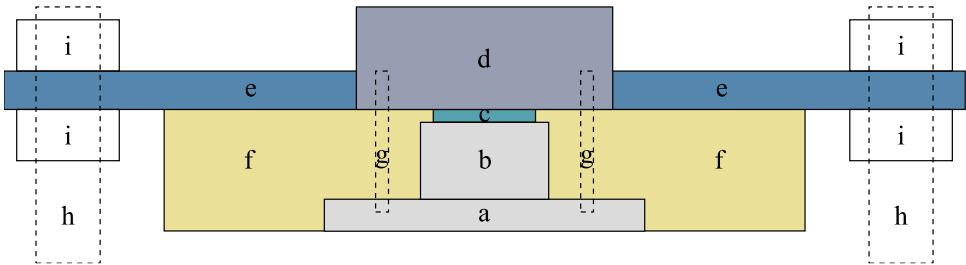


Figure 4.2: Conceptual sketch of design of one of the plate ensembles. (a) contact plate; (b) thermal block; (c) thermo-electric element; (d) heat sink and ventilator; (e) support plate; (f) thermal insulation; (g) plastic screws; (h) threaded rods; (i) positioning bolts.

Each plate ensemble is equipped with a heat flux sensor (hfs) and several temperature sensors, as detailed in the sketch in Figure 4.3. The heat flux sensor is placed in the central zone of the plate's contact surface, making the measured heat flux less susceptible to the influence of edge losses. The surface area of the heat flux sensor should be large enough to cover possible local inhomogeneities of the material like pores or grains. On the other hand, it should be small enough to be again less susceptible to edge losses. The effect of the size of the heat flux sensor is studied using numerical simulations in the next sections. An interface layer between the aluminium and the heat flux sensor is applied to provide thermal damping. Although time-averaged results are not influenced by this, the reduced effusivity will ensure less variability in the sensor's output. At the other side a contact layer protects the sensor from potential damage

from contact with hard samples. A relatively soft material is chosen to allow for a good contact with the sample surface, overcoming the minor roughness of the sample and reducing errors due to the thermal contact resistance. Furthermore, such a contact layer reduces the influence of the studied sample's conductivity on thermal bridging effects in the sensor's thermopiles (Bomberg and Solvason 1983). Finally, and most importantly, a levelling layer accommodates for the thickness of the sensor itself, ensuring the surface in contact with the sample is flat. A square hole the size of the heat flux sensor is cut out of this levelling layer. To promote a one-dimensional heat flow, it is important that the levelling layer's thermal conductivity is close to the sensor's thermal conductivity (Bomberg and Solvason 1985). This effect is numerically studied in the next section.

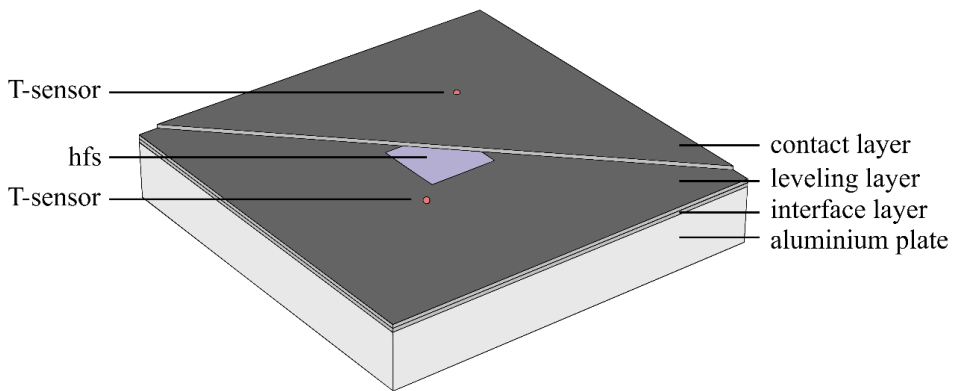


Figure 4.3: Overview of the temperature and heat flux sensors embedded in the layers on top of the aluminium plate.

A greenteg gSKIN XI heat flux sensor with a surface of $1.8 \times 1.8 \text{ cm}^2$ and a thickness of 0.5 mm is used because of its small size and good accuracy. Its small size ensures that the heat flux is measured only in the central zone and hence is less influenced by the edge losses. Furthermore, it also allows placing the temperature sensors closer to the centre, which is important for the accuracy as discussed in the next section. The heat flux sensors have a calibrated sensitivity in the order of $60 \mu\text{V}/\text{W}/\text{m}^2$ around room temperature, with a function defined to calculate the sensitivity at temperatures between 0°C and 50°C . A DAQ NI 9219 module with high resolution is used to read out the sensor's signal. This instrument is able to cope with the relatively low output of the sensors (on the order of $500 \mu\text{V}$) when measuring an insulating sample.

Two temperature sensors are embedded in each contact surface, their average value being considered as the surface temperature of the sample. The sensors should be as close as possible to – and preferably in contact with – the sample’s surface to avoid including an extra thermal contact resistance because of the local temperature jump. Ideally, the temperature should be measured in the central zone of the sample where also the heat flux is measured. However, to avoid a distortion of the heat flux by the sensors and the wires, they are located just outside the central zone. The influence of their location is studied in the next section. PT100 sensors are used for the set-up because of their high accuracy and stability over time. These temperature sensors are also used to control the experiment. A software routine programmed in LabVIEW continuously compares the measured temperatures with the required temperature and directs the thermoelectric elements to heat or cool the aluminium plates. A PID controller controls the intensity, ensuring a relatively fast and smooth transition to as well as the maintenance of the required plate temperatures.

Simulations

As discussed previously, the set-up should be designed to induce a one-dimensional temperature gradient through the material and heat flux sensor during a certain time. Several parameters like the thickness of the aluminium contact plate, the edge insulation thickness or the heat flux sensor size will directly influence the obtained temperature profile in the sample and hence the accuracy of the measurement. Numerical simulations are therefore performed to support several design choices for the construction of the HFM. The COMSOL Multiphysics package is used to build and solve the numerical model.

Simulation setup

All components shown in Figure 4.2 are modelled, except for the threaded rods since they have no influence on the thermal behaviour. Furthermore, all layers shown in Figure 4.3 are modelled as well, including the heat flux sensor. The temperature sensors and accompanying wires are not included. Only 1/4th of the actual set-up is modelled, considering the existing symmetry. The temperatures of both thermoelectric elements’ sides in contact with the aluminium contact block are set to respectively 5 K above or below the intended average sample temperature. As such, a temperature difference of approximately 10 K is obtained across the sample. A convective heat flux is imposed at all sides of the set-up in contact with the external environment. The temperature of the lab environment T_e is set to 20 °C, the heat transfer coefficient to the standard value of 8 W/m²K for the vertical sides and 50 W/m²K for the horizontal sides because of the forced air flow caused by the ventilators.

The construction parameters that varied during the simulations are listed in Table 4.1 together with the operational parameters. A full-factorial combination among the different parameters is considered, resulting in 5832 simulations. The choices for the parameters of the thermal conductivity of the levelling material are inspired by commercially available thermal interface materials. The thermal conductivity of the heat flux sensors is, corresponding to the technical data sheet, set to 0.75 W/mK. Apart from the construction and operational parameters, the sample thickness and thermal conductivity are also varied, to study the impact of the different parameters when measuring samples with different thermal resistances ($R_{sample} = d_{sample}/\lambda_{sample}$).

Table 4.1: Simulation parameters and their studied values.

Construction/operation parameters	Values
Aluminium contact plate thickness d_{alu} [cm]	0.5 – 1 – 1.5
Edge insulation thickness $d_{insulation}$ [cm]	1 – 2.5 – 5
Side length of heat flux sensor l_{hfs} [cm]	1.8 – 3.6
Thermal conductivity of levelling material λ_{lvl} [W/mK]	0.55 – 0.8 – 0.9
Location of temperature sensor [cm]	0 – 1 – 2 – 3
Average sample temperature T_{avg} [°C]	0 – 20 – 40
Sample parameters	
Sample thermal conductivity λ_{sample} [W/mK]	0.035 – 0.15 – 0.9
Sample thickness d_{sample} [cm]	1 – 2.5 – 4

After each simulation, the heat flux flowing through the heat flux sensors is obtained, together with the temperatures at the surfaces in contact with the sample. The latter is measured at the centre of the surface and at respectively 1 cm, 2 cm and 3 cm in x and y direction away from the centre.

Effect of parameters on measured thermal conductivity

The impact of the parameters on the accuracy of the temperature and heat flux measurement are only shortly discussed here. The numerical simulation results reveal the large impact of the aluminium plate thickness on the measured temperature difference across the sample as well as the big influence of the eccentricity of the temperature sensor location. Regarding the measured heat flux, it is shown that averaging results of the sensors at both sides of the sample largely cancels the influence of the thickness of the edge insulation as well as the temperature

of the environment. More details on the effects on the temperature and heat flux measurements can be found in (Van De Walle and Janssen 2019b).

The measurement of the heat flux and temperatures directly influence the calculated ETC, the focal point of this discussion. Figure 4.4 presents the relative errors on the obtained ETC as a function of the sample's thermal resistance, highlighting the impacts of the aluminium plate thickness and of the temperature sensor eccentricity. The location of the temperature sensors has a substantial influence on the measurement accuracy when measuring samples with low thermal resistance. This is due to the 2D heat flow effects causing an off-set between the measured temperature outside of the centre and the temperature in the centre. Increasing the thickness of the aluminium plate will improve the homogeneity of the temperature since it allows the heat to spread out more from underneath the Peltier element. An increasing sample thermal resistance has a similar smoothing effect on the temperature.

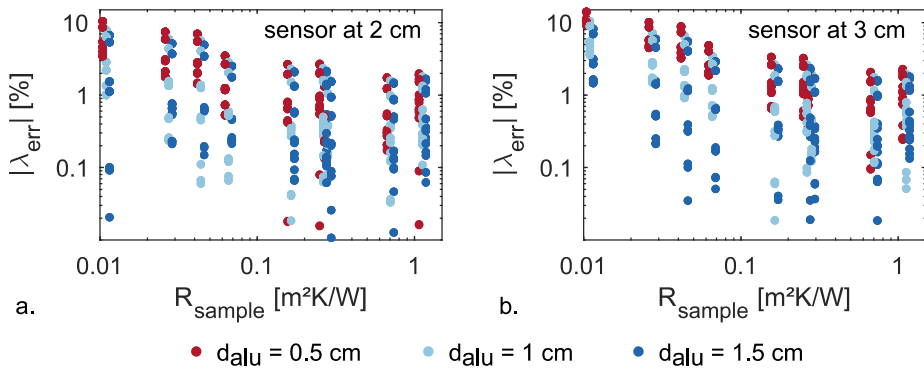


Figure 4.4: Impact of aluminum plate thickness on the measured thermal conductivity as a function of the sample's thermal resistance, when measuring the temperature at 2 cm eccentricity (a) or 3 cm eccentricity (b). Results at the same sample resistance but different aluminium thickness are slightly shifted for clarity.

The thermal conductivity of the levelling layer embedding the heat flux sensor is another important parameter influencing the accuracy of the measured thermal conductivity (Figure 4.5a). This is due to the local thermal bridge effect disturbing the 1D heat flow. Because of this effect, using a bigger heat flux sensor leads to lower deviations (Figure 4.5b). Indeed, the lower perimeter-to-surface ratio of a bigger sensor makes the thermal bridging effect less important. Probably, there is some upper limit to the heat flux sensor size, above which the effect of lateral heat flows to the environment becomes more important. Figure 4.5 shows results solely for the temperature sensor located at 2 cm eccentricity. The same conclusions apply when measuring the temperature at other eccentricities.

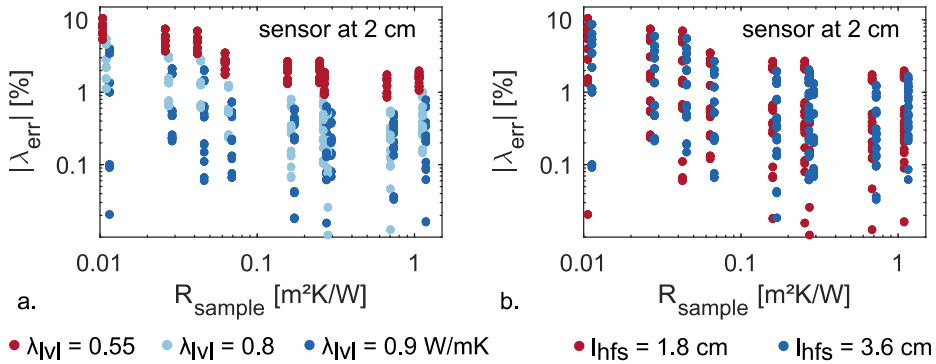


Figure 4.5: Effect of thermal conductivity of the levelling layer (a) and of the heat flux sensor size (b) on the measured thermal conductivity as a function of the sample's thermal resistance. Results at the same sample resistance but different levelling layer conductivity or sensor size are slightly shifted for clarity.

Finally, it should be noted that the above results only show the theoretical errors arising in the implemented model. Indeed, effects such as surface roughness, sensor deviation, non-parallelity of both sample surfaces, deviation in sample thickness measurement etc. are not taken into account, and could lead to an increase of the discussed errors. Some of them are accounted for by calibrating the set-up with a known reference material. The surface roughness (of both the sample and the contact plates), on the other hand, can induce an additional thermal resistance due to the resulting air layers across the sample. For samples with a low thermal resistance (small thickness and/or high thermal conductivity), these contact resistances will significantly affect the measured thermal conductivity. Procedures to account for this type of error are described elsewhere (Van De Walle and Janssen 2019b).

Implementation, calibration & round robin

For the design of the actual set-up, an aluminium plate thickness of 1 cm is chosen. The temperature sensors are placed at an eccentricity of 2 cm, as a trade-off between accurate measurement of the temperature difference without influencing the heat flux through the heat flux sensor. As levelling layer, a Gap Pad VO Soft from Bergquist with a thermal conductivity of 0.8 W/mK is selected, being close to the sensors' thermal conductivity of 0.75 W/mK. According to the simulations, the set-up should have deviations below 3 % for sample thermal resistances below 0.1 m²K/W, and below 0.3 % above 0.1 m²K/W. Illustratively, some photos of the assembled set-up are shown in Figure 4.6. It shows the controlling unit, both plate assemblies, the contact surface and a cellular glass sample with edge insulation.

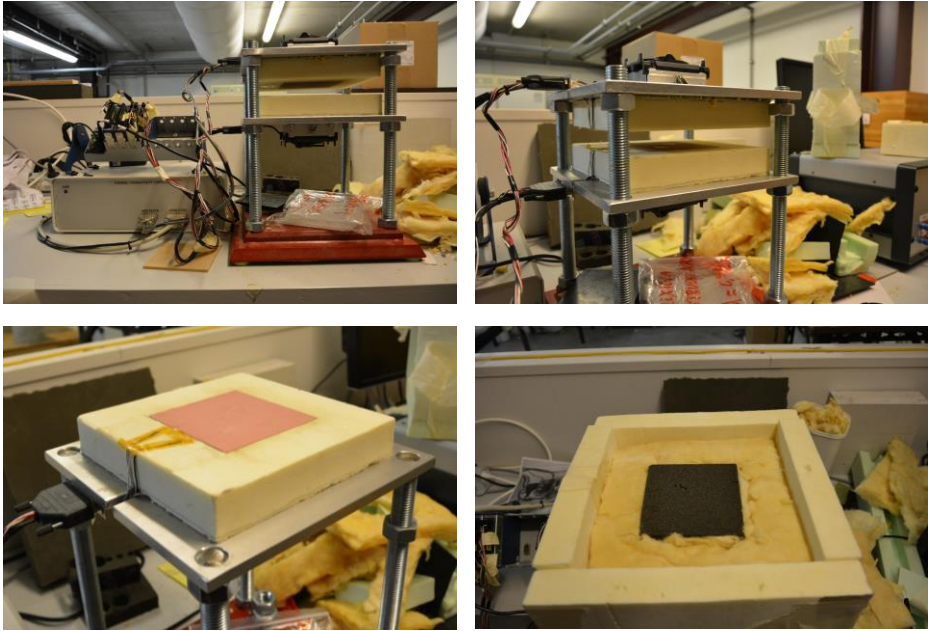


Figure 4.6: Photographs of small Heat Flow Meter setup showing the steering electronics (upper left), both plates (upper right), the contact zone of one plate (bottom left) and a sample put on the plate and surrounded by thermal insulation (bottom right).

Even within a well-designed HFM, a perfectly one-dimensional temperature gradient is never reached. Lateral heat flows will hence always distort the measured heat flux and thermal conductivity. Furthermore, little construction deviations, sensor inaccuracies or changing environment conditions will influence the HFM performance. Therefore, each set-up should be calibrated, defining a calibration factor S_{cal} [-] to account for the inevitable deviations occurring during real measurements. This factor is then multiplied with the measured thermal conductivity. It is important to stress that the calibration factor is set-up-specific, and can never be used for other (even highly similar) set-ups.

The calibration of the small HFM is demonstrated here. The mineral wool-like sample IRMM-440 provided by JRC is used (JRC 2019). The sample has dimensions of approximately $30 \times 30 \times 3.5 \text{ cm}^3$ with a thermal conductivity of 0.0332 W/mK at $20 \text{ }^\circ\text{C}$. The certified thermal conductivity is detailed for temperatures between $-10 \text{ }^\circ\text{C}$ and $+50 \text{ }^\circ\text{C}$ with uncertainty of 0.28 mW/mK at the 95 % confidence level. The low thermal conductivity of the sample means that its over-size is not a problem: the part of the sample that is not in contact with the hot and cold plate of the set-up (each $10 \times 10 \text{ cm}^2$) is considered as edge insulation. The measurement is performed at mean temperatures between $0 \text{ }^\circ\text{C}$ and $40 \text{ }^\circ\text{C}$, each time with a temperature

difference of 10 K. Both heat flow directions are tested by inverting the temperature gradient. The derived thermal conductivity is shown in Figure 4.7a.

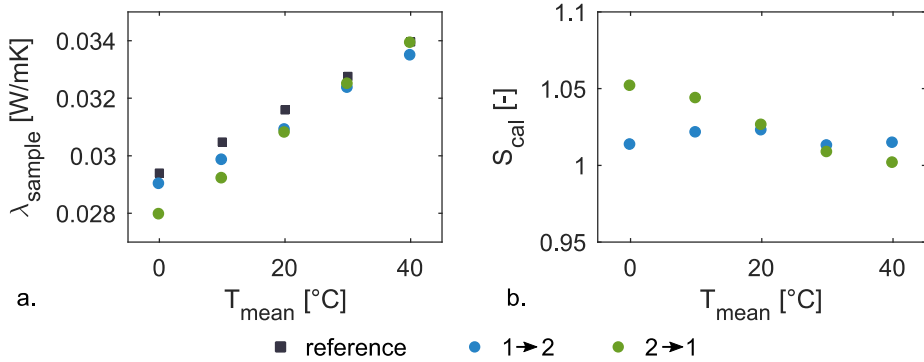


Figure 4.7: Measured thermal conductivity of reference sample with set-up without calibration (left) and calibration factor derived from the measured results (right).

As can be seen, the set-up measures the sample’s thermal conductivity already very well without calibration. Deviations are below 5% for all temperatures and directions. As predicted, this is somewhat higher than the theoretical accuracy of 1% obtained through the simulations, due to the sensor inaccuracies and imperfect implementation of the apparatus. The calibration factor S_{cal} dealing with these errors is derived by comparing the calculated thermal conductivity with the reference values. Results are shown in Figure 4.7b. The results underline the importance of defining a temperature-dependent and direction-dependent calibration factor.

The set-up’s performance is additionally validated in a round robin test with other laboratories using different techniques for measuring the ETC (Glorieux et al. 2017). Measurements are performed on five polymer-based insulation materials with thermal conductivities between 0.027 W/mK and 0.062 W/mK. Five transient and two stationary techniques are used, among which our 10 x 10 cm² HFM introduced previously. Figure 4.8 shows the measurement results of each technique versus the value measured by the HFM. As can be seen, results by the HFM correspond more or less to the average of values measured by all techniques. Very good agreement is furthermore obtained with the transient plane source (TPS) method and the hot wire dual method. For the low-conductivity samples, also a good agreement with the hot wire single is obtained. The hot ball results overestimate the true thermal conductivity, which is often the case for very-low-conductivity samples due to the heat losses via the wire. The modified transient plane source technique, finally, shows higher results for the low-

conductivity samples and lower results for the high-conductivity sample. A plausible explanation for this discrepancy is a not-fully corrected accounting for the heat losses through the side not in contact with the sample.

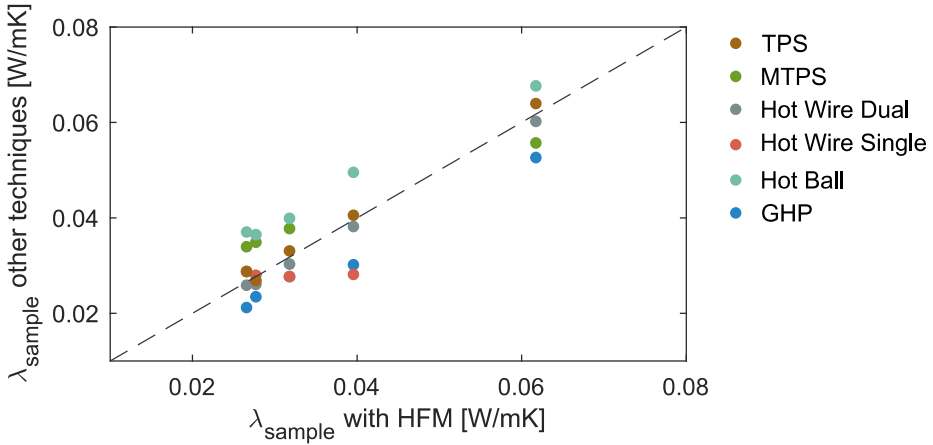


Figure 4.8: Results of the round robin test on five samples shown as a function of the measurement results obtained with the Heat Flow Meter (Glorieux et al., 2017).

Previous tests focus solely on materials with low thermal conductivities. Therefore, an additional test is performed on a Schott borofloat 33 solid glass sample of 1.9 cm thickness. This type of pure glass has a thermal conductivity around 1.2 W/mK at 90 °C according to the datasheet (SCHOTT, n.d.). The thermal conductivity measured by the setup at 20 °C is 1.16 W/mK, which agrees very well with this reference value. The slight underestimation is likely explained by the temperature difference. It needs to be mentioned though that the measurement accuracy for other, high-conducting materials may be less performant if the contact area is not equally smooth as was the case for the glass sample. The sample's surface roughness induces air layers between the hot/cold plate and the sample, inducing an extra contact resistance. In such cases, extra measures are required to obtain accurate results (Van De Walle and Janssen 2019b).

Based on the round robin results of Figure 4.8, the HFM's small calibration factor shown in Figure 4.7, and the good agreement of the measured glass thermal conductivity, it can be assumed that the implemented apparatus is properly and accurately functioning. Since its construction and validation, the set-up is being extensively used by multiple researchers from the Materials Engineering Department of KU Leuven to characterize their waste-based prototypes of porous building blocks.

4.3. Materials & methods

The pore-scale-heat-transfer model is validated by confronting the experimentally measured and the numerically predicted ETC for three real materials. The three materials used for this validation exercise are a sintered glass filter (ROBU), an acoustic absorber block (Reapor) and a cellular glass (Foamglass Perinsul S). All three materials are glass-based, but have a different type of pore structure, porosity, pore size distribution and/or gas component. They are all commercially available. μ CT scanning is applied to visualize the pore structure and to allow performing the numerical simulations on their true microstructural morphology. Besides, their porosity and pore size distribution are characterized experimentally to aid the interpretation of both experimental and numerical results. This section introduces the three materials and the applied experimental characterization methods.

4.3.1. Materials

Sintered glass filter

The sintered glass filter ROBU PI00 is used as a first validation material. The material has a granular type of microstructure, produced by sintering together finely milled borosilicate 3.3 glass particles. Typically applied to filter liquids, the material has an open pore structure with a reasonably well controlled porosity and narrow pore volume distribution. According to the manufacturer, the material has a porosity of 36 % (ROBU Glasfilter-Geraete GmbH n.d.). A photograph is shown in Figure 4.9.

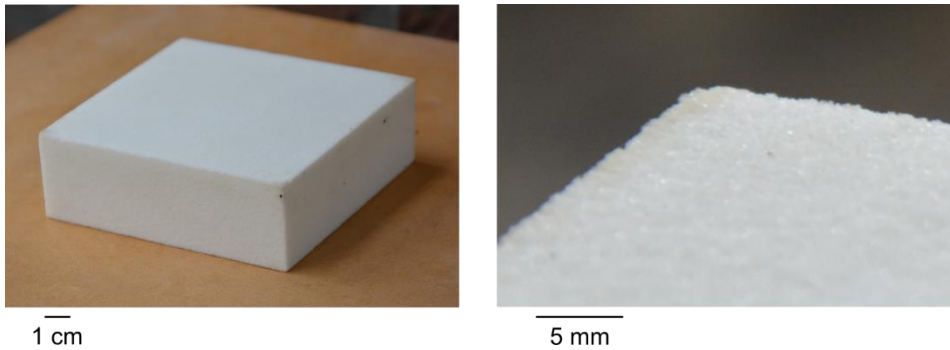


Figure 4.9: Photograph of sintered glass filter block and a zoom on a corner showing the surface roughness caused by the glass particles.

Acoustic absorber block

The second material is a Reapor porous block, a highly-porous material mainly applied for acoustic absorption. The production process is based on recycled glass and consists of sintering together expanded granules, hence leading to a pore structure with a two-scale type of pore volume distribution: a cellular structure inside the granules and a granular structure overall, both open-celled to maximize the acoustic absorptivity. The two-scale pore structure is clearly visible in Figure 4.10. The manufacturer specifies an ETC of 0.08 W/mK (Liaver GmbH & Co. KG 2014).

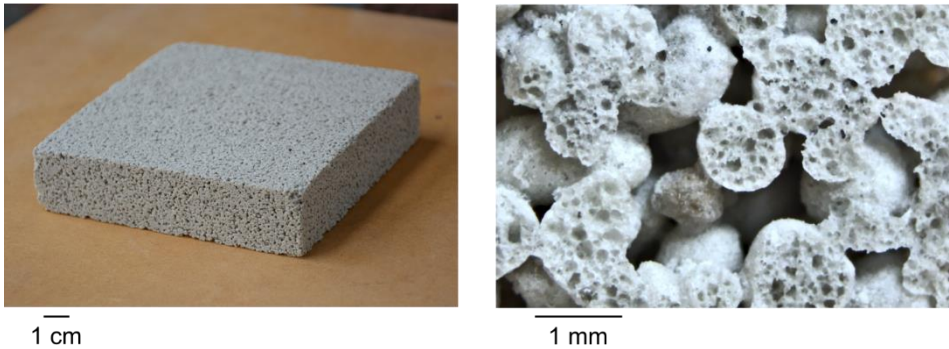


Figure 4.10: Photograph of Reapor block and its pore structure, showing the bimodal composition of cellular pores inside the granules and a larger pore space in between the granules.

Cellular glass

The third material, finally, is a highly porous cellular building block by Foamglas: Perinsul S. It is used typically as the base of a brick wall to reduce thermal bridging at the structural junction between floors and walls thanks to its combination of good structural and thermal properties. The production process consists of mixing partially recycled glass with several minerals and carbon powder. Heating will induce a foaming process creating a closed-cell pore structure filled with CO₂ gas. The resulting pore structure consists of mainly large pore cells and some smaller pore cells in the walls and struts. A photograph is shown in Figure 4.11. The manufacturer specifies an ETC of 0.05 W/mK at 10 °C (Pittsburgh Corning Europe NV 2018).

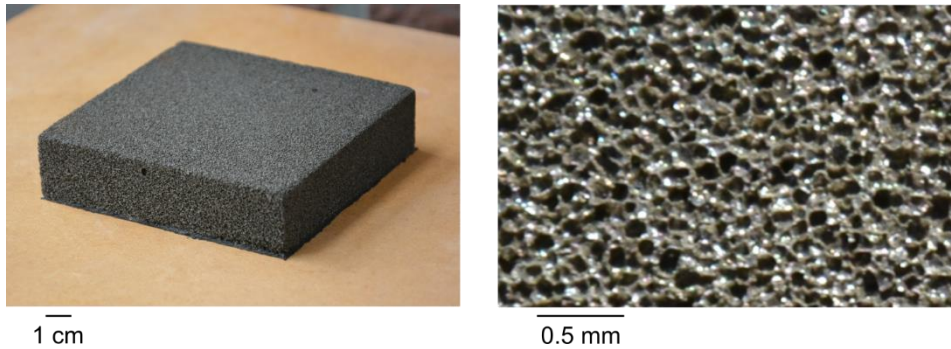


Figure 4.11: Photograph of cellular glass Perinsul S block and its pore structure.

4.3.2. Experimental methods

Pore structure

μ CT scanning is used to visualize the pore structure of all three materials. For most scans, a cylinder of a few millimetres diameter is extracted from the material to perform the scanning. A voxel side length (later called ‘the voxel size’) needs to be chosen, small enough to resolve the pore structure while not too small so the resulting image covers a representative part of the material. The resulting 3D images are also used as input for the numerical simulations. Scanning settings are chosen differently per material depending on the present pore structure so as to obtain optimal scanning results. Two machines are used for the scanning process: a Skyscan II72 and a GE Nanotom. Scanning and segmentation are for most samples performed by S. Claes of the Building Physics Section at KU Leuven.

Thermal conductivity

The thermal conductivity of each material is measured with the previously discussed Heat Flow Meter for samples of $10 \times 10 \text{ cm}^2$ surface area and a thickness d_{sample} . The setup is calibrated with a reference mineral wool sample and has an expected accuracy of better than 5 %. Several samples are cut from each material to obtain multiple results. The temperature difference between the hot and cold plate is always set to the standard value of 10 K, the average temperature is chosen differently per material. For the open-porous materials (glass filter and Reapor), the measurements are performed in two extreme conditions: oven-dry, obtained via oven-drying the samples for several days, and water-saturated, where all pores are filled with water via vacuum saturation. Both conditions are later on also used for predicting the ETC numerically, hence enlarging the set of validating comparisons.

Porosity

The porosity is one of the most influential parameters affecting the ETC of the porous material. Two techniques are employed to characterize the samples' total and open porosity. The first technique consists of simply comparing the dry bulk density of the material to the solid density of the matrix component, yielding the total porosity as shown in Eq. (4.2). The mass is measured in dry condition and the volume of the rectangular samples is measured with callipers. The density of the glass solid component is retrieved in literature (Fluegel 2007).

$$\phi = 1 - \rho_{sample}/\rho_{solid} \quad (4.2)$$

Additionally, the vacuum saturation technique is employed as well for measuring the open porosity of the sample (the pores that are somehow connected to the exterior environment). The procedure consists of first drying the samples, after which they are placed in a vacuum chamber. When vacuum conditions have settled in, water is allowed to enter the chamber, slowly immersing the samples. This way, all open pores are first completely evacuated and subsequently filled with water, leading to the water-saturated condition of the material. The mass of the saturated sample is subsequently measured in normal and submerged conditions (fully submerged in a water bath). With Archimedes' formula, it is then possible to calculate the sample's bulk density and open porosity, Eq. (4.3).

$$\phi_{open} = \frac{m_{saturated} - m_{dry}}{m_{saturated} - m_{submerged}} \quad (4.3)$$

Pore size distribution

The average pore size and size distribution are important parameters affecting the material's thermal performance. Although they can be derived directly from the μ CT images of the samples, they are here also characterized experimentally to allow for comparison. The Mercury Intrusion Porosimetry technique (MIP) is used for this purpose. The technique will force liquid mercury into the sample's pore space with increasing pressure. Since the contact angle of mercury on the glassy matrix is higher than 90 °, larger pores will be intruded first while smaller pores will be intruded only at higher pressures. The capillary pressure equation relates the applied mercury pressure to the minimum radius of the pores filled at that pressure. Measuring the intruding volume of mercury at each pressure step, the volumetric distribution of pore sizes is derived. More details can be found in (Giesche 2006). Typically, pore sizes

between a few nanometre and a few hundreds of micrometre can be characterized with this technique. The MIP apparatus used is a Micromeritics AutoPORE IV 9500.

4.4. Sintered glass filter

We start with discussing the validation on the sintered glass filter. The material has a single-scale pore size and is expected to be completely open-porous. Furthermore, its matrix consists of a single type of glass with known properties, making it ideal as a first validation material.

4.4.1. Experimental results

The porosity and ETC measurements are performed on 6 samples of $10 \times 10 \times 3.33 \text{ cm}^3$. The ETC measurement is performed at room temperature. The results are summarized in Table 4.2. The bulk densities obtained by both the mass method and vacuum saturation method agree very well with less than 2 %-points difference. The open porosity obtained with the vacuum saturation method is slightly lower than the total porosity obtained with the mass method, probably due to some loss of water content during the experimental process. The closeness of both porosities indicate the absence of closed porosity. Further on, the samples are supposed to have a total average porosity of 35.8 %.

Table 4.2: Experimental results of porosity and ETC measurement on sintered glass filter.

Measured property	Method	Average	Standard deviation
Solid density	Literature	2260.7 kg/m ³	n.a.
Bulk density	Mass method	1406.7 kg/m ³	6.1 kg/m ³
Bulk density	Vac. Sat.	1431.8 kg/m ³	4.9 kg/m ³
Open porosity	Vac. Sat.	35.8 %	0.2 %
Total porosity	Mass method	37.8 %	0.3 %
Dry ETC @ 20 °C	Heat Flow Meter	0.376 W/mK	0.008 W/mK
Saturated ETC @ 20 °C	Heat Flow Meter	0.889 W/mK	0.01 W/mK

The MIP measurement is performed on a small extracted sample of about $2 \times 1 \times 1 \text{ cm}^3$. The resulting pore size volumetric distribution is shown in Figure 4.12. The material has a relatively narrow pore size distribution ranging from 20 μm to 100 μm with a peak around 40 μm . All pores are hence properly visualizable in a single μCT scan.

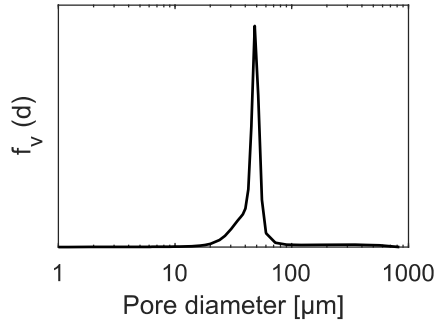


Figure 4.12: Pore size distribution of sintered glass filter obtained with MIP measurement.

Lastly, a total of 5 cylindrical samples are extracted from the sintered glass filter material, with diameters varying around 4 mm. 3 samples are scanned using the GE Nanotom with a voxel size of 2.5 μm . Two other samples are scanned using a Skyscan 1172 machine, with a voxel size of 1.9 μm and 2.9 μm respectively. Sample A and B are furthermore scanned at three different locations of the cylinder: bottom, middle and top. The different scanning settings allow to inspect their impact on the resulting images and simulation results. Sample details are specified in Table 4.3.

Table 4.3: Different scanning settings applied during the μCT scanning of the sintered glass filter.

Sample	Machine	Voxel size [μm]	Scanning location	Porosity after segmentation [%]
A	GE Nanotom	2.5	Bottom/middle/top	30.9/32.8/32.5
B	GE Nanotom	2.5	Bottom/middle/top	34.7/35.2/32.4
C	GE Nanotom	2.5	Middle	36.6
D	Skyscan 1172	1.9	Middle	36.6
E	Skyscan 1172	2.9	Middle	36.6

The porosities from the scans on sample C, D and E correspond well to the measured porosity shown in Table 4.2, while parts of sample A and B show larger deviations probably due to local inhomogeneities. A reconstructed slice of sample C is shown in Figure 4.13, together with its segmentation and a 3D render. One can clearly see the different glass particles sintered together. The particles seem to have similar volumes, but different shapes, orientations and degree of overlap (sintering).

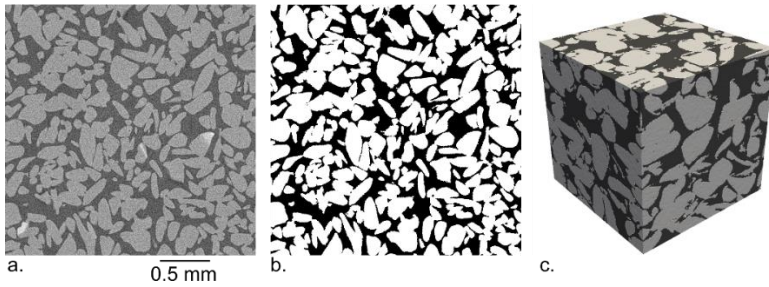


Figure 4.13: Grayscale slice (a), segmented slice (b) and 3D render (c) obtained via μ CT scanning on sintered glass filter.

4.4.2. Simulation setup

The model framework is applied to numerically predict the thermal conductivity of the sintered glass filter. Four subsamples are extracted from each of the segmented 3D images. The simulated image size of the subsamples from samples A, B, C, sample D and sample E is set to respectively 500^3 , 600^3 and 400^3 voxels, always giving a simulated cubic volume with a side length above 1 mm. The tetrahedral and triangular mesh size parameter is set to $10\ \mu\text{m}$, the edge points insertion size and the surface approximation size are set to half of the voxel size. Mesh refinement analysis shows no further improvement. The thermal conductivity of the solid glass particles is set to $1.13\ \text{W/mK}$, according to the manufacturer's datasheet (ROBU Glasfilter-Geraete GmbH n.d.). The thermal conductivity of the pores is set to $0.026\ \text{W/mK}$ for the oven-dry case (Huber and Harvey 2011) and $0.598\ \text{W/mK}$ for the water-saturated case (Ramires et al. 1995). Thermal radiation is expected to be negligible due to the low porosity and small average pore size (Solórzano et al. 2009). This is confirmed by a simulation on 1 subsample of sample C, revealing an increase of only 0.1% in the ETC when including thermal radiation. It is therefore not taken into account in the other simulations. Although having an open-porous pore structure, natural convection is equally considered negligible due the small pores and small sample thicknesses used during the measurements.

4.4.3. Results & discussion

The experimental and numerical results are shown in Figure 4.14a and c for the oven-dry and water-saturated cases respectively, together with the results predicted by 5 known analytical models. A power-law trendline is least-squares-fitted through all numerical results, showing the expected decrease of the ETC with increasing porosity for both cases. To allow for a reliable assessment of the model's accuracy, a zoom is shown for the region around the experimentally measured results in Figure 4.14b and d; the analytical models are not repeated in the zoom for clarity.

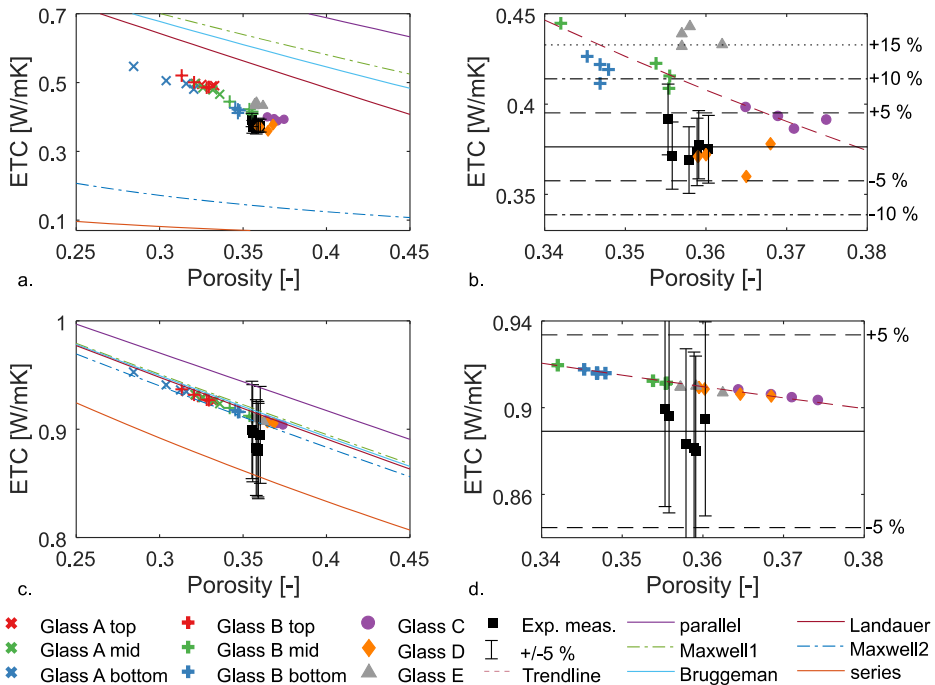


Figure 4.14: Comparison of experimental and simulation results for the sintered glass filter together with a zoom on the region around the experimental results in air-dry (a,b) and water-saturated (c,d) condition. Also shown are predictions by some analytical models: the parallel (Eq. (2.2)), the series (Eq. (2.1)), both Maxwell models (Eq. (2.3)&(2.4)), the Bruggeman (Eq. (2.5)) and the Landauer (Eq. (2.6)) model. Analytical models are not repeated in the zoom for clarity.

Starting with the oven-dry case, the results agree relatively well with the average measured ETC, showing a similar trend with porosity as the analytical models but with a highly improved accuracy. All results furthermore fall into the ‘granular region’ defined by Carson (Carson et al. 2005) as the region between the Maxwell 2 model and the Landauer model. For sample C and the bottom and middle of sample B, all scanned with a voxel size of $2.5\ \mu\text{m}$ and showing porosities close to the experimental, average deviations vary between 4.1 % and 11 %, differences occurring due to local inhomogeneities. The average results of sample D and E on the other hand, scanned at $1.9\ \mu\text{m}$ and $2.9\ \mu\text{m}$, perform respectively very well and slightly worse. This is probably explained by the differing voxel sizes of the scans. Indeed, as revealed by the verification study in the previous chapter, simulations on granular materials are relatively sensitive to the voxel size used in the geometric representation of the material’s microstructure. This effect is also clearly visible here in Figure 4.14b, showing an increasing accuracy with decreasing voxel size at approximately equal sample porosity. Lastly, the

simulations on sample A and the top side of sample B agree less with the experimentally measured thermal conductivity, due to the larger discrepancy between their porosity and the macroscale porosity. On the other hand, they clearly indicate the logical variation of the sample's ETC with changing porosity, similar to the analytical models. Samples with microstructural properties close to the average macroscale properties should hence be selected when trying to obtain a simulated thermal conductivity close to the material's macroscale ETC.

For the water-saturated case shown in Figure 4.14c and d, both the simulations and the analytical models give very similar results. The relative deviations with the experimental measurements are below 5 %, which is generally smaller compared with the oven-dry case. Furthermore, results are closer to the trendline fitted through all the simulations. This can be explained by the lower solid-fluid thermal conductivity ratio, rendering the relative impact of the microstructural properties like porosity, connectivity etc. less important.

Concluding, both the oven-dry and water-saturated simulation results agree relatively well with the experimental outcomes. The framework clearly outperforms common analytical models for high solid-fluid conductivity ratios. This demonstrates the importance of taking into account the true microstructural properties of the porous material when studying its ETC. However, samples with porosities close to the macroscale porosity should be selected to obtain results similar to the macroscale thermal conductivity. Furthermore, the applied voxel size plays an important role, indicating an increasing accuracy with decreasing voxel size. With proper settings, the model shows the capability to reliably study the thermal conductivity of granular porous materials and obtain results with deviations below 10 %.

4.5. Reapor porous block

The second validation exercise is performed on a Reapor porous block. The material has a much higher porosity than the sintered glass filter, and has furthermore a bimodal pore size distribution, making it a very different type of material and hence an interesting validation case.

4.5.1. Experimental results

The porosity, density and ETC are measured on 5 samples of $10 \times 10 \times 2 \text{ cm}^3$. Since the technical datasheet mentions a ETC of 0.08 W/mK at $10 \text{ }^\circ\text{C}$ average temperature, the ETC is also measured at this average temperature. Results of the experimental characterisation are summarized in Table 4.4.

Table 4.4: Experimental results of porosity and ETC measurement on Reapor block.

Measured property	Method	Average	Standard deviation
Solid density	Literature	2493.9 kg/m ³	/
Bulk density	Mass method	273.2 kg/m ³	5.4 kg/m ³
Bulk density	Vac. Sat.	262.8 kg/m ³	2.5 kg/m ³
Open porosity	Vac. Sat.	88.5 %	0.2 %
Total porosity	Mass method	89.0 %	0.2 %
Dry ETC @ 10 °C	Heat Flow Meter	0.084 W/mK	0.002 W/mK
Saturated ETC @ 10 °C	Heat Flow Meter	0.617 W/mK	0.014 W/mK

The MIP measurement is performed on a small extracted sample of about 2 x 1 x 1 cm³. The resulting pore size volumetric distribution is shown in Figure 4.15b. It can be noted that the material indeed has two pore classes: the first relates to the peak around 15 µm, representing the pore throats giving access to the cellular pores inside the granules. Part of the second pore class is indicated by the peak starting above 100 µm, corresponding to pore space in between the sintered granules with pore diameters in the millimetre range. Although these large pores cannot be characterized in more detail using the MIP setup, visual inspection of the sample clearly confirms the existence of these pores.

The bimodal character implies that separate µCT scans are required to characterize both pore space structures. For the porosity inside the granules (the intragranular scale), two scans are made on some extracted granules. The voxel size is set once to 1.5 µm and once to 1.6 µm. At the intergranular scale (pore space between the different granules) a scan is made on a cylinder of about 2.5 cm diameter, with a voxel size of 16 µm. All scans are performed using the GE Nanotom machine. During segmentation of the intergranular scans, the intragranular pores still visible inside the granules are artificially solidified since these were already visualized in the intragranular scan. A reconstructed slice of both scanned scales is shown in Figure 4.15, together with a segmented slice and a 3D render. At the intragranular scale, one can clearly see the cellular pore structure. At the intergranular scale, the granules are of similar volume and ellipsoid-like shape.

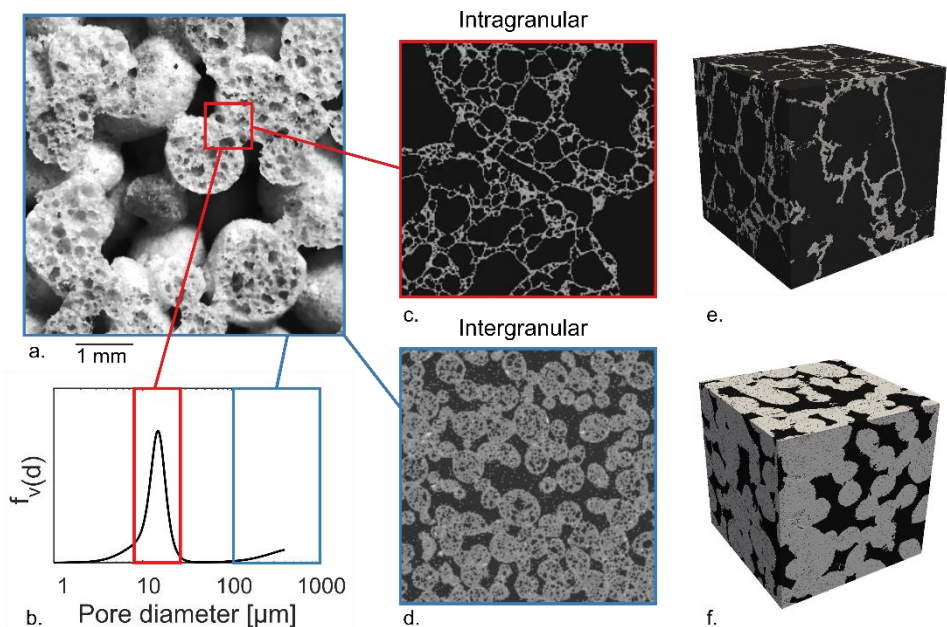


Figure 4.15: Photograph of pore structure (a) and pore size distribution of Reapor material (b). μCT slices of intra- and intergranular scale (c-d) and 3D render of both scales (e-f) of the Reapor material.

4.5.2. Simulation setup

The model framework is applied to predict the thermal conductivity of the Reapor material. As there is a clear separation between the intra- and intergranular pore spaces, a hierarchical approach is adopted to tackle the bimodal nature of the porosity: simulation results obtained on the intragranular level are first averaged and then used in the simulations performed on the intergranular scale. All simulations are performed at a mean sample temperature of 10 °C to allow for a correct comparison with the experimental measurements and the technical datasheet.

Simulations at intragranular scale

A total of 7 subsamples is extracted from both scans made at the intragranular scale. A simulated image size of 300^3 voxels is employed to ensure that every sample fits completely inside the granules. The tetrahedral and triangular mesh size parameter is set to 4.8 μm , the edge points insertion size and the surface approximation size are set to half of the voxel size. Mesh refinement analysis again shows no further improvement. Based on the chemical composition mentioned in the technical datasheet (Liaver GmbH & Co. KG 2014), the glass matrix thermal conductivity is determined to be 1.06 W/mK (Choudhary and Potter 2005).

The thermal conductivity of the pores is set to 0.025 W/mK for the air-dry case (Huber and Harvey 2011) and 0.578 W/mK for the water-saturated case for 10 °C mean temperature (Ramires et al. 1995). Thermal radiation is taken into account in the oven-dry case, using the previously described expanded Loeb model, setting the emissivity of the glass pore walls to 0.9 (Liley 2018). Thermal radiation is not taken into account in the water-saturated case: the relatively large absorption coefficient of water at room temperature virtually nullifies radiative heat exchange between opposing pore cell walls (Siegel and Howell 1992).

Simulations at intergranular scale

Five subsamples are extracted from the scan made at a voxel size of 16 μm , each having a simulated image size of 400^3 voxels and hence a side length of 6.4 mm. The tetrahedral and triangular mesh size parameter is set to 48 μm , the edge points insertion size and the surface approximation size are set to half of the voxel size. Mesh refinement analysis again shows no further improvement. The thermal conductivity of the (now considered completely solid) granules is set to the value corresponding to the average porosity encountered at the intragranular scale. Obviously, the thermal conductivity of the air or water inside the pores remains the same as in the lower-scale simulations. Thermal radiation is again taken into account using an emissivity of 0.9 for the glass pore walls (Liley 2018).

4.5.3. Results & discussion

Results are first discussed for the intragranular scale, and subsequently for the intergranular scale (the complete material).

Results at intragranular scale

The simulation results of the 7 subsamples extracted from sample 1 and 2 are shown in Figure 4.16 for the oven-dry (a) and water-saturated (b) case. A power-law trendline is least-squares-fitted through the results, showing the expected decrease of the thermal conductivity with increasing porosity. The rather large variation between the different samples is due to the small size of the simulated volumes, limited to fit inside the granules. The average porosity encountered in the simulated samples is 81.2 %, which results, according to the trendline, in an average thermal conductivity of 0.129 W/mK and 0.655 W/mK for the granules in the oven-dry and the water-saturated state. Thermal radiation accounts only for about 2 % of the calculated ETC for the oven-dry case, due to the small pore sizes inside the granules and the relatively low average sample temperature (10 °C).

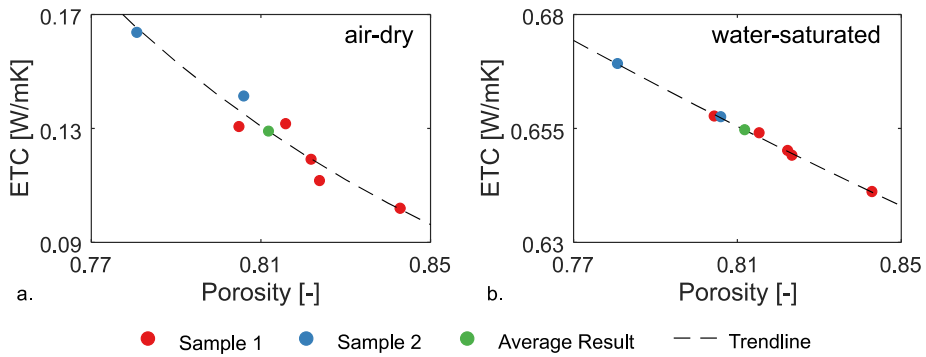


Figure 4.16: Simulated thermal conductivity results on intragranular scale of Reapor material.

Results at intergranular scale

The experimental and numerical results for the whole material are shown together with a zoom in Figure 4.17a and b for the oven-dry case, and in Figure 4.17c and d for the water-saturated case. Results predicted by the analytical models and the value retrieved in the manufacturer's technical datasheet (Liaver GmbH & Co. KG 2014) are also shown. A power-law trendline is least-squares-fitted through the numerical results. For the calculation of the porosity of the simulation samples, the calculated average porosity of 81.2 % is assumed inside all the granules, leading to overall porosities of 88 % which is very close to the experimentally measured values.

The simulated oven-dry thermal conductivities are relatively close to the experimental results, showing a decrease with porosity similar to the analytical models. On average, a relative deviation of about 5 % is achieved, indicating the good performance of the model framework and validating its application for two-scale hierarchical simulations. The framework performs furthermore much more accurate than the results predicted by the analytical models. For the oven-dry case, thermal radiation accounts for about 3 % of the total ETC. This rather low influence is explained by the small pore size inside the granules, the low macro-porosity between the granules and the low average sample temperature (10 °C). For the water-saturated case, simulations agree almost perfectly with the measurements, achieving deviations around 1 %. Similarly as in the sintered glass filter case, the model shows a better performance relative to the oven-dry case because of the lower solid-fluid thermal conductivity ratio. The results of the analytical models also agree very well with the experiments, for the same reason.

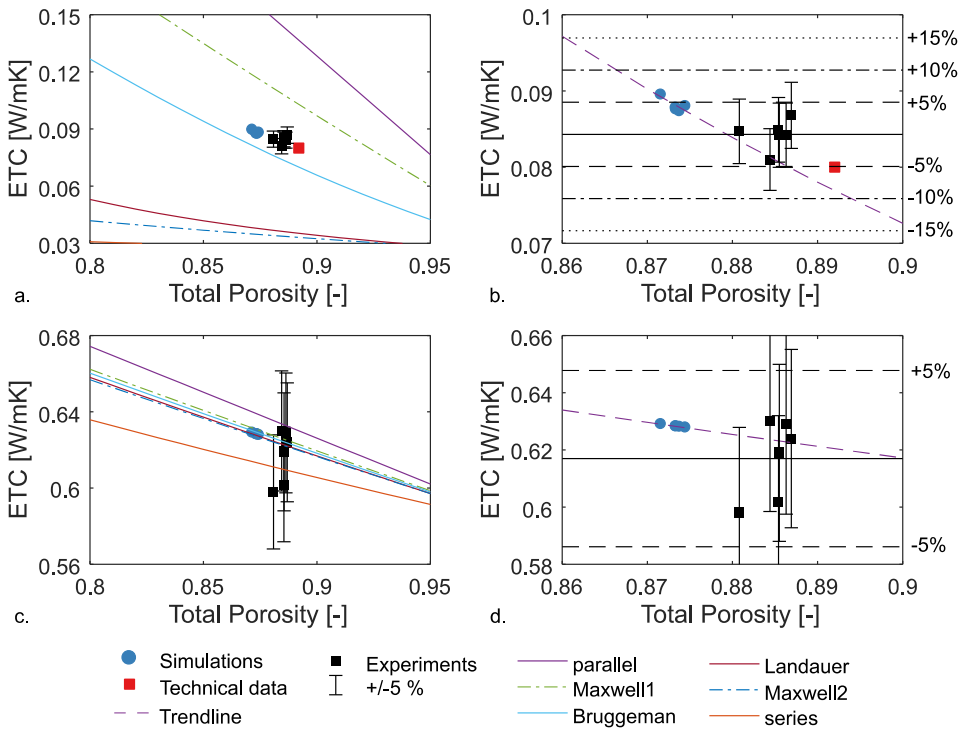


Figure 4.17: Comparison of experimental and simulation results for the Reapor material together with a zoom on the region around the experimental results in air-dry (a,b) and water-saturated (c,d) condition. The technical data is also shown for the air-dry case. Also shown are predictions by some analytical models: the parallel (Eq. (2.2)), the series (Eq. (2.1)), both Maxwell models (Eq. (2.3)&(2.4)), the Bruggeman (Eq. (2.5)) and the Landauer (Eq. (2.6)) model. Analytical models are not repeated in the zoom for clarity.

Concluding, the model framework allows to accurately predict the thermal conductivity of the Reapor material both in oven-dry and water-saturated conditions, indicating its capability to study the thermal conductivity of highly porous building blocks with a cellular, granular or even mixed pore structure. Furthermore, the possibility to apply the model in a hierarchical approach to study materials with a multimodal pore network is demonstrated to give good results, widening its applicability to a broad range of materials.

4.6. Cellular glass Perinsul S

A last validation exercise is performed on a Perinsul S block, a cellular glass material by Foamglas. The material has a very high porosity, and a bimodal type of pore structure, with small pore cells contained in the cell walls and struts. Additionally, the performance of the model to predict the temperature-dependent ETC is also studied for the cellular glass material by performing the validation at two different temperatures.

4.6.1. Experimental results

The experimental measurements are performed on three samples of $10 \times 10 \times 2.5 \text{ cm}^3$. Since the samples have a closed-cell pore structure, the bulk density and porosity are only determined via the mass method. The ETC is measured at $10 \text{ }^\circ\text{C}$ and $50 \text{ }^\circ\text{C}$. Results are summarized in Table 4.5.

Table 4.5: Experimental results of porosity and ETC measurement on cellular glass Perinsul S samples.

Measured property	Method	Average	Standard deviation
Solid density	Literature	2490.2 kg/m^3	/
Bulk density	Mass method	190.7 kg/m^3	11.0 kg/m^3
Bulk density	Vac. Sat.	/	/
Open porosity	Vac. Sat.	/	/
Total porosity	Mass method	92.3 %	0.4 %
Dry ETC @ $10 \text{ }^\circ\text{C}$	Heat Flow Meter	0.054 W/mK	0.003 W/mK
Dry ETC @ $50 \text{ }^\circ\text{C}$	Heat Flow Meter	0.059 W/mK	0.003 W/mK

The cellular glass has the highest porosity of the samples studied in this chapter (92.3 %) and the lowest ETC: 0.054 W/mK at $10 \text{ }^\circ\text{C}$. At a temperature of $50 \text{ }^\circ\text{C}$ the ETC is about 10 % higher, which is probably explained by the increase in gaseous conductivity and in thermal radiation with increasing temperature.

A μCT scan is performed on one sample using the Nanotom GE. Obtaining a good 3D image of the pore structure is more difficult for this type of material though. First of all, a small voxelsize of $2.5 \text{ }\mu\text{m}$ is needed to properly visualize the small pores in the cell walls of the large pores. The downside is that only a relatively small amount of the large pores are included in the scanned volume due to the limited sample size of 1000^3 voxels. A hierarchical approach similar as for the Reapor material could not be applied here, since there is no clear separation of scales. Secondly, the presence of small pores inside the thin cell walls complicate the

segmentation process due to the partial volume effect: a relatively larger amount of voxels are doubted to belong to either the solid or gaseous phase (Claes et al. 2019). These two factors partially explain the resulting porosity of the scanned sample being only 86.7 %, which is significantly lower than the 92.3 % obtained experimentally. Furthermore, since there is only one scanned sample available, simulation results cannot show a trend with increasing porosity. Therefore, the image set is expanded with two extra images obtained by artificially altering the original image through erosion of the solid matrix. A spherical erosion element of one voxel or three voxels respectively is used leading to higher porosity versions of the original sample. Whereas this alteration does not accord with the true pore structure of the material, it can still help in assessing the impact of the porosity. A slice and 3D render of the original image are shown in Figure 4.18, together with a slice of both altered versions of the 3D image.

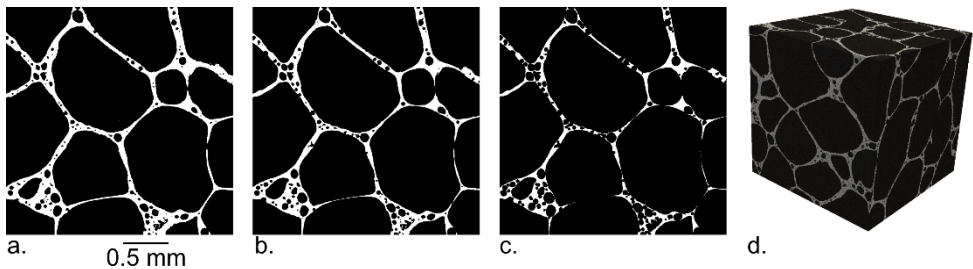


Figure 4.18: Slice after original segmentation (a) and after erosion with 1 element (b) and 3 elements (c) and a 3D render of the original cellular glass obtained via μ CT scanning (d).

4.6.2. Simulation setup

Simulations are performed on the original image and both altered versions of the original image, always on the full image size of 1000^3 voxels. Furthermore, each sample is simulated three times by changing the applied temperature gradient to the three principal directions (x, y and z). The porosity of the sample stays of course the same when changing the heat flow direction, but other parameters like the pores' slenderness factor or matrix connectivity will differ between the different orientations and can hence yield some spread of results.

All samples are simulated once at an average temperature of $10\text{ }^\circ\text{C}$ and once at $50\text{ }^\circ\text{C}$, as in the experimental measurements. The matrix thermal conductivity is set to 1.06 W/mK , similar to the Reapor material. The gas in the cellular glass pores consists of CO_2 , a consequence of the production process and the closed-cell porosity of the material. As a result, the gas pressure inside the pores might be different than the atmospheric gas pressure. Given the relatively large average pore size of the cellular glass, a potentially reduced gas pressure will have very little influence on the gaseous conductivity (less than 5 % reduction for a pore size of 1 mm

and a gas pressure of 1000 Pa (B. P. Jelle, Gustavsen, and Baetens 2010)). Hence, the atmospheric gas pressure thermal conductivity of 0.0154 W/mK and 0.0187 W/mK respectively is set for the gaseous conductivity at 10 °C and 50 °C (Huber and Harvey 2011). Thermal radiation is taken into account using the previously described expanded Loeb model, setting the emissivity of the glass pore walls to 0.9 (Liley 2018). The triangular mesh size parameter is set to 2.5 μm , the tetrahedral mesh size to 1.25 μm for the solid matrix and 5 μm for the pore space. The edge points insertion size and the surface approximation size are set to 1.5 respectively 0.5 times the voxel size. Mesh refinement analysis again shows no further significant impact on the numerical results.

4.6.3. Results & discussion

The simulation results for an average temperature of 10 °C are compared in Figure 4.19 with the experimentally obtained ETC of the material at 10 °C. Also shown is the technical data value for the thermal conductivity (Pittsburgh Corning Europe NV 2018). The three simulation results at 86.7% porosity correspond to the three main directions of the original sample, while values at other porosities correspond to the altered images.

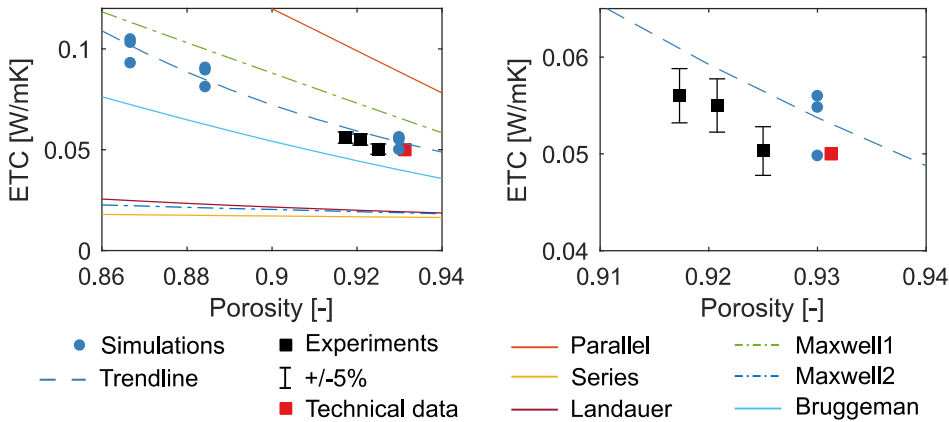


Figure 4.19: Comparison of experimental measurements and simulation results on cellular glass sample at 10 °C. The graph on the right zooms on the zone around the experimental measurements. Also shown are predictions by some analytical models: the parallel (Eq. (2.2)), the series (Eq. (2.1)), both Maxwell models (Eq. (2.3)&(2.4)), the Bruggeman (Eq. (2.5)) and the Landauer (Eq. (2.6)) model. The analytical models are not repeated in the zoom for clarity.

The porosity off-set of the original image causes a large discrepancy between the simulation and experimental results. The artificial increase of the porosity ensures a much better agreement, with only 5 % to 10 % deviation between the simulations trendline and the

experimental measurements at similar porosity. This underlines again the importance of an adequate representation of the pore structure to use the framework as a predictive model for real materials.

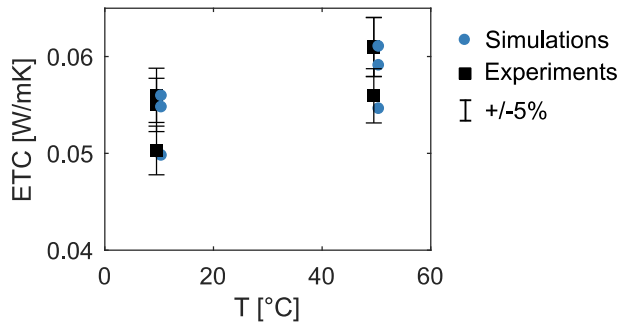


Figure 4.20: Comparison of effect of increasing temperature on experimentally and numerically obtained ETC of cellular glass. Results show a similar increase with temperature. Simulation and experimental results are slightly shifted on the temperature axis to improve readability.

The influence of the temperature on the ETC is shown in Figure 4.20 for the simulations performed on the altered image with the highest porosity (which is closest to the real material's porosity). Simulation results and experimental results agree relatively well, and furthermore show the same trend with increasing temperature. The increase with temperature in the numerical results is completely due to the increasing gaseous conductivity and thermal radiation. For a single sample, the contribution of thermal radiation is estimated by performing the same simulations without radiation, the difference with the original results considered as the macroscopic effective radiative conductivity. At 10 °C, it contributes only about 2 % of the total ETC, increasing to 3 % at 50 °C. Although this is an increase of 50 % of the thermal radiation contribution, its total contribution is still very small due to the relatively small pore size and the strongly conductive matrix. Such moderate influence of thermal radiation agrees with experimental results by, for example, Bourret et al. (2014) on geopolymers with similar characteristics. The impact of thermal radiation is hence too small to truly validate the implementation of the thermal radiation model. Nonetheless, the results indicate at least a correct prediction of the order of magnitude.

Concluding, predicting the ETC for the cellular glass proves to be more challenging. The complex pore structure does not allow to obtain a correct image of the pore structure while at the same time being representative for the whole material. When adapting the image to correspond better to the material's actual porosity, simulation results agree very well, within

10 % deviation. Furthermore, the increasing ETC with increasing temperature of such a highly porous building block can be predicted equally well.

4.7. Conclusions

This chapter discussed the validation of the model framework as presented in Chapter 3. First, a measurement apparatus for experimentally characterizing the thermal conductivity of small porous samples is discussed. The set-up shows good performance in comparison with other techniques. Subsequently, the actual validation of the framework is discussed on three different materials: a sintered glass filter, a Reapor block and a cellular glass block. Their porosity, pore size distribution and thermal conductivity are studied experimentally, while μ CT scanning is applied to characterize the pore structure. The model framework is applied to predict the ETC based on the scanned pore structures. For the Reapor block, a hierarchical approach to overcome the two-scale nature of the material is used.

For dry conditions, comparison with the experimental measurements shows deviations below 10 % when comparing for equal porosities, while for the saturated conditions these deviations decrease to below 5 %, which can be attributed to the lower solid-fluid conductivity ratio. Simulation results also indicate the importance of an adequate representation of the pore structure to obtain good agreement with experimental results. Indeed, a difference between the scanned and real porosity results in quite large deviations on the predicted ETC. Future improvements on the scanning of pore structure is hence needed to improve the prediction capability for real materials. Nonetheless the framework shows the capability to accurately predict the ETC of porous materials for a wide range of porosities and both cellular and granular pore structures.

Chapter 5

Parameter studies towards optimal pore structures

5.1. INTRODUCTION	109
5.2. EXPLORATORY PARAMETER STUDY	110
5.3. DETAILED PARAMETER STUDY	123
5.4. CONCLUSIONS	129

5.1. Introduction

A better understanding of the relation between the pore structure and the ETC of porous building blocks is needed to speed up the development of new blocks (a.o. based on recycled waste materials) with a focus on their thermal performance. Studies so far have often emphasised a single specific parameter like porosity, or did consider several parameters but with a restricted range of variation. This leaves doubt on the actual impact of the (combined) pore structure parameters, and obscures which parameters should be tackled first when tweaking the pore structure to obtain better ETC values.

In this chapter, the impact of the material's pore structure parameters and physical parameters is investigated with the model framework presented and validated in the foregoing chapters. Two sequential parameter studies are performed to this end: first, a broad study is performed considering for every parameter the full range of values encountered in typical porous building blocks. Several pore structures are randomly generated and their ETC's are calculated with the framework. Results from this first study allow to indicate the main trends and to compare the impact of the different parameters over their full range of values. The second study, on the other hand, zooms in on high-porosity and low-matrix-conductivity samples to quantify the potential influence of the other parameters when both porosity and matrix conductivity have already been optimized.

5.2. Exploratory parameter study

The first parameter study focusses on the full range of parameter values encountered in typical porous building blocks. The ETC of a random set of samples is predicted using the model framework presented and validated in the foregoing chapters. The pore structure parameters and the physical parameters are varied to cover the complete range of parameter values. Results are interpreted based on the varied parameters aiming to indicate the primary and secondary parameters and their potential impact on the ETC.

5.2.1. Methodology & Setup

The random bubble insertion (RBI) and watershed based (WSB) technique (discussed below) are used to each generate 50 different pore structures based on a set of specified parameters. With the physical properties (like matrix conductivity, ...) varying as well over the samples, their ETC is then predicted with the framework. First, the selection of the relevant parameters is discussed together with the space-filling sampling of the pore structure and physical factor parameter space. Subsequently, both pore structure generation techniques are described in more detail together with the size of the samples. Lastly, the setup for the thermal simulations with the model framework is discussed.

Parameter space

Studies performed in literature have mentioned a wide variety of pore structure parameters potentially influencing the ETC of a porous material. Here, we choose to study the impact of the three parameters most often mentioned and furthermore most easily controllable during the production process: the porosity, the average pore size, and the pore size distribution. For the latter, a lognormal distribution is used for all the samples. All three parameters are varied over the range shown in Table 5.1 to obtain a wide range of different pore structures. The width of the pore size distribution is defined by $v_{\text{norm, factor}}$, a factor that should be multiplied with the square of the average pore size to obtain the variance of the distribution. For each parameter set, two different generation algorithms are used, each yielding a different matrix morphology. Other variations of pore structure parameters, like e.g. different pore shapes, other types of pore size distributions, or anisotropic pore arrangements, are not studied here, to restrict the computational cost. Nonetheless, the model allows to address them in future studies.

Additionally, the physical properties of the phases constituting the material are also varied: the matrix conductivity λ_{mat} [W/mK], the type of gas and the wall emissivity ϵ [–]. Indeed, porous materials can be produced based on different solid materials, like polymers, cement-

based solids, glass, ..., each having different matrix conductivities. Furthermore, the matrix conductivity can be altered by including microporosity or other low-conductivity particles in the matrix. The variation of the type of gas inside the pores is inspired by gas-filled panels, described in literature as promising insulation materials (Baetens, Jelle, Gustavsen, et al. 2010). The wall emissivity, lastly, has also been put forward as a possible strategy to reduce the thermal radiation, notably also in gas-filled panels (Baetens, Jelle, Gustavsen, et al. 2010). Finally, the average temperature during the simulations is also taken as a variable parameter. Although strictly not a property of the porous material, we still consider this parameter since it might influence the impact of other pore scale parameters (like an increasing importance of pore size due to increasing radiation at higher temperatures). Hence, seven different parameters are selected as variable. They are summarized in Table 5.1, along with the minimum and maximum value considered per parameter. For each type of gas, the gaseous thermal conductivity at 20 °C is also shown as illustration.

Table 5.1: Studied parameters in the first parameter study and their range of values.

Parameter	Minimum	Maximum
ϕ	0.6	0.95
$d_{pore,mean}$	10 μm	2 mm
$v_{norm,factor}$	0.016	0.4
λ_{mat}	0.2 W/mK	2 W/mK
$\lambda_{gas,type}$	Xenon - Krypton - CO2 - Argon - Air	
$\lambda_{gas,20\text{ }^\circ\text{C}}$	5.5 - 9.1 - 16.2 - 18.1 - 25.7 mW/mK	
ϵ	0.1	0.9
T_{avg}	-10 °C	40 °C

The Sobol sequence is used to sample this 7-dimensional parameter space. This technique is known to provide a superior space-filling sampling of the multidimensional parameter space, even for a small amount of sample points. A 50 x 7 subset of random numbers between 0 and 1 is generated and projected linearly on the 7 parameters assuming a uniform distribution for each parameter. Since both the RBI and WSB technique used to generate the pore structures require the same input parameters, the same parameter set of 50 x 7 is used for both, resulting in 100 different pore structures.

Sample Generation

Two different techniques are used to generate a range of virtual materials: the random bubble insertion technique (RBI) and the watershed-based technique (WSB).

RBI generation

A random bubble insertion (RBI) algorithm is implemented based on the original proposed by She et al. (She, Zhang, and Jones 2014). It starts with generating a list of pore diameters according to a specific pore size distribution (i.e. lognormal). A random location in the cubic sample is assigned to every pore in the list, ensuring that the overlap with already present pores remains below a set threshold (here set to 20 % of the smallest diameter of both overlapping pores). If no location is found for the concerning pore, the algorithm skips this pore and continues with the next pore in the list. A 3D voxel image is finally generated based on the list of inserted pores. For porosities above 60 %, the algorithm is extended with a second pore generation sequence to overcome the increasingly time-consuming procedure of random localization at such high sphere packing densities. In this second generation sequence, pore diameters are again generated randomly according to the specified distribution and are immediately attempted to be inserted. Using the distance transform of the 3D voxel image, suited locations are retrieved easily prior to insertion. Pores that do no longer fit in the sample are skipped, hence favouring the generation of smaller pores filling up the remaining space. Figure 5.1 shows two examples of samples generated using the RBI algorithm with a lognormal distribution.

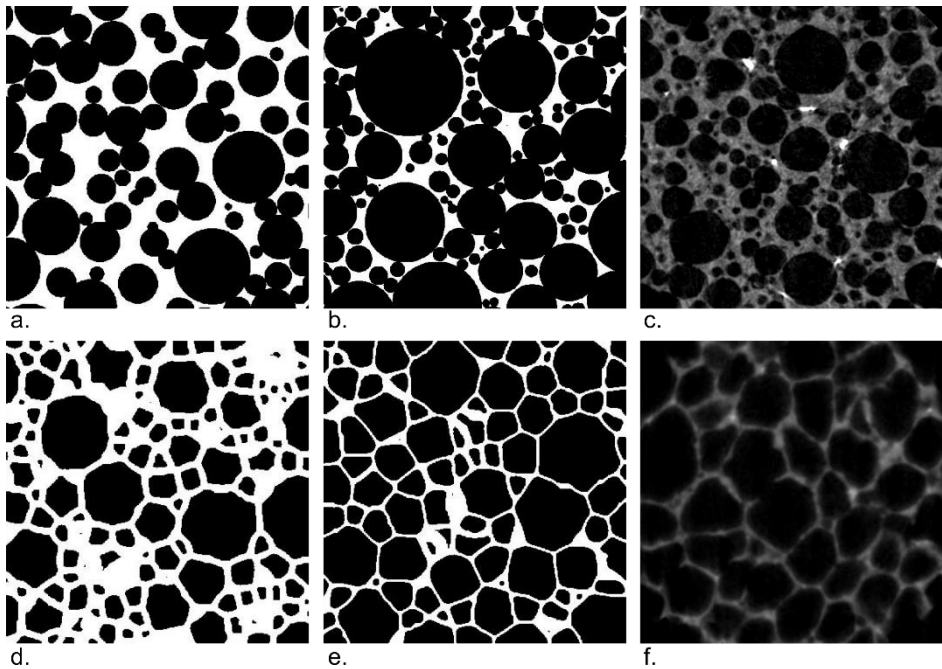


Figure 5.1: Slices of 4 different 3D samples, two generated with the RBI technique (a&b) and two generated with the WSB technique (d&e). Additionally, the pore structure of a waste-based porous building block with an RBI type of pore structure (c) and a pore structure of Multipor aerated concrete with a WSB type of pore structure (f) are shown for comparison. The image of the waste-based porous building block is a courtesy of Roberto E.M. Alarcón from the Materials Engineering Department of KU Leuven.

WSB generation

The WSB technique is a more recent generation method based on the Voronoi algorithm, but allowing to more easily control the pore size distribution. It starts with randomly filling a cubic volume with spheres similar as the RBI technique. Subsequently, a distance transform of the pore space and the inverse distance transform of the matrix space is performed and combined in one image. The watershed planes are then calculated from this combined image, and these are interpreted as the cell walls, leading to a foam-like type of pore structure of closed cells around each initially inserted sphere. Imposing a certain pore size distribution for the initially placed spheres' diameters allows to control the size distribution of the resulting cells. A regular lattice of equally sized, non-overlapping spheres would theoretically lead to the same pore structure as the Voronoi technique based on the centres of the spheres. Figure 5.1 shows two examples of samples generated with the WSB technique.

Sample size

Apart from the porosity, mean pore size and pore size distribution, the generation algorithms also expect a measure for the sample side length. This choice is not trivial, since it determines how many pores are included in each sample and thus whether the sample can be considered as being thermally representative for the complete porous material. Thermally representative means that the calculated ETC agrees closely with the true ETC of a porous material. Indeed, this may differ from the representative sample size for quantifying the porosity for example. Several authors have already studied the needed sample size for thermal representativeness, leading to prescribed side lengths ranging from 3 to 10 times the average pore diameter (Nait-Ali 2005; Haussener et al. 2009; Randrianalisoa et al. 2015; Patel and Talukdar 2018; Bracconi et al. 2018; M. Wang, Wang, Pan, Chen, et al. 2007). This relatively large variation of suggested minimum side lengths suggests that the RVE depends on other parameters as well, for example the porosity, but also the matrix conductivity as was discussed by Ganapathy et al. (Ganapathy et al. 2005). Furthermore, it is expected that the pore size distribution will influence the needed volume as well. Here, the choice is made to set this sample side length to 6 times $d_{pore,90}$ [m], the 90th percentile of pore sizes. In some preliminary simulations, this measure shows to provide a sound trade-off between the computational cost and the representativeness of the sample's ETC.

Simulation setup

The ETC of the generated samples is predicted with the numerical framework. The rejoinfactor is set at 0.6, used to split the pore space in different pore clusters. The expanded Loeb method is applied to model thermal radiation. The finite-element mesh of every sample is constructed with a triangular mesh size parameter of 2.5 voxels. The tetrahedral mesh size parameter is set to 2.5 voxels for the matrix and the smallest class of pores; the mesh size of the other pores is raised according to their size ratio relative to the smallest pore, to reduce the computational cost. All other needed input parameters are set to the associated values in the Sobol sample set.

5.2.2. Results & Discussion

The results for all 100 studied samples are discussed. First, the resulting pore structure of the generated samples is investigated, followed by a discussion on their predicted ETC.

Properties of generated samples

For every generated sample the porosity, average pore size and normalized variance factor is calculated directly from the 3D voxel image. The average pore size and volume distributions are obtained by calculating for every pore the radius of the equivalent sphere having the same volume. Figure 5.2 compares the obtained pore structure properties with the targeted properties to see if the both generation algorithms are able to produce the intended structures. Regarding the porosity, the RBI generated samples show a large discrepancy for samples with targeted porosities above ~70 %. This is due to their spherically shaped pores and the maximal overlap between the spheres, which induces an upper limit on the amount of pores that can be inserted. This maximum porosity depends furthermore on the pore size distribution: a wider distribution allows for smaller pores to fill up the space between larger pores, thus enabling higher porosities. This effect can be clearly observed when comparing the obtained porosities with the obtained variance factors (Figure 5.2d): at low variance factors, no samples with high porosities were generated (although these combinations were targeted in the Sobol sequence, as is clear from the grey markers that represent these targets). As a result, a positive correlation exists between the obtained pore size variance and porosity, which is accidental but inevitable given the applied generation algorithm. On the other hand, the obtained porosity of the WSB generated samples agrees much better with their targeted porosity (Figure 5.2a). The slight underestimation is fully due to the discrete representation of the samples: a higher resolution would improve the match between both. Nonetheless, there is also a correlation between the obtained porosity and pore size distribution width as is clear from Figure 5.2d, although it is a negative correlation contrary to the case for the RBI samples. The reason for this is not fully understood yet at this point, as the generation algorithm is relatively recent.

Regarding the average pore size, both sets of generated samples attain relatively well the targeted average pore size, although the WSB generated samples show slightly lower average pore sizes than intended (Figure 5.2b). This can be explained by the non-spherical pores in these samples, whose size is much harder to control during the generation. The obtained normalized variance factor, on the other hand, seems for both techniques to consistently overestimate the targeted variance factor. For the RBI samples, this is at least partially due to the fact that the algorithm will start filling the space between the larger pores with smaller pores in an attempt to reach its target porosity. For the WSB samples, it is again not completely

clear why this is happening, but it might be partially explained by the slight underestimation of the average pore size (which is used to normalize the variance).

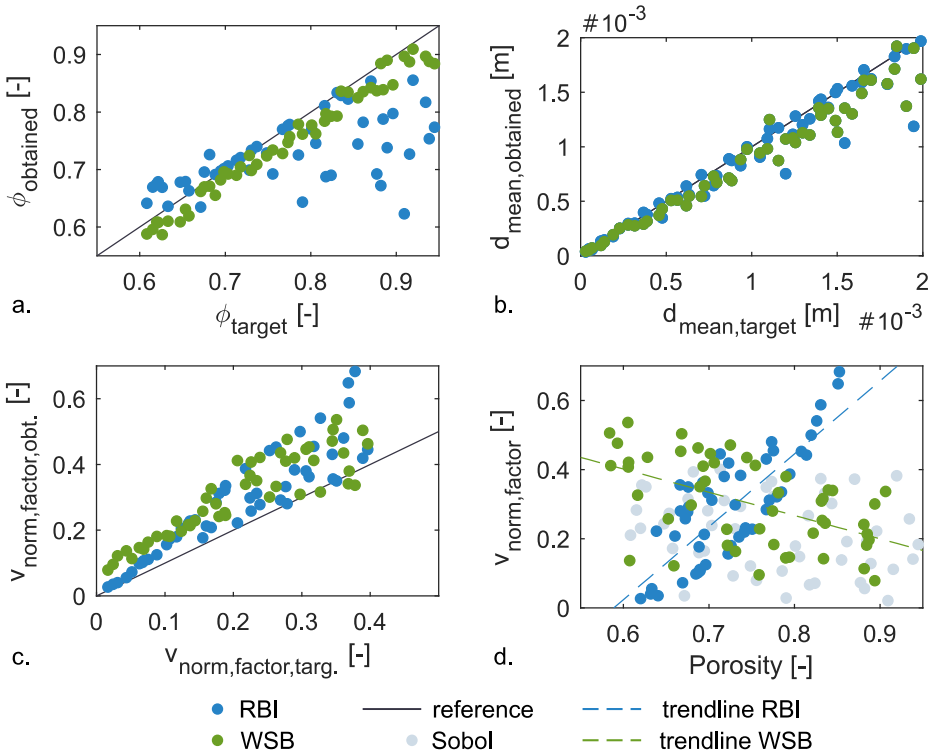


Figure 5.2: Confrontation of obtained porosity, pore size and normalized variance factor with targeted values (a, b & c), and the porosity versus the normalized variance factor of every sample showing the correlation between both (d).

The pore size and pore volume distribution are shown in Figure 5.3a-d, where the pore sizes are normalized by their average pore size to allow for comparison between different length scales. The target pore size variance is highlighted by the colour scale, and shows an expected wider distribution with larger target variance. Samples generated with the WSB technique show sometimes a wider distribution than their equivalent RBI samples: this is due to the algorithm creating cells around the initially seeded spheres. These cells will be slightly larger than the seeded spheres, thus leading to slightly larger pores.

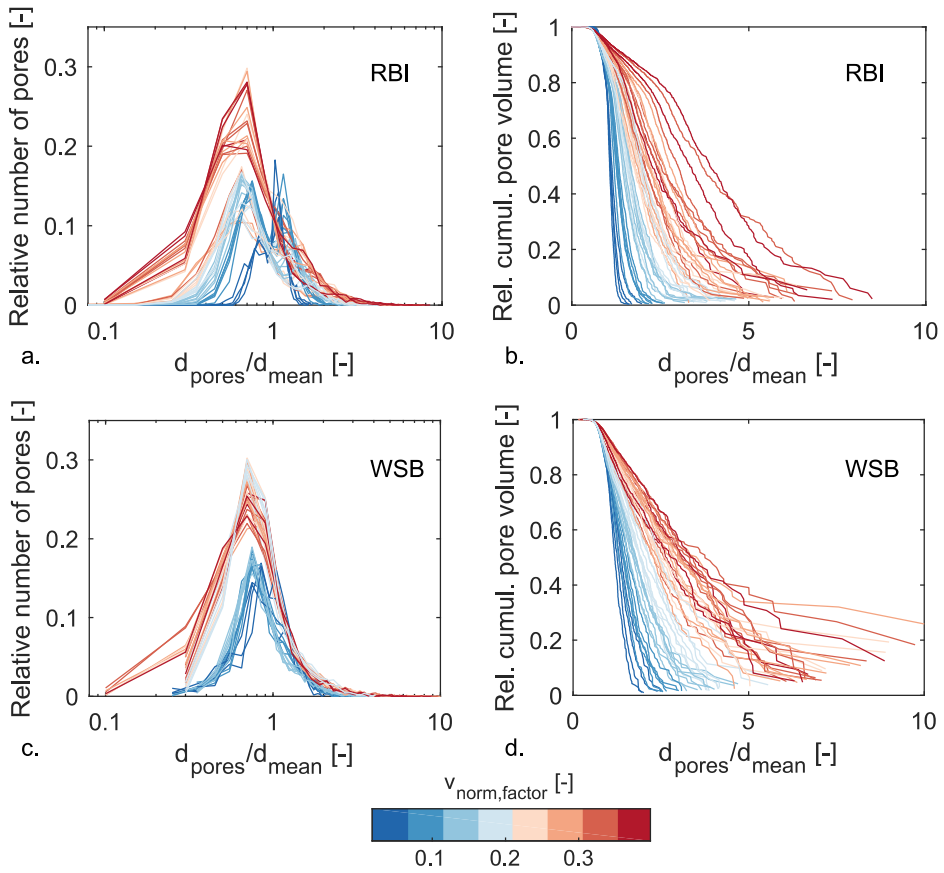


Figure 5.3: Pore size distribution shown as a relative amount of pores as function of normalized pore size (a/c) and cumulative pore volume distribution as function of normalized pore size (b/d), for RBI (a-b) and WSB (c-d) generated samples.

Simulated ETC

Visual interpretation

The predicted ETC of all samples generated with the RBI or the WSB technique are shown in Figure 5.4, as a function of the different varying parameters. The actual sample porosity, average pore size and normalised variance factor are used instead of the target values. For each graph, a linear trendline is least-squares-fitted through the results serving as a visual guideline.

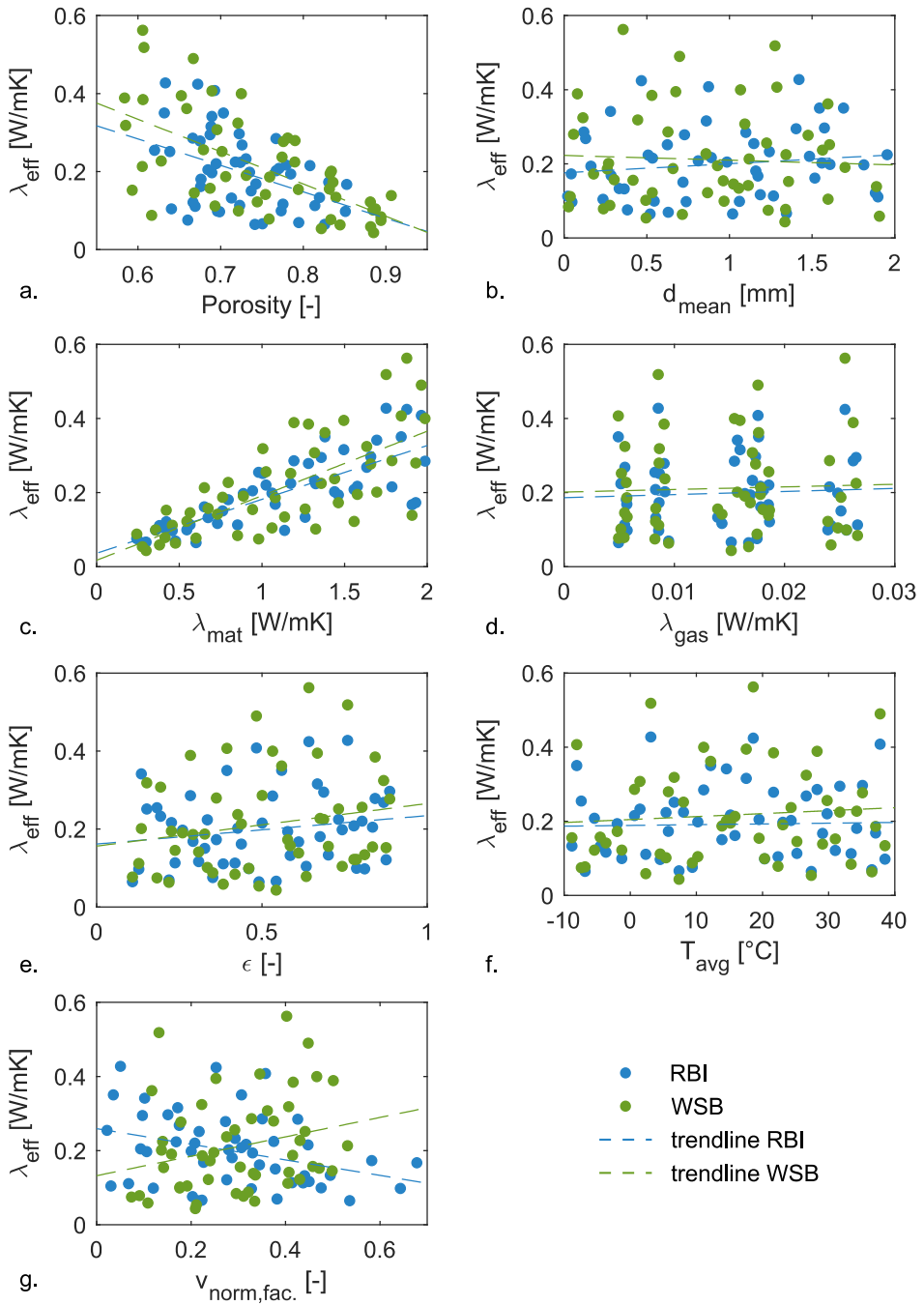


Figure 5.4: Predicted ETC for all samples as a function of porosity (a), average pore size (b), matrix conductivity (c), gaseous conductivity (d), emissivity (e), average temperature (f) and normalised variance factor (g).

It can be noticed that the thermal conductivity of the matrix and the porosity have by far the largest influence on the resulting ETC. All other parameters, on the other hand, show only small trends in comparison with these two parameters. A slightly increasing trend can be noticed with increasing gaseous thermal conductivity, as is expected. Furthermore, a similar increase can be noticed with increasing emissivity and temperature due to increasing thermal radiation in the pore space. Regarding the average pore size, it shows an increasing trend for the RBI samples and a slightly decreasing trend for the WSB samples. This is not expected since an increasing pore size will increase the effects of thermal radiation. However, the noticed trends are very small compared to the spread of the results, indicating that this is a matter of coincidence and that the parameter has only a secondary influence compared to the porosity and the matrix conductivity.

Graph g in Figure 5.4 shows the effect of the variance factor (which influences the pore size distribution width) on the ETC. For the RBI samples, a negative trend is observed, while for the WSB samples a positive trend is noted. This is probably explained by the correlation between the variance factor and the samples' porosity discussed before. Indeed, an increasing porosity was noted with increasing variance factor for the RBI samples, and vice versa for the WSB samples, explaining the observed trends in graph g. Hence, no real conclusions can be made here on the influence of the variance factor, although it is assumed that its influence is at least moderate. Future work should hence focus on improving the generation techniques to avoid a correlation between the porosity and the variance factor of a generated sample.

Linear regression model

To expand these visual observations and conclusions, a linear regression of the predicted ETC is made as a function of the 7 pore structure/physical parameters. A first order model is used, calculating an approximate ETC $\hat{\lambda}_{eff}$ as shown in Eq. (5.1). The product of the matrix conductivity and the porosity is added as an extra term to the regression model since an earlier test with a second order model indicated its significant impact on the predicted ETC.

$$\hat{\lambda}_{eff} = b_0 + \sum_{i=1}^7 b_i * \bar{x}_i + b_8 * \bar{\phi} * \bar{\lambda}_{mat} \quad (5.1)$$

The coefficients b [W/mK] are fitted with the least-squares model to obtain a good predictive regression model. The values \bar{x}_i [-] represent the normalized independent variables (the pore structural and physical parameters), normalized so their values all fall in between 0 and 1. Normalizing the independent variables allows to compare the obtained coefficients for

variables with different units (i.e. the emissivity and the average pore size), showing to which extent the corresponding parameter – on average – influences the ETC in the parameter domain considered. The combination term of the porosity and matrix conductivity will require to fix one of both when assessing the impact of the other (meaning that, for example, the impact of the matrix conductivity depends on the porosity at hand). The calculated coefficients are summarized in Table 5.2 together with the p-value of the respective coefficient.

Table 5.2: Obtained coefficients for the regression model for the first order terms and the second order terms.

Parameter	RBI		WSB	
	p-value	Coeff. b [W/mK]	p-value	Coeff. b [W/mK]
cte	< 0.001	0.060	< 0.001	0.063
ϕ	< 0.001	-0.061	< 0.001	-0.063
$d_{pore,mean}$	< 0.001	-0.009	< 0.001	0.008
$v_{norm,factor}$	< 0.001	0.025	0.86	$-4 * 10^{-4}$
λ_{mat}	< 0.001	0.428	< 0.001	0.523
λ_{gas}	< 0.001	0.023	< 0.001	0.021
ϵ	0.73	$-5.8 * 10^{-4}$	0.93	$-2 * 10^{-4}$
T_{avg}	0.02	-0.004	0.01	0.005
$\phi * \lambda_{mat}$	< 0.001	-0.311	< 0.001	-0.456

All parameters except for the emissivity and the variance factor in case of the WSB samples have a p-value well below 0.05, indicating that there is significant evidence in the dataset that they influence the resulting ETC. For both types of samples, the porosity, the matrix conductivity and the product of both clearly have the largest coefficients and thus the largest impact on the ETC (as was already indicated by the plots in Figure 5.4), followed by the gaseous conductivity, the average pore size and the temperature. The regression model furthermore allows to quantify the expected average decrease of the ETC: for example, increasing the porosity from 60 % to 85 % reduces the ETC by 0.061 W/mK for RBI samples with a matrix conductivity of 0.2 W/mK, while reducing the pore size from 1 mm to 10 μ m reduces the ETC only by 0.009 W/mK. Comparably, at a porosity of about 85 %, reducing the matrix conductivity from 2 W/mK to 0.2 W/mK leads to a reduction of the ETC with about 0.117 W/mK, and even more at lower porosities.

The emissivity seems to have a negligible impact on the ETC. The variance factor seems to have a non-negligible impact for the RBI samples, but a very low impact for the WSB samples. However, the variance factor is heavily correlated with the porosity for the both types of samples, so the obtained regression coefficients should be interpreted carefully. The coefficients for all other parameters are quite similar in the equations for both types of pore structures, differences occurring because of their different pore structure type and slightly different (obtained) parameter range.

Normalization of ETC by matrix conductivity

The strong influence of the matrix conductivity is partially cancelled out by normalizing the predicted ETC by their corresponding λ_{mat} . The results for all samples are shown in Figure 5.5 for the RBI samples (a) and WSB samples (b), as a function of sample porosity and highlighting the matrix conductivity with the colour scale. Results seem to indicate two things: first of all, the ETC is relatively more strongly reduced for a easily conducting solid. Indeed, samples with a high matrix conductivity are consistently at the lower boundary of the point cloud. Of course, their real ETC will still be higher due to this high matrix conductivity. The other effect that can be noticed is the larger spread of results at lower matrix conductivities. While high matrix conductivity results form more or less a line, the group of low matrix conductivity values shows differences of more than 5 % at similar porosities. This seems to indicate that the other varied parameters (gaseous conductivity, pore size, variance, ...) have a relatively larger impact at low matrix conductivities. This also suggests that the varied pore structure parameters hardly influence the solid conduction mechanism: indeed, at high matrix conductivity, most heat will flow through the matrix, so if the ETC stays relatively invariant at equal porosity, this heat flow mechanisms is hardly changed. On the other hand, at low matrix conductivities, an important part of the heat is transferred through the gaseous phase in the form of conduction and thermal radiation, both expectedly influenced by the varying parameters hence explaining the larger spread of results.

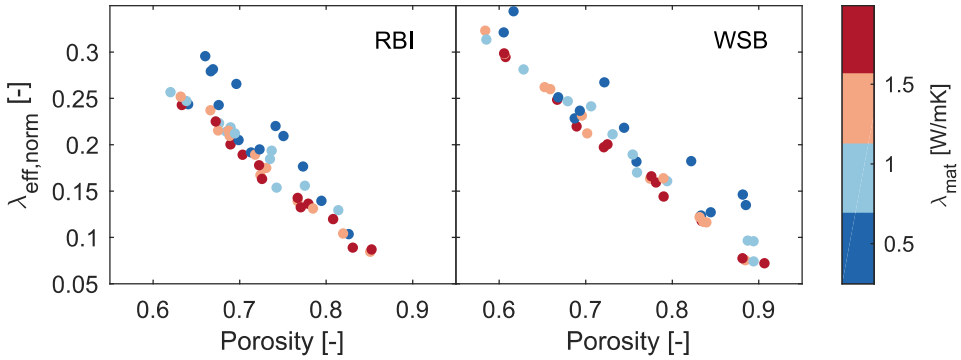


Figure 5.5: ETC normalized by the matrix conductivity for the RBI (a) and WSB (b) generated samples as a function of porosity. The colours highlight the influence of the matrix conductivity.

Lastly, the RBI and WSB generated samples are based on the exact same sample set. Hence, each time, two samples have been generated with similar average pore size, emissivity, variance, porosity etc. Their pore structure will be different though due to the different generation algorithms, making it interesting to compare both sets of results. Figure 5.6 shows the normalized ETC predicted for the samples generated by both generation techniques as a function of their attained porosity. The normalized ETC predicted for the RBI samples is on average lower than for the WSB samples at similar porosity.

The different performance of the RBI and WSB generated samples is almost completely due to their different pore structure type: other parameters (like pore size, emissivity, ...) are generally the same for both generated sets of samples. The fact that also at low porosity the RBI samples perform on average better suggests that it is due to a change in the way heat is transferred through the solid: indeed, at low porosities solid conduction is accountable for the largest part of the heat transfer. A potential explanation for the different performance could hence be their different ratio of solid material located in the cell struts versus the cell walls, also called the strut factor $f_s [-]$ in literature. As already mentioned in the literature survey in Chapter 2, Glicksmann & Torpey (1989) predicted that material located in cell walls is more favourable to conduct heat compared to material located in struts. This effect was also confirmed with numerical simulations for high-porosity foams by Coquard & Baillis (2009). The spherical pore shapes in the RBI generated samples will intrinsically lead to a higher concentration of material in the cell struts compared to the WSB samples, where all cell walls are more or less equally thick. This might hence explain the better performance of the RBI

samples. Even so, the effect of the pore structure type on the ETC is still of secondary importance compared to the porosity and the matrix conductivity.

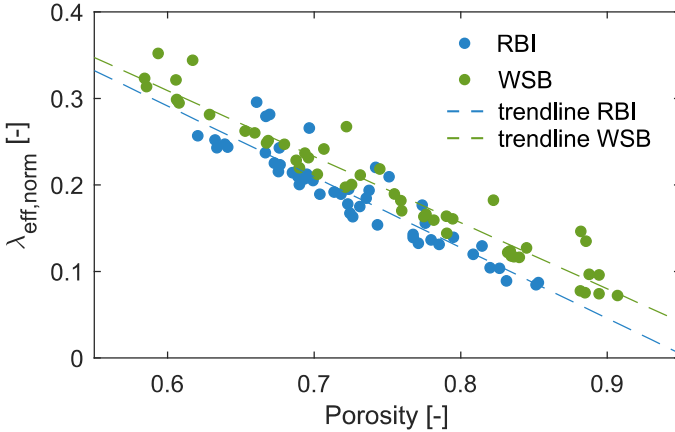


Figure 5.6: Predicted ETC normalized by the matrix conductivity for all samples generated by the RBI and the WSB technique.

5.3. Detailed parameter study

The results from the exploratory study clearly indicate the need to first focus on increasing the porosity and decreasing the matrix conductivity when trying to reduce the ETC of a porous material. The detailed parameter study zooms in on the region of high porosities and low matrix conductivities, to allow indicating the potential of the other parameters when these two parameters have already been tackled. Furthermore, a full-factorial sampling of the parameter space is employed to allow a more quantitative interpretation of the obtained reduction of the ETC when varying a certain parameter.

5.3.1. Methodology & Setup

The methodology and setup are mostly the same as in the previous parameter study: a set of pore structures is randomly generated and their ETC is predicted with the model framework. The parameter space is sampled in a different manner though as discussed, see below. That discussion is followed by a short description of the porous sample generation and simulation setup.

Parameter space

To allow for a more quantitative comparison between the different simulated samples, a full-factorial approach is employed for this second study. Every parameter can take two values,

where the second value supposedly leads to a reduced ETC (except for the $v_{norm, factor}$, whose influence is uncertain). All possible combinations between the parameters are simulated. The studied parameters are the same as in the first parameter study, except for the emissivity and the temperature, both having a minor impact on the ETC as was demonstrated in the previous study. Hence, an emissivity of 0.9 is assumed for all samples, which corresponds to the emissivity of most typical materials used to produce porous building blocks. The temperature is set to 10 °C in accordance with the usual characterization practice of the ETC of insulation materials. The studied parameter values are summarized in Table 5.3. Additionally to the pore structural and physical parameters, the random seed to start the random pore structure generation process can also take two different values. This means there are each time two samples with a different pore structure but similar porosity, pore size, variance and other physical properties. The full-factorial sampling of all the properties leads hence to 64 different samples.

Table 5.3: Studied parameters in the second parameter study and their two possible values.

Parameter	Value 1	Value 2
ϕ	0.9	0.95
$d_{pore, mean}$	1 mm	10 μm
$v_{norm, factor}$	0.4	0.04
λ_{mat}	0.5 W/mK	0.2 W/mK
$\lambda_{gas, type}$	Air	Xenon
$\lambda_{gas, 20^\circ\text{C}}$	24.9 mW/mK	5.3 mW/mK
<i>seed</i>	1	2
ϵ	0.9	
T_{avg}	10 °C	

Sample generation

Contrary to the first parameter study, only the WSB technique is used to generate the pore structures. Since high-porosity samples are envisioned here, the RBI technique is less suitable due to the maximum packing density associated with spheres randomly distributed in a cube. The foam-like pore structure of the WSB technique allows to reach much higher porosities. Furthermore, the voxel count is increased to 800³ to allow an improved representation of the thin cell walls at such high porosities. Generated samples generally look similar to the ones presented in Figure 5.1d&e.

Simulation setup

The simulation setup is similar to the first parameter study. The ETC of the generated samples is predicted with the numerical framework. The expanded Loeb method is applied to account for thermal radiation inside the pore space. The finite-element mesh of every sample is constructed with the same mesh size parameters as in the first study, accounting for the increased resolution in this second study. All other needed input parameters are set to the associated values of the full-factorial sampling set of the values in Table 5.3.

5.3.2. Results & Discussion

Properties of generated samples

For every generated sample the porosity, average pore size and normalized variance factor is calculated directly from the 3D voxel image. The average pore size and volume distributions are obtained by calculating for every pore the radius of the equivalent sphere having the same volume. Figure 5.7 compares the obtained pore structure properties with the targeted properties.

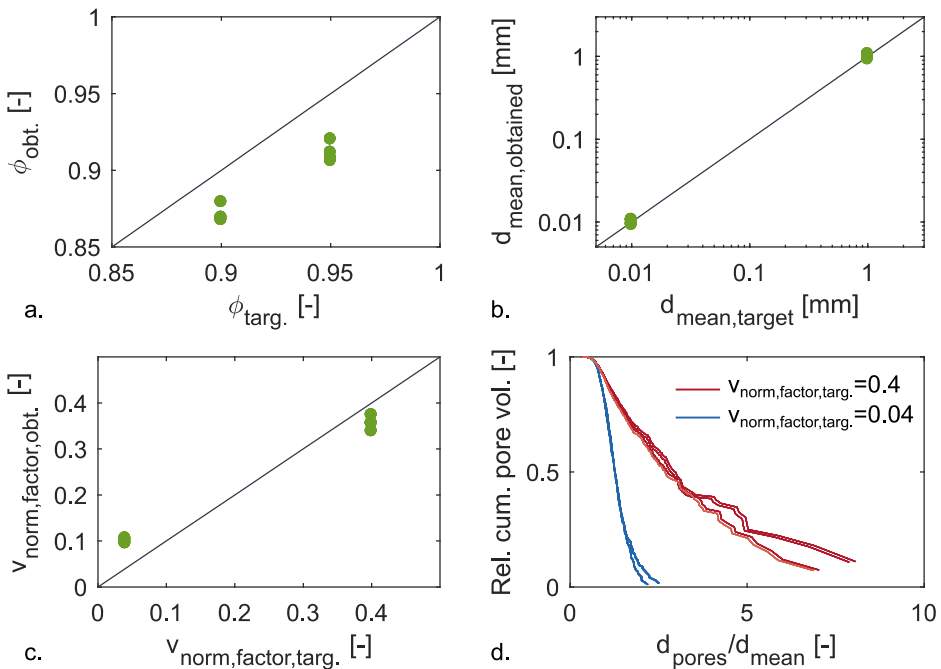


Figure 5.7: Comparison of the pore structure properties of the generated samples with their targeted property values.

The obtained porosity of the samples is, as expected, lower than the targeted porosity, around 87 % and 92 % instead of 90 % and 95 % respectively. This is due to how the generation algorithm targets a chosen porosity combined with the finite discretization with voxels. The obtained mean pore diameters on the other hand agree very well with the targeted values. The normalized variance factors of the samples differs again from the targeted one, probably also due to how the generation algorithm generates the pore structure, although more research is needed to clearly pinpoint the exact cause as was discussed in Section 5.2.2. Figure 5.7d shows that a clear difference in pore size distribution is obtained between the samples with high and low targeted variance.

Simulated ETC

The predicted ETC of every sample is displayed in Figure 5.8a-e as a function of the different parameters. They show again a significant influence of the porosity and the matrix conductivity, even in the more limited range between 87 % and 92 %. At these high porosities and low matrix conductivities, the gaseous conductivity seems to have a similar influence as the matrix conductivity. Replacing the air with a less conducting gas can thus lead to a significant improvement in this context. Also the pore size has a more outspoken influence: its reducing effect on the thermal radiation is more outspoken in these conditions compared to the results of the broad parameter study. Its impact is less than the one of the gaseous conductivity though.

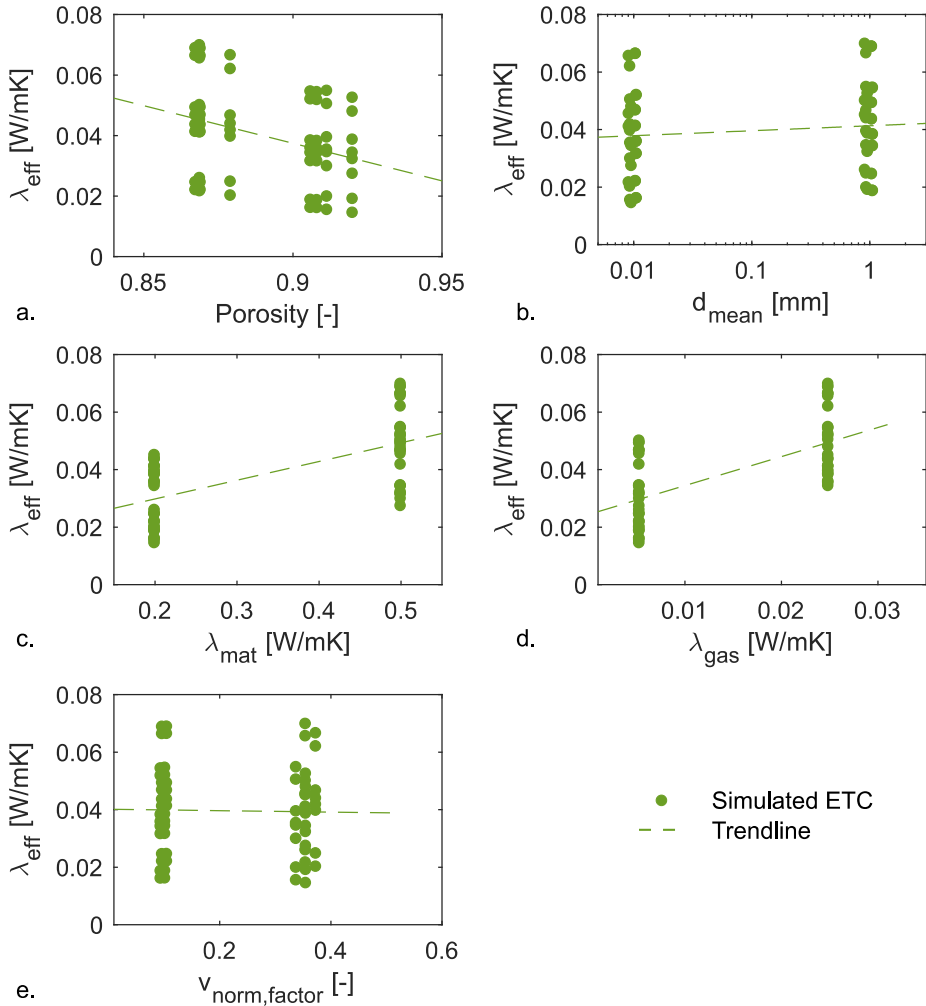


Figure 5.8: Predicted ETC of the samples as a function of the different pore scale parameters.

The full-factorial sampling of the parameter space allows to directly quantify the reducing impact of one parameter when all other parameters stay constant. This *reduction potential* RP [-] is calculated for every parameter 'x', comparing the predicted ETC of the samples whose only difference is their value for the respective parameter 'x' (Eq. (5.2)).

$$RP_{x:1 \rightarrow 2} = \frac{\lambda_{\text{eff},x=1} - \lambda_{\text{eff},x=2}}{\lambda_{\text{eff},x=1}} \quad (5.2)$$

This reduction potential depends on the values of the other parameters: reducing the gaseous conductivity expectedly has a larger RP for high-porosity, low-matrix-conductivity samples.

The obtained *RP* values for every parameter considering the variation of all other parameters is shown in Figure 5.9. The median value is also indicated. For the impact of the variance, the light-coloured points depict the values of all samples, while the dark points depict results filtered for the correlation between the variance and the porosity.

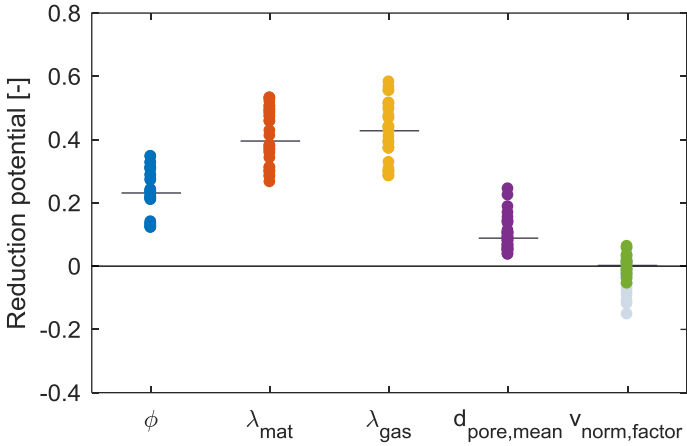


Figure 5.9: Potential relative reduction of the ETC when adapting the respective parameter from value 1 to value 2 as noted in Table 5.3. The horizontal lines denote the median reduction potential per parameter. For the normalized variance factor, the grey dots represent all obtained results, while the green dots represent the results filtered for the correlation with the porosity.

The matrix conductivity and the porosity have again a large reduction potential, reducing the ETC respectively between 25 % to 55 % when reducing from 0.5 W/mK to 0.2 W/mK, and between 10 % and 37 % when increasing the porosity from 87 % to 92 %. However, results show that the gaseous conductivity has the largest reduction potential given the studied parameter range. For samples with a porosity of 92 %, a matrix conductivity of 0.2 W/mK and a small pore size of 10 μm , the ETC reduces almost 60 % when replacing the air inside the pore with low-conducting Xenon gas. At the other side of the spectrum ($\phi = 87 \%$, $\lambda_{mat} = 0.5 \text{ W/mK}$ and $d_{mean,pore} = 1 \text{ mm}$), the ETC reduces with about 27 %, all other pore structures having a reduction potential in between both extremes. Reducing the pore size has a smaller impact, potentially leading to a reduction of 25 %, but only for the cases with a high porosity and low matrix conductivity ($\phi = 92 \%$ & $\lambda_{mat} = 0.2 \text{ W/mK}$). Its median reduction potential is around 10 %. The pore size distribution width, finally, filtered for the correlation with the porosity, has a relatively small impact at these high porosities and low matrix conductivities: reducing the pore size distribution width can either increase or decrease the resulting ETC up to 6 %. Closer analysis shows that this depends on the average pore size: at a large average

pore size (in casu ~1 mm), a more narrow pore size distribution results in a lower ETC. This is likely due to the presence of very large pores in such samples where thermal radiation contributes importantly to the ETC. At small average pore size (in casu ~10 μm), thermal radiation is negligible even in the relatively larger pores of about 50 μm . The ETC in such cases actually increases when the pore size distribution becomes more narrow, contrary to the case for an average pore size in the millimetre range. This may be due to an decreasing matrix tortuosity at narrowing pore size distributions, although more research is needed to investigate this hypothesis.

5.4. Conclusions

In this chapter, two parameter studies have been performed to analyse the impact of pore scale and physical parameters on the ETC of porous building blocks. A first exploratory study covers a wide range of values for every parameter. 100 different pore structures are generated using two different generation algorithms and varying pore scale and physical parameters. Prediction of their ETC with the developed numerical framework indicate that the matrix conductivity and the porosity are by far the most important parameters affecting the ETC. A material with a low matrix conductivity should be used while creating as much porosity as possible to reduce the ETC. Apart from these parameters, the type of pore structure has a secondary influence: samples generated with the RBI technique show on average a slightly lower ETC compared to samples generated with the WSB technique for similar porosities. This is probably explained by the strut concentration factor f_s , which is expectedly higher for the RBI samples. All other studied parameters (pore size, pore size distribution, emissivity, gaseous conductivity and temperature) have a much lower influence.

The second detailed parameter study zooms in on the influence of these secondary parameters for samples with a high porosity and low matrix conductivity. 64 pore structures are randomly generated with a full-factorial sampling of the parameter space. The reduction potential of every parameter is assessed by comparing the predicted ETC for two samples with the same properties except for the respective parameter. Results indicate that reducing the gaseous conductivity for such high-porosity, low matrix conductivity pore structures has the largest impact: the ETC reduces between 30 % and 60 % when replacing the air inside the pores with Xenon gas. Reducing the average pore size from 1 mm to 10 μm has a reduction potential between 5 % to 25 %, while the pore size distribution width has a very limited influence.

Concluding, the parameter studies show that increasing the porosity and reducing the matrix conductivity are clearly the most important actions when aiming to reduce the ETC of porous building blocks. For materials with already high porosities (>90 %) and low matrix conductivities (<0.5 W/mK), reducing the gaseous conductivity can lead to a strong reduction as well, while reducing the average pore size can will only have a minor impact compared to these parameters. The pore size distribution width has only a very limited influence.

Part II

-

Nanoscale effects on the ETC of porous
building materials

Introduction to Part II

As concluded in the parameter studies on the ETC of porous building blocks, a high porosity is essential to reduce the ETC. At this high porosity then, gaseous conduction accounts for the largest part of the heat transfer through the material, effectively imposing the lower limit of the material's ETC (Solórzano et al. 2009). The need for even better performing insulation materials has inspired researchers to focus on strategies for reducing that gaseous conductivity (Cuce et al. 2014; Berge and Johansson 2012; Schiavoni et al. 2016; Bjørn Petter Jelle 2011). Materials with nanosized pores and/or low gas pressures have been put forward as most promising (B. P. Jelle, Gustavsen, and Baetens 2010). Indeed, both measures have, both theoretically and experimentally, been shown to lessen the actual conduction through the gas and accordingly the total heat transfer through the material (Kennard 1938; Notario et al. 2015). Aerogel, for example, is a material with pore sizes in the range of a few tens of nanometres, and has ETC's as low as 0.014 W/mK at room temperature, lower than the thermal conductivity of standard air (Bjørn Petter Jelle, Baetens, and Gustavsen 2011). Vacuum insulation panels, where the gas pressure in the pores is decreased to about 100 Pa, have been shown to have ETC's down to 0.004 W/mK at the center (Baetens, Jelle, Thue, et al. 2010; Berge and Johansson 2012). Other new developments exploiting these effects are also heavily researched, like nanocellular foams (Notario, Pinto, and Rodriguez-Perez 2016; Forest et al. 2015; Costeux 2014; G. Wang, Zhao, Mark, et al. 2017) or hollow-nanosphere-based materials (Y.-H. Li, Li, and Tao 2014; Gao et al. 2015; Demouchali, Pourmahdian, and Hadavand 2016; Hu, Wu, and Sun 2018).

Complementary to the effect on the gaseous conductivity, the presence of nanosized pores can also influence the solid conduction and pore radiation processes. Indeed, reduced solid conductivities have been noticed when the solid domain is on the order of a few 100 nm (Cahill et al. 2003; Gang Chen 2000; Coquil, Fang, and Pilon 2011), while pore radiation has been observed to increase due to coherence and near-field effects (Howell, Mengüç, and Siegel 2016; Joulain 2007; Rousseau et al. 2009). The observed impacts on all of the involved heat transfer mechanisms invalidate the previously developed model framework for studying materials where such effects are relevant. A modification of the model framework is hence needed in order to assess their potential for porous building materials.

Theoretical considerations have shown that the gaseous conductivity reduces when the pore structure's characteristic length (i.e. the pore size) is on the order of the heat carriers' (the gas molecules) mean free path in between two collisions. This mean free path is about 60 nm for standard air at room temperature and atmospheric pressure, explaining the quest for nanoporous insulation materials. At decreasing gas pressures the mean free path increases, implying that these reducing gaseous conductivities can occur already at larger pore sizes. We will still refer to it as a nanoscale effect though, since it is described by the same formalism. For solid conduction, heat is transferred through atomic vibrations which can be part of waves travelling over distances from a few nanometres to hundreds of nanometres, depending on the atomic structure and properties. Size effects on the solid conduction are hence also important at the nanoscale and are therefore also referred to as nanoscale effects. Regarding pore scale radiation, coherence effects and near-field radiation phenomena are typically deemed to be important when the characteristic length is on the order of the radiation wavelength (i.e. $\sim 10 \mu\text{m}$ at room temperature). In line with the denomination of the size effects on the gaseous and solid conductivity, we will also refer to them as nanoscale effects though.

The chapters in Part II are aimed at a better understanding of the mentioned nanoscale effects and assessing their potential in reducing the ETC of porous building materials. In Chapter 6 the fundamentals behind heat transfer at the nanoscale are shortly revisited before discussing modelling attempts in literature specifically aimed at nanoporous or low-gas-pressure materials. Chapter 7 presents the necessary modifications on the previously presented model framework to allow predicting the ETC of porous materials with such nanoscale dimensions. It ends with a comparison of the framework with experimental measurements from literature to validate the framework's performance. Chapter 8, finally, discusses a parameter study similar to Chapter 5 to assess the combined influence of selected pore structure parameters on the ETC and highlight potential optimization strategies.

The work presented in Part II is focussed primarily on materials with (nearly-)closed cellular pore structure. Such pore structure topologies have been shown to combine low thermal conductivities with strong structural properties (Ashby and Medalist 1983; Gibson and Ashby 1997) and are hence of particular interest for building materials. Examples of cellular materials with nanoscale features are nanocellular foams or hollow-silica-nanosphere materials, whose microstructures are shown in Figure II.1a&b. Materials with aerogel-like microstructure are not considered here: they have a highly open-celled, wire-like microstructure made of granules (Figure II.1c), which requires another modelling strategy than presented here.

Furthermore, their insulation potential has been studied to a large extent already, and relevant information can be found in the extensive literature.

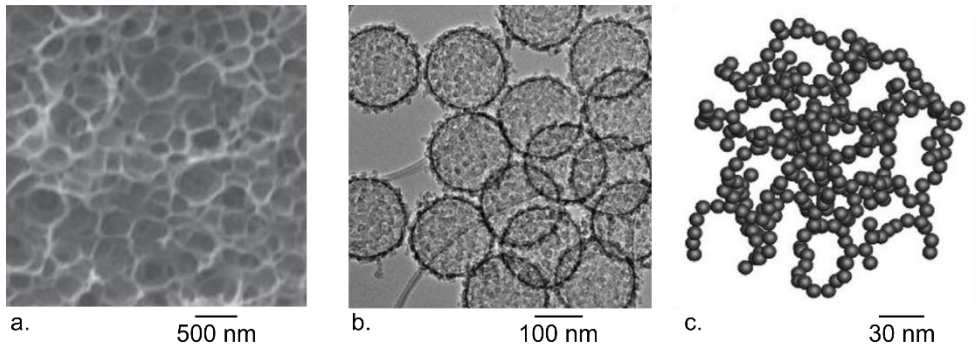


Figure II.1: microstructure of nanocellular foam (a) (G. Wang, Zhao, Mark, et al. 2017), hollow silica nanospheres (b) (Demouchali, Pourmahdian, and Hadavand 2016) and conceptual view of solid structure of aerogel (c) (Y. Zhao, Tang, and Du 2015).

State-of-the-art on modelling of heat transfer in nanoporous and low-gas-pressure material

6.1. INTRODUCTION	137
6.2. GASEOUS CONDUCTION	138
6.3. SOLID CONDUCTION	146
6.4. PORE SCALE RADIATION	155
6.5. CONCLUSIONS	160

6.1. Introduction

Nanoscale effects, caused by reducing pore sizes and/or low gas pressures, change all heat transfer mechanisms involved at the pore scale and hence mandate different modelling strategies than described in Part I to predict the ETC of materials where such effects are at play. This chapter presents an overview on modelling paradigms proposed in literature to account for (part of) these nanoscale effects. The sections zoom in successively on each heat transfer mechanism, each time starting with a discussion on the fundamental physics behind the transfer mechanism. Indeed, a solid understanding of the physics is necessary to interpret the literature and assess the importance and impact of the nanoscale effects on the respective heat transfer mechanism. Subsequently, strategies to model the respective heat transfer mechanisms in the presence of nanoscale effects are surveyed. This is each time followed by a discussion on several analytical and numerical models proposed in literature for predicting the effect on the macroscopic ETC.

6.2. Gaseous conduction

We start the discussion with the gaseous conduction mechanism. In highly porous materials used for insulation applications, conduction through the gaseous phase typically accounts for the largest part of the total heat transfer through the material (Solórzano et al. 2009). In their search for superinsulating materials, most studies focus on reducing this heat transfer mechanism by reducing the pore sizes down to the nanoscale range, as is done in aerogels, nanocellular foams or hollow-silica-nanosphere-based materials. Another strategy, applied in vacuum insulation panels, is decreasing the gas pressure, which is founded on the same effect as a reducing pore size, as will be discussed further on. First, a short description of the physics governing gaseous heat conduction is given together with an analytical framework that allows to interpret intuitively the impact of such nanoscale effects. Subsequently, some strategies presented in literature to model gaseous conduction at the nanoscale are surveyed.

6.2.1. Fundamentals

Physical background & definitions

Gaseous conduction originates from the microscopic movement of gas molecules. Each molecule has a certain amount of energy, with molecules in zones of higher temperature on average in possession of more energy. Moving around in random directions, energy is transported over small distances and partially exchanged with other molecules upon collision. This will, on average, cause heat to flow from the warmer side of the gas to the colder side. Macroscopically, this translates to a diffusive process that can be described with Fourier's heat law and a gaseous thermal conductivity. Gaseous conduction should not be confused with natural convection, where a global macroscopic movement of particles occurs on top of their microscopic movements.

A comprehensive and intuitive picture of the gaseous conduction mechanism is given by the kinetic theory of gases framework, described for example in the seminal book of Kennard (1938). It allows studying macroscopic properties like the gaseous thermal conductivity and to interpret the influences of a reducing gas pressure or pore size. It describes the gas as molecule particles flying around randomly, each carrying an amount of energy and exchanging energy via collisions. Averaging the transfer of heat to a macroscopic level, the framework defines an expression, Eq. (6.1), for the thermal conductivity λ_{gas} [W/mK] of such a gas (Jiji 2009; Z. M. Zhang 2007; Kennard 1938):

$$\lambda_{gas} = \frac{1}{3} * c_{V,gas} * \rho_{gas} * v_{avg,gas} * L_{MFP} \quad (6.1)$$

Here, $c_{V,gas}$ [J/kgK] is the specific heat at constant volume, ρ_{gas} [kg/m³] the mass density, $v_{avg,gas}$ [m/s] the average speed of the gas molecules and L_{MFP} [m] the mean free path of the gas molecules. This mean free path L_{MFP} represents the average distance a gas molecule travels between two successive collisions (i.e. about 58 nm for air at 20 °C and atmospheric pressure). It depends, among others, on the gas pressure and on the dimension of the surrounding cavity: in small cavities the gas molecules will collide more frequently with the cavity walls, reducing the mean free path and hence altering the actual gaseous thermal conductivity.

Effect of domain size and gas pressure

Through Eq. (6.1), the kinetic theory of gases highlights the effect of several parameters on the gaseous thermal conductivity. The specific heat of the gas depends solely on the temperature (assuming no interaction between the molecules except on collision) and is either constant or rising with increasing temperature when additional modes of energy storage come available (rotational, vibrational). In the relatively minor temperature range that building materials are subjected to, it can safely be assumed constant. The average speed also only depends on the temperature and increases as well with increasing temperature. Hence, the effect of a reducing pore size or gas pressure manifests itself through a changing mass density and mean free path.

When a gas is confined inside a pore cavity, gas molecules will from time to time collide with the pore walls instead of just with each other. As such, heat is conducted through the gas from one pore side to the other. This affects the actual (or effective) mean free path $L_{MFP,eff}$ [m] of the molecules, which can be estimated with Matthiessen's rule as the sum of the inverse mean path length travelled in a bulk gas ($L_{MFP,bulk}$) and the mean path length due to collisions with the pore boundary ($L_{MFP,bdy}$), see Eq. (6.2) (Jiji 2009). The impact of such boundary scattering events relative to particle-particle scattering is often indicated through the Knudsen number, defined as the ratio of the bulk gas mean free path to the characteristic length of the system d_{char} [m] (i.e. the pore size), see Eq. (6.3).

$$1/L_{MFP,eff} = 1/L_{MFP,bulk} + 1/L_{MFP,bdy} \quad (6.2)$$

$$Kn = L_{MFP,bulk}/d_{char} \quad (6.3)$$

When the pores are relatively big, the amount of collisions with the wall is still relatively small, and the Knudsen number will be low (<0.1). In that case, the effective mean free path almost

equals the bulk mean free path $L_{MFP,bulk}$ [m]. This regime is often called the diffusive regime, since the heat flow is diffusive from a macroscopic point of view. However, when the pore size reduces to the order of the bulk mean free path, molecules will collide relatively more often with the pore boundaries, at a Knudsen number around 1. The effective mean free path hence reduces, and so will the gaseous conductivity. At further reducing pore size (and high Knudsen numbers >10), gas molecules travel directly from one pore boundary to the other, which is in the limit called the ballistic regime. The mean free path is in that case only influenced by the boundaries and is called the boundary mean free path $L_{MFP,bdy}$ [m]. Through Matthiessen's rule, it is clear that when the boundary mean free path decreases (because of a decreasing pore size for example), the effective mean free path falls as well. Gas molecules can hence transport their heat energy over smaller distances only, an effect that reduces the bulk gaseous thermal conductivity, as is obvious from Eq. (6.1).

At reducing gas pressure, on the other hand, the mass density of the gas will reduce according to the ideal gas law. At the same time, the bulk mean free path will increase since there are less molecules present to collide with. Both effects counteract each other in Eq. (6.1), leading to the bulk gaseous thermal conductivity hardly changing with gas pressure. However, when confined in a pore cavity, the gas molecules will at reducing pressure already 'feel' the cavity walls in relatively larger pore sizes. Indeed, since the bulk mean free path of the gas increases at reducing pressure, the effect of the pore confinement becomes already relevant at relatively larger pore sizes. Hence, the thermal conductivity of a gas confined in a cavity will reduce as well at reducing gas pressures. We will equally refer to this effect when discussing 'nanoscale effects'.

6.2.2. Modelling of gaseous conduction in the presence of nanoscale effects

To assess the potential effect of the nanoscale effects (reducing pore size and/or gas pressure), several modelling strategies have been developed in literature. First, some models focusing on the gaseous conduction transfer in nanoporous or low-gas-pressure conditions are discussed. Subsequently, models presented in literature for the prediction of the ETC taking such effects into account are surveyed.

Modelling gaseous heat transfer

Analytical modelling strategies

Most studies attempt to propose an adapted gaseous conductivity that can be used in Fourier's conduction law to model the changed gaseous heat transfer. Analytical equations for the gaseous conductivity often employ the gas kinetic theory as theoretical framework. The mean free path length depends on the gas pressure and on the domain size, and can be estimated using Matthiessen's rule in Eq. (6.2). The bulk mean free path (for bulk gas without boundary effects) is defined as in Eq. (6.4), with k_B [$m^2 kg/s^2 K$] the Boltzmann constant, $d_{molecule}$ [m] the diameter of the gas molecules and p [Pa] the gas pressure. The boundary mean free path, on the other hand, is usually equalized to a characteristic pore scale dimension like the average pore diameter.

$$L_{MFP,bulk} = \frac{k_B * T}{\sqrt{2} * \pi * d_{molecule}^2 * p} \quad (6.4)$$

A simple model for the effective gaseous conductivity can then be derived from the kinetic theory formula and Matthiessen's rule, see Eq. (6.5). This model has been applied in literature for diverse types of materials (Woodside and Messmer 1961; Hu, Wu, and Sun 2018).

$$\lambda_{gas,kin} = \frac{\lambda_{gas,bulk}}{1 + Kn} \quad (6.5)$$

This simple model does not consider the finite efficiency of the energy-exchange between gas molecules and pore walls. Kennard (1938) therefore derived a more detailed equation for the gaseous conductivity when confined between two parallel plates at a distance d [m]. It is shown here in the format presented by Zhang (2007) in Eq. (6.6).

$$\lambda_{gas,K-z} = \frac{\lambda_{gas,bulk}}{1 + Kn * \frac{2-a}{a} * \frac{9\gamma_{heat} - 5}{\gamma_{heat} + 1} * \sqrt{\frac{T_{avg,FM}}{T_{avg,DF}}}} \quad (6.6)$$

Here, a [-] is the thermal accommodation coefficient representing the efficiency of energy-exchange, γ_{heat} [-] the specific heat ratio, $T_{avg,FM}$ the average temperature in the gas under a free molecular regime and $T_{avg,DF}$ [K] the same for a diffusive regime (both are practically equal in case the temperature difference over the plates is smaller than the cold surface temperature, which is always the case in porous materials in building applications). Eq. (6.6) shows a similar effect of a reducing pore size or gas pressure as Eq. (6.5), but it agrees better

quantitatively with experimental measurements. Kaganer (1969) simplified the complex form of Eq. (6.6) to Eq. (6.7) using a factor β_{kag} [-]. Its value is typically chosen between 1.5 and 2 for air-filled pores, assuming a thermal accommodation coefficient between 0.9 and 1. Thanks to its simplicity and good agreement with experiments, this expression has been used extensively in literature to predict the gaseous conductivity in pores with reducing pore size or gas pressure (Kan et al. 2015; B. P. Jelle, Gustavsen, and Baetens 2010; Obori et al. 2019; G. Wang, Zhao, Wang, et al. 2017; C. Bi, Tang, and Hu 2014).

$$\lambda_{gas,Kag} = \frac{\lambda_{gas,bulk}}{1 + 2 * \beta_{kag} * Kn} \quad (6.7)$$

Eq. (6.6) and (6.7) were originally solely derived for gaseous conduction between parallel plates. Machrafi & Lebon (2015) used extensive irreversible thermodynamics to derive an expression specifically for spherical pores, as shown in Eq. (6.8). Wolf & Strieder (1994) used variational principles to come to an upper-bound expression for the gaseous conductivity in spherical pores. Their full equation (depending on multiple integrals) is not repeated here, but is also a function of Knudsen number, thermal accommodation coefficient and bulk gas properties.

$$\lambda_{gas,M-L} = \frac{3 * \lambda_{gas,bulk}}{4 * \pi^2 * Kn^2} * \left(\frac{2 * \pi * Kn}{\arctan(2 * \pi * Kn)} - 1 \right) \quad (6.8)$$

Zhu et al. (2017) derived a model based on Zeng's model (1995) for arbitrary pore geometries. They express the mean free path in a pore as a function of the pore volume $V [m^3]$ to pore surface $S [m^2]$ ratio, coming to Eq. (6.9). The formula can be expressed as a function of the Knudsen number, defining the characteristic size as in Eq. (6.10).

$$\lambda_{gas,Zhu} = \frac{\lambda_{gas,bulk}}{1 + L_{MFP,bulk} * 0.5 * a * \frac{S}{V}} = \frac{\lambda_{gas,bulk}}{1 + Kn_{Zhu}} \quad (6.9)$$

$$d_{characteristic} = \frac{2 * V}{a * S} \quad (6.10)$$

Eq. (6.5) till (6.9) all calculate the gaseous conductivity as a function of the Knudsen number. However, the Knudsen number is not equally defined in all studies. Despite the seemingly simple definition of Kn in Eq. (6.3), different calculation formulas are present in literature. Indeed, the concept of a characteristic length is quite ambiguous and has been equalized to the plate separation distance, the pore diameter, the ratio of the pore volume and surface or

some other length measure. Secondly, the bulk mean free path for the gas molecules has also been calculated differently in literature. Kennard (1938), Zhang (2007) and Kaganer (1969) for example use the definition in Eq. (6.4), which corresponds to the actual physical distance travelled by sphere-like gas molecules in between successive collisions (around 58 nm for standard air at room temperature and atmospheric pressure). Machrafi & Lebon (2015) and Jiji (2009) on the other hand use the mean free path for energy exchange calculated by reversing Eq. (6.1), which is around 180 nm for standard air at room temperature and atmospheric pressure. Application of the analytical models requires hence a correct understanding of their derivation. Figure 6.1 shows results for all presented equations as a function of the pore size and the gas pressure, assuming a thermal accommodation coefficient of 0.9 taking into account the different definitions of the Knudsen number. The models by Machrafi & Lebon (2015) and by Zhu et al. (2017) (Eq. (6.8) and (6.9)) have been applied for a spherical pore, the others for gaseous conduction between parallel plates. They all present very similar trends and agree at least qualitatively with experimental measurements of the gaseous conductivity at different Knudsen regimes (Notario et al. 2015).

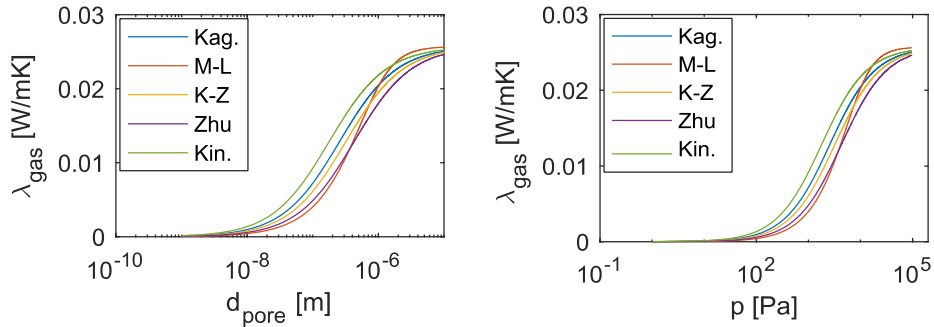


Figure 6.1: prediction of gaseous conductivity by selected analytical models as a function of pore size at atmospheric pressure (a), and as a function of gas pressure for a pore size of 10 μm (b). The selected analytical models are Eq. (6.7) by Kaganer (1969), Eq. (6.8) by Machrafi & Lebon (2015), Eq. (6.6) by Kennard (1938) & Zhang (2007), Eq. (6.9) by Zhu et al. (2017) and Eq. (6.5) from kinetic theory.

Other models (analytical and empirical) similar to the previously presented equations have been derived as well (i.e. focussing explicitly on aerogel materials) and can be found in other extensive overviews (Raed 2013; Y.-L. He and Xie 2015; J. J. Zhao et al. 2012b).

Numerical modelling strategies

Numerical modelling of the gaseous heat transfer and the impact of possible nanoscale effects usually involves solving the Boltzmann equation for particle trajectories or performing

Molecular Dynamics simulations. Both methods model the movement of gas molecules and the associated transfer of heat. For example, the gaseous heat transfer between parallel plates has been investigated by solving the Boltzmann equation with the Direct Simulation Monte Carlo (DSMC) method (Denpoh 1998) and with the finite difference method (Kosuge 2001; Ohwada 1996). Simulation results showed similar trends as the analytical models discussed previously. Zhu et al. (2017) used the DSMC technique to model the gaseous conductivity in a cuboid nanopore. Bi et al. (2014) used the Molecular Dynamics technique to study the gaseous conductivity in both closed cell and open cell pores in aerogels. They showed that closed cell pores have lower gaseous conductivities at equal pore size because of the increased scattering. Other examples can be found in specialized literature (Rader et al. 2006; Shan and Wang 2013). Such detailed modelling of the gas molecule streams is typically quite computationally intensive though, inhibiting their application for large complex geometries like complete pore structures.

Modelling the impact on the effective thermal conductivity

Some models have been proposed in literature to study the impact of such reducing gaseous conductivity on the ETC of a porous material. A short survey is given here.

Analytical modelling strategies

Analytical approaches are typically based on expressions for porous materials without nanoscale effects like the ones presented in Chapter 2. The gaseous conductivity is then adapted to account for the potential nanoscale effects. Kan et al. (2015) studied for example the ETC of vacuum insulation panels using the 'parallel' analytical model (Eq. (2.2)). They adapted the gaseous conductivity for the gaseous pressure using Kaganer's model (Eq. (6.7)). Hu et al. (2018) followed the same approach for nanoporous materials. Wolf & Strieder (1994) based their analytical model on Russel's equation using their own developed relation based on variational approach for the gaseous conductivity. Minnich & Chen (2007) based their analytical model on the Maxwell relation (Eq. (2.3)) and adapted the gaseous conductivity with kinetic theory using the pore diameter as the boundary mean free path. Machrafi & Lebon (2015) used the same approach but used their own derived expression (Eq. (6.8)) for the reducing gaseous conductivity. Wang et al. (2017) derived a new analytical model for the conductive ETC based on a unit cell with either closed or open pore structure. They use the kinetic theory to include the nanoscale effects on the gaseous conductivity.

Results predicted by some selected models are shown in Figure 6.2a as a function of porosity for a pore size of 10 nm, and in Figure 6.2b as a function of pore size for a porosity of 90 %. The model by Hu, Wu & Sun (2018) only considers nanoscale effects on the gaseous conduction, while the models of Minnich & Chen (2007), Machrafi & Lebon (2015) and Wang et al. (2017) include nanoscale effects on the solid conductivity as well (see Section 6.3). All four models show similar trends as function of porosity and pore size, but rather large discrepancies due to the different assumed pore structures and accounting of nanoscale effects.

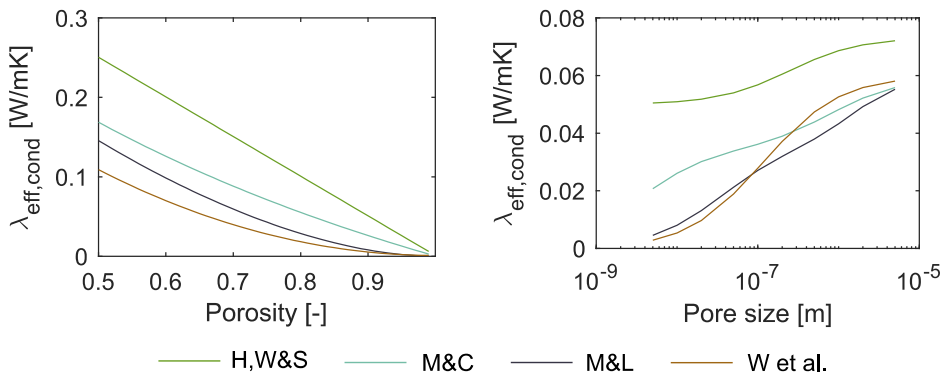


Figure 6.2: Prediction by selected analytical models of the ETC, for the case of pores of 10 nm diameter (a) and for the case of a porosity of 90 % (b). Properties assumed in the calculation are: $\lambda_{\text{mat}} = 0.5 \text{ W/mK}$, $C_{\text{mat}} = 2 * 10^6 \text{ MJ/m}^3$, $v_{\text{ph,mat}} = 300 \text{ m/s}$, $\lambda_{\text{gas}} = 0.0257 \text{ W/mK}$, $C_{\text{gas}} = 1240 \text{ J/m}^3$, $v_{\text{gas}} = 300 \text{ m/s}$, $T = 293.15 \text{ K}$, $p = 101325 \text{ Pa}$. The selected analytical models are by Hu, Wu & Sun (H,W&S, 2018), Minnich & Chen (M&C, 2007), Machrafi & Lebon (M&L, 2015) and Wang et al. (W et al., 2017).

Several other analytical models have been derived specifically for aerogels. They are not discussed here, but can be found in reviews by (Y.-L. He and Xie 2015; J. J. Zhao et al. 2012b).

Numerical modelling strategies

Numerical efforts for predicting the ETC of porous materials accounting for the altering gaseous conductivity have mainly been focussed on aerogel materials. A few models for cellular materials have been developed as well. Li et al. (2014) for example studied the combined heat transfer through a material made of hollow spheres. They solved the Fourier heat conduction on a unit cell and used Kaganer's model to adapt the gaseous conductivity dependent on the sphere diameter. They indicated a high influence of the pore size and of the contact area between the overlapping hollow spheres. Ferkl et al. (2013) presented a numerical model for nanoporous cellular materials simplifying the pore structure as a one-dimensional

structure of parallel solid slabs and gas pores. Fourier's conduction law was again applied to model the heat transfer, with a size correction for the gaseous conductivity. Numerical results agreed relatively well with experimental data, but they argued that a 3D model is needed to obtain better quantitative agreement.

6.3. Solid conduction

As was shown in Part I, the solid matrix conductivity is an important parameter influencing the material's ETC. With reducing pore size, the characteristic dimensions of the pore walls decreases as well (at constant porosity). Similarly to gaseous conduction, solid conduction can also be affected by domain-size-dependent effects, like the reduced heat dissipation in micro-electronical components or extremely high conductivities in nanowires. The process of solid conduction is more complex than gaseous conduction though. This section starts again with a short discussion on the fundamental physics of solid conduction and the expected domain size dependencies. Subsequently a number of models for the nanoscale effect on the solid conduction mechanism and on the resulting ETC are surveyed.

6.3.1. Fundamentals

Physical background & definitions

In electrically insulating materials, heat conduction occurs because of atoms oscillating around their equilibrium position. Atoms in zones of higher temperature will vibrate more intensely, transferring energy to their neighbouring atoms in zones of lower temperature via their connecting bonds. The amount of heat transfer through the material depends heavily on the type of material (atomic structure, type of bonds, ...) and the temperature, as is clear from Figure 6.3.

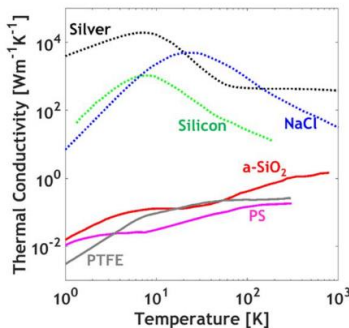


Figure 6.3: Solid thermal conductivity of metallic, crystalline and amorphous materials at different temperatures (Kommandur 2017).

Materials with more amorphous atomic structures (glasses, polymers, ...) typically show a continuous increase of the conductivity with increasing temperature until a certain plateau, while the conductivity of crystalline materials peaks and subsequently decreases with increasing temperature. Understanding the behaviour of the thermal conductivity in solids has been a research subject for many years already. Detailed accounts can be found in (Gang Chen 2005) or (Z. M. Zhang 2007). Here, we discuss two model formalisms useful to explain the qualitative behaviour of the factors influencing the solid thermal conductivity.

The first is the Einstein model formalism. He proposed to model all atoms as independent (uncorrelated) oscillators, vibrating all at the same frequency but at different phases (Cahill and Pohl 1988). Energy is transferred to the directly neighbouring atoms, travelling randomly through the solid at microscopic scale, and from the hot to the cold side macroscopically. For crystalline materials, the model severely underestimates the thermal conductivity of most solids though, and furthermore does not explain the temperature-dependency of the thermal conductivity (Cahill and Pohl 1989; Kommandur and Yee 2017). For amorphous materials on the other hand, Cahill et al. (1990) discussed that Einstein's model of randomly oscillating atoms provides a quite correct physical picture and (qualitatively) predicts their temperature dependence. Based on the Einstein model, they presented an improved methodology for such materials by considering small groups of atoms as one harmonic oscillator and a distribution of vibration frequencies (Pohl 2006). The model is often called the 'minimum thermal conductivity model', depicting the lowest value a solid consisting of a certain set of atoms can reach by changing its atomic structure⁵. The increase with temperature of the thermal conductivity until a certain plateau is explained by the increasing specific heat which also shows such a trend with increasing temperature (Cahill, Watson, and Pohl 1992): more energy levels (quanta) become available to store and transfer energy. The formula for the minimum thermal conductivity is shown in Eq. (6.11) where k_B is the Boltzmann constant, N [$1/m^3$] is the atom number density, v_i [m/s] is the sound velocity of one of the three considered polarizations (two transversal, one longitudinal), T [K] is the temperature and Θ_i [K] is the Debye temperature. The summation is performed over the three modes:

$$\lambda_{solid,min} = \left(\frac{\pi}{6}\right)^{\frac{1}{3}} * k_B * N^{\frac{2}{3}} * \sum_i v_i * \left(\frac{T}{\Theta_i}\right)^2 * \int_0^{\Theta_i/T} \frac{x^3 * e^x}{(e^x - 1)^2} dx \quad (6.11)$$

⁵ Recently it was shown that even lower thermal conductivities can be attained in a highly anisotropic atomic structure (Z. Chen and Dames 2015).

The formula indicates that materials with a higher atom density (more closely packed atoms) and a higher speed of sound show larger solid conductivities. The speed of sound is related to the stiffness of the bonds between the atoms, explaining why ‘rigid’ materials typically show higher conductivities. Allen et al. (1999) proposed an even more detailed framework to understand heat conduction in amorphous materials. They divide the spectrum of vibrations in amorphous materials in three regions, where the modes in each region correspond to a certain heat carrier type: propagons, diffusons and locons (these show similarities with phonons in crystalline materials, which are discussed further on). These different heat carriers will respond differently to for example a reducing domain size, as is shortly discussed for phonons in the next section. A proper consideration of the different types of heat carriers requires atomistic simulations though, which is out of scope here. The reader is referred to the literature for further details (Allen et al. 1999; DeAngelis et al. 2019; Lv and Henry 2016b; Wingert et al. 2016; Seyf et al. 2017).

Alternatively, Debye recognized that in crystalline materials the atomic vibrations are actually not independent but are part of waves spreading throughout the material (Jiji 2009; Z. M. Zhang 2007). Modal analysis allows to break down the complex combination of waves to elementary waves of frequency ω in a certain spectrum. An energy quantum of such elementary wave is called a phonon, similar to the concept of a photon in thermal radiation. Debye proposed a simple model for the thermal conductivity in analogy to the kinetic theory for gasses: phonons are considered as particles flying around randomly and colliding with each other or other irregularities in the crystal like domain boundaries or impurities (Cahill and Pohl 1988). Therefore, it is sometimes called the phonon gas model (PGM). The thermal conductivity can then be predicted as shown in Eq. (6.12), where c_V [J/kgK] is the specific heat at constant volume, ρ_s [kg/m³] the mass density of the solid, v_g [m/s] is the mean (group) speed of phonon wave packets which is on the order of the speed of sound, and L_{MFP} [m] is the mean free path a phonon travels before scattering:

$$\lambda_{solid} = \frac{1}{3} * c_V * \rho_s * v_g * L_{MFP} \quad (6.12)$$

The previously discussed concept of phonons actually refers to the acoustic type of phonons. In crystals with more than 1 atom per primitive unit cell, there will be (apart from acoustic phonons) also optical phonons, which are out-of-phase vibrations of the atoms constituting the unit cell. These phonons hardly contribute to the thermal conduction process though, as their group velocity is very low, and they are hence usually not considered in Eq. (6.12) (Jiji

2009). To better account for the highly frequency-dependent properties of the phonons, sometimes an integral version of Eq. (6.12) is proposed, shown in Eq. (6.13) where C_V [J/m^3] is the specific heat per unit volume. This equation better accounts for the dispersion of the phonons' group velocity in the material and the fact that phonons with low frequencies experience less scattering effects of small impurities or grain boundaries than high frequency phonons (Z. Wang 2012).

$$\lambda_{solid} = \frac{1}{3} * \int C_V(\omega) * v_g(\omega) * L_{MFP}(\omega) * d\omega \quad (6.13)$$

Debye's model is able to reproduce the typical temperature dependency of crystalline materials shown in Figure 6.3. The initial increase with increasing temperature is explained by the increasing specific heat owing to the increasing amount of available phonon modes. The subsequent peak and decrease follow from the increasing amount of scattering due to the rising amount of phonons: this causes an increase in the scattering probability and hence reduces their mean free path. From Eq. (6.12) it follows that an increasing mass density and speed of sound increase the solid thermal conductivity: heavy, stiff materials generally have higher thermal conductivities. To reduce the (intrinsic) solid thermal conductivity, one can reduce the mean free path, for example by adding impurities or by inducing grain boundaries (poly-crystallinity). Such poly-crystallinity indeed reduces the solid thermal conductivity through a reduced mean free path inside the grains, but also through the interface resistance between the grains (also known as Kapitza resistance) (H. Dong, Wen, and Melnik 2014)2014 H Dong. The other option, explored in more detail in the next section, is reducing the phonon mean free path by reducing the domain size of the solid.

Effect of domain size

The effect of a reducing domain size has been mainly investigated for crystalline materials, due to their application in micro-electronics. For such materials, the effect can be qualitatively understood with Debye's model through a reducing mean free path: the scattering probability increases due to increased scattering with the domain boundaries.

In amorphous materials, heat is transported via propagons, diffusons and locons (Allen et al. 1999; Seyf et al. 2017). It has been shown that propagons can experience a similar size effect as phonons in crystalline materials. For diffusons and locons, the size effect is much less understood though, and is suspected to be only important at much smaller length scales (DeAngelis et al. 2019). Hence, the observed reduction of the solid conductivity depends

largely on the initial contribution of the propagons to the total conductivity (Wingert et al. 2016). Measurement results have for example shown reductions at film thickness below 1 μm for amorphous silicon (Wingert et al. 2016), but only at film thicknesses below 20 nm for polystyrene films (Ma and Tian 2015), although it has also been claimed that the observed reductions are at least partially caused by a changing interfacial thermal resistance. Coquil et al. (2009) measured the ETC of different nanoporous amorphous silica with pore sizes between 3 and 18 nm. They concluded that there was no influence of the pore size and thus also no changing solid conductivity, which they attributed to heat being mainly carried by localized nonpropagating vibrational modes. Hence, predicting the size effect on the amorphous solid conductivity is still a very complex task requiring a detailed atomistic simulation to properly distinguish between the participating vibration modes (Lv and Henry 2016a; Saaskilahti et al. 2016).

6.3.2. Modelling of solid conduction

First, some general models regarding solid heat transfer in solid domains with nanoscale dimensions are discussed. Subsequently, models presented in literature for the prediction of the ETC taking such effects into account are surveyed.

Modelling of solid conduction in reduced domain sizes

Analytical modelling strategies

Analytical approaches typically focus on calculating an adapted solid conductivity to estimate the nanoscale effect on the solid conduction mechanism. Thanks to the similarity between phonons and gas molecules, the kinetic theory framework is often applied to that end. This requires (similar as for the case of gaseous conduction) the determination of a boundary mean free path that can be combined with the bulk mean free path through Matthiessen's rule (Eq. (6.2)).

Jiji (2009) summarizes analytical approximations for calculating the anisotropic effective mean free path in the case of heat conduction parallel and perpendicular to thin films. For parallel conduction, the equations depend on the specularity, the degree to which thermal waves are scattered in a specular or diffuse manner: more diffuse reflections lead to lower thermal conductivities. The formula is a complex equation with integrals, but for the case where all scattering is diffuse (a reasonable assumption for most porous materials), a simplified form of the expressions is possible, see Eq. (6.14). This equation predicts immediately the *effective* mean free path. Apart from the film thickness d_{wall} [m], it depends

thus also on the bulk mean free path. For the perpendicular case, an expression based on similarity with thermal radiation is given in Eq. (6.15), depending on the phonon absorptivity α_{ph} [-], which is the degree with which the energy of a wave is absorbed on collision with the boundary.

$$L_{MFP,eff,||} = \frac{L_{MFP,bulk}}{1 + \frac{3 * L_{MFP,bulk}}{8 * d_{film}}} \quad (6.14)$$

$$L_{MFP,bdy,\perp} = \frac{3}{4} * \frac{d_{wall}}{2 - \alpha_{ph}} \quad (6.15)$$

Expressions for other types of geometries (i.e. nanowires) exist as well in literature, but are less applicable to the cellular porous media considered in this study.

Numerical modelling strategies

Numerical modelling allows for a better prediction of the nanoscale effects for more irregular configurations, including the possible anisotropy. Different strategies have been developed to model these effects, like molecular dynamics methods solving the full motion of the atoms in their lattice (Schelling, Phillpot, and Koblinski 2002), phonon Boltzmann solution techniques tracking the motion and scattering of phonons in the solid system (Lemonnier 2007; Randrianalisoa and Baillis 2008; Guo and Wang 2016), or phonon hydrodynamic methods generalizing the macroscopic Fourier heat law using the equivalence with fluid dynamics to incorporate nanoscale effects (Alvarez, Jou, and Sellitto 2010; Guo and Wang 2015). Examples for different types of geometries like thin films or nanowires can be found in the literature. A full overview of these methods is out of scope here, for more information the reader is referred to i.e. review papers (Guo and Wang 2015; Bao et al. 2018), or specialized books on the matter (Gang Chen 2005; Volz 2007; Z. M. Zhang 2007).

Modelling the effect on the effective thermal conductivity

Analytical studies

Similarly as for the case of gaseous conduction, the effect on the ETC caused by nanoscale effects on the solid conduction mechanism has often been studied by adapting the solid conductivity in one of the analytical expressions proposed for conventional porous materials. Proposed procedures calculate the boundary mean free path and use the kinetic theory framework to calculate the reducing solid conductivity of the matrix. Minnich & Chen (2007) for example use Maxwell's model for the ETC and proposed a formula for the reducing solid

conductivity in a porous material with spherical pores of radius r_p [m] and porosity ϕ [-]. Their formula for the boundary mean free path is shown in Eq. (6.16). Machrafi & Lebon (2015) expanded the methodology by Minnich & Chen (2007) to ensure that the mean free path goes to zero at a porosity of 100 % (Eq. (6.17)). Wang et al. (2017) developed a new analytical model for the ETC of foam-like materials. They equated the boundary mean free path to the pore wall thickness (Eq. (6.18)). All three presented formulas predict direction-independent boundary mean free paths though, while it was discussed before that typically highly anisotropic behaviour is encountered in nanoscale heat conduction. The three discussed publications also include a calculation methodology to estimate the effect of the pore size on the gaseous conductivity (see previous section), hence accounting for both solid and gaseous heat transfer and the potential nanoscale effects.

$$L_{MFP,M-C} = \frac{4 * r_p}{3 * \phi} \quad (6.16)$$

$$L_{MFP,M-L} = \frac{4 * r_p}{3 * \phi} * (1 - \phi) \quad (6.17)$$

$$L_{MFP,W} = d_{wall} \quad (6.18)$$

Models based on other formalisms than the phonon gas model have been derived as well to predict the ETC of porous materials with nanoscale features. Alvarez et al. (2010) for example presented Eq. (6.19) for materials containing spherical pores, derived from the phonon hydrodynamics formalism. The model only considers solid conduction and the effect of phonon scattering with pore boundaries. The characteristic size in the Knudsen number was taken as the pore radius.

$$\lambda_{eff,cond,Atv} = \frac{\lambda_s}{\frac{1}{(1-\phi)^3} + \frac{9}{2} * \phi * \frac{(Kn)^2}{1 + 0.864 + 0.29 \exp\left(-\frac{1.25}{Kn}\right)} * \left(1 + \frac{3}{\sqrt{2}} * \sqrt{\phi}\right)} \quad (6.19)$$

Prasher (2006) presented an equation (Eq. (6.20)) for materials with cylindrical nanopores aligned transversely to the main heat flow direction, based on the analogy between phonons and photons. They also only considered conduction through the solid matrix (and the associated nanoscale effects). The factor F [-] is the viewfactor representing how all pore-matrix interfaces see each other inside the matrix phase and can be obtained from radiation

simulations considering the matrix as the transparent phase and pores as opaque objects, or by fitting predicted values with experiments.

$$\lambda_{eff,cond,Prasher} = \frac{\lambda_s * \frac{3}{4} * \frac{d_{pore} * \sqrt{\frac{\pi}{4\phi}}}{L_{MFP,bulk}}}{\frac{3 * (1 + \phi)}{4 * (1 - \phi)} * \frac{d_{pore} * \sqrt{\frac{\pi}{4\phi}}}{L_{MFP,bulk}} + \frac{1}{F}} \quad (6.20)$$

Tarkhanyan & Niarchos (2013) considered the porous medium as a homogeneous medium with an adapted effective mean free path dependent on the pore structure properties. Using the kinetic theory, the ETC is then calculated based on the effective mean free path, and can be calculated as in Eq. (6.21). Again, only solid conduction is considered. A very similar model was developed by Dettori et al. (2015), adding '0.5 * ϕ ' as an extra term in the summation in the numerator in Eq. (6.21).

$$\lambda_{eff,cond,Tark} = \lambda_{s,bulk} \frac{1 - \phi}{1 + \frac{L_{MFP,bulk}}{d_{pore}} * \frac{3\phi}{2}} \quad (6.21)$$

Figure 6.4 repeats the prediction of the ETC by some analytical models already shown in Figure 6.2, and expands them with the model 'A,J&S' by Alvarez et al. (2010) that focusses purely on solid conduction. The model 'H,W&S' by Hu, Wu & Sun (2018) only considers nanoscale effects on the gaseous conduction, while the other three models consider effects on both mechanisms. The ETC predicted by Alvarez' model is significantly lower than the other models, certainly at these high porosities. This is partially explained by the fact that only solid conduction (and the associated nanoscale effect) is taken into account, while gaseous conduction becomes relatively more important at increasing porosity.

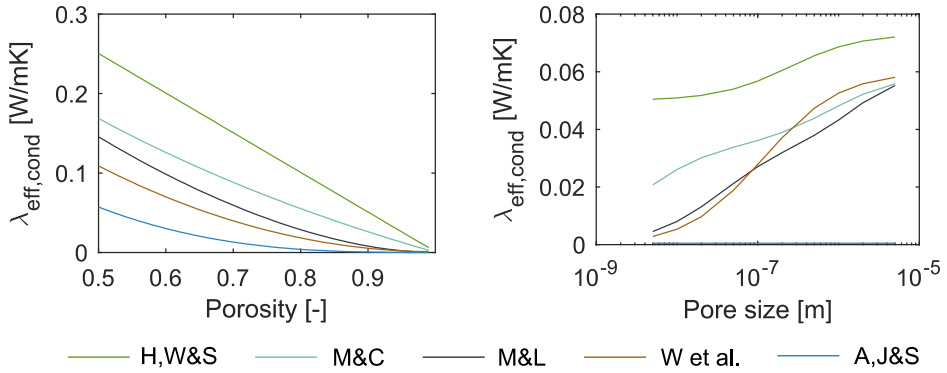


Figure 6.4: Prediction by selected analytical models of the ETC, for the case of pores of 10 nm diameter (a) and for the case of a porosity of 90 % (b). Properties assumed in the calculation are: $\lambda_{\text{mat}} = 0.5 \text{ W/mK}$, $C_{\text{mat}} = 2 * 10^6 \text{ MJ/m}^3$, $v_{\text{ph,mat}} = 300 \text{ m/s}$, $\lambda_{\text{gas}} = 0.0257 \text{ W/mK}$, $C_{\text{gas}} = 1240 \text{ J/m}^3$, $v_{\text{gas}} = 300 \text{ m/s}$, $T = 293.15 \text{ K}$, $p = 101325 \text{ Pa}$. The selected analytical models are by Hu, Wu & Sun (H,W&S, 2018), Minnich & Chen (M&C, 2007), Machrafi & Lebon (M&L, 2015), Wang et al. (W et al., 2017) and Eq. (6.19) by Alvarez et al. (2010).

For aerogel type of materials, which have a more ‘wire-like’ matrix structure, multiple equations have been derived as well. Since they are not really applicable to the type of cellular materials discussed in this work, the reader is referred to the literature for more details, i.e. (C. Bi and Tang 2013).

Numerical studies

Detailed numerical simulation of the solid conduction mechanism in pore structures with nanoscale features is very costly from a computational point of view. Some studies on simple pore structures have been performed in literature using molecular dynamics (Dettori et al. 2015; Coquil et al. 2009; J. Fang and Pilon 2011; Sundarram and Li 2013) or phonon Boltzmann simulations (Miyazaki et al. 2010; Tang, Bi, and Fu 2013; Hua and Cao 2017; R. Coquard et al. 2013) to get a detailed picture of the heat transfer through the solid matrix in porous materials with nanopores. Typically, they show a strong dependence on the pore size explained by the increasing scattering of the phonons with the pore boundaries. Apart from their simplified pore structure geometries, they typically also neglect gaseous conduction and thermal radiation, which seems only reasonable in low-porosity materials with a high matrix conductivity.

6.4. Pore scale radiation

In Part I, thermal radiation was modelled as a process of energy transfer between the pore surfaces. Stefan-Boltzmann's law for blackbody radiation and a material-dependent emissivity were used to describe the physical process, making abstraction of the radiation's wave-nature. This approach can be insufficient though when the length scale (e.g. the pore wall thickness or pore size) is on the order of the radiation wavelength. Two different effects at these lengths scales have been discussed in literature. The first is the increasing transmission through pore walls with decreasing thickness and the associated constructive and destructive interference due to multiple reflections. The second effect is the near-field radiative heat transfer causing energy transfer exceeding Planck's black body limit. Both effects require taking into account the wave nature of thermal radiation. A short revisit of the physical background and concepts important for understanding the discussed effects is detailed in the next section. Subsequently, modelling strategies for thermal radiation and its effect on the ETC proposed in literature are surveyed.

6.4.1. Fundamentals

Physical background & definitions

Thermal radiation refers to the spectrum of electromagnetic radiation emitted due to the internal thermal state of a material. Random oscillations of charges in the material generate electromagnetic waves carrying energy away from the material. According to Planck's law, an ideal blackbody at temperature T emits a spectral radiation intensity or radiance $i'_\lambda [W/(m^2 \cdot sr \cdot wavelength)]$ as described by Eq. (6.22), where h is the Planck constant, k_B is the Boltzmann constant and $c [m/s]$ is the speed of the waves in the medium. This speed can be inferred from the speed of light in vacuum $c_0 [m/s]$ and the medium's refractive index $n [-]$, Eq. (6.23).

$$i'_\lambda(\lambda, T, \Omega) = \frac{2 * h * c^2}{\lambda^5 * \left(\exp\left(\frac{h * c}{k_B * \lambda * T}\right) - 1 \right)} \quad (6.22)$$

$$c = \frac{c_0}{n} \quad (6.23)$$

The electrical field of an electromagnetic wave propagating in a medium can be generally described as in Eq. (6.24), where \vec{E}_0 is the amplitude vector, \vec{k} is the wave vector normal to the wavefront (and typically pointing along the travelling direction) with magnitude equal to

the angular wavenumber k [rad/m], \vec{r} [m] is the position vector, ω [rad/s] the angular frequency and t [s] the time. The magnetic component has a similar formula and is always perpendicular to the electrical field.

$$\vec{E} = \vec{E}_0 * e^{i*(\vec{k}*\vec{r}-\omega*t)} \quad (6.24)$$

The angular wavenumber k is proportional to the inverse of the wavelength of the propagating wave (Eq. (6.25)) and can be written as a function of the medium refractive's index n and the wavelength in vacuum λ_0 [m].

$$k = \frac{2\pi}{\lambda} = \frac{2\pi n}{\lambda_0} \quad (6.25)$$

Inside real materials, propagating electromagnetic waves will be attenuated as they travel through the medium. This is usually brought into Eq. (6.24) via a complex refractive index $\hat{n} = n + i\kappa$, where κ [-] is the absorption coefficient of the material. Substituting the complex refractive index in Eq. (6.24) and (6.25), we obtain Eq. (6.26) for the propagating wave, with a decaying amplitude for the electrical (and similar for the magnetic) field, with \vec{k}_u the wave vector with unit length. It is important not to confuse the absorption coefficient κ occurring in the complex refractive index with the absorption coefficient μ [1/m] defined earlier in Chapter 3 on the modelling framework. Indeed, the first designates the absorption of the electrical field, while the second designated the absorption of the radiation energy. Both are related though through Eq. (6.27), since the energy carried by an electromagnetic field is proportional to the square of the electrical field's amplitude.

$$\vec{E} = \vec{E}_0 * e^{-\frac{2\pi\kappa}{\lambda_0}*\vec{k}_u*\vec{r}} * e^{i*(\frac{2\pi n}{\lambda_0}*\vec{k}_u*\vec{r}-\omega*t)} \quad (6.26)$$

$$\mu = \frac{4\pi\kappa}{\lambda_0} \quad (6.27)$$

Effect of domain size

As stated, there are two phenomena that can occur in porous media with reducing length scales that require considering the wave nature of thermal radiation: transmission through pore walls with possible interference effects, and near-field radiation between pore walls close to each other. Both are discussed in the next two sections.

Transmission through thin solid films and interference effect

As predicted by Eq. (6.26), the amplitude of the electric field of the electromagnetic waves decays as the waves travel through an absorbing solid. When incident on a solid with limited thickness, part of the radiation intensity will transfer through the solid film instead of being reflected or absorbed. Hence, the solid becomes optically thin, demanding a different treatment of the radiation problem than the surface-to-surface model developed in Part I.

Secondly, when radiation is incident on a thin film (e.g a pore wall), interference effects can further alter the amount of radiation transmitted through or reflected by the pore wall (Born and Wolf 2003). This can be understood by the conceptual sketch in Figure 6.5. Imagine two radiation waves, one reflecting from the first solid-gas interface and the other from the second solid-gas interface of the thin solid film. Both reflecting waves can interfere constructively or destructively, increasing or decreasing the reflectance (and vice versa for the transmittance) of the solid film (G. Wang, Wang, et al. 2017).

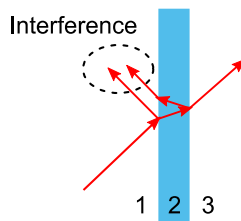


Figure 6.5: Illustration of transmission and reflection through a thin film with potential interference of waves reflecting from both interfaces of the thin film. The thin film is designated with number '2', the vacuum space before and after the thin film with number '1' & '3'.

This *thin film interference effect* hence alters the reflectance and transmittance of the solid, depending on the radiation wavelengths and the solid's thickness and complex refractive index. It will manifest itself more strongly at film thicknesses on the order of and smaller than the radiation wavelength, since the waves reflecting off the second solid-gas interface experience less absorption during their travel inside the film and can contribute more to the constructive and destructive interference.

For the sake of completeness, the discussed effects can also occur in microporous materials with pore dimensions of hundreds of micrometres, when the pore walls are only a few micron thick. This is limited to very high porosity foams though, as was already argued in Chapter 3, which are out of scope for this work and were thus not treated so far.

Near-field thermal radiation

The second effect occurring at reducing length scales is near-field thermal radiation (Howell, Mengüç, and Siegel 2016; Rousseau et al. 2009). Planck's blackbody distribution predicts the upper limit for the amount of thermal radiation power emitted by an object at temperature T as $\sigma_{SB} * T^4$. However, when two objects are placed very close to each other (the separation distance being on the order or smaller than the radiation wavelength) tunnelling of evanescent electromagnetic thermal waves can increase the amount of radiation flux significantly (Mulet et al. 2002; Z. M. Zhang 2007). Such evanescent waves occur because of the phenomenon of total internal reflection (TIR): an electromagnetic wave generated inside a medium with high refractive index that hits an interface with a medium of lower refractive index at an incident angle larger than the critical angle θ_{crit} will not travel into the second medium but will be reflected completely. This induces also a wave parallel to the interface with amplitude decaying exponentially in the second medium perpendicular to the interface.

Such evanescent waves are hence not travelling into the second medium and do not contribute to the far-field radiation emitted by medium 1. However, when an object is brought within a distance close enough to the interface, the evanescent wave will activate the charges in the second medium, resulting in an energy transfer from medium 1 to medium 3 (called the tunnelling effect). Hence, the total thermal radiation can exceed the maximum blackbody value predicted by Planck's law. An illustration of such plane wave and the resulting evanescent wave is shown in Figure 6.6.

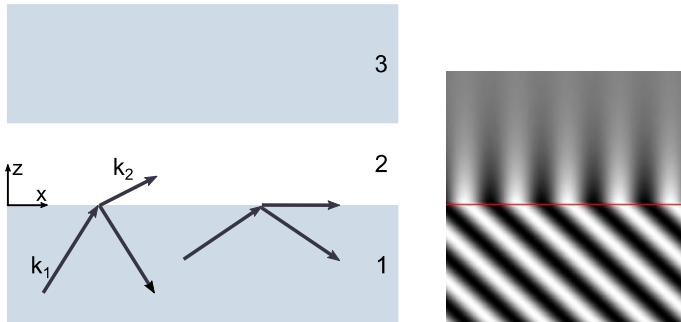


Figure 6.6: Conceptual sketch of total internal reflection of plane wave in medium 1 when the angle is larger than the critical angle (a). Illustration of plane wave in medium 1 causing an evanescent wave in medium 2 travelling parallel to the interface (b) (adapted from picture on Wikipedia (Wikipedia n.d.) licensed under CC BY-SA 3.0).

Apart from the TIR effect, evanescent waves can also originate from the resonant coupling between randomly fluctuating optical phonons (atomic vibration waves) and electromagnetic

waves. This coupling causes hybrid waves called surface phonon polaritons, which are quasi-monochromatic standing waves at the surface with an evanescent magnitude in both directions perpendicular to the surface (Rousseau, Laroche, and Greffet 2009; Howell, Mengüç, and Siegel 2016). Similarly to the evanescent waves occurring because of the TIR effect, they can increase the radiative heat transfer between two objects when separated at small distance.

6.4.2. Modelling of pore scale radiation

State of the art on modelling of thermal radiation

The Fresnel equations, detailed in Appendix A, can be used to calculate analytically the transmittance, reflectance and absorbance of a solid thin film taking into account the interference effects (Born and Wolf 2003). Bouguer's analytical law (presented in Chapter 3) for the transmissivity can also be used to estimate the amount of thermal radiation transmitted through the pore wall (De Micco and Aldao 2006). However, it does not consider the interference effect.

Regarding near-field radiation, no simple analytical equations have been presented to predict the increase of thermal radiation (to the best of the author's knowledge). Quantifying the effect of evanescent waves requires the full solution of the Maxwell equations considering an extra term representing the random chaotic movement of charges (i.e. dipoles) that cause the emission of electromagnetic radiation. Such numerical models have been presented for simple geometries like parallel plates, the reader is referred to literature for more details.

Effect on ETC and radiative conductivity

Analytical studies

Analytical approaches for thermal radiation in porous media usually calculate a macroscopic radiative conductivity that should be summed with the macroscopic conductive conductivity. The model by De Micco and Aldao (2006), for example (already mentioned in the literature survey of Chapter 2) proposes an expression based on parallel solid plates taking into account the transmission of thermal radiation through the pore walls. The interference effect was not included. Another previously mentioned analytical modelling strategy is the Rosseland diffusion approximation, predicting the macroscopic radiative conductivity based on an analytically calculated mean extinction coefficient. For high porosity polymer foams, some authors have presented expressions to calculate the mean extinction coefficient, taking into account the transmission and interference effect on the reflectance and transmittance of the

pore walls (i.e. R. Coquard, Baillis, and Quenard 2009). Lastly, Wang et al. (2017; 2018) recently presented an analytical model for thermal radiation in nanocellular foams, based on the model by De Micco and Aldao (2006). They proposed a more realistic pore structure of cubic pores arranged in a simple cubic manner and expanded the equations to correct for the interference effect using the Fresnel equations (Appendix A).

Numerical studies

Similarly as for the analytical models, Chapter 2 discussed already some numerical models considering the radiation transmission and interference effects for high porosity polymeric materials with pores in the micro- and millimetre range (Randrianalisoa and Baillis 2010; R. Coquard, Baillis, and Maire 2010; Rémi Coquard, Randrianalisoa, and Baillis 2013; Ferkl, Pokorný, and Kosek 2014). Nonetheless, such modelling strategies might be expanded to nanoporous materials as well. Currently, models focussing on thermal radiation in nanoporous materials are typically aimed at aerogel materials though, the reader is referred to literature for more details (R. Coquard et al. 2013; J. J. Zhao et al. 2012a; Enguehard 2007; Lallich, Enguehard, and Baillis 2009; Baillis, Coquard, and Moura 2015).

Lastly, the effect of near-field radiation has also been studied numerically though mainly for simple geometries like parallel plates (Cahill et al. 2014). In the context of porous materials, Jing Li et al. (J. Li et al. 2015) studied near-field radiation in a cylindrical and spherical pore of diameter l to 50 nm incorporated in a silica matrix at 305 K average temperature. They modelled the atomic lattice and used fluctuational electrodynamics combined with Maxwell's equations to simulate the electromagnetic radiation inside the pore. They showed a strongly increasing equivalent radiative conductivity over several orders of magnitude with reducing pore size due to the tunnelling of evanescent waves.

6.5. Conclusions

This chapter gives an overview of the nanoscale effects on each heat transfer mechanism discussed in literature. The fundamental physics behind the different physics have been revisited. It was shown that the gaseous conductivity decreases with decreasing pore size and/or gas pressure due to the decrease of the effective mean free path of the gas molecules. The importance of this effect can be estimated through the Knudsen number: the higher this number, the more important the reducing effect of the pore size and the gas pressure. Solid conduction was shown to reduce as well with reducing domain size, although the effect is strongly dependent on the type of matrix structure: crystalline or amorphous. Regarding

thermal radiation, finally, two effects at reducing length scales that are sometimes discussed in literature are reviewed: the transmission with interference effects through thin pore walls, and the near-field radiative heat transfer between solid objects at nanometer separation. Both effects can increase the importance of thermal radiation and the resulting ETC.

A number of analytical and numerical models presented in literature to model the concerning heat transfer mechanisms and the total heat transfer in porous media have been surveyed. The analytical models are usually based on analytical models presented for ordinary porous media, with modifications of the solid and gaseous conductivities depending on the pore size and gas pressure. They show a large variation between each other due to the assumed physical models and simplified pore structures. Some numerical modelling strategies for the heat transfer with nanoscale effects have been presented as well, allowing to obtain a more detailed picture of the pore structure influence on the respective heat transfer mechanisms. Their application on actual pore structures with complex geometry is still computationally costly though. To reduce the computational complexity, they typically focus on one heat transfer mechanism, simplifying or omitting the other mechanisms. This limits their applicability to certain porosity ranges or pore sizes. Lastly, the majority of numerical work regarding the prediction of the ETC has focused on aerogel types of materials. The lack of validated numerical models for cellular materials clouds the potential benefits of nanosized pores and reduced gas pressures on the reduction of the ETC.

Chapter 7

Implementation and validation of the model framework for pore scale heat transfer with nanoscale effects⁶

7.1. INTRODUCTION	163
7.2. EXPANSION OF THE MODEL FRAMEWORK	164
7.3. VALIDATION OF MODEL FRAMEWORK	179
7.4. CONCLUSIONS	189

7.1. Introduction

The model framework as presented in Part I simulates heat transfer through the porous material as a diffusion process with a known thermal conductivity for all the phases involved. At reducing length scales and gas pressures, nanoscale effects can cause the actual heat flow to deviate from this classical physical description of thermal conduction. When the domain size is on the order of a heat carrier's mean free path, these carriers experience the effect of the domain boundary, which can significantly influence the total heat flow through the porous material (G. Chen, Borca-Tasciuc, and Yang 2004; Jiji 2009; Z. M. Zhang 2007). Similarly, in Part I thermal radiation has been modelled as a surface-to-surface process, neglecting the wave-nature and the phase information of the electromagnetic waves. When the domain size is on the order of the wavelength of the waves, coherence effects can come into play invalidating this classical description of the radiative heat transfer process.

Many authors have recently indicated that such nanoscale effects can reduce the total heat flow through porous materials with pore size distributions in the nanoscale range. Examples are materials like aerogel or nanocellular foams that aim to exploit such effects by reducing the pore size (B. P. Jelle, Gustavsen, and Baetens 2010; S. Liu, Duvigneau, and Vancso 2015).

⁶ Part of this chapter is submitted for publication in a special issue of Journal of Building Physics

To be able to study the impact of such nanoscale effects on the insulating performance, the model framework is to be expanded to include these effects in the prediction of the ETC.

This chapter presents the extension of the model framework to incorporate nanoscale effects on the total heat flow through the porous material. For simplicity, the framework is kept largely the same, starting again from a 3D image of the pore structure and creating a finite element mesh to perform the simulation. In line with the previous work in Part I, the conductive heat transfer mechanisms are still modelled as conductive processes: the nanoscale effects on the different heat transfer mechanisms are accounted for by adapting the respective conductivities based on the pore structure characteristics. Regarding radiative heat transfer, a macroscopic method defining an effective radiative conductivity will be explored. The methodology for calculating these effective conductivities is presented in the next sections per heat transfer mechanism: gaseous conduction, solid conduction and thermal radiation. Natural convection is again not discussed, as the reducing pore sizes further nullify its contribution to the total heat flow. While in Part I both granular and cellular materials were considered, Part II will focus exclusively on (closed-cell) cellular materials, for which higher porosities and hence lower conductivities can be reached. Examples of such materials with nanoscale characteristics are nanocellular foams and hollow-silica-nanosphere-based materials. Highly-open-cell materials like aerogels are not considered in this work, for this material type the reader is referred to the extensive existing literature (i.e. C. Bi, Tang, and Hu 2014; Y. L. He and Xie 2015; Baillis, Coquard, and Moura 2015).

The last part of this chapter will focus on the validation of the expanded framework with experimental measurements from literature. Two sets of nanocellular foams with different porosity ranges and pore sizes from a few 100 of nanometre to a few micrometre are used for the validation exercise.

7.2. Expansion of the model framework

7.2.1. Gaseous heat conduction

In high-porosity materials used for building applications, conduction through the gaseous phase typically accounts for the largest part of the total heat transfer through the material (Solórzano et al. 2009). In search for superinsulating materials, most studies focus on reducing this heat transfer mechanism by proposing to reduce the pore size and/or the gas pressure, as is done in aerogels, nanocellular foams, hollow-silica-nanosphere-based materials or vacuum insulation panels.

In this work, the kinetic theory of gases framework is used to model the gaseous conduction and study the impact of reducing pore sizes and gas pressures. Although less accurate than more detailed simulations strategies like the Lattice Boltzmann technique or the Direct Simulation Monte Carlo (DSMC) technique, the framework provides reasonably accurate results and an intuitive picture of the effects of reducing the pore size and/or the gas pressure. Furthermore, it allows to extend the previously developed numerical model in a straightforward way, as will be shown further on. First, the kinetic theory of gases is briefly revisited, after which the calculation methodology is developed and validated.

Modelling framework

As described in Chapter 6, the kinetic theory of gases framework considers the gas as molecule particles flying around randomly and exchanging energy upon collision. It assumes the gas to behave like an ideal gas, meaning gas molecules occupy a negligible space (dilute) and only interact through elastic collisions. Such conditions are indeed valid for most gases around room temperature and at atmospheric pressure or below. The framework allows to deduce a formula for the gaseous conductivity λ_{gas} [W/mK], repeated here for convenience (Eq. (7.1)).

$$\lambda_{gas} = \frac{1}{3} * c_{V,gas} * \rho_{gas} * v_{avg,gas} * L_{MFP} \quad (7.1)$$

with $c_{V,gas}$ [J/kgK] the specific heat at constant volume, ρ_{gas} [kg/m^3] the mass density, $v_{avg,gas}$ [m/s] the average speed of the gas molecules and L_{MFP} [m] the mean free path of the gas molecules. The specific heat depends on the gas temperature and is tabulated for most gases. The mass density depends on gas pressure p_{gas} [Pa] and temperature T_{gas} [K] and can be calculated using the ideal gas law shown in Eq. (7.2), knowing the specific gas constant $R_{specific,gas}$ [J/kgK]. The average molecule speed, $v_{avg,gas}$ [m/s], is a representation of the whole speed distribution of the gas molecules. Jiji (2009) proposed to approximate this speed by its root-mean-square value, and hence it depends on the specific gas constant $R_{specific}$ and the gas temperature T_{gas} as shown in Eq. (7.3).

$$\rho_{gas} = \frac{p_{gas}}{R_{specific,gas} * T_{gas}} \quad (7.2)$$

$$v_{avg,gas} = \sqrt{3 * R_{specific,gas} * T_{gas}} \quad (7.3)$$

The mean free path, finally, depends on the pressure and the temperature of the gas as well as on the gas molecule properties. For example, for air at 20 °C and atmospheric pressure, the mean free path is about 58 nm.

When applying Eq. (7.1) with property values found in literature, results consistently underestimate the true gaseous thermal conductivity. As argued by both Zhang (2007) and Jiji (2009), this is because the average distance between collisions is the mean free path for momentum transfer, and not for energy transfer. Often, a factor depending on the specific heat ratios γ is introduced in Eq. (7.1) to correct for this issue. However, here we follow the solution proposed by Jiji (2009), defining a ‘mean free path for energy exchange’ that should be used in Eq. (7.1) instead of the physical distance between two collisions. This *energy-exchange mean free path* can be deduced from Eq. (7.1) using a tabulated value for the gaseous thermal conductivity. For air at 20 °C and atmospheric pressure, this leads for example to an energy-exchange mean free path of 180 nm, roughly 3 times higher than the physical mean free path.

As discussed in Chapter 6, the mean free path changes with changes in gas pressure and pore dimension. This effect can be estimated with Matthiessen’s rule, repeated here in Eq. (7.4) for convenience. The effective mean free path depends hence on the (*energy-exchange*) *bulk mean free path* and the *boundary mean free path*.

$$1/L_{MFP,eff} = 1/L_{MFP,bulk} + 1/L_{MFP,bdy} \quad (7.4)$$

To calculate the gaseous conductivity inside a pore, one needs thus to calculate the boundary mean free path imposed by the pore boundaries. Expectedly, this boundary mean free path will depend on the pore size and the pore shape. Besides, it also depends on the efficiency of energy exchange between the gas molecule and the pore wall, an effect sometimes referred to as the interface resistance or Kapitza resistance. Similarly to the energy-exchange bulk mean free path, an *energy-exchange boundary mean free path* could hence be defined. For simple configurations like gas confined between parallel plates, analytical expressions were derived as described by Zhang (2007) or Kaganer (1969). For other configurations like spherical pores, often the same expression is then used using the pore diameter instead of the inter-plate distance due to a lack of better alternatives. As such, the effect of the pore shape is often not taken into account correctly. Therefore, a new methodology is proposed here.

New calculation methodology for $L_{MFP,eff}$

Detailed modelling of the confinement effect or reducing gas pressure inside a pore cavity on the effective mean free path can be performed by for example Boltzmann models. To avoid the associated complexity and computational cost, a new analytical model is developed. The proposed methodology approximates the boundary energy-exchange mean free path based on the analogy between gaseous conduction and pore scale radiation. The boundary mean free path relates to the effect a gas molecule experiences from the surrounding boundaries. Thus, by definition it boils down to a situation where no interaction with other gas molecules occurs. To calculate this effect, we turn to the analogy with pore scale radiation. Indeed, radiation is often modelled as a process between surfaces, without any interaction between the photons. Considering the photons as particles, it hence shows great similarity with the process of gas molecules travelling directly between boundaries without scattering with other gas particles. Furthermore, similar to gaseous conduction, the kinetic theory framework allows to formulate an expression for the radiative conductivity as shown in Eq. (7.5) (Gang Chen 2005; Jiji 2009).

$$\lambda_{rad} = \frac{1}{3} * C_{rad} * v_{rad} * L_{MFP,rad} \quad (7.5)$$

The specific heat C_{rad} [J/m^3K] and speed of the photons v_{rad} [m/s] is defined as shown in Eq. (7.6) and Eq. (7.7), with v_{light} [m/s] the speed of light.

$$C_{rad} = \frac{16 * \sigma * T^3}{v_{light}} \quad (7.6)$$

$$v_{rad} = v_{light} \quad (7.7)$$

The effective mean free path for thermal radiation can again be calculated using Matthiessen's rule (Eq. (6.2)). The bulk mean free path of photons is usually several orders of magnitude larger than the cavity size when travelling inside a cavity filled with a non-absorbing medium as air. Hence, for thermal radiation, the effective mean free path equals the boundary mean free path, as shown in Eq. (7.8).

$$1/L_{MFP,eff,rad} = 1/L_{MFP,bulk,rad} + 1/L_{MFP,bdy,rad} \cong 1/L_{MFP,bdy,rad} \quad (7.8)$$

This boundary mean free path for thermal radiation can be deduced by comparing Eq. (7.5) with previously derived equations in literature for the radiative thermal conductivity in pores. In Chapter 3, a model based on the methodology of Loeb (1954) was presented to calculate the

radiative conductivity inside a pore cavity as a function of the pore size and shape. The equations are repeated here in Eq. (7.9) to Eq. (7.11). The pore size is characterized by its mean distance d_x [m] between the opposing pore walls in the general heat flow direction x . The factor C_x [-] combines the influence of the wall emissivity and the pore's directional slenderness factor $S_{f,x}$ [-]. This slenderness factor characterizes the pore shape and is defined as the ratio between the mean distance between the opposing pore walls in the 3 main directions (d_x, d_y, d_z). As follows logically from Eq. (7.10), the slenderness factor depends on the general heat flow direction, so possible anisotropic effects can be included.

$$\lambda_{rad,pore} = 4 * \sigma * T^3 * d_{x,mean} * C_x(\epsilon, S_{f,x}) \quad (7.9)$$

$$S_{f,x} = \frac{d_z * d_y}{d_x^2} \quad (7.10)$$

$$C_i = \begin{cases} \left(\frac{0.6615 + 2.4642 * S_{f,i}}{0.3526 + 2.8103 * S_{f,i} + 0.0189 * S_{f,i}^2} \right)^{1.673 - 3.5092 * \epsilon} * (0.7051 * \epsilon)^{0.9604} \\ \frac{\epsilon}{2 - \epsilon} \quad (\text{for } S_{f,i} > 8) \end{cases} \quad (7.11)$$

By now equalizing Eq. (7.5) and (7.9), we can deduce an expression for the boundary mean free path for radiation, see Eq. (7.12). Note that this is also an 'energy-exchange' boundary mean free path, since it is not the actual distance a photon travels but is also influenced by the efficiency of energy exchange through the emissivity.

$$L_{MFP,rad,boundary,x} = \frac{3}{4} * d_{x,mean} * C_x(\epsilon, S_{f,x}) \quad (7.12)$$

As argued before, the wave-particle duality of photons allows to interpret all photons as particles flying from surface to surface. This means the pore boundaries have a similar 'confinement' effect on the mean free path travelled by a single photon as they have on a single gas particle (provided there is no collision with other gas particles). Hence, a similar equation as Eq. (7.12) can be derived for the energy-exchange boundary mean free path of gas molecules. Of course, in Eq. (7.12), the wall emissivity is still present, which is not applicable for gas particles. However, a similar factor characterizes the efficiency of energy transfer between gas molecules and a boundary: the thermal accommodation coefficient a [-]. This factor is defined as in Eq. (7.13) (Kennard 1938).

$$a = \frac{E_i - E_r}{E_i - E_w} \approx \frac{T_i - T_r}{T_i - T_w} \quad (7.13)$$

Where E_i [J] is the energy of the molecules coming from the gas and hitting the wall, E_r is the energy of the molecules coming back from the wall after collision, and E_w is the energy of the molecules coming back from the wall if they would be perfectly ‘accommodated’, meaning that they have the same temperature as the wall. If a equals 1, a gas particle hitting the wall will reflect only after exchanging energy so that perfect thermal equilibrium with the wall is reached, while if its value equals 0, no energy transfer takes place between the wall and the gas molecules during the collision. As shown in Eq. (7.14) till Eq. (7.17), the radiative absorptivity α_{rad} [-] of a surface y can be rewritten to have a similar physical meaning as the accommodation coefficient. Here, $I_{hem.,tot,y}$ [W/m^2] is the total amount of incoming radiation on surface y , $E_{b,y}$ [W/m^2] is the total amount of radiation emitted by surface y if it was a blackbody and ρ_{rad} [-] is the surface’s radiative reflectivity.

$$\alpha_{rad} * I_{hem.,tot,y} = (1 - \rho_{rad}) * I_{hem.,tot,y} \quad (7.14)$$

↓

$$\alpha_{rad} * I_{hem.,tot,y} - \alpha_{rad} * E_{b,y} = (1 - \rho_{rad}) * I_{hem.,tot,y} - \alpha_{rad} * E_{b,y} \quad (7.15)$$

↓

$$\alpha_{rad} = \frac{I_{hem.,tot,y} - \rho_{rad} * I_{hem.,tot,y} - \alpha_{rad} * E_{b,y}}{I_{hem.,tot,y} - E_{b,y}} \quad (7.16)$$

The term $\rho_{rad} * I_{hem.,tot,y} + \alpha_{rad} * E_{b,y}$ describes the total amount of radiation leaving the gray surface y (the emissivity being equal to the absorptivity), so we can rewrite this as in Eq. (7.17), where $E_{y'}$ [W/m^2] is the total amount of energy leaving surface y via radiation.

$$\alpha_{rad} = \frac{I_{hem.,tot} - E_{y'}}{I_{hem.,tot} - E_{b,y}} \quad (7.17)$$

Eq. (7.17) shows the same terms and form for the radiative absorptivity as Eq. (7.13) for the gas molecules accommodation coefficient, confirming their similar physical meaning. Hence, we can replace the emissivity with the thermal accommodation coefficient in Eq. (7.12) to obtain finally an expression for the energy-exchange boundary mean free path for gas molecules confined in a pore cavity (Eq. (7.18)).

$$L_{MFP,gas,boundary} = \frac{3}{4} * d_x * C_x(a, S_{f,x}) \quad (7.18)$$

Combining Eq. (7.18) with Eq. (7.1)-(7.4) allows quantifying the gaseous conductivity in any pore taking into account its size, shape, gas pressure and gas-boundary interaction. As an example, the calculated room temperature thermal conductivity of air in a spherical pore is shown in Figure 7.1a for different pore sizes and gas pressures, assuming a thermal accommodation coefficient of 0.9 (often assumed in nanoscale gaseous heat transfer (Z. M. Zhang 2007)). Figure 7.1b shows the influence of the pore diameter and a varying thermal accommodation coefficient at atmospheric pressure. Both graphs clearly illustrate the expected decrease of the thermal conductivity with reducing pore size, gas pressure and/or thermal accommodation coefficient.

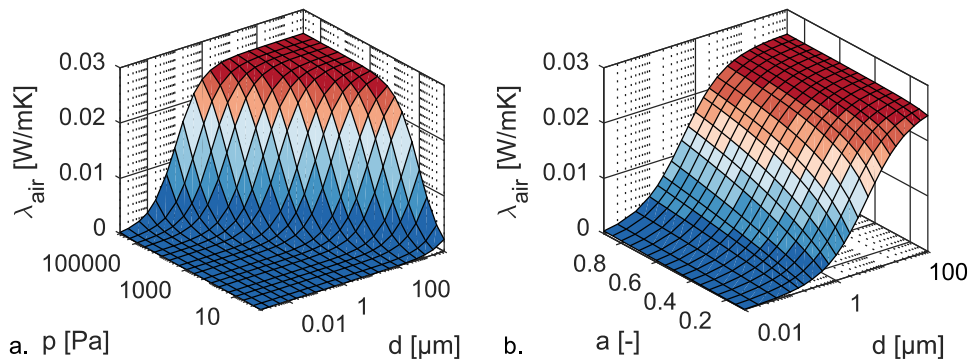


Figure 7.1: Predicted gaseous thermal conductivity in a spherical pore with varying diameter and pressure and thermal accommodation coefficient of 0.9 (a), and with varying diameter and accommodation coefficient at atmospheric pressure (b).

Validation of gaseous prediction model

The gaseous conductivity calculation methodology is validated against results found in literature. First, the gaseous conductivity between two parallel plates is studied, for the cases of reducing gas pressures and reducing separation distances. Subsequently, the gaseous conductivity in a cuboid pore with nanoscale dimensions is studied.

Gas confined between parallel plates

Results of two studies are used here to validate the proposed calculation method for the gaseous conductivity. First, experimental results performed by Braun and Frohn (1976) on the thermal conductivity of Argon gas are studied. The gas was confined between two plates with 1 mm separation, while the average temperature was kept at 323 K. The gas pressure was varied from 8.5 Pa to 66735 Pa. The thermal accommodation coefficient of the plates was 0.7385. Additionally, the numerical results obtained by Denpoh (1998) with the DSMC technique on

the thermal conductivity of N2 gas are used. The gas was kept at 343 K average temperature and atmospheric pressure. The plate separation distance was varied between 1.6 nm and 22 μm . Furthermore, Denpoh (1998) explored the effect of different thermal accommodation coefficients by considering three values: 1, 0.5 and 0.1. Details about both studies are summarized in Table 7.1.

Table 7.1: Summary of studies used to validate the gaseous conductivity calculation methodology.

Study	Config.	Gas	T [K]	p [Pa]	Size [m]	a [-]
Braun & Frohn 1976	// plates	Ar	323	8.5 - 66735	$1 * 10^{-3}$	0.7385
Denpoh 1998	// plates	N ₂	343	101325	$1.6 * 10^{-9}$ - $22 * 10^{-6}$	0.1/0.5 /1
Zhu et al. 2017	Cuboid	Ar	300	101000	$24 * 10^{-9}$ - $1.4 * 10^{-6}$	1

Using the proposed calculation method, the gaseous conductivities in both presented studies are predicted. Necessary properties of the bulk gas ($c_{v,gas}$, $\lambda_{bulk,gas}$ & $R_{specific}$) are found in specialized literature (ToolBox 2004; NIST 2018). The obtained results are compared with the results of both studies in Figure 7.2a. Results are shown as a function of the plate separation distance normalized by the collision mean free path of the respective gas. As can be seen, results agree very well with the literature results, both for the case of a reducing gas pressure (Braun & Frohn 1976) and a reducing separation distance (Denpoh 1998). Furthermore, the effect of the thermal accommodation coefficient is very well predicted using the energy-exchange boundary mean free path calculation. Also shown are the results obtained with Zhang's (Z. M. Zhang 2007) analytical expression for gaseous heat conduction between parallel plates (Eq. (6.6)). As expected, results agree also very well.

Gas in a cuboid pore

Zhu et al. (2017) numerically studied the gaseous conductivity of Argon gas confined in a cuboid pore using the DSMC technique. The gas was set to atmospheric pressure and a temperature of 300 K, the thermal accommodation coefficient to 1. The pore's side length was varied between 24 nm and 1.4 μm . Details are again summarized in Table 7.1. The proposed methodology is again applied to calculate the gaseous conductivities for the cases presented in the study by Zhu et al. (2017). Results are shown in Figure 7.2b. Again, a very good

agreement is obtained between the numerical results obtained through the proposed model and the DSMC technique. Also shown are the results obtained using the analytical expression for gaseous conduction between parallel plates (Eq. (6.6)) (Z. M. Zhang 2007). This time, less agreement is obtained with Zhang’s model. This is due to the cuboid shape of the pore influencing the gaseous conductivity, while the analytical expression was derived for parallel plates. This highlights the importance of taking the pore shape into account, as is done in the newly proposed methodology.

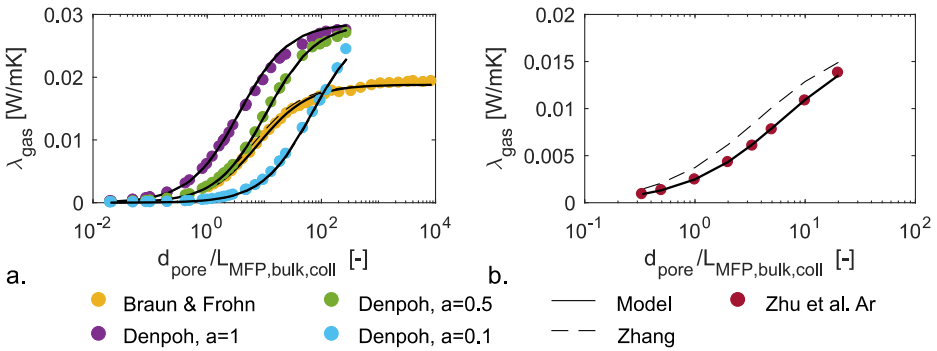


Figure 7.2: Gaseous conductivity results predicted by the new model agree very well with experimental and numerical results in literature, both for gas confined between parallel plates (a), and gas confined in a cuboid pore (b).

Implementation in model framework

The calculation procedure is very similar to the procedure described in Part I for the calculation of the radiative conductivity. First the complete pore space is split in different pore clusters via a distance transform and watershed algorithm, dependent on a specified rejoin factor. For every pore, the directional slenderness factor S_f is calculated based on the mean separation distance between all the surfaces in the three main directions (x,y,z). Subsequently, the boundary mean free path in each pore is calculated with Eq. (7.18) based on a specified accommodation coefficient. To calculate the resulting gaseous conductivity in the pore, the model requires specifying the bulk gas conductivity $\lambda_{gas} [W/mK]$, the specific gas constant $R_{specific,gas} [J/kgK]$, the gas pressure $p [Pa]$ and the average temperature $T_{avg} [K]$, which is taken as the average temperature of the sample. The whole procedure hence calculates a separate gaseous thermal conductivity for every pore cluster based on its pore size, pore shape, gas pressure and gas-boundary interaction.

7.2.2. Solid heat conduction

As was shown in Part I, the solid conductivity is an important parameter influencing the material's effective thermal conductivity. With reducing pore size, the characteristic dimensions of the cell walls reduce as well (at constant porosity). Similarly to gaseous conduction, solid conduction can also show domain-size-dependent effects, like the reduced heat dissipation in micro-electronical components or extremely high conductivities in nanowires. As was clear from the physical description in Chapter 6, the process of solid conduction is more complex than gaseous conduction though, partially because of the different types of atomic arrangements.

For crystalline materials, the phonon gas model is sometimes used to estimate the size effect on the solid conductivity, considering collisions with the solid boundaries via a reducing boundary mean free path. However, common materials used for producing building blocks are either amorphous (polymers, glass, ...) or poly-crystalline, since they possess lower thermal conductivities than typical crystalline materials. When applying the phonon gas model to such amorphous or poly-crystalline materials, the typical bulk mean free path is on the order of a few nanometre due to the high atomic disorder in both types of materials. This means that the effect of the boundary mean free path will only become relevant when the characteristic size drops somewhere below 10 nanometre (a few atoms thick). Hence, it will be negligible for most materials as was argued by (Ferkel et al. 2013; Hu, Wu, and Sun 2018).

However, in amorphous materials, the phonon gas model is not valid, since heat is transported via propagons, diffusons and locons (Allen et al. 1999; Seyf et al. 2017). It has been shown that propagons can experience a similar size effect as phonons in crystalline materials. For diffusons and locons, on the other hand, the size effect is much less understood though, and is suspected to be only important at much smaller length scales (DeAngelis et al. 2019). Hence, the observed reduction of the solid conductivity depends largely on the initial contribution of the propagons to the total conductivity (Wingert et al. 2016). Predicting the size effect on the amorphous solid conductivity is a still a very complex task requiring a detailed atomistic simulation to properly distinguish between the participating vibration modes (Lv and Henry 2016a; Sääskilähti et al. 2016). This is out of the scope for this work though. Together with the expectedly limited influence in amorphous and poly-crystalline materials, it is therefore decided to not include any size effects on the solid conductivity here, but simply maintain the solid conductivity as an a-priori known parameter.

7.2.3. Radiative heat transfer

In Part I, thermal radiation was modelled as a process of energy transfer between the pore surfaces. At reducing pore size and cell wall thickness, two effects have been discussed in literature that can invalidate this surface-to-surface approach (see Chapter 6): the first is the increasing transmission through cell walls with decreasing thickness and the possibly associated effect of constructive and destructive interference due to multiple reflections. The second effect is the phenomenon of near-field radiative heat transfer causing energy transfer exceeding Planck's black body limit. Both effects require taking into account the wave nature of thermal radiation. The first effect will be incorporated by adopting an analytical model proposed in literature, as detailed in the next section. The effect of near-field radiation, on the other hand, will be shown to be negligible for the type of materials studied in this work.

Accounting for transmission through thin cell walls

With reducing pore size, the pore wall thickness reduces as well, increasing the importance of transmission and interference effects as was discussed in Chapter 6. The previously presented Loeb model might thus underestimate the contribution of thermal radiation to the total heat transfer in nanoporous materials. Therefore, a different modelling strategy is needed.

As discussed in Chapter 6, a few detailed numerical strategies have been proposed in literature for modelling radiation through partially transparent cell walls. However, at this point, their implementation complexity and associated computation cost seem unjustified for the expected secondary importance of thermal radiation in the material porosity ranges and room temperature applications studied in this work. Therefore, the choice is made to adopt the analytical approach proposed by Wang et al. (2017; 2018), showing good agreement with experimental measurements on XPS foams. They propose to calculate an effective radiative conductivity for the whole porous sample based on the pore structure parameters and sum the obtained value with the sample's conduction-only effective conductivity (Eq. (7.19)). The conduction-only conductivity is obtained with the numerical framework taking into account the nanoscale effect on the gaseous conduction.

$$\lambda_{eff} = \lambda_{cond,eff} + \lambda_{rad,eff} \quad (7.19)$$

Wang et al.'s radiative conductivity calculation method is based on the model proposed by De Micco & Aldao (2006) for radiation through a set of parallel plates (discussed in Chapter 2), but assumes a different more realistic pore structure and takes into account the thin-film-

interference effect. To come to an analytical expression for the effective radiative conductivity, Wang et al. simplified the pore structure as a set of cubic pores ordered in a simple cubic manner (Figure 7.3). The matrix hence consists of three orthogonal slabs, two parallel and one perpendicular to the general heat transfer direction. Thermal radiation will interact with the cell walls by reflection, transmission and absorption. Since the roughness of the cell walls is relatively small compared to the wavelength of the thermal radiation ($\sim 10 \mu\text{m}$ at room temperature), all reflection is assumed to be specular.

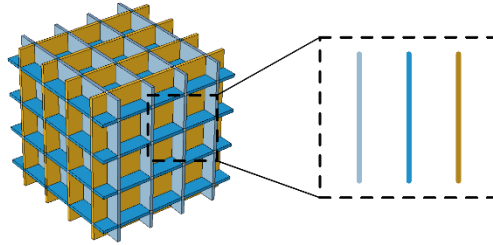


Figure 7.3: Assumed pore structure and unit cell in thermal radiation model of Wang et al. (2017,2018)

The pore walls that are parallel to the direction of general heat flow will hence only contribute to the attenuation of the radiation by absorption, since the specular reflection will not change the component of the wave's direction parallel to the general heat transfer direction. The cell walls perpendicular to the heat flow will attenuate the radiation both by absorption and reflection. Hence, Wang et al. (2017) simplified such a unit cell as three pore walls parallel to each other, all three absorbing equally the thermal radiation while only the first reflects thermal radiation. Similar to De Micco and Aldao (2006), they showed that the effective radiative conductivity for a material with such pore structure can be calculated as in Eq. (7.20), with T_{net}^{unit} [-] the net transmittance of the unit cell, d_{sample} [m] the sample thickness, d_{pore} [m] the pore diameter and d_{wall} [m] the cell wall thickness.

$$\lambda_{rad,eff} = \frac{4 * \sigma_{SB} * T_{avg}^3 * d_{sample}}{1 + \frac{d_{sample}}{d_{pore} + d_{wall}} * \left(\frac{1}{T_{net}^{unit}} - 1 \right)} \quad (7.20)$$

The net transmittance of the unit cell is defined as the part of the radiation incident on the unit cell reaching the other side of the unit cell due to partial transmission plus re-emission of the absorbed radiation. This depends on the hemispherical total reflectance, absorbance and transmittance of every cell wall. Assuming the cell walls can be modelled as thin films, these properties can be calculated using the Fresnel formulae and the complex refractive

indices of the gaseous and solid phase (Born and Wolf 2003). These formulae are also described in the paper by Wang et al. (2017) but contain a lot of mathematical and typographical errors. A correction (initiated by the author and promotor of this thesis) is published in Wang et al. (2018). However, the used notation and omission of some assumptions complicate a straight-forward implementation of the proposed model. Therefore, a full account of the model and the equations is summarized in Appendix A.

As illustration, Figure 7.4 shows the hemispherical total reflectance and transmittance for a cell wall as function of its thickness for different absorption coefficients κ_{solid} , at a temperature of 293.15 K and with the real part of the refractive index 1.5 or 2. For thick cell walls, the reflectance is constant and depends only on the real part of the refractive index. With decreasing thickness, the reflectance first increases due to constructive interference of waves reflecting from both interfaces of the cell wall. It reaches a maximum, after which it decreases again towards zero because an increasingly large part of the radiation spectrum starts to experience destructive interference. In the case of no absorption ($\kappa_{solid} = 0$), the transmittance equals 1 minus the reflectance, explaining the behaviour shown in Figure 7.4b. In case of absorption in the cell wall, the transmittance decreases with increasing thickness as is also expected from Bouguer's law, although the interference effects cause some bumps in the course. It is thus clear from both graphs in Figure 7.4 that the interference effects affect the reflectance, transmittance and absorbance significantly and should be taken into account in the radiative heat transfer.

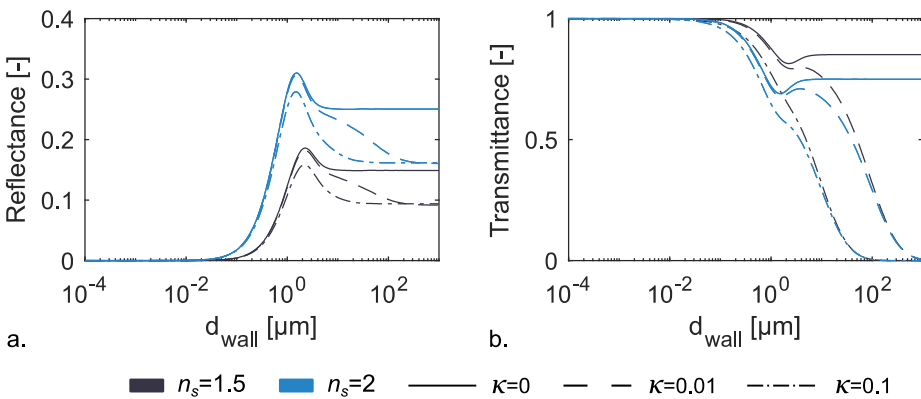


Figure 7.4: Hemispherical total reflectance (a) and hemispherical total transmittance (b) of a cell wall for different absorption coefficients κ_{solid} at 293.15 K and a refractive index n of 1.5 or 2 as a function of cell wall thickness d_{wall} .

The methodology calculates a radiative conductivity dependent on the following parameters: solid matrix' complex refractive index $n + i\kappa$, cell wall thickness d_{wall} , temperature T , pore size d_{pore} and sample thickness d_{sample} . Figure 7.5 shows the effective radiative conductivity for a sample with constant porosity of 90 % and thickness of 5 cm (the pore size is related to the cell wall thickness, given the cubic pore structure and a constant porosity). As can be seen, even when the solid material doesn't absorb radiation ($\kappa = 0$), the thermal radiation is still partially extinct in the sample due to reflections at the cell wall interfaces. With decreasing pore size, the radiative conductivity first decreases because of an increasing amount of cells and cell walls reflecting the thermal radiation. This was also predicted by the expanded Loeb methodology, through the reducing mean distance of the pores. Furthermore, the decreasing effect is larger for a higher refractive index n because of the higher associated reflectance (see Figure 7.4). After reaching a certain minimum, the conductivity increases again due to the decreasing reflectance of the thin cell walls as was shown in Figure 7.4a. In case the solid material absorbs radiation, the conductivity shows the same behaviour, increasing till a value where radiation extinction is solely due to absorption in the cell walls.

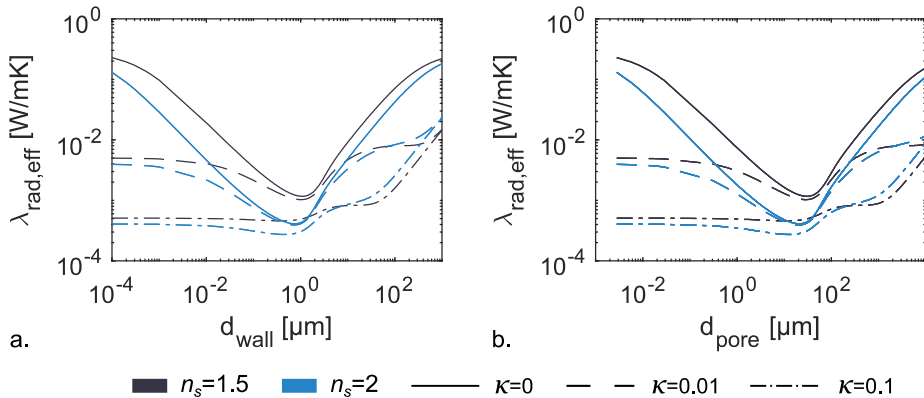


Figure 7.5: effective radiative conductivity for a sample of 5 cm thick and 90 % porosity, for different absorption coefficients κ_{solid} at 293.15 K and a refractive index n of 1.5 or 2 as a function of cell wall thickness d_{wall} (a) and pore size d_{pore} (b).

Near-field thermal radiation

The second effect occurring at reducing length scales is near-field thermal radiation. Tunnelling of evanescent waves can increase the exchanged thermal radiation between two surfaces to several orders of magnitude above Planck's law for blackbody radiation (Z. M. Zhang 2007; Joulain 2007; Howell, Mengüç, and Siegel 2016).

Quantifying the effect of evanescent waves requires the full solution of the Maxwell equations considering an extra term representing the random chaotic movement of charges (i.e. dipoles) that cause the emission of electromagnetic radiation. A number of studies have performed such calculations for simple geometries like parallel plates separated by a vacuum or for one plate and one spherical object at nanometre distance. One study was found studying the phenomenon in circular and spherical pores in a porous material at 305 K average temperature (J. Li et al. 2015). They performed the simulations for several pore diameters and presented the results also as an equivalent radiative conductivity in the pore as shown in Figure 7.6. As can be seen there is an increase of the pore’s radiative conductivity with decreasing pore size, contrary to what would be found with Loeb’s method when only considering blackbody far-field radiation.

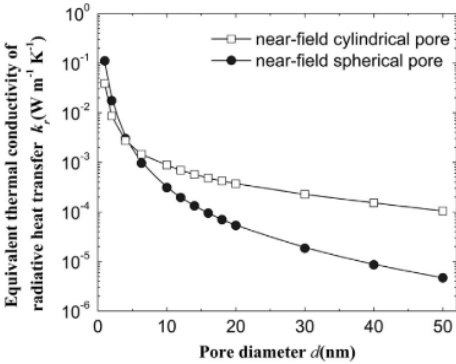


Figure 7.6: Equivalent radiative conductivity in a pore as a function of the pore diameter (Jing Li et al.).

Although there is a significant increasing effect, the equivalent radiative conductivity for a spherical pore is according to Li et al. (J. Li et al. 2015) still below 10^{-4} W/mK for pores with diameters down to 15 nm. Considering that the gaseous conductivity in such nanopore is – according to the model presented in this chapter – still one order of magnitude larger, the influence of the near-field thermal radiation is relatively limited. Together with the fact that direct simulation of the tunnelling effects of evanescent waves is currently computationally extremely expensive it is decided here to not take this mode of heat transfer into account.

Implementation in the model framework

Thermal radiation through the porous material is accounted for by calculating an effective radiative conductivity that can be summed with the effective conductive conductivity. Wang et al.’s calculation methodology (2017; 2018) is used taking into account the transmission

through the cell walls and the interference effects. The presented equations are implemented in Matlab, requiring as input the complex refractive index of the solid material comprising the cell walls, the average cell wall thickness and average pore size, the sample thickness and the average temperature. The average cell wall thickness is determined from the 3D image by first calculating the skeleton of the pore matrix and subsequently determining the thickness at every location of the skeleton via a distance transform. The average cell wall thickness is then calculated as a cell-wall-area-weighted average. Another possibility is to use analytical equations derived by geometrical simplification of the pore structure, as for example in Eq. (7.21) for a cubic pore structure as shown in Figure 7.3.

$$d_{wall} = \left(\frac{1}{(\phi)^{\frac{1}{3}}} - 1 \right) * d_{pore} \quad (7.21)$$

7.3. Validation of model framework

In this section, the framework's performance as a whole is validated. Indeed, the framework's aim is to predict the ETC of a porous material where all heat transfer mechanisms and corresponding nanoscale effects occur at the same time. To this end, the framework is applied to study the ETC of two sets of nanocellular foams experimentally characterized in literature. 3D images of the pore structure are generated based on the details presented in both studies and serve as input for the numerical simulations performed with the model.

7.3.1. Materials & methods

Two sets of measurements on nanocellular foams are used to validate the model framework: a set of foams with high porosities (around 90 %) and a set of foams with low porosities (around 60 %). Similar to better known and often used microcellular foams like PUR and XPS, these foams are made of a polymer matrix containing pores with nanoscale dimensions. Although currently only producible in small amounts and small dimensions, several literature papers discuss the potential improvements of such foams regarding thermal and structural properties (Costeux 2014).

Validation material sets

The first set consists of measurements on 4 high-porosity foams produced and characterized by Wang, Zhao et al. (2017), with pore sizes between 205 nm and 4.63 μm , and porosities between 86 % and 91 %. The samples are produced starting from pure solid polymethyl methacrylate (PMMA), adding increasing amounts of thermoplastic polyurethane (TPU) to

create different resulting pore structures. The second set of results comprises 7 foam samples produced and characterized by Notario et al. (2015). The samples' porosities are relatively low, between 52 % and 64 %, and pore sizes vary in the range of 220 nm to 970 nm. These samples stem from PMMA/MAM blends, with again varying mixtures to obtain different types of foam samples. Samples in both validation sets have a closed cell pore structure. Details of both measurement sets are summarized in Table 7.2. The thermal conductivity of the foams was in both studies measured using a Hot Disk instrument, a technique based on the transient plane source method. Results are also summarized in Table 7.2.

Table 7.2: Summary of properties of both sets of nanocellular foam samples used for the validation exercise.

Study	# samples	Material	Porosity	Pore size	ETC
Wang et al. (2017)	4	PMMA(>99%) / TPU	86 % - 91 %	205 nm - 4.63 μm	0.025 W/mK - 0.038 W/mK
Notario et al. (2015)	7	PMMA(>90%) / MAM	52 % - 64 %	235 nm - 970 nm	0.084 W/mK - 0.107 W/mK

Virtual generation of pore structures

Given that no actual μCT images are available, a virtual generation algorithm is employed to create foam-like pore structures mimicking the materials' true pore structures. The generation algorithm, as described by Randrianalisoa et al. (2013), is based on the Voronoi technique. First, a number of seeding points are located on a body-centred cubic lattice in a cubic volume, and subsequently slightly displaced in a random direction according to a perturbation factor. The Voronoi technique will divide the volume in separate cells based on the seeding points. The thickness of the cell walls is varied to obtain different porosities for the same pore locations. A strut-rounding algorithm based on dilation and erosion with a spherical element was implemented to obtain more round edges at the joints (struts) between two cell walls, which results in more realistic microstructures.

For both sets of measurement results, three different pore structures are randomly generated with a perturbation factor of 0.3 and an image grid size of 500^3 voxels. For the set by Wang, Zhao et al. (2017), the cell wall thickness of each sample is varied three times and the voxel size 4 times, obtaining $3 \times 3 \times 4$ or 36 simulated samples covering a region between 83 % and 91 % porosity and between 205 nm and 4.63 μm average pore size. For the set by Notario et al. (2015), the cell wall thicknesses are varied 5 times and voxel sizes 4 times, obtaining 60

samples covering a region of 50 % to 68 % porosity and an average pore size between 220 nm and 970 nm. Figure 7.7 compares a SEM picture of a sample from each set with a slice of one of the generated samples. A 3D render of a generated sample’s matrix structure is also shown.

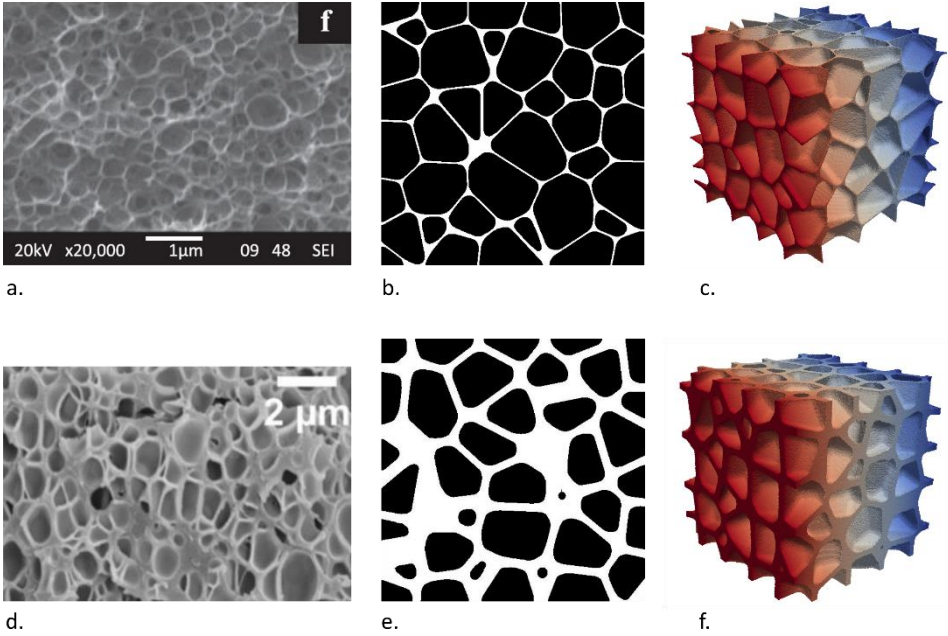


Figure 7.7: SEM picture of a foam sample by Wang, Zhao et al. (2017) (a) and by Notario et al. (2015) (d), slice of a virtually generated sample (b-e) and a 3D render of a generated pore structure (c-f).

7.3.2. High-porosity foams

Simulation setup

The effective thermal conductivity of all 36 generated samples is predicted with the model framework. The thermal conductivity of the solid PMMA matrix is set to 0.2098 W/mK, consistent to the value measured by Wang, Zhao et al. (2017) on a solid sample. The properties of the air inside the pores are found in literature or calculated using the equations presented in the chapter on the model framework and are summarized in Table 7.3. A thermal accommodation coefficient of 0.9 was assumed for the air-PMMA interface, a value common for most air-boundary interactions (Z. M. Zhang 2007). The gas temperature and pressure are taken as 23 °C and 101325 Pa, similar as during the experiments. The mesh is constructed with a maximum radius of 3 voxel sizes for the surface elements and the tetrahedral elements in the matrix structure, and 9 voxel sizes for the tetrahedral elements in the pores.

For the radiative part, the model by Wang et al. (2017) is used as explained previously. The complex refractive index of the PMMA matrix is approximated as $1.47+0.02i$ for the most pertinent wavelength of $10\ \mu\text{m}$ of room temperature thermal radiation (Berisha et al. 2016). The cell wall thickness is deduced from the 3D image of the generated samples by a distance transformation algorithm and is weight-averaged by the cell wall area. The sample thickness is taken as 1 cm, comparable to the dimensions of the measured foam samples in Wang, Zhao et al. (2017). The total effective conductivity is finally obtained by summing the conductive part obtained using the 3D model with the radiative part obtained using the analytical model.

Table 7.3: Thermophysical properties of air at $23\ ^\circ\text{C}$ and atmospheric pressure.

Property	Value
$R_{specific}$ (Engineering ToolBox, 2004)	287 J/kgK
ρ_{air} (calculated)	1.19 kg/m ³
c_V (NIST)	717 J/kgK
v_{rms} (calculated)	505 m/s
$\lambda_{air,bulk}$ (NIST)	0.0259 W/mK

Results & discussion

The conduction-only results obtained using the 3D model for the 36 simulated samples are compared with the 4 experimental results in Figure 7.8a. Results are presented as function of the samples' porosity while the colour highlights the pore size of the sample. A power-law trendline is least-squares-fitted through the simulations for every pore size. The error bars on the experimental measurements present the +/- 5 % uncertainty associated with the Hot Disk sensor. As can be seen, the conduction-only results agree already very well with all 4 measurements. Deviations with the per-pore-size simulation trendlines are below 10 % at the corresponding porosity, for all pore sizes. Simulation results in all cases underestimate the experimental values, which can be attributed to the fact that thermal radiation is not yet accounted for at this point. Simulation results furthermore confirm the expected decrease of the thermal conductivity with increasing porosity and/or decreasing pore size. A decrease of over 40 % when reducing the pore size from $4.6\ \mu\text{m}$ to $205\ \text{nm}$ is found at these relatively high porosities.

Simulation results for the radiative conductivity are shown in Figure 7.8b. They show an increasing trend with porosity due to the decreasing amount of absorbing material in the

samples. Furthermore, they also highlight an increasing trend with decreasing pore size, contrary to the conduction-only results. This is explained by the decreasing cell wall thickness for decreasing pore sizes. The effect of the increasing transmissivity of such thin cell walls outweighs the counteracting effect of an increasing number of cell walls per meter of sample thickness. The absolute values of the radiative conductivity are relatively small, due to the high absorption coefficient of the PMMA material constituting the matrix.

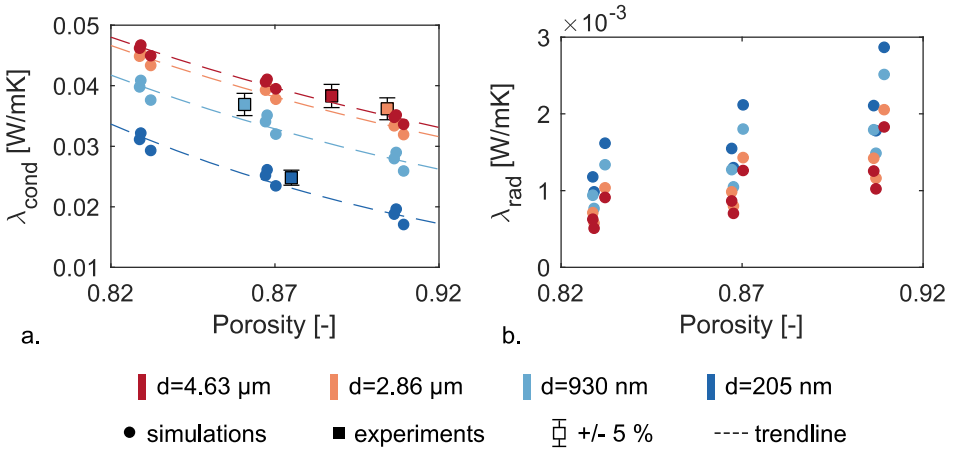


Figure 7.8: Comparison of simulated conductive effective conductivities with experimental results (a) and predicted radiative effective conductivities at varying porosity and pore size (b).

The results for the combined effective conductivity of the simulated samples are shown in Figure 7.9. As can be seen, including the thermal radiation improves the agreement between the simulation results and the experimental results. Only a 5 % difference occurs at the respective porosity with the corresponding simulation trendlines. This indicates the well-performance of the model and its capability of predicting the effect of decreasing the pore size to nanoscale dimensions. Lastly, the good agreement of the model with the experimental measurements supports the assumption made in the model framework that the cell wall thickness of the amorphous PMMA matrix will have a negligible influence on the solid conductivity (which was kept constant in all simulations). However, the high porosity of the tested samples translates to a relatively small contribution of solid conduction through the material: a changing solid conductivity would hence have only a minor effect on the total ETC.

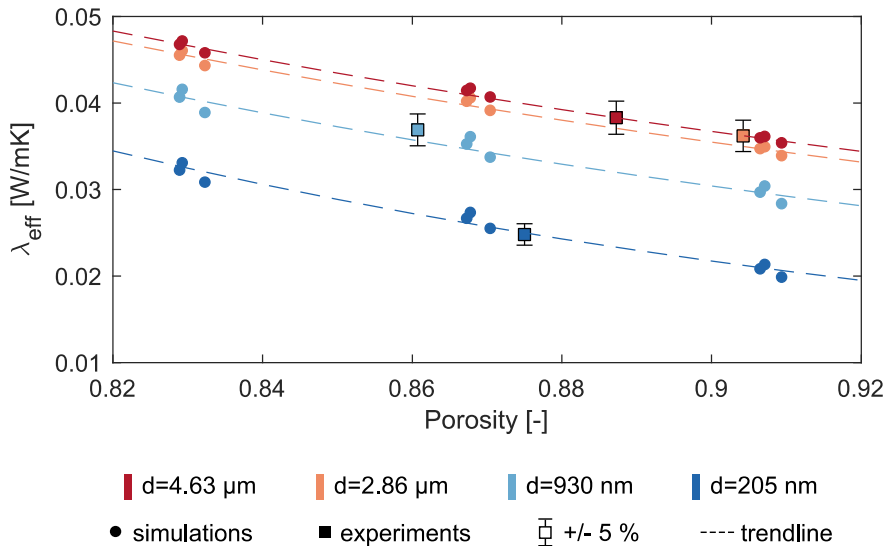


Figure 7.9: Comparison of simulated total ETC with experimental results for high-porosity foams of Wang et al. (2017).

The simulation and experimental results also allow to assess the potential improvement of reducing the pore size. Indeed, a reduction of about 30 % is found when reducing the pore size from 4.6 μm to 205 nm at 83 % porosity, mounting even to 40 % reduction at 91 % porosity. For the studied material at 83 % porosity, decreasing the pore size seems to have almost the same effect as increasing the porosity with 10 %-points. Of course, in low-porosity materials (<65 %) or materials with a high matrix conductivity, the effect of a reducing pore size will be less pronounced, since gaseous conduction is less pertinent in that case. Furthermore, for materials with a less absorbing solid matrix, thermal radiation will play a more important role at increasing porosities and decreasing pore sizes. Indeed, for the studied material, radiative heat transfer contributed only 2 – 15 % to the total thermal conductivity, depending on the pore size, porosity and wall thickness.

7.3.3. Low-porosity foams

Simulation setup

The effective thermal conductivity of all 60 generated samples is predicted with the model framework. The thermal conductivity of the solid PMMA/MAM matrix is this time set to 0.215 W/mK, as was measured by Notario et al. (2015). The gas temperature and pressure are taken as 23 °C and 101325 Pa, which is the same as during the experiments performed by Notario et

al (2015). The properties of the air inside the pores are hence also the same and are summarized in Table 7.3. A thermal accommodation coefficient of 0.9 is again assumed for the air-PMMA interface. The same mesh size parameters are used as for the previously studied samples: a maximum radius of 3 voxel sizes for the surface elements and the tetrahedral elements in the matrix structure, and 9 voxel sizes for the tetrahedral elements in the pores. Thermal radiation is expectedly negligible due to the relatively low porosity of the sample and the high absorption coefficient of the matrix. Nonetheless, the effective radiative conductivity is again calculated using Wang et al.'s model (2017) with a complex refractive index of $1.47+0.02i$, similar as the one used in the previous section.

Results & discussion

The conduction-only results are compared with the experimental measurements in Figure 7.10a. Results are presented as function of the samples' porosity while the colour highlights the (approximate) pore size of the sample. A power-law trendline is least-squares-fitted through the simulations for every pore size. The error bars on the experimental measurements present the +/- 5 % uncertainty associated with the Hot Disk sensor. Numerical results seem to consistently underestimate the experimental measurements with about 15 % to 20 %, although the main trends with increasing porosity and decreasing pore size seem to agree relatively well though. The calculated radiative conductivities, shown in Figure 7.10b, are very low and account for less than 1 % of the total ETC, which is expected considering the low porosity of the studied foams and the relatively high absorption coefficient of the complex refractive index. The simulated total ETC values, shown in Figure 7.10c, hence also show a similar underestimation of 15 % to 20 % of the experimental measurements. To allow for a better comparison of observed relative reductions of the ETC with reducing pore size and porosity, the simulated total ETC's and the experimental ETC's are both normalized in Figure 7.10d by their respective result at 52 % porosity and a pore size of 820 nm. A fairly good agreement between the numerical and experimental results is obtained in that case, meaning the model provides at least a good prediction of the relative effect of a reducing pore size and porosity.

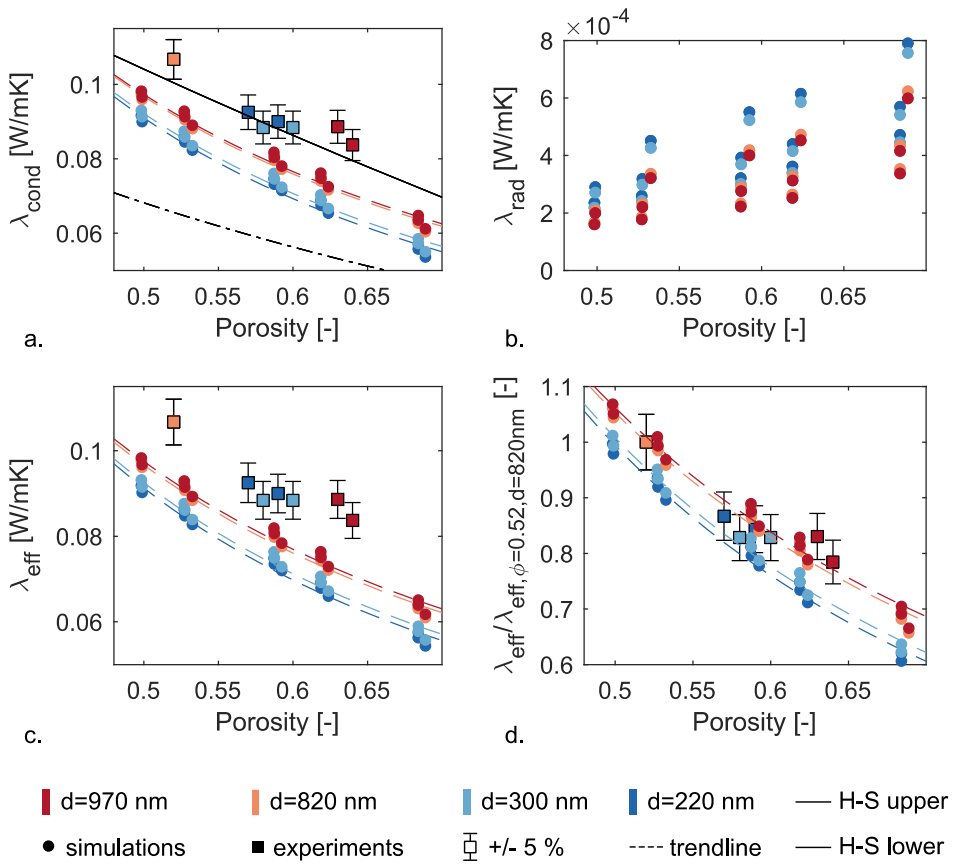


Figure 7.10: comparison of simulated effective conductivities and experimental measurements (a). Simulated effective radiative conductivities (b). Comparison of simulated and experimental ETC (c). Comparison of simulated and experimental ETC normalized by their respective value at porosity 52 % and pore size 820 nm.

A first explanation for the observed underestimation of the actual ETC could be a misprediction of one of the different heat transfer mechanisms. For example, it could be that the model overestimates the reduction of the gaseous conduction in the nanopores. However, for the foams with average pore size around $1 \mu\text{m}$, the ETC is equally underestimated while almost no reduction of the gaseous conductivity is predicted at this pore size. Another explanation could be a consistent underestimation of the contribution of thermal radiation. However, the radiation model was already validated by Wang et al. (2017), and also showed good agreement with the sample set discussed in the previous section. It should be mentioned though that the sample thickness of the measured samples was not mentioned by Notario et al. (2015). Hence, a thickness of 1 cm was assumed in our simulations, similar to the case of Wang, Zhao et al.'s

sample set (2017). If the sample thickness during measurement was much lower though, a higher radiative conductivity could be the case due to transmission through the sample as a whole. Finally, one could assume that errors arise due to the fact that nanoscale effects on the solid conductivity are not implemented in the model framework. These effects would lead to even lower ETC's though, if pertinent at all in the amorphous PMMA matrix. To match the simulations results with the experiments, one would actually have to increase the solid conductivity instead of a possible reducing solid conductivity.

Another source for errors might be that the generated pore structure doesn't correspond well with the actual pore structure of the sample. Indeed, the quality of the virtually generated pore structures could only be assessed by visual comparison with a 2D SEM photograph of the sample (Figure 7.7). Taking into account the rather low influence of the pore morphology on the ETC of cellular samples however (see Chapter 5), it is expectedly not possible to explain a 15 % to 20 % discrepancy solely by a difference in the pore structure. Additionally, Notario et al. (2015) calculated the anisotropy ratio and concluded that the samples all show quasi-isotropic pore structures. However, this last statement presents some unexpected behaviour in Figure 7.10a when comparing the experimental results with the Hashin & Shtickmann analytical models (Eq. (2.3)&(2.4)), calculated with the solid thermal conductivity of 0.215 W/mK used in the simulations, and the gaseous conductivity of air (hence without considering reductions due to nanosized pores). As discussed in Chapter 2, the H-S models provide lower and upper limits to the conductive ETC of isotropic cellular materials. The experimental measurements fall either just below or even above the upper limit though. As argued before, it is not excludable that this is (partially) due to a higher contribution of thermal radiation in case the measured samples were very thin. However, another explanation might be that the actual solid conductivity of the matrix inside the samples is higher than the proposed valued of 0.215 W/mK. Indeed, the thermal conductivity of polymers is known to be strongly dependent on its atomic structure, with literature for example presenting values ranging between 0.17 W/mK to 0.25 W/mK for PMMA. Liu et al. (2014) and Ma and Tian (2015) showed through atomistic simulations of the heat conduction in polystyrene thin films that the entanglement of the polymer chains influences the solid conduction strongly. Hence, although Notario et al. (2015) measured the solid conductivity of a pure PMMA sample to be 0.215 W/mK, it could be that the entanglement of the polymer chains changed during the

foaming process, thus leading to a different solid thermal conductivity⁷. Although it's impossible to profoundly test this hypothesis, the simulations were redone with a solid thermal conductivity of 0.25 W/mK to estimate the potential effect on the ETC. Results are summarized in Figure 7.11, where the analytical H-S models were also recalculated with the adapted solid conductivity.

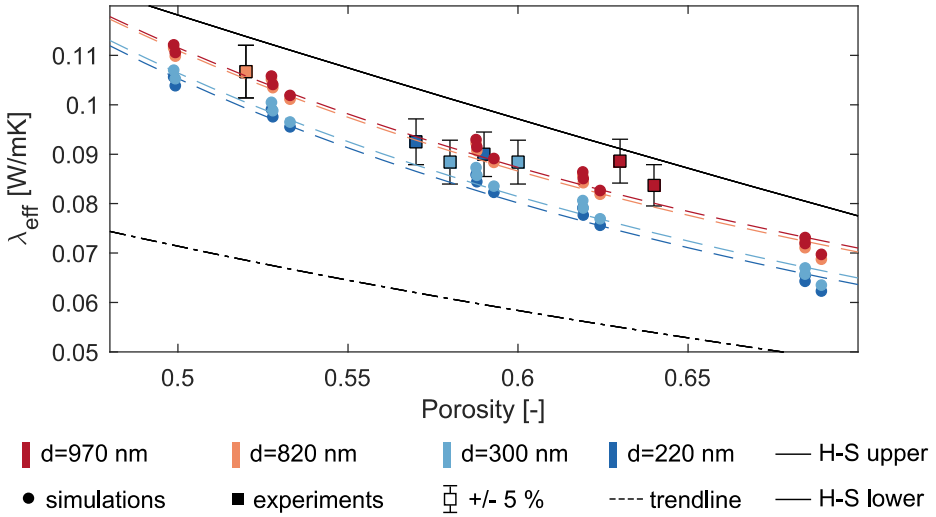


Figure 7.11: Comparison of simulated total ETC with increased solid thermal conductivity of 0.25 W/mK with experimental results of Notario et al. (2015) on low-porosity foams.

With the adapted solid conductivity, absolute values agree much better with experimental measurements, with discrepancies between 5 % and 10 %. Furthermore, the experimental measurements now fall in between both H-S bounds as is expected for isotropic structures with limited contribution of thermal radiation. Figure 7.11 also shows that framework predicts similar effects of a reducing pore size and porosity on the ETC as measured by the experiments, validating its applicability for the optimization of the ETC of porous materials including nanoscale effects.

⁷ The effect of a changing solid conductivity could also be present in the results by Wang et al. discussed in the previous section since they were also made from PMMA. The good agreement between numerical and experimental results does not suggest this however. Furthermore, even if the atomic structure changed, its effect would be relatively lower due to the higher porosity of those samples and hence the lower contribution of solid conduction to the ETC.

7.4. Conclusions

In this chapter, the extension of the model framework to simulate heat transfer through porous materials with reducing pore dimensions and/or gas pressures is discussed. Regarding the gaseous conductivity, an analytical calculation methodology is proposed based on the kinetic theory framework and the equivalence with thermal radiation inside cavities. The methodology takes into account the pore size, the (directional) shape, the gas pressure and the accommodation coefficient. Validation with experimental and numerical results from literature indicate a good agreement. The effect on the solid conductivity, on the other hand, is much more complex to properly predict and the impact is deemed to be relatively low for the materials studied in this thesis. Hence, it was decided to keep the solid conductivity as a predefined constant. Finally, the analytical model by Wang et al. (G. Wang, Wang, et al. 2017) is presented to model thermal radiation on a macroscopic level taking into account the transmission and interference effects. Near-field radiation was discussed to be of negligible importance in the materials targeted with the model.

Subsequently the numerical framework was validated with experimental measurements found in literature on nanocellular foams. The Voronoi technique was used to virtually generate pore structures mimicking the actual pore structures and showed good visual agreement. Simulations on the set of high-porosity foams (86 % to 91 %) agreed very well with the experimentally measured ETC's, for all pore sizes (205 nm to 4.63 μm). Adding the effective radiative conductivity, the discrepancies were on the order of 5 %. Furthermore, reductions between 30 % and 40 % were observed when reducing the pore size from 4.63 μm to 205 nm at these high porosities. On the other hand, simulations on the low-porosity foams (52 % to 64 %) consistently underestimated the experimental ETC with 15 % to 20 %. It was argued that this is either due to an underestimation of the thermal radiation – in case a very thin sample was used during the measurements – or due to a higher effective solid conductivity of the PMMA matrix due to a changing atomic structure. Simulations with a higher literature value of the PMMA's solid conductivity agreed much better with experimental results and predict the same size and porosity effects noticed during the experiments. Finally, simulation results on both sets of nanocellular foams suggest that the size effect on the solid conductivity of the amorphous PMMA matrix is indeed negligible. This supports the decision to keep the solid conductivity as a constant in the model framework for such amorphous polymer materials. Concluding, the model framework predicts very well the reducing effect of an increasing porosity and decreasing pore size on the ETC for cellular materials. Since the

implemented physical description of the gaseous conduction in the model basically functions the same for low-gas-pressure samples, it is expected that equally good results will also be obtained for these types of materials.

Chapter 8

Parameter studies towards optimal pore structures for porous building blocks with nanoscale features

8.1. INTRODUCTION	191
8.2. EXPLORATORY PARAMETER STUDY	192
8.3. DETAILED PARAMETER STUDY	201
8.4. CONCLUSIONS	208

8.1. Introduction

Reducing the pore size to the nanoscale has been put forward as an innovative strategy to reduce the ETC of porous building materials, as it may virtually nullify the conduction through the gaseous phase. As such, it has shown promising results for creating superinsulating materials like aerogels or nanocellular foams. Similarly, reducing the gaseous pressure has shown a same potential in vacuum insulation panels. However, most studies have focussed on the ETC of one specific material or on studying only the gaseous conductivity when predicting the impact on the ETC, clouding the potential effect at different porosity ranges, matrix conductivity etc. occurring in porous building materials.

In this chapter, the impact of the material's pore structure parameters and physical parameters is investigated with the nanoscale model framework presented and validated in the foregoing chapters. Similar to what was done in Chapter 5, two parameter studies are performed to this end: first, an exploratory study is performed considering for every parameter the full range of values encountered in typical porous building blocks. Several pore structures are randomly generated, and their ETC is calculated with the framework. Results from this first study allow to indicate the main trends and to compare the impact of the different parameters over their full range of values. The second, detailed study, on the other hand, zooms in on high-porosity

and low-matrix-conductivity samples to quantify the potential impact of the other parameters when both the porosity and the matrix conductivity have been optimized. Focus is placed on the effect of a reducing pore size on the ETC. The effect of a reducing gas pressure is not studied but will have a similar impact.

8.2. Exploratory parameter study

8.2.1. Methodology & setup

The ETC of 100 virtually generated pore structures are predicted with the model framework. The pore structures have different pore structure parameters (porosity, pore size, ...) and physical parameters (matrix conductivity, ...), allowing to investigate the impact on the ETC. First the selection of the relevant parameters is discussed, followed by the simulation setup. Subsequently, the predicted ETC's of the different samples are discussed and interpreted.

Parameter space

Similarly as in Chapter 5, the impact of the porosity, average pore size and pore size distribution are studied. The same ranges are used for the porosity (between 60 % and 95 %) and the normalised variance factor (0.016 to 0.4), see Table 8.1. The average pore size, on the other hand, is now varied between 1 nanometre and 10 μm to assess the impact of a pore size reducing to the nanoscale. The RBI and WSB technique are both used again to generate the pore structures and obtain two different types of pore structure morphologies.

Table 8.1: Studies parameters and their range of values.

Parameter	Minimum	Maximum
ϕ	0.6	0.95
$d_{pore,mean}$	1 nm	10 μm
$v_{norm,factor}$	0.016	0.4
λ_{mat}	0.2 W/mK	2 W/mK
$a_{therm.accomm.}$	0	0.9
n_s	1	2.5
κ_s	0.001	0.1
T_{avg}	-10 °C	40 °C

Additionally, the impact of the physical parameters is studied as well. The solid matrix conductivity is varied between 0.2 W/mK and 2 W/mK agreeing with the range of materials

used to produce porous building materials. The type of gas inside the pores is now always kept as 'air': the gaseous conductivity will hence only depend on the varying pore size, the thermal accommodation coefficient and the average temperature, all three varied according to the range in Table 8.1. Regarding thermal radiation, the impact of both parts of the complex refractive index $n_s + i\kappa_s$ of the material constituting the matrix is also investigated. Their variation range shown in Table 8.1 is inspired by typical values found in literature for solid materials. Furthermore, some authors have discussed the possibility to add absorbing particles to the matrix to increase the absorption coefficient and reduce the radiative heat transfer. The average temperature is again varied between -10 °C and 40 °C to investigate potential temperature-dependencies of the different parameters on the ETC. Lastly, the gas pressure is not varied in this case study but kept at atmospheric pressure (101325 Pa). Indeed, the effect of a changing gas pressure is expectedly similar to reducing the pore confinement. Furthermore, several studies in literature have already focussed on vacuum insulation strategies.

The Sobol sequence technique is again used to sample the whole parameter space. A 50 x 8 subset is projected on the parameter ranges assuming a uniform distribution, after logarithmically scaling the average pore size and absorption coefficient to ensure an adequate representation over their spanned scales. The Sobol set is based on the one previously used in Chapter 5, meaning the same combinations of porosity and normalised variance factor appear. This allows to use both sets of 50 samples generated by the RBI and WSB algorithm in Chapter 5, rescaling their geometry to conform with the newly assigned average pore size. This reduces the computational cost associated with the virtual generation and meshing of the pore structures. Some examples of generated pore structures were already shown Figure 5.1. The side length of each sample is set to 6 times $d_{pore,90}$ [m], the 90th percentile of pore sizes. For more details regarding the generation of the pore structures, the reader is referred to Chapter 5.

Simulation setup

The ETC of the generated samples is predicted with the numerical framework. The rejoinfactor is set at 0.6, used to split the pore space in different pore clusters. For each pore, the gaseous conductivity of the air inside is calculated with the framework proposed in Chapter 7, taking into account the pore size, shape, thermal accommodation coefficient and average temperature. Thermal radiation is modelled with the macroscopic method of Wang, based on the average cell wall thickness, which is determined from the samples' 3D images as a cell-

wall-area average. An actual sample thickness of 10 cm is assumed in the radiation calculation. All other needed input parameters are set to the associated values in the Sobol sample set.

8.2.2. Results & discussion

The results for all 100 studied samples are discussed, starting with an investigation of the pore structure properties of the samples and followed by a discussion on their predicted ETC.

Properties of generated samples

The obtained porosity, average pore size, normalised variance factor are calculated directly from the 3D voxel image. For the porosity and the normalised variance factor, the exact same results are obtained as in Chapter 5, since the same pore structures are used. Hence, the same correlation between both parameters is present here: a positive correlation for the RBI samples, and a negative correlation for the WSB samples. These correlations are due to the respective generation algorithms as was discussed in Chapter 5.

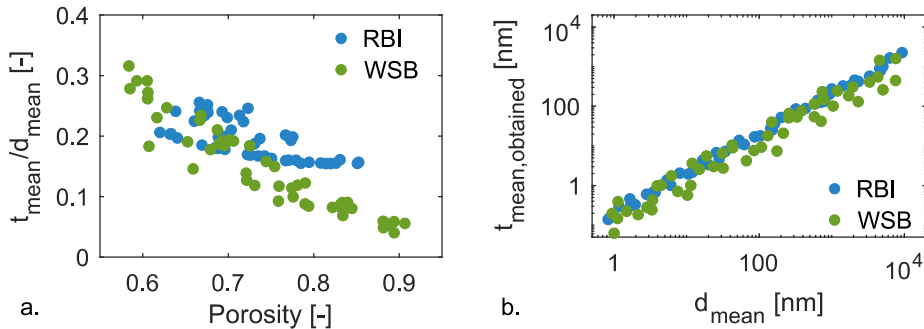


Figure 8.1: average cell wall thickness as a function of porosity (normalized by average pore size) (a), and as a function of average pore size (b) for RBI and WSB samples.

The average pore wall thickness, an important parameter in the calculation of the radiative conductivity, is calculated based on a distance transform and skeletonization of the matrix structure (see Chapter 7). The obtained values are shown in Figure 8.1 as a function of the samples' porosity (a) and average pore size (b). As can be expected, the pore wall thickness decreases with decreasing average pore size and with increasing porosity. Furthermore, from geometrical considerations it can be deduced that the ratio of the average wall thickness to average pore size increases with increasing pore size distribution width. This (partially) explains why the pore wall thickness of RBI samples at porosities roughly above 80 % is consistently larger than the pore wall thickness of the WSB samples: only RBI samples with a very wide pore size distribution are able to reach such high porosities. This will affect the

comparison of the radiative conductivity for both types of samples, as discussed in the next section.

Simulated ETC results

Visual interpretation

The predicted ETC of every sample generated by the RBI and WSB techniques is summarized in Figure 8.2 as a function of the different pore structure and physical parameters. Similarly as for the samples in Chapter 5, the porosity and the matrix conductivity appear to be the most influential parameters. The large effect of the variance factor is again explained by the correlation between the variance and the porosity, as was discussed already in Chapter 5. All other parameters show the expected effects, though with only a secondary importance: an increasing absorption coefficient and refractive index decrease the contribution of thermal radiation and hence also the ETC. A decreasing average temperature decreases the gaseous conductivity and the contribution of thermal radiation. A decreasing thermal accommodation coefficient also decreases the gaseous conductivity. Even, the average pore size shows only a small decreasing effect with decreasing pore size, although the pore size decreases here from a few micrometre down to a few nanometre.

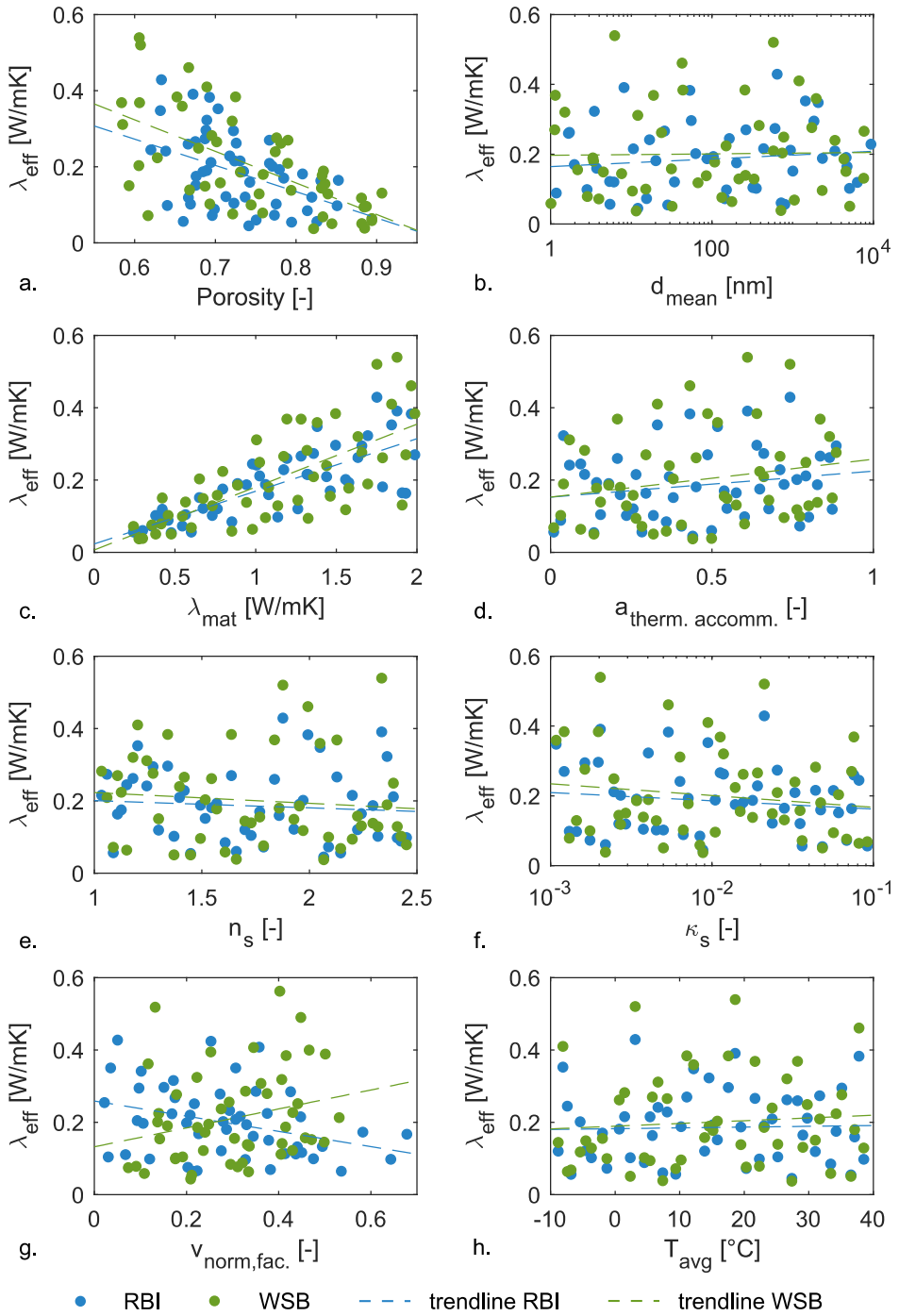


Figure 8.2: Predicted ETC as a function of the different parameters for both RBI and WSB generated samples.

The impact of the average pore size is investigated a bit deeper by studying its influence on the different heat transfer mechanisms. Figure 8.3 shows the effective radiative conductivity as a function of the average pore size (a) and the radiative contribution to the total ETC (b). There is a clear increasing trend with decreasing pore size, explained by the reducing cell wall thickness and the associated reducing cell wall reflectance and transmittance. The WSB samples show a slightly higher radiative conductivity on average, which is probably also caused by the thinner pore walls as was already indicated in Figure 8.1. Nonetheless, even at very small pore sizes, the thermal radiation contribution is fairly limited and stays below 10 % of the total ETC (for the porosity range studied here).

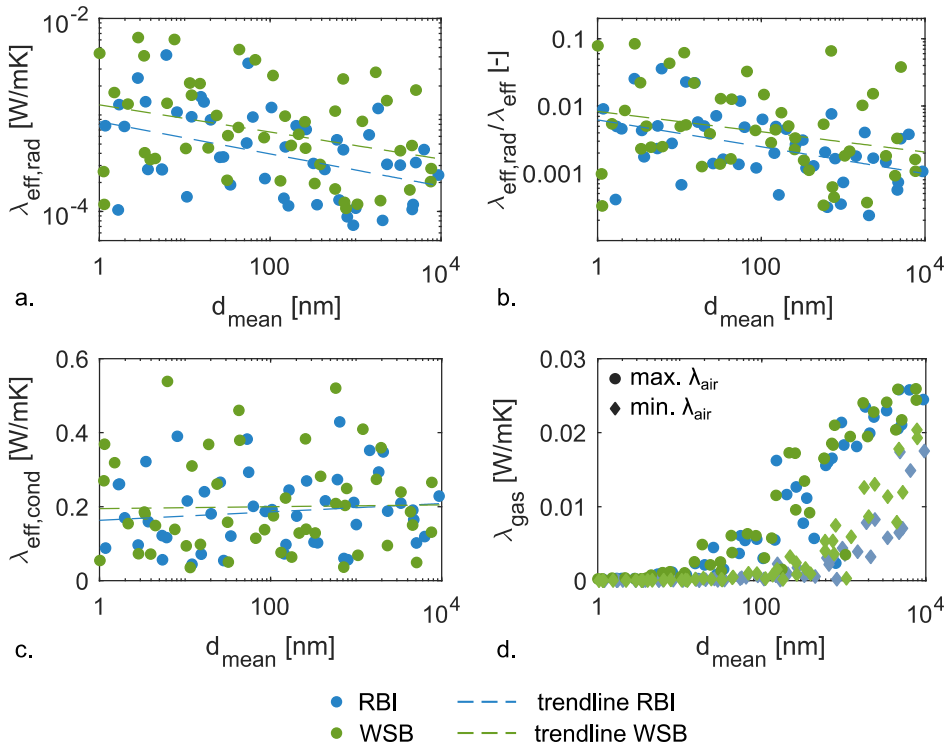


Figure 8.3: Effective radiative conductivity for every sample as a function of the average pore size (a) and its contribution to the total ETC (b). Effective conductive conductivity as a function of the average pore size (c). Maximum and minimum gaseous conductivity in the samples as a function of the average pore size (d).

This increase of the radiative contribution when the average pore size reduces explains the limited obtained reductions of the ETC when reducing the pore size to the nanoscale. However, even without considering thermal radiation, the conduction-only ETC shows a similar rather small reducing effect of the pore size (Figure 8.3c). Even though the gaseous

conductivity decreases significantly (Figure 8.3d), its effect is hardly noticeable due to the wide range of porosities and matrix conductivities studied here.

Linear regression model

To expand these visual observations and conclusions, a linear regression of the predicted ETC is made as a function of the 8 pore structural and physical parameters. A first order model is used, calculating an approximate ETC $\hat{\lambda}_{eff}$ as shown in Eq. (8.1). The product of the matrix conductivity and the porosity is added as an extra term to the regression model since an earlier test with a second order model indicated its significant impact on the predicted ETC.

$$\hat{\lambda}_{eff} = b_0 + \sum_{i=1}^8 b_i * \bar{x}_i + b_9 * \bar{\phi} * \bar{\lambda}_{mat} \quad (8.1)$$

The coefficients b [W/mK] are fitted with the least-squares model to obtain a good predictive regression model. The values \bar{x}_i [-] represent the normalized independent variables (the pore structural and physical parameters), normalized so their values all fall in between 0 and 1. Such normalization allows to compare the obtained coefficients for variables with different units (i.e. the porosity and the matrix conductivity). Hence, the coefficients' magnitudes can be directly compared, showing to which extent the corresponding parameter – on average – influences the ETC in the parameter domain considered. The calculated coefficients are summarized in Table 8.2 together with the p-value of the respective coefficient.

Table 8.2: Obtained coefficients for the regression model for the first order terms and the second order terms. The coefficients with a corresponding p-value below 0.05 are highlighted.

Parameter	RBI		WSB	
	p-value	Coeff. b [W/mK]	p-value	Coeff. b [W/mK]
cte	$< 10^{-3}$	0.059	$< 10^{-3}$	0.085
ϕ	$< 10^{-3}$	-0.057	$< 10^{-3}$	-0.068
$d_{pore,mean}$	$< 10^{-3}$	0.034	$< 10^{-3}$	0.025
$v_{norm, factor}$	0.01	0.016	0.002	-0.011
λ_{mat}	$< 10^{-3}$	0.428	$< 10^{-3}$	0.520
$a_{therm,accomm}$	0.25	0.004	0.08	0.006
n_s	0.92	$-3 * 10^{-4}$	0.85	$-5 * 10^{-4}$
κ_s	0.51	-0.003	0.50	-0.002
T_{avg}	0.17	0.004	0.23	0.003
$\phi * \lambda_{mat}$	$< 10^{-3}$	-0.313	$< 10^{-3}$	-0.433

The porosity, pore size, matrix conductivity and the product term have a very low p-value, indicating that there is significant evidence in the dataset that they influence the resulting ETC. The thermal accommodation coefficient, the complex refractive index and the temperature have higher p-values: although they will have an influence on the ETC (as implemented in the numerical model), it cannot be clearly inferred from the limited studied dataset. The variance factor also has a low p-value, but is again correlated with the porosity.

For both types of samples, the porosity, the matrix conductivity and the product of both clearly have the largest coefficients and thus the largest impact on the ETC (as was already indicated by the plots in Figure 8.2), followed by the average pore size. The other parameters have an even lower impact on the ETC. The regression model allows to quantify the expected average decrease of the ETC: for example, increasing the porosity from 60 % to 85 % reduces the ETC by 0.057 W/mK for RBI samples with a matrix conductivity of 0.2 W/mK, while reducing the pore size from 10 μm to 1 nm reduces the ETC only by 0.034 W/mK. Remember that in Chapter 5, it was determined that decreasing the pore size from 1 mm to 10 μm reduced the ETC only by 0.009 W/mK, indicating that the decrease towards nanopores is more efficient. Nonetheless, increasing the porosity still leads to more improvement, even for materials with a low matrix conductivity.

Normalization of ETC by matrix conductivity

The ETC of every sample normalized by its matrix conductivity is shown in Figure 8.4, once highlighting the impact of the matrix conductivity λ_{mat} (a) and once highlighting the influence of the gaseous conductivity λ_{air} (b). Similarly as in Chapter 5, the ETC of samples with easily conducting matrix are reduced a little bit stronger, although the effect seems much smaller here than it was the case for the samples in Chapter 5. This is probably explained by the expectedly stronger effect of the reducing gaseous conductivity on the ETC of a low matrix conductivity sample. Indeed, Figure 8.4b shows that a lower gaseous conductivity leads to a smaller normalized ETC at equal porosity. Nonetheless, the effect is – as was mentioned before – relatively small.

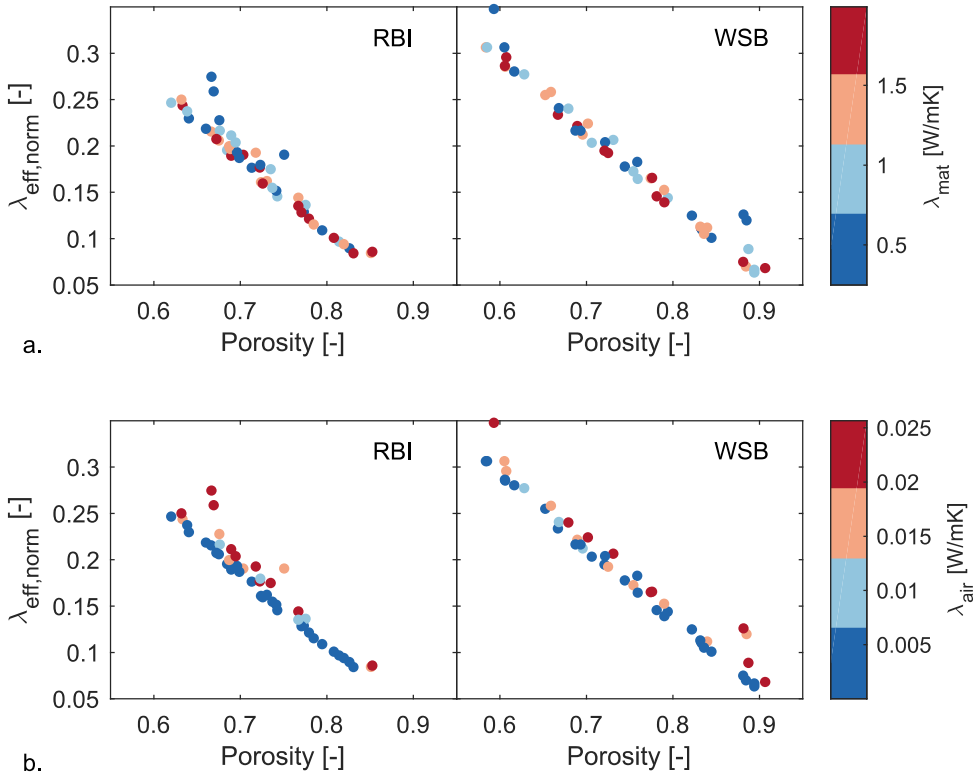


Figure 8.4: ETC normalized by the matrix conductivity as a function of porosity for the RBI and WSB samples, once highlighting the effect of the matrix conductivity (a), and once highlighting the effect of the gaseous conductivity (b).

Lastly, the samples generated by both techniques are compared to each other in Figure 8.5, showing their normalized ETC as a function of the sample's porosity. From the trendlines, it is obvious that the RBI samples perform on average better than the WSB samples, which was also concluded in Chapter 5. It was argued that this is probably explained to the difference in the way heat is conducted through the solid matrix, since the RBI samples also perform better in the low-porosity range. Their different performance is then due to their different type of pore structure: RBI samples have a relatively larger concentration of material in the cell struts compared to the cell walls than WSB samples, which is captured in the strut factor f_s [-]. As argued by Glicksmann & Torpey (1989) and by Coquard & Baillis (2009), a higher strut factor reduces the ETC, explaining the observed performances in Figure 8.5. Nonetheless, the effect is still of only secondary importance compared to the effect of the porosity and the matrix conductivity.

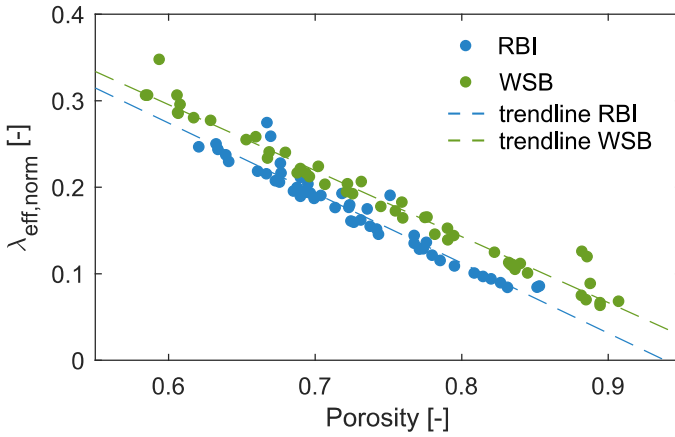


Figure 8.5: Predicted ETC normalized by the matrix conductivity for all samples generated by the RBI and the WSB technique.

8.3. Detailed parameter study

Results from the first parameter study clearly indicate the need to first focus on increasing the porosity and decreasing the matrix conductivity when trying to reduce the ETC of a porous material, while reducing the pore size to the nanoscale has only a small impact given the wide parameter range. The second parameter study zooms in on the region at high porosities and low matrix conductivities, to allow indicating the potential of the pore size and other parameters in that region. Furthermore, a full-factorial sampling of the parameter space is employed to allow a more quantitative interpretation of the obtained reduction of the ETC when varying a certain parameter.

8.3.1. Methodology & setup

The methodology and setup are mostly the same as in the previous parameter study: a set of pore structures is randomly generated and their ETC is predicted with the model framework. The parameter space, sample generation and simulation setup are discussed below.

Parameter space

A full-factorial approach is employed for this second study: every parameter can take two values, where the second value supposedly leads to a reduced ETC. All possible combinations between the parameters are simulated. The studied parameters are the same as in the first parameter study, except for the thermal accommodation coefficient, the temperature and the real and complex part of the refractive index $n_s + i\kappa_s$. The first two have only a minor impact

on the ETC as was demonstrated in the previous study and are set to 0.9 and 10 °C respectively. The real part of the refractive index is rather hard to control in reality and is also kept constant to limit the number of studied cases. A value of 1.5 is chosen so the emissivity of a fully opaque wall would be around 0.9, similar to the set emissivity in the second parameter study in Chapter 5. The studied parameter values are summarized in Table 8.3. Additionally to the pore structure and physical parameters, the random seed to start the random pore structure generation process can also take two different values. This means there are each time two samples with a different pore structure but similar porosity, pore size, variance and other physical properties. The full-factorial sampling of all the properties leads hence to 64 samples with different properties.

Table 8.3: Studies parameters in the second parameter study and their two possible values.

Parameter	Value 1	Value 2
ϕ	0.9	0.95
$d_{pore,mean}$	500 nm	50 nm
$v_{norm,factor}$	0.4	0.04
λ_{mat}	0.5 W/mK	0.2 W/mK
κ_s	0.001	0.1
$seed$	1	2
n_s	1.5	
$a_{therm,accomm}$	0.9	
T_{avg}	10 °C	
p_{gas}	101325 Pa	

Sample generation

Since the porosity, variance and seed values are the same as in Chapter 5 section 5.3, the same pore structures generated back then are used here, rescaling the pore size to the nanoscale. This will allow comparing the results obtained on the nanoscale with the results obtained previously on the microscale. Consequentially, only the WSB technique has been used to generate the pore structures since it allows to reach much higher porosities. Furthermore, the resolution is also increased to 800³ compared to section 8.2, to improve the representation of the thin cell walls at the envisioned high porosities. Generated samples look similar to the ones presented in Figure 5.1.

Simulation setup

The simulation setup is similar to the first parameter study. The ETC of the generated samples is predicted with the numerical framework that was expanded for nanoscale simulations. The finite-element mesh of every sample is constructed with the same mesh size parameters as in the first study, accounting for the increased resolution in this second study. All other needed input parameters are set to the associated values of the full-factorial sampling set of the values in Table 8.3.

8.3.2. Results & discussion

Properties of generated samples

The properties of the generated samples have already been discussed in section 5.3.2 of Chapter 5. The obtained porosity of the samples is, as expected, lower than the targeted porosity, around 87 % and 92 % instead of 90 % and 95 % respectively, due to the WSB algorithm implementation and the finite discretization. The obtained mean pore diameters are now of course in the nanoscale range, and agree very well with the targeted pore diameters. The normalized variance factors of the samples differs again from the targeted one, probably also due to how the generation algorithm generates the pore structure.

Simulated ETC

The predicted ETC of every sample is displayed in Figure 8.6a-e as a function of the different parameters. They show again a significant influence of the porosity and the matrix conductivity, even in the more limited range between 87 % and 92 %. At these high porosities and low matrix conductivities, thermal radiation is expected to have a more important contribution, explaining the strong effect of the absorption coefficient κ_s on the ETC.

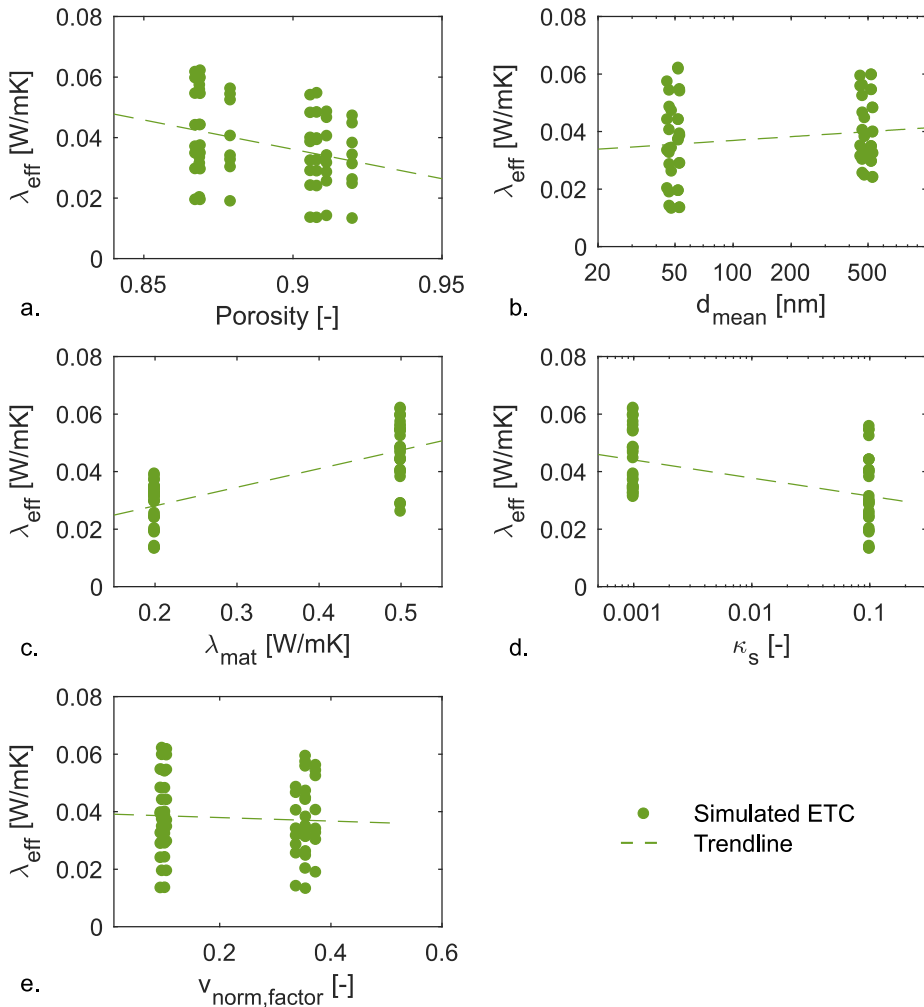


Figure 8.6: Predicted ETC for all samples as a function of the different pore scale parameters.

The effect of reducing the pore size to a few tens of nanometre is also more outspoken at these high porosities/low matrix conductivities, but seems to be still limited. Looking at the separately calculated conduction-only and radiation-only thermal conductivities $\lambda_{eff,cond}$ and $\lambda_{eff,rad}$, it shows how the beneficial effect of a reducing pore size is partially countered by an increasing radiative conductivity (Figure 8.7). A combined decrease of the pore size with an increase of the absorption coefficient will hence lead to the strongest reduction of the ETC.

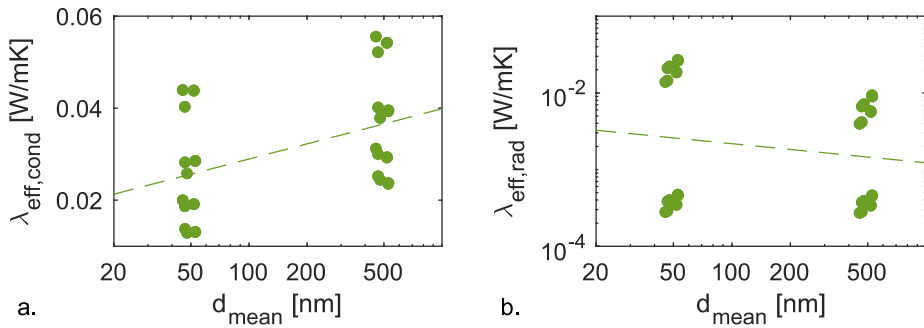


Figure 8.7: Predicted effective conductive (a) and radiative (b) conductivity as a function of the average pore size.

The full-factorial sampling of the parameter space allows to directly quantify the reducing impact of one parameter when all other parameters stay constant. As was defined in Chapter 5, this *reduction potential* RP [-] is calculated for every parameter ‘ x ’, comparing the predicted ETC of the samples whose only difference is their value for the respective parameter ‘ x ’ (Eq. (8.2)).

$$RP_{x:1 \rightarrow 2} = \frac{\lambda_{eff,x=1} - \lambda_{eff,x=2}}{\lambda_{eff,x=1}} \quad (8.2)$$

The obtained RP values for every parameter considering the variation of all other parameters is shown in Figure 8.8. The median value is also indicated. For the impact of the variance, the light-coloured points depict the values of all samples, while the dark points depict results filtered for the correlation between the variance and the porosity.

The matrix conductivity has again a large and obvious reduction potential, reducing the ETC between 25 % to 55 % when reducing from 0.5 W/mK to 0.2 W/mK. Increasing the porosity, on the other hand, can also lead to a strong reduction (up to 40 %), but can also, inversely, cause an increase of the ETC for some samples. Indeed, for samples with a low matrix conductivity, small pore size and low absorption coefficient, the ETC actually increases with about 5 % when increasing the porosity from 87 % to 92 %, due to the increasing contribution of thermal radiation. This indicates the existence of an optimum porosity depending on all the other pore structure and physical parameters, as was already suggested by some authors (Placido, Arduini-Schuster, and Kuhn 2005; Ferkl, Pokorný, and Kosek 2014). The potentially strong impact of thermal radiation for the studied nanoscale materials is also visible in Figure 8.8: increasing the absorption coefficient of the material can lead to more than 65 % reduction

of the ETC, in case of high-porosity low-matrix conductivity samples with an average pore size of 50 nm. Indeed, as expected by the thermal radiation model presented in Chapter 7, thermal radiation will have an increasingly important contribution with thinning cell walls (due to increasing porosities and decreasing pore sizes) and lower absorption coefficients. On the other hand, for the samples with 87 % porosity, a matrix conductivity of 0.2 W/mK and an average pore size of 500 nm, the obtained reduction of the ETC is only 6 % when increasing the absorption coefficient from 0.001 to 0.1. The magnitude of the absorption coefficient also influences the impact of the pore size distribution width.

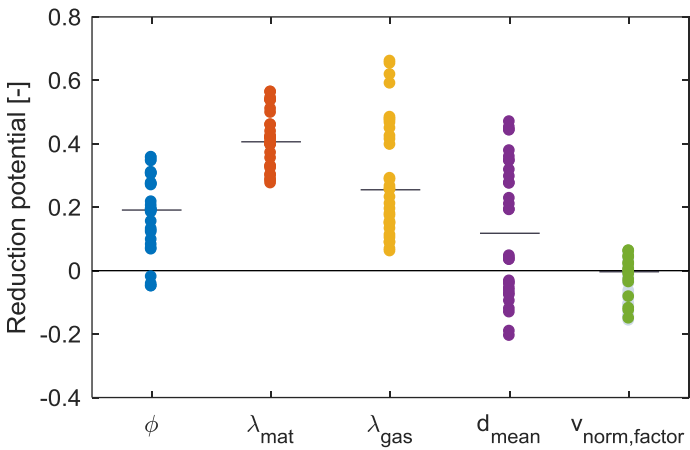


Figure 8.8: Potential relative reduction of the ETC when adapting the respective parameter from value 1 to value 2 as noted in Table 8.3. The horizontal lines denote the median reduction potential per parameter. For the normalized variance factor, the grey dots represent all obtained results, while the green dots represent the results filtered for the correlation with the porosity.

The importance of the thermal radiation also explains the obtained results for the reduction potential of the average pore size: decreasing the pore size from 500 nm to 50 nm can lead to a reduction of the ETC with 50 % (thanks to the reducing gaseous conductivity), but also to an increase of the ETC with 20 % (due to the increasing thermal radiation through the thinning cell walls). Examining the results show that all samples with an absorption coefficient of 0.001 have an *RP* between -20 % and 5 %, showing that reducing the pore size further to the nanoscale has probably a negative effect for materials consisting of low-absorbing solids. This can also be concluded from Figure 8.9, where the calculated ETC values are plotted as a function of the average pore size. The graph is complemented with the results from the parameter study in section 5.3, where indeed, the same porosity, matrix conductivity and pore size distribution width values have been used, but average pore sizes in the micrometre range.

Furthermore, the refractive index of 1.5 adopted in the current parameter study results in an emissivity of 0.9, which is the value adopted for the opaque cell walls in the mentioned parameter study of section 5.3.

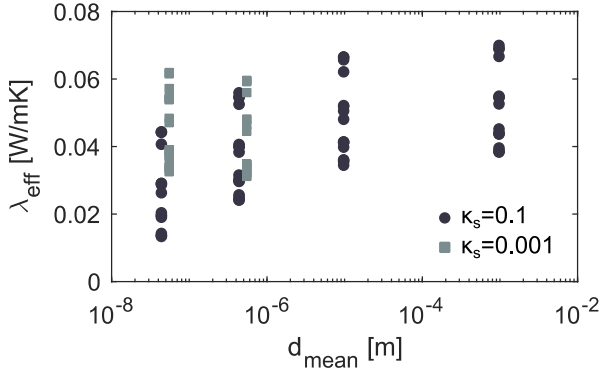


Figure 8.9: Predicted ETC as a function of the average pore size for the samples studied in section 8.3 with nanoscale pores and the similar samples in section 5.3 with microscale pores.

Figure 8.9 shows how for low-absorbing materials an optimal pore size exists, below which the ETC increases again. Reducing the pore size from the millimeter to the nanometer range should hence only be performed for materials with good absorptive properties regarding thermal radiation.

Reducing the pore size distribution width can, according to Figure 8.8, either reduce the ETC ($RP > 0$) or increase the ETC ($RP < 0$). Closer analysis shows that this depends on the magnitude of the absorption coefficient κ_s : when κ_s is large (in casu: 0.1), the ETC decreases for more narrow pore size distributions. This is explained by the presence of larger pores in wider distributions in which the gaseous conductivity is not reduced as much. Inversely, when κ_s is low, the ETC increases with reducing pore size distribution width. The much more relevant contribution of thermal radiation at such low absorption coefficient is probably less suppressed by a narrow pore size distribution. Even so, the impact of the pore size distribution width remains relatively small compared to the other parameters.

Lastly, Figure 8.9 shows a large spread in ETC values at every average pore size, indicating it might still be better to just increase the porosity and decrease the matrix conductivity instead of reducing the pore size to the nanoscale. These results hence underline once more how the reduction potential of the pore scale parameters heavily depend on each other and the

importance of taking into account all the relevant pore scale parameters and heat transfer mechanisms.

8.4. Conclusions

In this chapter, two parameter studies have been performed to analyse the additional benefit of reducing the pore size to the nanoscale. The first parameter study investigated the ETC of 100 different pore structures with the developed numerical framework. Results indicate that – for the wide range of parameter values considered – the porosity and the matrix conductivity are still by far the most important parameters, as was also the case for the samples without nanoscale characteristics studied in Chapter 5. The effect of a decreasing pore size has only a secondary decreasing effect on the ETC, similarly as the thermal accommodation coefficient, the complex refractive index and the average temperature. Additionally, it was also shown that an RBI type of pore structure performs on average slightly better than a WSB type of pore structure, which was explained by the higher strut factor for RBI samples.

The second parameter study zooms in on the high-porosity low-matrix-conductivity parameter region. 64 pore structures are randomly generated with a full-factorial sampling of the parameter space. The reduction potential of every parameter is assessed by comparing the predicted ETC for two samples with the same properties except for the respective parameter. Results indicated a larger impact of the pore size, possible reducing the ETC with over 50 % when reducing the pore size from 0.5 μm to 50 nm. On the other hand, for low-absorbing materials, such pore size reduction could actually have a negative impact and increase the ETC instead of providing the envisioned reduction. Similar conclusions observations are made for the impact of the porosity, due to the important contribution of thermal radiation at these high porosities and low matrix conductivities. Increasing the absorption coefficient of the matrix is shown to have the largest potential impact in the considered parameter value range.

In conclusion, priority should always be given to reducing the matrix conductivity and – depending on the contribution of thermal radiation – to increasing the porosity, when attempting to reduce the ETC. When both parameters have been optimized and a high radiation absorption coefficient is present, reducing the pore size can induce a desired optimization of the ETC. Lastly, both studies show how the developed model can be applied in future studies to identify such optimum combination of parameters in presence of certain restrictions (like maximum porosity etc.).

Conclusions & future work

9.1. CONCLUSIONS	209
9.2. FUTURE WORK.....	213

9.1. Conclusions

This thesis targets the numerical prediction of the ETC of porous building blocks, to improve the understanding of the relation between the ETC and the pore scale parameters. In the first part, the work focused on the more conventional porous building blocks with pore sizes in the micrometre to millimetre range. The second part expanded on this work to include the impact of nanoscale pore sizes and/or low gas pressures on the resulting ETC.

The work started with a survey on the variety of analytical and numerical models proposed in the literature to predict the ETC based on the pore structure. 3D numerical modelling showed the most potential to truly include all the relevant pore structure properties. Simulations on virtually generated pore structures and actual pore structures obtained via imaging techniques showed interesting possibilities. Efforts so far had mainly emphasised other types of materials than porous building blocks, or did neglect certain heat transfer mechanisms. Moreover, most studies focussed on the impact of one or a few parameters, clouding their combined impacts on the ETC and the optimal routes to improved porous building blocks.

Inspired by the literature survey, a novel numerical framework has been developed. The model uses 3D voxel images to represent virtual or actual pore structures, and finite elements to simulate the heat transfer at the pore scale. The conductive heat transfer mechanisms are modelled with Fourier's conduction law, assigning the respective thermal conductivities to the matrix phase and the pore space. The predicted conductive heat transfer through the material agrees very well with analytical and numerical reference results for regular arrays of spherical pores, verifying the correct implementation. Radiation heat transfer is similarly implemented in the model as a conductive process by calculating local equivalent radiative conductivities

for every pore (cluster) in the pore space. The calculation procedure is based on Loeb's original method, comprising a large amount of detailed radiation simulations in 2D and 3D pores with different sizes, shapes, orientations and emissivities. This has resulted in the development of a new analytical equation encompassing a newly defined directional shape factor to better account for the effect of the shape of the pore on the pore scale radiative conductivity. The predicted contribution of thermal radiation to the total ETC agrees very well with detailed simulations on 2D pore structures. Comparison with simulations on a 3D pore structure indicated larger discrepancies, but still a correct order of magnitude. In cases where thermal radiation is not the major mode of heat transport through the material, the implemented methodology should suffice to properly account for its contribution. The developed model and the used implementation methodology shows how to perform pore scale heat transfer simulations including all relevant heat transfer mechanisms with a reasonable amount of computation cost. Furthermore, the freedom regarding the pore structure geometry imposes no restrictions towards the types of porous building blocks able to be studied.

To validate the model framework, a new Heat Flow Meter apparatus has been designed and implemented, facilitating measurements of small samples under special conditions. The setup was used in a validation exercise with three different porous materials: a sintered glass filter, a Reapor acoustic block and a cellular glass, wherein the model framework was used to predict their ETC based on μ CT images of their actual pore structure. Discrepancies on the order of 10 % with the experimental outcomes are obtained when the simulated pore structure has a porosity similar to the actual porosity. These results validate the model's performance for predicting the ETC based on the pore structure. The outcomes underline the importance of high-quality images of the actual pore structure, to ensure the correspondence between the simulated and actual pore structure and to thus improve the accuracy of the predicted ETC. This equally emphasises the need for further development of imaging techniques and image processing algorithms to allow the use of the model as a characterization tool for real porous materials. The simulations on the sintered glass filter additionally revealed a significant impact of the image resolution on the predicted ETC. Lastly, the influence of the average temperature on the ETC was also accurately predicted for the cellular glass sample. Results showed that thermal radiation has a relatively low influence around room temperature in such materials with high matrix conductivity. These validation exercises constitute the largest validation efforts performed so far in literature for such pore scale heat transfer simulations, both regarding the diversity of pore structures studied and the true representation of their pore

structure using μ CT scanning. It demonstrates furthermore the predictive potential of pore scale heat transfer simulations and the possibility to use such framework for detailed studies on the impact of the pore scale parameters on the ETC.

The framework was finally applied in a first optimization study for porous building blocks with pore sizes from a few micrometres to a few millimetres. Two parameter studies were performed. In the first study, 100 pore structures were virtually generated with two different generation algorithms and with varying pore scale and physical parameters, and the ETC of each sample was predicted with the framework. Results indicated that the porosity and the matrix conductivity are by far the most important parameters and should hence always be the primary target of optimization efforts. Besides these parameters, the type of pore structure has an important secondary impact: pore structures with spherical pores perform on average better than foam-like pore structures, which is probably explained by the higher strut factor of the pore structures with spherical pores. On the other hand, foam-like pore structures can more easily reach high porosities, explaining their typical use in high performance insulations. The variations of all other parameters like pore size, wall emissivity, ... revealed only minor impacts on the ETC. The second parameter study zoomed in on the high-porosity low-matrix-conductivity region to further quantify the impact of the secondary parameters in that zone. It showed that the gaseous conductivity can have a large impact in such case, potentially reducing the ETC with 60 % when replacing air with xenon gas. Similarly but to a lesser extent, decreasing the pore size from 1 mm to 10 μ m can lead to a reduction of about 27 % in the optimal case. The results also show that the obtained reduction depends strongly on the other parameters. As such, the results from both parameter studies contribute to a more quantitative characterization of the combined impact of certain pore scale parameters, over the wide range of values encountered in typical porous building blocks.

The second part of this thesis started with introducing the fundamentals of the heat transfer physics and why their macroscopic description fails at the nanoscale. Different modelling strategies for such nanoscale heat transfer in porous materials were surveyed. Most studies so far focussed on aerogel materials though, clouding the potential benefits for cellular materials, certainly in combination with other varying pore scale properties.

Expanding on the work performed in the first part, it was decided to adapt the already developed model framework by modelling the different heat transfer mechanisms again as conductive processes. A novel calculation methodology to derive the local gaseous

conductivity in every pore based on its size, shape and thermal accommodation coefficient was derived using the analogy with thermal radiation. The new procedure showed very good agreement with experimental and numerical characterization of the gaseous conductivity in the presence of nanoscale effects detailed in literature. Regarding solid conduction, it was argued that a relatively low impact of the domain size on the solid conductivity is suspected for the studied amorphous and poly-crystalline materials. This, together with the current complexity of accurately predicting the size effect on this mechanism, led to the decision to keep the solid thermal conductivity as an a-priori defined parameter. Thermal radiation, finally, was modelled on a macroscopic level, because the increasing transmission through the thinning pore walls invalidates the earlier pore-wall-to-pore-wall approach. An analytical model found in literature was employed taking into account the thin film interference effect occurring in thin pore walls. As such, the model framework allows to perform detailed simulations on the pore scale heat transfer in the presence of nanoscale features, while considering the true pore structure.

The expanded model framework was validated by comparing predictions of the ETC of virtually generated nanocellular foams with experimental outcomes found in literature. For high-porosity foams, excellent agreement was obtained with deviations on the order of 5%. This validated the implementation of the gaseous conductivity model and the thermal radiation model. For the low-porosity foams the predicted values underestimated the experimental outcomes significantly. However, it was argued that the experimental values were unexpectedly high given the porosity and matrix conductivity specified by the authors. It was argued that the tested samples were either very thin – increasing the thermal radiation – or that the polymer's matrix conductivity had increased during the foaming process. Assuming a higher, literature-based thermal conductivity for the polymer during the simulations, a much better agreement was obtained with discrepancies again on the order of 5%. This validation exercise demonstrates furthermore the viability of such pore scale heat transfer simulations on random pore structures in the presence of nanoscale features.

Finally, the model framework was applied to extend the optimization study performed in the first part. The same 100 pore structures generated before were used, rescaling them to obtain average pore sizes in the nanoscale range. Results indicated again the major influence of the porosity and the matrix conductivity on the ETC. The nanoscale pore sizes reduced the gaseous conductivity inside the pores significantly, but the overall impact on the ETC was relatively small given the large porosity and matrix conductivity range assumed for the study.

A second parameter study therefore zoomed in on the region of high porosities and low matrix conductivities. In that region, decreasing the pore size to 50 nm could indeed lead to a reduction of the ETC with about XX% However, results also demonstrated the existence of optimal porosities and pore sizes due to the increasing contribution of thermal radiation. A combined increase of the absorption coefficient of the solid material is therefore primordial to fully enjoy the potential of nanoscale pore sizes. Furthermore, results again showed how the impact of the different pore scale parameters are highly interdependent. For specific optimization cases, the developed framework can thus be of great help in identifying the optimal routes towards reduced ETC's.

Summarizing, the work in this thesis has led to the development and validation of a comprehensive framework accounting for all relevant heat transfer mechanisms in typical porous building blocks. Furthermore, the framework is designed for maximum freedom regarding the input geometry, imposing no prerequisites regarding the pore structure morphology and allowing application for the wide range of pore structures encountered in building blocks. Subsequently, the framework has been applied in some large-scale parameter studies to study the impact of the pore scale parameters, covering the full range of values typically encountered. Lastly, the development, validation and application of the framework have been performed for both microscale and nanoscale pore sizes, contributing to the versatility of the framework and the generality of the conclusions made regarding the impact of the pore scale parameters.

9.2. Future work

Based on the work performed in this study, several improvements and future developments can be formulated.

9.2.1. Framework workflow improvement

The current framework has been implemented for robust operation, wherever possible trying to be computationally efficient as well. However, the whole procedure for generating, meshing and simulating a single pore structure currently takes about 6 hours depending on the type of pore structure and discretization settings. This computation time is mainly spent during the image generation, the preprocessing and the meshing part. It is without question that some of the implemented algorithms can still be optimized. Furthermore, other meshing algorithms allowing for parallel operation can be envisioned to improve the efficiency of the framework. This in turn can facilitate the model's use for large parameter studies.

9.2.2. Representation of the pore structure

An adequate representation of the pore structure has been shown to be primordial to obtain simulated ETC values close to the actual ones. Current imaging techniques like μ CT scanning are already able to obtain good images of the pore structure, but a smaller voxel size is needed to properly visualize pore structures whose pore walls are only a few micron thick (i.e. the cellular glass). Additionally, segmentation techniques, differentiating the matrix and the pore space voxels, need to improve as well to leave less doubt on the validity of the obtained pore structure.

Concurrently, new virtual generation techniques for random generation of pore structures are to be developed. Current algorithms indeed not always produced the pore structure initially envisioned. Hence, new techniques should focus on producing pore structures with controlled porosity, average pore size and pore size distribution. Furthermore, techniques should aim at the generation of different types of pore structures, with different shapes of pores and different matrix morphologies.

The work presented in this study has mainly focussed on pore structures with a monomodal pore size distribution, with the exception of the Reapor material. However, cellular concrete often shows pore size distributions spanning multiple orders of magnitude, from nanometre to millimetre. Currently, only a hierarchical approach has been tested to predict the ETC in case of multimodal pore structures (for the Reapor material). However, other techniques have been presented in literature to deal with such multimodal pore structures, like the multiscale finite element technique. More research towards such multiscale modelling techniques is needed to properly model the heat transfer in the case of multimodal pore structures.

Finally, the pore structures used for the simulations on the nanocellular foams were virtually generated as no actual material samples were available. Furthermore, even in case they were, obtaining an accurate 3D representation of such a nanoscale pore structure is still a daunting task, requiring voxel sizes of a few nanometre. Some efforts towards this have been made using the FIB-SEM technique, but more research is needed to easily apply such novel techniques for the characterization of nanoporous materials.

9.2.3. Improved physical modelling

For conventional high-porosity materials, the current implementation of thermal radiation shows an underestimation of the radiative contribution to the ETC. Although reasonable for the studied porous building blocks, a more detailed implementation as noted in the literature

survey is opportune to increase the model's accuracy for high-porosity materials, certainly for the case of semi-transparent pore walls.

Similarly, the nanoscale effect on solid conduction is currently not implemented in the model. A detailed implementation should account for the type of atomic structure and the expected anisotropy in the solid phase. Such detailed modelling was deemed not worth the cost at this point, but all future improvements of simulation algorithms and computational power could facilitate its implementation, allowing to reduce the uncertainty regarding its contribution.

Lastly, the framework has so far been aimed at completely dry materials containing only a gaseous phase inside the pores. In reality, porous building materials are typically subjected to moisture loads as well. The high thermal conductivity of water and the moisture transport through the pore structure can significantly impact the ETC. Future investigations on the combined pore scale hygrothermal behaviour can shed light on this effect

9.2.4. Application of the model in new parameter studies

The parameter studies performed in Chapter 5 and Chapter 8 indicated the general and more detailed effect of several pore scale parameters. The performed studies were limited to monomodal pore structures with one type of pore shape though. Recently, architected cellular materials are increasingly being researched, allowing for practically pore scale design of the pore space and more exotic pore structures. In light of these developments, the model framework can be used to study the effect of other types of pore structures, with for example ellipsoid shaped pores (aligned or randomly oriented), multimodal pore structures (using the hierarchical approach employed in Chapter 4), etc. Equally, the effect on the ETC of filling part of the pore space with phase-change materials (to increase the heat capacity of the porous material) can be studied with the presented framework. Lastly, application of the model in a concrete optimization study for one specific material can also lead to additional insights: specific operations could be done to virtually alter the existing pore structure (i.e. filling the smallest/largest pores, eroding the matrix, opening the cell walls between pores, ...) and predict each time the effect on the ETC without the need for actually creating the envisioned material.

Analytical model for macroscopic radiative conductivity considering transmission and interference

A.1. Introduction

In this thesis the model proposed by G. Wang, Wang et al. (2017) is used to predict the macroscopic radiative conductivity of porous materials where significant transmission and interference effects can occur. The original paper by G. Wang, Wang et al. (2017) includes a lot of errors though, both in the presented equations as in the numerical solution used to discuss the impact of several parameters on the radiative conductivity. A correction was urged by the author and the promotor of this work and is published in G. Wang et al. (2018). However, both published papers don't permit for a direct and straight-forward implementation of the proposed model due to overly complex notations and leaving out crucial equations and assumptions. Therefore, the complete model is detailed below.

A.2. Model overview

In Part I, thermal radiation was taken into account through Loeb's method: a radiative conductivity is calculated in every pore to simulate the surface-to-surface radiation. With reducing pore size, the matrix cell wall thickness will reduce as well. Below a certain thickness, thermal radiation will travel partially through the cell wall as was already discussed in the introduction to the expansion of Loeb's method using Bouguer's law (Chapter 3). Thus, the surface-to-surface model is expectedly not valid for nano-porous cellular materials and might underestimate the contribution of thermal radiation to the total heat transfer.

Chapter 2 discussed several modelling strategies to deal with thermal radiation in porous media that consist of semi-transparent cell walls. These range from simple analytical solutions to detailed simulations of the local coupled conduction and thermal radiation in a multiphase manner (see Chapter 2). Here, the analytical approach proposed by Wang et al. (Wang et al., 2018; Wang et al., 2017a) is adopted because it shows very good agreement with

experimentally measured data. They propose to calculate an effective radiative conductivity for the whole porous sample based on the pore structure parameters and sum the obtained value with the sample’s conduction-only effective conductivity (Eq. (97)). The conduction-only conductivity is obtained with the numerical framework taking into account the nanoscale effect on the gaseous conduction.

$$\lambda_{eff} = \lambda_{cond,eff} + \lambda_{rad,eff} \tag{97}$$

Wang’s radiative conductivity calculation method is based on the model proposed by De Micco & Aldao (2006) for radiation through a set of parallel plates (discussed in Chapter 2), but assumes a different more realistic pore structure and takes into account the thin-film-interference effect. To come to an analytical expression for the effective radiative conductivity, Wang et al. (2017) simplified the pore structure as a set of cubic pores ordered in a simple cubic manner (Figure 84). The matrix hence consists of three orthogonal slabs, two parallel and one perpendicular to the general heat transfer direction. Thermal radiation will interact with the cell walls by reflection, transmission and absorption. Since the roughness of the cell walls is relatively small compared to the wavelength of the thermal radiation (~10 μm at room temperature), all reflection is assumed to be specular.

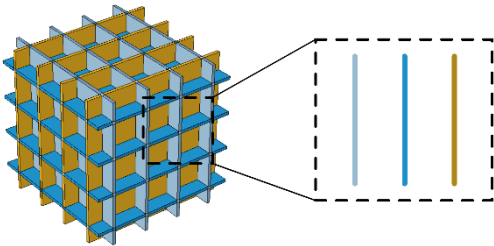


Figure 84: Assumed pore structure and unit cell in thermal radiation model of Wang et al. (2017,2018)

The matrix walls that are parallel to the direction of general heat flow will hence only contribute to the attenuation of the radiation by absorption, since the specular reflection will not change the component of the wave’s direction parallel to the general heat transfer direction. The cell walls perpendicular to the heat flow will attenuate the radiation both by absorption and reflection. Hence, Wang et al. (2017) simplified such a unit cell as three pore walls parallel to each other, all three absorbing equally the thermal radiation while only the first reflects thermal radiation. Similar to De Micco and Aldao (2006), they showed that the effective radiative conductivity for a material with such pore structure can be calculated as in

Eq. (98), with T_{net}^{unit} [-] the net transmittance of the unit cell, d_{sample} [m] the sample thickness, d_{pore} [m] the pore diameter and d_{wall} [m] the cell wall thickness.

$$\lambda_{rad,eff} = \frac{4 * \sigma_{SB} * T_{avg}^3 * d_{sample}}{1 + \frac{d_{sample}}{d_{pore} + d_{wall}} * \left(\frac{1}{T_{net}^{unit}} - 1 \right)} \quad (98)$$

The net transmittance of the unit cell is defined as the part of the radiation incident on the unit cell reaching the other side of the unit cell due to partial transmission plus re-emission of the absorbed radiation. Wang et al. showed that for the unit cell shown in Figure 84, the net transmittance is a function of each cell wall's hemispherical total reflectance \bar{R}_f [-] and transmittance \bar{T}_f [-] (Eq. (99)).

$$T_{net}^{unit} = \frac{(1 + \bar{T}_f - \bar{R}_f) * (\bar{T}_f + \bar{R}_f)}{2 - (1 - \bar{T}_f + \bar{R}_f) * (1 - \bar{T}_f - \bar{R}_f)} \quad (99)$$

Wang et al. (2017) described the formulae to calculate these total hemispherical properties based on the Fresnel formulae and the refractive indices of the gaseous and solid phase. However, some mathematical and typographic errors were made in the original work. Therefore, the formulae are described here in full extent, as was also (partially) done in a correction paper initiated by the author of this thesis (Wang et al. 2018).

The total hemispherical reflectance of one cell wall is defined as the ratio of reflected versus incident radiation energy coming from all directions and for all wavelengths (Eq. (100)). The fluxes can be written as integrals over all wavelengths and solid angles of the incident and reflected directional spectral intensities $I_\lambda(\lambda, T, \Omega)$ [$W/(m^2 \cdot sr \cdot \mu m)$], with $R_f(\lambda, \Omega)$ [-] the directional spectral reflectance of the cell wall. Assuming the cell wall is irradiated by a diffuse blackbody intensity at temperature T , the directional spectral intensity can be expressed by Planck's law. In Eq. (100), it is convenient to change the infinitesimal solid angle $d\Omega$ using spherical coordinates as $\sin(\theta) * d\theta * d\phi$, with θ the zenith and ϕ the azimuth angle. θ_1 is the zenith angle of the incident radiation.

$$\bar{R}_f = \frac{I_{hem,tot,refl}}{I_{hem,tot,inci}} = \frac{\int_{\lambda_{min}}^{\lambda_{max}} \int_{\Omega=0}^{2\pi} R_f(\lambda, \Omega) * I_\lambda(\lambda, T, \Omega) * d\Omega * \cos(\theta_1) dA * d\lambda}{\int_{\lambda_{min}}^{\lambda_{max}} \int_{\Omega=0}^{2\pi} I_\lambda(\lambda, T, \Omega) * d\Omega * \cos(\theta_1) dA * d\lambda} \quad (100)$$

Assuming azimuthal symmetry, Eq. (100) simplifies to Eq. (101). A similar deduction can be made for the total hemispherical transmittance (Eq. (102)), with $T_f(\lambda, \theta_1, \phi)$ [-] the spectral directional transmittance of the cell wall.

$$\bar{R}_f = \frac{\int_{\lambda_{min}}^{\lambda_{max}} \int_{\theta_1=0}^{\pi/2} R_f(\lambda, \theta_1, \phi) * I_\lambda(\lambda, T, \Omega) * 2\pi * \sin(\theta_1) * \cos(\theta_1) * d\theta_1 * d\lambda}{\int_{\lambda_{min}}^{\lambda_{max}} \pi * I_\lambda(\lambda, T, \Omega) * d\lambda} \quad (101)$$

$$\bar{T}_f = \frac{\int_{\lambda_{min}}^{\lambda_{max}} \int_{\theta_1=0}^{\pi/2} T_f(\lambda, \theta_1, \phi) * I_\lambda(\lambda, T, \Omega) * 2\pi * \sin(\theta_1) * \cos(\theta_1) * d\theta_1 * d\lambda}{\int_{\lambda_{min}}^{\lambda_{max}} \pi * I_\lambda(\lambda, T, \Omega) * d\lambda} \quad (102)$$

Calculating the spectral directional properties requires taking into account the wave nature of the thermal radiation. Firstly, the spectral directional reflectance and transmittance depend on the polarization of the electromagnetic waves (perpendicular or parallel to the plane of incidence). Assuming that the polarization of the electromagnetic waves is randomly distributed, the total transmittance and reflectance are simply the average of values at both polarizations (Eq. (103) & (104))

$$R_f(\lambda, \theta_1, \phi) = \frac{R_{f,\perp}(\lambda, \theta_1, \phi) + R_{f,\parallel}(\lambda, \theta_1, \phi)}{2} \quad (103)$$

$$T_f(\lambda, \theta_1, \phi) = \frac{T_{f,\perp}(\lambda, \theta_1, \phi) + T_{f,\parallel}(\lambda, \theta_1, \phi)}{2} \quad (104)$$

The directional spectral reflectance at a certain polarization is defined as the square of the absolute value of the reflection coefficient for the electromagnetic wave (Eq. (105) for perpendicular polarization, similar equations for parallel not shown). The transmittance through a cell wall surrounded by two identical phases (the gas) is defined as in Eq. (106) (a factor different from 1 should be added in the case of non-identical phases).

$$R_{f,\perp}(\lambda, \theta_1, \phi) = |r_\perp|^2 \quad (105)$$

$$T_{f,\perp}(\lambda, \theta_1, \phi) = |t_\perp|^2 \quad (106)$$

The cell wall's reflection and transmission coefficient r and t for both polarizations can be derived with the Fresnel formulae for interaction of electromagnetic waves with thin films (Born and Wolf 2003). They depend on the reflection and transmission happening at both interfaces of the cell wall with the gas phase (illustrated in Figure 85) and the thickness of the cell wall d_{wall} [m].

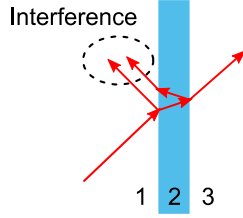


Figure 85: Illustration of transmission and reflection through thin film with potential interference of waves reflecting from both interfaces of the thin film.

For the perpendicular coefficients, the formulae are given in Eq. (107) and (108). The formulae for the parallel polarization are similar and not repeated here. The formulas inherently account for the potential interference effects due to reflections and phase changes at both interfaces of the cell wall. Indeed, at specific cell wall thicknesses, a radiation wave reflected from the second interface can interact destructively with the waves reflected at the first interface, reducing the reflectance and increasing the transmittance. Similarly, constructive interference will increase the reflectance and reduce the transmittance.

$$r_{\perp} = \frac{r_{12,\perp} + r_{23,\perp} * e^{2*i*\frac{2*\pi}{\lambda}*\hat{n}_2*\cos(\theta_2)*d_{wall}}}{1 + r_{12,\perp} * r_{23,\perp} * e^{2*i*\frac{2*\pi}{\lambda}*\hat{n}_2*\cos(\theta_2)*d_{wall}}} \quad (107)$$

$$t_{\perp} = \frac{t_{12,\perp} * t_{23,\perp} * e^{i*\frac{2*\pi}{\lambda}*\hat{n}_2*\cos(\theta_2)*d_{wall}}}{1 + r_{12,\perp} * r_{23,\perp} * e^{2*i*\frac{2*\pi}{\lambda}*\hat{n}_2*\cos(\theta_2)*d_{wall}}} \quad (108)$$

The interface reflection and transmission coefficients r_{ij} and t_{ij} depend on the refractive index of the gas ($n_1 = n_3$) and the complex refractive index of the matrix phase in the cell wall ($\hat{n}_2 = n_2 + i\kappa_2$), where κ_2 is the absorption coefficient of the solid material. The coefficients also depend on the polarization of the incident wave and are given in Eq. (109) to Eq. (112).

$$r_{12,\perp} = \frac{n_1 * \cos(\theta_1) - \hat{n}_2 * \cos(\theta_2)}{n_1 * \cos(\theta_1) + \hat{n}_2 * \cos(\theta_2)} \quad (109)$$

$$t_{12,\perp} = \frac{2 * n_1 * \cos(\theta_1)}{n_1 * \cos(\theta_1) + \hat{n}_2 * \cos(\theta_2)} \quad (110)$$

$$r_{12,\parallel} = \frac{\frac{1}{n_1} * \cos(\theta_1) - \frac{1}{\hat{n}_2} * \cos(\theta_2)}{\frac{1}{n_1} * \cos(\theta_1) + \frac{1}{\hat{n}_2} * \cos(\theta_2)} \quad (111)$$

$$t_{12,\parallel} = \frac{\frac{2}{n_1} * \cos(\theta_1)}{\frac{1}{n_1} * \cos(\theta_1) + \frac{1}{\hat{n}_2} * \cos(\theta_2)} \quad (112)$$

The angle θ_2 can be calculated with Snell's law (Eq. (113)). For the reflection coefficients and transmission coefficients at the second interface (2-3), the formulas are equivalent to Eq. (109) to Eq. (112) and are not repeated here.

$$n_1 * \sin(\theta_1) = \hat{n}_2 * \sin(\theta_2) \quad (113)$$

With the previous presented equations, the total hemispherical reflectance and transmittance of every cell wall can be calculated, which are combined in Eq. (99) to give the net transmittance of a unit cell of the pore structure shown in Figure 84. This allows to calculate finally the effective radiative conductivity with Eq. (98), taking into account the transmission through and absorption in the cell walls and possible interference effects. The radiative conductivity hence depends on the following parameters: solid matrix' complex refractive index $n + i\kappa$, cell wall thickness d_{wall} , temperature T , pore size d_{pore} and sample thickness d_{sample} . Figure 86 shows the total hemispherical reflectance and transmittance for a cell wall as function of its thickness for different absorption coefficients κ_{solid} , at a temperature of 293.15 K and with the real part of the refractive index 1.5 or 2. For thick cell walls, the reflectance is constant and equals the reflectivity (which is indeed for a lot of materials on the order of 0.1). With decreasing thickness, the reflectance first increases due to constructive interference of waves reflecting from both interfaces of the cell wall. It reaches a maximum, after which it decreases again towards zero because an increasingly large part of the radiation spectrum starts to experience destructive interference. In the case of no absorption ($\kappa_{solid} = 0$), the transmittance equals one minus the reflectance, explaining the behaviour shown in Figure 86b. In case of absorption in the cell wall, the transmittance decreases with increasing thickness as is also expected from Bouguer's law, although the interference effects cause some bumps in the course. It is thus clear from both graphs in Figure 86 that the interference effects affect the reflectance, transmittance and absorbance significantly and should be taken into account in the radiative heat transfer.

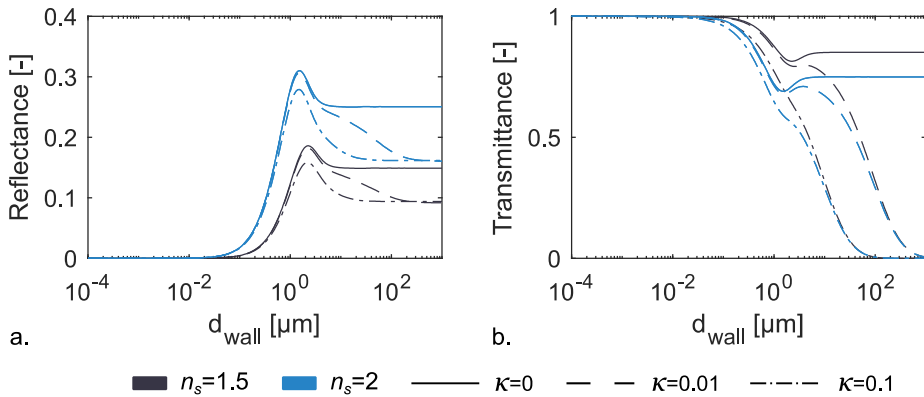


Figure 86: Hemispherical total reflectance (a) and hemispherical total transmittance of a cell wall for different absorption coefficients κ_{solid} at 293.15 K and a refractive index n of 1.5 and 2 as a function of cell wall thickness d_{wall} .

Figure 87 shows the effective radiative conductivity for a sample with constant porosity of 90 % and thickness of 5 cm (the pore size is related to the cell wall thickness, given the cubic pore structure and a constant porosity). As can be seen, even when the solid material doesn't absorb radiation ($\kappa = 0$), the thermal radiation is still partially extinct in the sample due to reflections at the cell wall interfaces. With decreasing pore size, the radiative conductivity first decreases because of an increasing amount of cells and cell walls reflecting the thermal radiation. This was also predicted the expanded Loeb methodology, through the reducing mean distance of the pores. After reaching a certain minimum, the conductivity increases again due to the decreasing reflectance of the thin cell walls as was shown in Figure 86a. In case the solid material absorbs radiation, the conductivity shows the same behaviour, increasing till a value where radiation extinction is solely due to absorption in the cell walls.

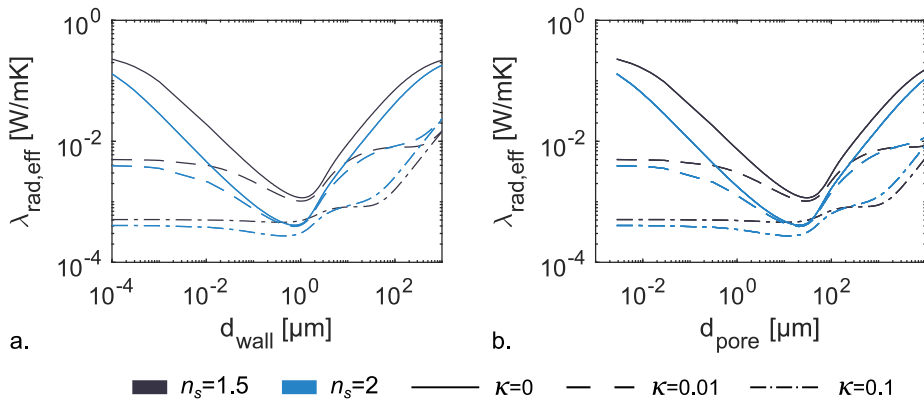


Figure 87: effective radiative conductivity for a sample of 5 cm thick and 90 % porosity, for different absorption coefficients κ_{solid} at 293.15 K and a refractive index n of 1.5 and 2 as a function of cell wall thickness d_{wall} (a) and pore size d_{pore} (b).

Wang et al. (2017a) validated the presented analytical calculation of the effective radiative conductivity with literature data on XPS foams. Good agreement was obtained in predicting the radiative component, with relative deviations below 10 %.

Curriculum Vitae

Personal information

Wouter Van De Walle
14/10/1991
Belgian
Kasteelstraat 28
3370 Roosbeek, Belgium
wouter.vandewalle@outlook.com

Research position

2014 – 2019 **Ph.D. student at Building Physics Section, Department of Civil Engineering, KU Leuven**
Thesis (promotor prof. Hans Janssen): *'Prediction of the effective thermal conductivity of porous building blocks based on their pore structure'*.

Education

2012 – 2014 **KU Leuven: Master of Engineering: Civil Engineering**
Masterthesis (promotor prof. Hans Janssen): *'Analysis of numerical solution techniques for hygrothermal building simulations'*.

2009 – 2012 **KU Leuven: Bachelor of Engineering Science (major in Civil Engineering)**

Awards & Grants

16-17 & 17-18 **Gouden Krijtje**: best teaching assistant in category 'Civil Engineering' & 'Engineering-Architecture'.

2016 **Best paper award** at conference *'Central European Symposium on Building Physics 2016'*, for publication titled *'A thermal conductivity prediction model for porous building blocks'*.

2015 **Best presentation award** at symposium *'Building Physics Days'* organised by KU Leuven, UGent & TU Eindhoven.

2015 **Personal Ph.D. grant** by the IWT institute (Agency for Innovation by Science and Technology).

Publications

International journals

- Van De Walle W., Janssen H. (2016). *A Thermal Conductivity Prediction Model for Porous Building Blocks*. *Bauphysik* 38(6) (pp. 340-347).

- **Van De Walle W.**, Claes S. & Janssen H. (2018). *Implementation and validation of a 3D image-based prediction model for the thermal conductivity of cellular and granular porous building blocks*. Construction & Building Materials 182 (pp. 427-440).
- **Van De Walle W.**, Janssen H. (2019). *A 3D model to predict the influence of nanoscale pores or reduced gas pressures on the effective thermal conductivity of cellular porous building materials*. Journal of Building Physics. Accepted for publication.

Contributions to Scientific Books

- **Van De Walle W.**, Janssen H. (2019). *The Heat Flow Meter apparatus – principles, design and operation*. Chapter in *The art of Measuring in Thermal Sciences*, eds. J. Meyer & M. de Paepe. Submitted.

Conference proceedings

- **Van De Walle W.**, Janssen H. (2019). *Impact of pore scale parameters on the thermal conductivity of porous building blocks*. Central European Symposium on Building Physics 2019 (CESBP2019). Prague, Czech Republic, 2-5 September 2019. Accepted for publication.
- **Van De Walle W.**, Janssen H. (2018). *Predicting the thermal conductivity of porous building materials with nanopores or reduced gas pressures*. 7th International Building Physics Conference. Syracuse, New York, USA, 23-26 September 2018 (pp. 55-60).
- Vereecken E., **Van De Walle W.**, Roels S. (2018). *An experimental test setup to determine the vapour permeability of brick masonry*. 10th International Masonry Conference. Milan, Italy, 9-11 July 2018 (pp. 1248-1256).
- **Van De Walle W.**, Janssen H. (2017). *Validation of a 3D pore scale prediction model for the thermal conductivity of porous building materials*. 11th Nordic Symposium on Building Physics (NSB2017). Trondheim, Norway, 11-14 June 2017 (pp. 225-230).
- Vanpachtenbeke M., **Van De Walle W.**, Janssen H., Roels S. (2015). *Analysis of coupling strategies for building simulation programs*. Energy Procedia: Vol. 78. IBPC 2015. Turijn (pp. 2554-2559).

Bibliography

- Ackermann, Simon, Jonathan R. Scheffé, Jonas Duss, and Aldo Steinfeld. 2014. "Morphological Characterization and Effective Thermal Conductivity of Dual-Scale Reticulated Porous Structures." *Materials* 7 (11): 7173–95. <https://doi.org/10.3390/ma7117173>.
- Ahern, A., G. Verbist, D. Weaire, R. Phelan, and H. Fleurent. 2005. "The Conductivity of Foams: A Generalisation of the Electrical to the Thermal Case." *Colloids and Surfaces A: Physicochemical and Engineering Aspects* 263 (1-3 SPEC. ISS.): 275–79. <https://doi.org/10.1016/j.colsurfa.2005.01.026>.
- Allen, Philip B., Joseph L. Feldman, Jaroslav Fabian, and Frederick Wooten. 1999. "Diffusons, Locons and Propagons: Character of Atomic Vibrations in Amorphous Si." *Philosophical Magazine B: Physics of Condensed Matter; Statistical Mechanics, Electronic, Optical and Magnetic Properties* 79 (11-12): 1715–31. <https://doi.org/10.1080/13642819908223054>.
- Alliez, Pierre, Clément Jamin, Laurent Rineau, Stéphane Tayeb, Jane Tournois, and Mariette Yvinec. 2015. "3D Mesh Generation." In *CGAL User and Reference Manual*, edited by CGAL Editorial Board, 4.5. CGAL Editorial Board.
- Almanza, O., L. O. Arcos Rábago, M. A. Rodríguez-Pérez, A. González, and J. A. De Saja. 2001. "Structure-Property Relationships in Polyolefin Foams." *Journal of Macromolecular Science - Physics* 40 B (3-4): 603–13. <https://doi.org/10.1081/MB-100106180>.
- Altun, Ozge, Y Erhan Boke, and Soner Alanyali. 2011. "Numerical Modeling of Thermal Conductivity of Air-Plasma-Sprayed Zirconia with Different Porosity Levels." *Journal of Thermal Science and Technology* 31 (1): 77–84.
- Alvarez, F. X., D. Jou, and A. Sellitto. 2010. "Pore-Size Dependence of the Thermal Conductivity of Porous Silicon: A Phonon Hydrodynamic Approach." *Applied Physics Letters* 97 (3): 033103. <https://doi.org/10.1063/1.3462936>.
- Arcaro, Sabrina, Bianca Goulart de Oliveira Maia, Marcelo Tramontin Souza, Francielly Roussenq Cesconeto, Laura Granados, and Antonio Pedro Novaes de Oliveira. 2016. "Thermal Insulating Foams Produced From Glass Waste and Banana Leaves." *Materials Research* 19 (5): 1064–69. <https://doi.org/10.1590/1980-5373-MR-2015-0539>.
- Arduini-Schuster, M., J. Manara, and C. Vo. 2015. "Experimental Characterization and Theoretical Modeling of the Infrared-Optical Properties and the Thermal Conductivity of Foams." *International Journal of Thermal Sciences* 98: 156–64. <https://doi.org/10.1016/j.ijthermalsci.2015.07.015>.
- Asaad, Yousri. 1955. "A Study on the Thermal Conductivity of Fluid-Bearing Porous Rocks." University of California, Berkeley.
- Ashby, M. F., and R. F. Mehl Medalist. 1983. "The Mechanical Properties of Cellular Solids." *Metallurgical Transactions A* 14 (9): 1755–69.

- Askari, R., S. Taheri, and S. H. Hejazi. 2015. "Thermal Conductivity of Granular Porous Media: A Pore Scale Modeling Approach." *AIP Advances* 5 (9). <https://doi.org/10.1063/1.4930258>.
- Aurangzeb, Zulqurnain Ali, Samia Faiz Gurmani, and Asghari Maqsood. 2006. "Simultaneous Measurement of Thermal Conductivity, Thermal Diffusivity and Prediction of Effective Thermal Conductivity of Porous Consolidated Igneous Rocks at Room Temperature." *Journal of Physics D: Applied Physics* 39 (17): 3876–81. <https://doi.org/10.1088/0022-3727/39/17/025>.
- Aurangzeb, Liaqat Ali Khan, and Asghari Maqsood. 2007. "Prediction of Effective Thermal Conductivity of Porous Consolidated Media as a Function of Temperature: A Test Example of Limestones." *Journal of Physics D: Applied Physics* 40 (16): 4953–58. <https://doi.org/10.1088/0022-3727/40/16/030>.
- Baetens, Ruben, Bjørn Petter Jelle, Arild Gustavsen, and Steinar Grynning. 2010. "Gas-Filled Panels for Building Applications: A State-of-the-Art Review." *Energy and Buildings* 42 (11): 1969–75. <https://doi.org/10.1016/j.enbuild.2010.06.019>.
- Baetens, Ruben, Bjørn Petter Jelle, Jan Vincent Thue, Martin J. Tenpierik, Steinar Grynning, Sivert Uvsløkk, and Arild Gustavsen. 2010. "Vacuum Insulation Panels for Building Applications: A Review and Beyond." *Energy and Buildings* 42 (2): 147–72. <https://doi.org/10.1016/j.enbuild.2009.09.005>.
- Baghban, Mohammad Hajmohammadian, Per Jostein Hovde, and Stefan Jacobsen. 2013. "Analytical and Experimental Study on Thermal Conductivity of Hardened Cement Pastes." *Materials and Structures/Materiaux et Constructions* 46 (9): 1537–46. <https://doi.org/10.1617/s11527-012-9995-y>.
- Baillis, Dominique, R. Coquard, and L. M. Moura. 2015. "Heat Transfer in Cellulose-Based Aerogels: Analytical Modelling and Measurements." *Energy* 84: 732–44. <https://doi.org/10.1016/j.energy.2015.03.039>.
- Baillis, Dominique, Remi Coquard, Jaona Randrianalisoa, Leonid a. Dombrovsky, and Raymond Viskanta. 2013. "Thermal Radiation Properties of Highly Porous Cellular Foams." *Special Topics & Reviews in Porous Media - An International Journal* 4 (2): III–36. <https://doi.org/10.1615/SpecialTopicsRevPorousMedia.v4.i2.20>.
- Baillis, Dominique, and Jean-François Sacadura. 2000. "Thermal Radiation Properties of Dispersed Media: Theoretical Prediction and Experimental Characterization." *Journal of Quantitative Spectroscopy and Radiative Transfer* 67: 327–63.
- Bakker, K. 1997. "Using the Finite Element Method to Compute the Influence of Complex Porosity and Inclusion Structures on the Thermal and Electrical Conductivity." *International Journal of Heat and Mass Transfer* 40 (15): 3503–11.
- Bakker, K, H Kwast, and E.H.P. Cordfunke. 1995. "The Contribution of Thermal Radiation to the Thermal Conductivity of Porous UO₂." *Journal of Nuclear Materials* 223: 135–42.

- Bao, Hua, Jie Chen, Xiaokun Gu, and Bingyang Cao. 2018. "A Review of Simulation Methods in Micro/Nanoscale Heat Conduction." *ES Energy & Environment*. <https://doi.org/10.30919/esee8c149>.
- Barbuta, Marinela, Roxana Dana Bucur, Sorin Mihai Cimpeanu, Gigel Paraschiv, and Daniel Bucur. 2015. "Wastes in Building Materials Industry." In , 81–99. Intech Open.
- Batool, Farnaz, and Vivek Bindiganavile. 2017. "Air-Void Size Distribution of Cement Based Foam and Its Effect on Thermal Conductivity." *Construction and Building Materials* 149: 17–28. <https://doi.org/10.1016/j.conbuildmat.2017.05.114>.
- Batty, W.J., S.D. Probert, and P.W. O'Callaghan. 1984. "Apparent Thermal Conductivities of High-Porosity Cellular Insulants." *Applied Energy* 18 (2): 117–35. [https://doi.org/10.1016/0306-2619\(84\)90049-7](https://doi.org/10.1016/0306-2619(84)90049-7).
- Bauer, T.H. 1993. "A General Analytical Approach toward the Thermal Conductivity of Porous Media." *International Journal of Heat and Mass Transfer* 36 (1): 4181–91. [https://doi.org/10.1016/0017-9310\(93\)90080-P](https://doi.org/10.1016/0017-9310(93)90080-P).
- Bentz, Dale P. 2006. "Measurement and Microstructure-Based Modeling of the Thermal Conductivity of Fire Resistive Materials," no. September.
- Berge, Axel, and P Å R Johansson. 2012. "Literature Review of High Performance Thermal Insulation." *Building Physics*.
- Berisha, Sebastian, Thomas van Dijk, Rohit Bhargava, P. Scott Carney, and David Mayerich. 2016. "BIM-Sim: Interactive Simulation of Broadband Imaging Using Mie Theory." *Microscopy and Microanalysis* 22 (S3): 1438–39. <https://doi.org/10.1017/S1431927616008035>.
- Bhattacharya, A., V. V. Calmidi, and R. L. Mahajan. 2002. "Thermophysical Properties of High Porosity Metal Foams." *International Journal of Heat and Mass Transfer* 45 (5): 1017–31. [https://doi.org/10.1016/S0017-9310\(01\)00220-4](https://doi.org/10.1016/S0017-9310(01)00220-4).
- Bi, C., and G. H. Tang. 2013. "Effective Thermal Conductivity of the Solid Backbone of Aerogel." *International Journal of Heat and Mass Transfer* 64: 452–56. <https://doi.org/10.1016/j.ijheatmasstransfer.2013.04.053>.
- Bi, C., G. H. Tang, and Z. J. Hu. 2014. "Heat Conduction Modeling in 3-D Ordered Structures for Prediction of Aerogel Thermal Conductivity." *International Journal of Heat and Mass Transfer* 73: 103–9. <https://doi.org/10.1016/j.ijheatmasstransfer.2014.01.058>.
- Bi, Cheng, Gui-hua Tang, Qiang Sheng, and Bo Fu. 2014. "Study on Thermal Conductivity of Gas Phase in Nano-Porous Aerogel," no. September: 7–10.
- Boltcheva, Dobrina, Mariette Yvinec, Jean-daniel Boissonnat, Dobrina Boltcheva, Mariette Yvinec, and Jean-daniel Boissonnat Mesh. 2009. "Mesh Generation from 3D Multi-Material Images To Cite This Version.:" *Medical Image Computing and Computer-Assisted Intervention*, 283–90.

- Bomberg, M., and K. R. Solvason. 1983. "Comments on Calibration and Design of a Heat Flow Meter." *Thermal Insulation, Materials, and Systems for Energy Conservation in the '80s*, no. II: 277–92.
- . 1985. "Discussion of Heat Flow Meter Apparatus and Transfer Standards Used for Error Analysis." In *Guarded Hot Plate and Heat Flow Meter Methodology - ASTM STP 879*, edited by C. J. Shirliff and R. P. Tye, 140–53. Philadelphia: American Society for Testing and Materials.
- Born, Max, and Emil Wolf. 2003. *Principles of Optics*. 7th expand. Cambridge: Cambridge University Press.
- Bouret, Julie, Aurelie Michot, Nicolas Tessier-Doyen, B. Nait-Ali, Fabienne Pennec, Arnaud Alzina, Jerome Vicente, Claire S. Peyratout, and David S. Smith. 2014. "Thermal Conductivity of Very Porous Kaolin-Based Ceramics." Edited by M. A. White. *Journal of the American Ceramic Society* 97 (3): 938–44. <https://doi.org/10.1111/jace.12767>.
- Brabant, Loes, J. Vlassenbroeck, Y. De Witte, V. Cnudde, M. Boone, J. Dewanckele, and L. Van Hoorebeke. 2011. "Three-Dimensional Analysis of High-Resolution X-Ray Computed Tomography Data with Morpho+." *Microscopy and Microanalysis* 17 (2): 252–63. <https://doi.org/10.1017/S1431927610094389>.
- Bracconi, Mauro, Matteo Ambrosetti, Matteo Maestri, Gianpiero Groppi, and Enrico Tronconi. 2018. "A Fundamental Analysis of the Influence of the Geometrical Properties on the Effective Thermal Conductivity of Open-Cell Foams." *Chemical Engineering and Processing - Process Intensification* 129 (April): 181–89. <https://doi.org/10.1016/j.cep.2018.04.018>.
- Braun, D., and A. Frohn. 1976. "Heat Transfer in Simple Monatomic Gases and in Binary Mixtures of Monatomic Gases." *International Journal of Heat and Mass Transfer* 19 (11): 1329–35. [https://doi.org/10.1016/0017-9310\(76\)90085-5](https://doi.org/10.1016/0017-9310(76)90085-5).
- Bruggeman, D. A. G. 1935. "Berechnung Verschiedener Physikalischer Konstanten von Heterogenen Substanzen. I. Dielektrizitätskonstanten Und Leitfähigkeiten Der Mischkörper Aus Isotropen Substanzen." *Annalen Der Physik* 416 (7): 636–64.
- Cahill, D. G., Paul V. Braun, Gang Chen, David R. Clarke, Shanhui Fan, Kenneth E. Goodson, Pawel Keblinski, et al. 2014. "Nanoscale Thermal Transport. II. 2003-2012." *Applied Physics Reviews* 1 (1): 1–45. <https://doi.org/10.1063/1.4832615>.
- Cahill, D. G., Wayne K. Ford, Kenneth E. Goodson, Gerald D. Mahan, Arun Majumdar, Humphrey J. Maris, Roberto Merlin, and Simon R. Phillpot. 2003. "Nanoscale Thermal Transport." *Journal of Applied Physics* 93 (2): 793. <https://doi.org/10.1063/1.1524305>.
- Cahill, D. G., and R.O. Pohl. 1988. "Lattice Vibrations And Heat Transport In Crystals And Glasses." *Annual Review of Physical Chemistry* 39 (2): 93–121. <https://doi.org/10.1146/annurev.physchem.39.1.93>.
- . 1989. "Heat Flow and Lattice Vibrations in Glasses." *Solid State Communications* 70:

927–30.

- Cahill, D. G., S. K. Watson, and R. O. Pohl. 1992. “Lower Limit to the Thermal Conductivity of Disordered Crystals.” *Physical Review B* 46 (10): 6131–40. <https://doi.org/10.1103/PhysRevB.46.6131>.
- Cahill, D.G., R.B. Stephens, R.H. Tait, S.K. Watson, and R.O. Pohl. 1990. “Thermal Conductivity and Lattice Vibrations in Glasses.” In *Thermal Conductivity, Volume 21*, edited by C.J. Cremers and H.A. Fine, 3–16. New York: Plenum Press.
- Carson, James K., Simon J. Lovatt, David J. Tanner, and Andrew C. Cleland. 2005. “Thermal Conductivity Bounds for Isotropic, Porous Materials.” *International Journal of Heat and Mass Transfer* 48 (11): 2150–58. <https://doi.org/10.1016/j.ijheatmasstransfer.2004.12.032>.
- Chai, Y., X. H. Yang, M. Zhao, Z. Y. Chen, X. Z. Meng, L. W. Jin, Q. L. Zhang, and W. J. Hu. 2017. “Study of Microstructure-Based Effective Thermal Conductivity of Graphite Foam.” *Journal of Heat Transfer* 139 (5): 052004. <https://doi.org/10.1115/1.4036002>.
- Chapelle, Lucie. 2016. “Characterization and Modelling of the Mechanical Properties of Mineral Wool,” 142.
- Chen, G., D. Borca-Tasciuc, and R.G. Yang. 2004. “Nanoscale Heat Transfer.” *Encyclopedia of Nanoscience and Nanotechnology* 7: 429–59.
- Chen, Gang. 2000. “Phonon Heat Conduction in Nanostructures.” *International Journal of Thermal Sciences* 39 (4): 471–80. [https://doi.org/10.1016/S1290-0729\(00\)00202-7](https://doi.org/10.1016/S1290-0729(00)00202-7).
- . 2005. *Nanoscale Energy Transport and Conversion: A Parallel Treatment of Electrons, Molecules, Phonons and Photons*. New York: Oxford University Press.
- Chen, Jiaqi, Miao Zhang, Hao Wang, and Liang Li. 2015. “Evaluation of Thermal Conductivity of Asphalt Concrete with Heterogeneous Microstructure.” *Applied Thermal Engineering* 84: 368–74. <https://doi.org/10.1016/j.applthermaleng.2015.03.070>.
- Chen, Zhen, and Chris Dames. 2015. “An Anisotropic Model for the Minimum Thermal Conductivity.” *Applied Physics Letters* 107.
- Cheng, H., and S. Torquato. 1997. “Effective Conductivity of Periodic Arrays of Spheres with Interfacial Resistance.” *Proceeding of the Royal Society of London. Series A, Mathematical and Physical Sciences* 453 (1956): 145–61.
- Childs, Gregg E., Lewis J. Ericks, and Robert L. Powell. 1973. *Thermal Conductivity of Solids At Room Temperature and Below*. National Bureau of Standards.
- Choudhary, M. K., and R. M. Potter. 2005. “Heat Transfer in Glass-Forming Melts.” In *Properties of Glass-Formation Melts*, edited by D. L. Pye, A. Montenaro, and I. Joseph, 1st ed. Boca Raton, Florida: CRC Press.
- Claes, Steven. 2015. “Pore Classification System and Upscaling Strategy in Travertine Reservoir

Rocks.” KU Leuven.

- Claes, Steven, Wouter Van De Walle, Muhammad Islahuddin, and Hans Janssen. 2019. “The Application of Computed Tomography for Characterising the Pore Structure of Porous Building Materials (Submitted).” *Journal of Building Physics*.
- Clyne, T W, I O Golosnoy, J C Tan, and a E Markaki. 2006. “Porous Materials for Thermal Management under Extreme Conditions.” *Philosophical Transactions. Series A, Mathematical, Physical, and Engineering Sciences* 364 (1838): 125–46. <https://doi.org/10.1098/rsta.2005.1682>.
- Collishaw, P. G., and J. R. G. Evans. 1994. “An Assessment of Expressions for the Apparent Thermal Conductivity of Cellular Materials.” *Journal of Materials Science* 29 (9): 2261–73.
- Coquard, R., and D. Baillis. 2006. “Modeling of Heat Transfer in Low-Density EPS Foams.” *Journal of Heat Transfer* 128 (6): 538. <https://doi.org/10.1115/1.2188464>.
- . 2009. “Numerical Investigation of Conductive Heat Transfer in High-Porosity Foams.” *Acta Materialia* 57 (18): 5466–79. <https://doi.org/10.1016/j.actamat.2009.07.044>.
- Coquard, R., D. Baillis, and E. Maire. 2010. “Numerical Investigation of the Radiative Properties of Polymeric Foams from Tomographic Images.” *Journal of Thermophysics and Heat Transfer* 24 (3): 647–58. <https://doi.org/10.2514/1.46988>.
- Coquard, R., D. Baillis, and D. Quenard. 2009. “Radiative Properties of Expanded Polystyrene Foams.” *Journal of Heat Transfer* 131 (1): 012702. <https://doi.org/10.1115/1.2994764>.
- Coquard, R., Dominique Baillis, V. Grigorova, F. Enguehard, D. Quenard, and P. Levitz. 2013. “Heat Transfer in New Cellulose-Based Nano-Porous Aerogels: Modelling and Measurements.” *Journal of Non-Crystalline Solids* 363 (1): 103–15. <https://doi.org/10.1016/j.jnoncrysol.2012.11.053>.
- Coquard, R., Dominique Baillis, and J. Randrianalisoa. 2011. “Homogeneous Phase and Multi-Phase Approaches for Modeling Radiative Transfer in Foams.” *International Journal of Thermal Sciences* 50 (9): 1648–63. <https://doi.org/10.1016/j.ijthermalsci.2011.04.012>.
- Coquard, R., D. Rochais, and D. Baillis. 2009. “Experimental Investigations of the Coupled Conductive and Radiative Heat Transfer in Metallic/Ceramic Foams.” *International Journal of Heat and Mass Transfer* 52 (21–22): 4907–18. <https://doi.org/10.1016/j.ijheatmasstransfer.2009.05.015>.
- Coquard, R, D Rochais, and D Baillis. 2010. “Conductive and Radiative Heat Transfer in Ceramic and Metal Foams at Fire Temperatures.” *Fire Technology* 48 (3): 699–732. <https://doi.org/10.1007/s10694-010-0167-8>.
- Coquard, Rémi, Jaona Randrianalisoa, and Dominique Baillis. 2013. “Computational Prediction of Radiative Properties of Polymer Closed-Cell Foams with Random Structure.” *Journal of Porous Media* 16 (2): 137–54.

- Coquil, Thomas, Jin Fang, and Laurent Pilon. 2011. "Molecular Dynamics Study of the Thermal Conductivity of Amorphous Nanoporous Silica." *International Journal of Heat and Mass Transfer* 54 (21-22): 4540-48. <https://doi.org/10.1016/j.ijheatmasstransfer.2011.06.024>.
- Coquil, Thomas, Erik K. Richman, Neal J. Hutchinson, Sarah H. Tolbert, and Laurent Pilon. 2009. "Thermal Conductivity of Cubic and Hexagonal Mesoporous Silica Thin Films." *Journal of Applied Physics* 106 (3): 1-11. <https://doi.org/10.1063/1.3182826>.
- Costeux, Stéphane. 2014. "CO₂-Blown Nanocellular Foams." *Journal of Applied Polymer Science* 131 (23): 41293. <https://doi.org/10.1002/app.41293>.
- Cuce, Erdem, Pinar Mert Cuce, Christopher J. Wood, and Saffa B. Riffat. 2014. "Toward Aerogel Based Thermal Superinsulation in Buildings: A Comprehensive Review." *Renewable and Sustainable Energy Reviews* 34: 273-99. <https://doi.org/10.1016/j.rser.2014.03.017>.
- Cunsolo, Salvatore, Dominique Baillis, and Nicola Bianco. 2019. "Improved Monte Carlo Methods for Computational Modelling of Thermal Radiation Applied to Porous Cellular Materials." *International Journal of Thermal Sciences* 137 (November 2018): 161-79. <https://doi.org/10.1016/j.ijthermalsci.2018.11.011>.
- Cunsolo, Salvatore, Rémi Coquard, Dominique Baillis, and Nicola Bianco. 2016. "Radiative Properties Modeling of Open Cell Solid Foam: Review and New Analytical Law." *International Journal of Thermal Sciences* 104: 122-34. <https://doi.org/10.1016/j.ijthermalsci.2015.12.017>.
- DeAngelis, Freddy, Murali Gopal Muraleedharan, Jaeyun Moon, Hamid Reza Seyf, Austin J Minnich, Alan J.H. McGaughey, and Asegun Henry. 2019. "Thermal Transport in Disordered Materials." *Nanoscale and Microscale Thermophysical Engineering* 23 (2): 81-116. <https://doi.org/10.1103/PhysRevLett.31.466>.
- Demouchali, S Kazemidoust, S Pourmahdian, and B Shirkavand Hadavand. 2016. "Synthesis of Hollow Silica Nanospheres with Raspberry-like Morphology by Sacrificial Polystyrene Templates for Thermal Insulation Applications" 2013 (November): 1-2.
- Denissen, Jos, Lubica Kriskova, and Yiannis Pontikes. 2019. "Kinetics of Pore Formation and Resulting Properties of Lightweight Inorganic Polymers." *Journal of the American Ceramic Society*, no. September 2018: 3940-50. <https://doi.org/10.1111/jace.16301>.
- Denpoh, Kazuki. 1998. "Modeling of Rarefied Gas Heat Conduction between Wafer and Susceptor." *IEEE Transactions on Semiconductor Manufacturing* 11 (1): 25-29. <https://doi.org/10.1109/66.661281>.
- Dettori, Riccardo, Claudio Melis, Xavier Cartoix??, Riccardo Rurali, and Luciano Colombo. 2015. "Model for Thermal Conductivity in Nanoporous Silicon from Atomistic Simulations." *Physical Review B - Condensed Matter and Materials Physics* 91 (5): 1-10. <https://doi.org/10.1103/PhysRevB.91.054305>.
- Do, Chi T., Dale P. Bentz, and Paul E. Stutzman. 2007. "Microstructure and Thermal Conductivity of Hydrated Calcium Silicate Board Materials." *Journal of Building Physics*

31 (1): 55–67. <https://doi.org/10.1177/1744259107079020>.

- Dombrovsky, L, and D Baillis. 2010. *Thermal Radiation in Disperse Systems: An Engineering Approach*. Begell House.
- Dong, Huicong, Bin Wen, and Roderick Melnik. 2014. “Relative Importance of Grain Boundaries and Size Effects in Thermal Conductivity of Nanocrystalline Materials.” *Scientific Reports* 4: 7037. <https://doi.org/10.1038/srep07037>.
- Dong, Yan-Hao, Chang-An Wang, Liang-Fa Hu, and Jun Zhou. 2012. “Numerical Calculations of Effective Thermal Conductivity of Porous Ceramics by Image-Based Finite Element Method.” *Frontiers of Materials Science* 6 (1): 79–86. <https://doi.org/10.1007/s11706-012-0156-6>.
- Drochytka, Rostislav, Jiří Zach, Azra Korjenic, and Jitka Hroudová. 2013. “Improving the Energy Efficiency in Buildings While Reducing the Waste Using Autoclaved Aerated Concrete Made from Power Industry Waste.” *Energy and Buildings* 58: 319–23. <https://doi.org/10.1016/j.enbuild.2012.10.029>.
- Druma, A. M., M. K. Alam, and C. Druma. 2004. “Analysis of Thermal Conduction in Carbon Foams.” *International Journal of Thermal Sciences* 43 (7): 689–95. <https://doi.org/10.1016/j.ijthermalsci.2003.12.004>.
- Dyck, Nolan J., and Anthony G. Straatman. 2015. “A New Approach to Digital Generation of Spherical Void Phase Porous Media Microstructures.” *International Journal of Heat and Mass Transfer* 81: 470–77. <https://doi.org/10.1016/j.ijheatmasstransfer.2014.10.017>.
- . 2016. “Radiative Property Characterization of Spherical Void Phase Graphitic Foam.” *International Journal of Heat and Mass Transfer* 92: 1201–4. <https://doi.org/10.1016/j.ijheatmasstransfer.2015.09.065>.
- EEA. 2017. “Final Energy Consumption by Sector and Fuel.” <https://www.eea.europa.eu/data-and-maps/indicators/final-energy-consumption-by-sector-9/assessment-1>.
- Enguehard, Franck. 2007. “Multi-Scale Modeling of Radiation Heat Transfer through Nanoporous Superinsulating Materials.” *International Journal of Thermophysics* 28 (5): 1693–1717. <https://doi.org/10.1007/s10765-006-0143-1>.
- Eurostat. 2016. “Material Flow Accounts - Statistics Explained.” https://ec.europa.eu/eurostat/statistics-explained/index.php?title=Material_flow_accounts_statistics_-_material_footprints.
- Fang, Jin, and Laurent Pilon. 2011. “Scaling Laws for Thermal Conductivity of Crystalline Nanoporous Silicon Based on Molecular Dynamics Simulations.” *Journal of Applied Physics* 110 (6). <https://doi.org/10.1063/1.3638054>.
- Fang, Q, and D A Boas. 2009. “Tetrahedral Mesh Generation from Volumetric Binary and Gray Scale Images.” In *Proceedings IEEE International Symposium on Biomedical Imaging*, 1142–45.

- Ferkl, Pavel, Richard Pokorný, Marek Bobák, and Juraj Kosek. 2013. "Heat Transfer in One-Dimensional Micro- and Nano-Cellular Foams." *Chemical Engineering Science* 97 (June): 50–58. <https://doi.org/10.1016/j.ces.2013.04.018>.
- Ferkl, Pavel, Richard Pokorný, and Juraj Kosek. 2014. "Multiphase Approach to Coupled Conduction–Radiation Heat Transfer in Reconstructed Polymeric Foams." *International Journal of Thermal Sciences* 83: 68–79. <https://doi.org/10.1016/j.ijthermalsci.2014.04.013>.
- Fiala, Lukáš, Miloš Jerman, Pavel Reiterman, and Robert Černý. 2018. "Determination of Thermal Conductivity of Silicate Matrix for Applications in Effective Media Theory." *International Journal of Thermophysics* 39 (2): 28. <https://doi.org/10.1007/s10765-017-2347-y>.
- Fiedler, Thomas, Eusebio Solórzano, Francisco Garcia-Moreno, Andreas Öchsner, Irina V. Belova, and Graeme E. Murch. 2009. "Lattice Monte Carlo and Experimental Analyses of the Thermal Conductivity of Random-Shaped Cellular Aluminum." *Advanced Engineering Materials* 11 (10): 843–47. <https://doi.org/10.1002/adem.200900132>.
- Fitzgerald, S P, and W Strieder. 1998. "Radiation Perpendicular to the Symmetry Axis of Prolate and Oblate Cavities." *AIChE Journal* 44 (11): 2351–59.
- Fluegel, Alexander. 2007. "Global Model for Calculating the Room-Temperature Glass Density from the Composition." *Journal of the American Ceramic Society* 90 (8): 2622–25.
- Forest, C., P. Chaumont, P. Cassagnau, B. Swoboda, and P. Sonntag. 2015. "Polymer Nano-Foams for Insulating Applications Prepared from CO₂foaming." *Progress in Polymer Science* 41 (C): 122–45. <https://doi.org/10.1016/j.progpolymsci.2014.07.001>.
- Gaiselmann, Gerd, Matthias Neumann, Volker Schmidt, Omar Pecho, Thomas Hocker, and Lorenz Holzer. 2014. "Quantitative Relationships between Microstructure and Effective Transport Properties Based on Virtual Materials Testing." *AIChE Journal* 60 (6): 1983–99. <https://doi.org/10.1002/aic>.
- Ganapathy, Deepak, Kulwinder Singh, Patrick E. Phelan, and Ravi Prasher. 2005. "An Effective Unit Cell Approach to Compute the Thermal Conductivity of Composites With Cylindrical Particles." *Journal of Heat Transfer* 127 (6): 553–59. <https://doi.org/10.1115/1.1915387>.
- Gao, T, B P Jelle, L I C Sandberg, and A Gustavsen. 2015. "Thermal Conductivity of Monodisperse Silica Nanospheres." *Journal of Porous Media* 18 (10): 941–47. <https://doi.org/10.1615/JPorMedia.2015012218>.
- Gibson, Lorna J., and M. F. Ashby. 1997. *Cellular Solids: Structure and Properties*. 2nd ed. Cambridge University Press.
- Giesche, Herbert. 2006. "Mercury Porosimetry: A General (Practical) Overview." *Particle and Particle Systems Characterization* 23 (1): 9–19. <https://doi.org/10.1002/ppsc.200601009>.

- Glicksman, L. R., M. Schuetz, and M. Sinofsky. 1987. "Radiation Heat Transfer in Foam Insulation." *International Journal of Heat and Mass Transfer* 30 (1): 187–97. [https://doi.org/10.1016/0017-9310\(87\)90071-8](https://doi.org/10.1016/0017-9310(87)90071-8).
- Glicksman, L. R., and M. Torpey. 1989. "Factors Governing Heat Transfer Through Closed Cell Foam Insulation." *Journal of Thermal Insulation* 12: 257–69.
- Glorieux, Christ, Jan Hudec, Jonathan Guarachi, Kelly Martinez, Jose Jesus Agustin Flores Cuaute, Ludovic Kubicar, Vlastimil Bohac, et al. 2017. "Round Robin Test between Different Heat Transport Techniques Characterizing Low Thermal Conductivity Materials." Logan, Utah, USA.
- Goual, M S, A Bali, and M Quéneudec. 1999. "Effective Thermal Conductivity of Clayey Aerated Concrete in the Dry State : Experimental Results and Modelling." *Journal of Physics D: Applied Physics* 32 (23): 3041–46.
- Guo, Yangyu, and Moran Wang. 2015. "Phonon Hydrodynamics and Its Applications in Nanoscale Heat Transport." *Physics Reports* 595: 1–44. <https://doi.org/10.1016/j.physrep.2015.07.003>.
- . 2016. "Lattice Boltzmann Modeling of Phonon Transpor." *Journal of Computational Physics* 315: 1–15. <https://doi.org/10.1016/j.jcp.2016.03.041>.
- Gustafsson, Silas E. 1991. "Transient Plane Source Techniques for Thermal Conductivity and Thermal Diffusivity Measurements of Solid Materials." *Review of Scientific Instruments* 62: 797.
- Hashin, Z., and S. Shtrikman. 1962. "A Variational Approach to the Theory of the Effective Magnetic Permeability of Multiphase Materials." *Journal of Applied Physics* 33: 3125.
- Haussener, Sophia, Patrick Coray, Wojciech Lipiński, Peter Wyss, and Aldo Steinfeld. 2009. "Tomography-Based Heat and Mass Transfer Characterization of Reticulate Porous Ceramics for High-Temperature Processing." *Journal of Heat Transfer* 132 (2): 023305. <https://doi.org/10.1115/1.4000226>.
- He, Ya-Ling, and Tao Xie. 2015. "Advances of Thermal Conductivity Models of Nanoscale Silica Aerogel Insulation Material." *Applied Thermal Engineering*. <https://doi.org/10.1016/j.applthermaleng.2015.02.013>.
- He, Ya Ling, and Tao Xie. 2015. "Advances of Thermal Conductivity Models of Nanoscale Silica Aerogel Insulation Material." *Applied Thermal Engineering* 81: 28–50. <https://doi.org/10.1016/j.applthermaleng.2015.02.013>.
- Herczeg, Marton, David McKinnon, Leonidas Milios, Ioannis Bakas, Erik Klaassens, Katarina Svatikova, and Oscar Widerberg. 2014. "Resource Efficiency in the Building Sector." Rotterdam. [http://ec.europa.eu/environment/eussd/pdf/Resource efficiency in the building sector.pdf](http://ec.europa.eu/environment/eussd/pdf/Resource_efficiency_in_the_building_sector.pdf).
- Herman, Gabor T. 2009. *Fundamentals of Computerized Tomography: Image Reconstruction*

from *Projections*. 2nd ed. Springer London.

- Horai, Ki-iti, and G. Simmons. 1969. "Thermal Conductivity of Rock-Forming Minerals." *Earth and Planetary Science Letters* 6 (5): 359–68. [https://doi.org/10.1016/0012-821X\(69\)90186-1](https://doi.org/10.1016/0012-821X(69)90186-1).
- Howell, John R., M. Pinar Mengüç, and Robert Siegel. 2016. "Near-Field Thermal Radiation." In *Thermal Radiation Heat Transfer*, 6th ed., 795–828. Boca Raton, FL: CRC Press.
- Hsu, Pei-feng, and John R. Howells. 1992. "Measurements of Thermal Conductivity and Optical Properties of Porous Partially Stabilized Zirconia." *Experimental Heat Transfer* 5 (4): 293–313.
- Hu, Feng, Siyu Wu, and Yugang Sun. 2018. "Hollow-Structured Materials for Thermal Insulation." *Advanced Materials* 1801001: 1–17. <https://doi.org/10.1002/adma.201801001>.
- Hua, Yu Chao, and Bing Yang Cao. 2017. "Cross-Plane Heat Conduction in Nanoporous Silicon Thin Films by Phonon Boltzmann Transport Equation and Monte Carlo Simulations." *Applied Thermal Engineering* 131: 1401–8. <https://doi.org/10.1016/j.applthermaleng.2016.05.157>.
- Huber, Marcia L., and Allan H. Harvey. 2011. "Thermal Conductivity of Gases." In *CRC Handbook of Chemistry and Physics*, 92nd ed., 240–41. Boca Raton, Florida: CRC-Press. http://www.engineersedge.com/heat_transfer/thermal-conductivity-gases.htm.
- Jaggiwanram, and Ramvir Singh. 2004. "Effective Thermal Conductivity of Highly Porous Two-Phase Systems." *Applied Thermal Engineering* 24 (17–18): 2727–35. <https://doi.org/10.1016/j.applthermaleng.2004.03.010>.
- Jelle, B. P., A. Gustavsen, and R. Baetens. 2010. "The Path to the High Performance Thermal Building Insulation Materials and Solutions of Tomorrow." *Journal of Building Physics* 34 (2): 99–123. <https://doi.org/10.1177/1744259110372782>.
- Jelle, Bjørn Petter. 2011. "Traditional, State-of-the-Art and Future Thermal Building Insulation Materials and Solutions - Properties, Requirements and Possibilities." *Energy and Buildings* 43 (10): 2549–63. <https://doi.org/10.1016/j.enbuild.2011.05.015>.
- Jelle, Bjørn Petter, Ruben Baetens, and Arild Gustavsen. 2011. "Aerogel Insulation for Building Applications: A State-of-the-Art Review." *Energy and Buildings* 43 (4): 761–69. <https://doi.org/10.1002/9783527670819.ch45>.
- Ji, Ru, Zuotai Zhang, Lili Liu, and Xidong Wang. 2014. "Development of the Random Simulation Model for Estimating the Effective Thermal Conductivity of Insulation Materials." *Building and Environment* 80 (October): 221–27. <https://doi.org/10.1016/j.buildenv.2014.05.033>.
- Jiji, Latif M. 2009. *Heat Conduction*. 3rd ed.
- Jin, Hua, Yu Wang, Qiang Zheng, Hu Liu, and Edmund Chadwick. 2017. "Experimental Study and Modelling of the Thermal Conductivity of Sandy Soils of Different Porosities and

- Water Contents.” *Applied Sciences* 7 (2): 119. <https://doi.org/10.3390/app7020119>.
- Joulain, Karl. 2007. “Radiative Transfer on Short Length Scales.” In , edited by Sebastian Volz, 107:107–31. Springer Berlin Heidelberg.
- JRC. 2019. “Certificate of Analysis IRMM - 440.” <https://crm.jrc.ec.europa.eu/p/40456/40495/By-analyte-group/Thermal-properties/IRMM-440A-RESIN-BONDED-FIBRE-BOARD-thermal-conductivity/IRMM-440A>.
- Kaddouri, W., A. El Moumen, T. Kanit, S. Madani, and A. Imad. 2016. “On the Effect of Inclusion Shape on Effective Thermal Conductivity of Heterogeneous Materials.” *Mechanics of Materials* 92: 28–41. <https://doi.org/10.1016/j.mechmat.2015.08.010>.
- Kaemmerlen, A., C. Vo, F. Asllanaj, G. Jeandel, and D. Baillis. 2010. “Radiative Properties of Extruded Polystyrene Foams: Predictive Model and Experimental Results.” *Journal of Quantitative Spectroscopy and Radiative Transfer* 111 (6): 865–77. <https://doi.org/10.1016/j.jqsrt.2009.11.018>.
- Kaganer. 1969. “Thermal Insulation in Cryogenic Engineering.”
- Kamseu, E., Zénabou N.M. Ngouloure, B. Nait-Ali, S. Zekeng, U. C. Melo, S. Rossignol, and C. Leonelli. 2015. “Cumulative Pore Volume, Pore Size Distribution and Phases Percolation in Porous Inorganic Polymer Composites: Relation Microstructure and Effective Thermal Conductivity.” *Energy and Buildings* 88: 45–56. <https://doi.org/10.1016/j.enbuild.2014.11.066>.
- Kan, Ankang, Liyun Kang, Chong Wang, and Dan Cao. 2015. “A Simple and Effective Model for Prediction of Effective Thermal Conductivity of Vacuum Insulation Panels.” *Future Cities and Environment* 1 (1): 4. <https://doi.org/10.1186/s40984-015-0001-z>.
- Kaur, Manpreet, Seung Min Han, and Woo Soo Kim. 2016. “Three-Dimensionally Printed Cellular Architecture Materials: Perspectives on Fabrication, Material Advances, and Applications.” *MRS Communications* 7 (1): 8–19. <https://doi.org/10.1557/mrc.2016.62>.
- Kennard, Earle H. 1938. *Kinetic Theory of Gases*. 1st ed. New York: McGraw-Hill.
- Kommandur, Sampath, and Shannon K. Yee. 2017. “An Empirical Model to Predict Temperature-Dependent Thermal Conductivity of Amorphous Polymers.” *Journal of Polymer Science, Part B: Polymer Physics* 55 (15): 1160–70. <https://doi.org/10.1002/polb.24365>.
- Kosuge, Shingo. 2001. “Heat Transfer in a Gas Mixture between Two Parallel Plates: Finite-Difference Analysis of the Boltzmann Equation.” *AIP Conference Proceedings* 585 (2001): 289–96. <https://doi.org/10.1063/1.1407574>.
- Kriskova, Lubica, Peter Tom Jones, Hans Janssen, and Bart Blanpain. 2015. “Synthesis and Characterisation of Porous Inorganic Polymers from Fayalite Slag,” 15–18.
- Kubičár, L’Udovít, Viliam Vretenár, Vladimír Štofanič, and Vlastimil Boháč. 2010. “Hot-Ball

- Method for Measuring Thermal Conductivity.” *International Journal of Thermophysics* 31 (10): 1904–18. <https://doi.org/10.1007/s10765-008-0544-4>.
- Kuhn, J., H. P. Ebert, M. C. Arduini-Schuster, D. Büttner, and J. Fricke. 1992. “Thermal Transport in Polystyrene and Polyurethane Foam Insulations.” *International Journal of Heat and Mass Transfer* 35 (7): 1795–1801. [https://doi.org/10.1016/0017-9310\(92\)90150-Q](https://doi.org/10.1016/0017-9310(92)90150-Q).
- Kunii, Daizo, and J. M. Smith. 1960. “Heat Transfer Characteristics of Porous Rocks.” *AIChE Journal* 6 (1): 71–78.
- Lallich, Sylvain, Franck Enguehard, and Dominique Baillis. 2009. “Experimental Determination and Modeling of the Radiative Properties of Silica Nanoporous Matrices.” *Journal of Heat Transfer* 131 (8): 082701. <https://doi.org/10.1115/1.3109999>.
- Landauer, Rolf. 1952. “The Electrical Resistance of Binary Metallic Mixtures.” *Journal of Applied Physics* 23 (7): 779–84.
- Laurent, J. P. 1991. “La Conductivité Thermique ‘à Sec’ Des Bétons Cellulaires Autoclavés: Un Modèle Conceptuel.” *Materials and Structures* 24 (3): 221–26. <https://doi.org/10.1007/BF02472988>.
- Lemonnier, Denis. 2007. “Solution of the Boltzmann Equation for Phonon Transport.” In *Microscale and Nanoscale Heat Transfer*, edited by Sebastian Volz, Topics in, 77–106. Springer Berlin Heidelberg.
- Li, Jing, Yanhui Feng, Xinxin Zhang, Congliang Huang, and Ge Wang. 2015. “Near-Field Radiative Heat Transfer across a Pore and Its Effects on Thermal Conductivity of Mesoporous Silica.” *Physica B: Condensed Matter* 456: 237–43. <https://doi.org/10.1016/j.physb.2014.09.005>.
- Li, Xiang Yu, Xiao Long Zhao, Xiang Yong Guo, and Li Qiang Cao. 2011. “A New Theoretical Equation for Effective Thermal Conductivity of Cellular Concrete.” *Applied Mechanics and Materials* 71–78: 1228–32. <https://doi.org/10.4028/www.scientific.net/AMM.71-78.1228>.
- Li, Yun-Han, Zeng-Yao Li, and Wen-Quan Tao. 2014. “An Ideal Nano-Porous Insulation Material: Design, Modeling and Numerical Validation.” *Applied Thermal Engineering* 72 (1): 34–40. <https://doi.org/10.1016/j.applthermaleng.2013.12.041>.
- Liaver GmbH & Co. KG. 2014. “Data Sheet Reapor.” 2014. http://www.liaver.com/fileadmin/user_upload/pdf/Datasheet_Reapor_2014.pdf.
- Liley, P.E. 2018. “Emissivity of Solids.” *Heat Exchanger Design Handbook*, Multimedia Edition. 2018. <https://doi.org/10.1615/hedhme.a.000530>.
- Liu, Jun, Shenghong Ju, Yifu Ding, and Ronggui Yang. 2014. “Size Effect on the Thermal Conductivity of Ultrathin Polystyrene Films.” *Applied Physics Letters* 104 (15). <https://doi.org/10.1063/1.4871737>.

- Liu, Shanqiu, Joost Duvigneau, and G. Julius Vancso. 2015. "Nanocellular Polymer Foams as Promising High Performance Thermal Insulation Materials." *European Polymer Journal* 65: 33–45. <https://doi.org/10.1016/j.eurpolymj.2015.01.039>.
- Loeb, Arthur. 1954. "Thermal Conductivity: VIII, A Theory of Thermal Conductivity of Porous Materials." *Journal of the American Ceramic Society* 37 (2): 96–99.
- Loretz, Mathilde, Eric Maire, and D. Baillis. 2008. "Analytical Modelling of the Radiative Properties of Metallic Foams: Contribution of X-Ray Tomography." *Advanced Engineering Materials* 10 (4): 352–60. <https://doi.org/10.1002/adem.200700334>.
- Lu, T.J., and C. Chen. 1999. "Thermal Transport and Fire Retardance Properties of Cellular Aluminium Alloys." *Acta Materialia* 47 (5): 1469–85. [https://doi.org/10.1016/S1359-6454\(99\)00037-3](https://doi.org/10.1016/S1359-6454(99)00037-3).
- Lv, Wei, and Asegun Henry. 2016a. "Direct Calculation of Modal Contributions to Thermal Conductivity via Green–Kubo Modal Analysis." *New Journal of Physics* 18 (1): 13028. <http://stacks.iop.org/1367-2630/18/i=1/a=013028>.
- . 2016b. "Examining the Validity of the Phonon Gas Model in Amorphous Materials." *Scientific Reports* 6: 1–8. <https://doi.org/10.1038/srep37675>.
- Ma, Hao, and Zhiting Tian. 2015. "Effects of Polymer Chain Confinement on Thermal Conductivity of Ultrathin Amorphous Polystyrene Films." *Applied Physics Letters* 107 (7). <https://doi.org/10.1063/1.4929426>.
- Machrafi, Hatim, and Georgy Lebon. 2015. "Size and Porosity Effects on Thermal Conductivity of Nanoporous Material with an Extension to Nanoporous Particles Embedded in a Host Matrix." *Physics Letters, Section A: General, Atomic and Solid State Physics* 379 (12–13): 968–73. <https://doi.org/10.1016/j.physleta.2015.01.027>.
- Maxwell, James Clerk. 1873. *A Treatise on Electricity and Magnetism*. 1st ed. Oxford: Clarendon Press.
- McKenzie, D.R., R.C. McPhedran, and G.H. Derrick. 1978. "The Conductivity of Lattices of Spheres II. The Body Centred and Face Centred Cubic Lattices." *Proceeding of the Royal Society of London. Series A, Mathematical and Physical Sciences* 362 (1709): 211–32.
- Medri, Valentina, and Andrea Ruffini. 2012. "The Influence of Process Parameters on in Situ Inorganic Foaming of Alkali-Bonded SiC Based Foams." *Ceramics International* 38 (4): 3351–59. <https://doi.org/10.1016/j.ceramint.2011.12.045>.
- Mendes, Miguel A. A., Subhashis Ray, and Dimosthenis Trimis. 2013. "A Simple and Efficient Method for the Evaluation of Effective Thermal Conductivity of Open-Cell Foam-like Structures." *International Journal of Heat and Mass Transfer* 66 (November): 412–22. <https://doi.org/10.1016/j.ijheatmasstransfer.2013.07.032>.
- Mendes, Miguel A. A., Valeria Skibina, Prabal Talukdar, Rhena Wulf, Ulrich Gross, Dimosthenis Trimis, and Subhashis Ray. 2014. "Experimental Validation of Simplified

- Conduction-Radiation Models for Evaluation of Effective Thermal Conductivity of Open-Cell Metal Foams at High Temperatures.” *International Journal of Heat and Mass Transfer* 78: 112–20. <https://doi.org/10.1016/j.ijheatmasstransfer.2014.05.058>.
- Mendes, Miguel A. A., Prabal Talukdar, Subhashis Ray, and Dimosthenis Trimis. 2014. “Detailed and Simplified Models for Evaluation of Effective Thermal Conductivity of Open-Cell Porous Foams at High Temperatures in Presence of Thermal Radiation.” *International Journal of Heat and Mass Transfer* 68: 612–24. <https://doi.org/10.1016/j.ijheatmasstransfer.2013.09.071>.
- Micco, C. De, and C. M. Aldao. 2005. “Radiation Contribution to the Thermal Conductivity of Plastic Foams.” *Journal of Polymer Science Part B: Polymer Physics* 43 (2): 190–92. <https://doi.org/10.1002/polb.20313>.
- Micco, C De, and C M Aldao. 2006. “ON THE PREDICTION OF THE RADIATION TERM IN THE THERMAL CONDUCTIVITY OF PLASTIC FOAMS.” *Latin American Applied Research* 36: 193–97.
- Minnich, Austin, and Gang Chen. 2007. “Modified Effective Medium Formulation for the Thermal Conductivity of Nanocomposites.” *Applied Physics Letters* 91 (7): 9–12. <https://doi.org/10.1063/1.2771040>.
- Miyazaki, K, S Tanaka, D C7 - 051018 Nagai, and Asme. 2010. “Heat Conduction of a Porous Material.” *Proceedings of the Asme Micro/Nanoscale Heat and Mass Transfer International Conference, Vol 3* 134 (May 2012): 159–66. <https://doi.org/10.1115/1.4005709>.
- Monier, Véronique, Mathieu Hestin, Anne-Claire Impériale, Louis Prat, Gillian Hobbs, Katherine Adams, Marie Pairon, et al. 2017. “Resource Efficient Use of Mixed Wastes.”
- Mulet, Jean-Philippe, Karl Joulain, Rémi Carminati, and Jean-Jacques Greffet. 2002. “Enhanced Radiative Heat Transfer At Nanometric Distances.” *Microscale Thermophysical Engineering* 6 (3): 209–22. <https://doi.org/10.1080/10893950290053321>.
- Nait-Ali, B. 2005. “Elaboration, Caractérisation et Modélisation de Matériaux Poreux. Influence de La Structure Poreuse Sur La Conductivité Thermique Effective.” Université de Limoges.
- Nait-Ali, B., K. Haberko, H. Vesteghem, J. Absi, and D. S. Smith. 2006. “Thermal Conductivity of Highly Porous Zirconia.” *Journal of the European Ceramic Society* 26 (16): 3567–74. <https://doi.org/10.1016/j.jeurceramsoc.2005.11.011>.
- Nait-Ali, B., K. Haberko, H. Vesteghem, J. Absi, and D.S. Smith. 2007. “Preparation and Thermal Conductivity Characterisation of Highly Porous Ceramics.” *Journal of the European Ceramic Society* 27 (2–3): 1345–50. <https://doi.org/10.1016/j.jeurceramsoc.2006.04.025>.
- Ngouloure, Zénabou N.M., B. Nait-Ali, S. Zekeng, E. Kamseu, U. C. Melo, D. Smith, and C.

- Leonelli. 2015. "Recycled Natural Wastes in Metakaolin Based Porous Geopolymers for Insulating Applications." *Journal of Building Engineering* 3: 58–69. <https://doi.org/10.1016/j.jobe.2015.06.006>.
- Nielsen, Lars, Hans-Peter Ebert, Frank Hemberger, Jochen Fricke, Anja Biedermann, Michael Reichelt, and Udo Rotermund. 2000. "Thermal Conductivity of Nonporous Polyurethane." *High Temperatures-High Pressures* 32 (6): 701–7. <https://doi.org/10.1068/htwu69>.
- NIST. 2018. "NIST Chemistry WebBook SRD 69 - Thermophysical Properties of Fluid Systems." 2018. <https://webbook.nist.gov/chemistry/fluid/>.
- Notario, B., J. Pinto, and M. A. Rodriguez-Perez. 2016. "Nanoporous Polymeric Materials: A New Class of Materials with Enhanced Properties." *Progress in Materials Science* 78–79: 93–139. <https://doi.org/10.1016/j.pmatsci.2016.02.002>.
- Notario, B., J. Pinto, E. Solorzano, J. A. De Saja, M. Dumon, and M. A. Rodríguez-Pérez. 2015. "Experimental Validation of the Knudsen Effect in Nanocellular Polymeric Foams." *Polymer (United Kingdom)* 56: 57–67. <https://doi.org/10.1016/j.polymer.2014.10.006>.
- Obori, Masanao, Donguk Suh, Shunsuke Yamasaki, Takashi Kodama, Tsuguyuki Saito, Akira Isogai, and Junichiro Shiomi. 2019. "Parametric Model to Analyze the Components of the Thermal Conductivity of a Cellulose-Nanofibril Aerogel." *Physical Review Applied* 11 (2): 1. <https://doi.org/10.1103/PhysRevApplied.11.024044>.
- Öchsner, Andreas, Seyed Mohammad Hossein Hosseini, Markus Merkel, Sio-long Ao, Alan Hoi-Shou Chan, Hideki Katagiri, and Li Xu. 2009. "Numerical Simulation of Thermal and Mechanical Properties of Sintered Perforated Hollow Sphere Structures (PHSS)." *AIP Conference Proceedings* 11: 16–30. <https://doi.org/10.1063/1.3256244>.
- Öchsner, Andreas, and Graeme Murch. 2010. *Heat Transfer in Multi-Phase Materials*. Springer. Vol. 5. <https://doi.org/10.1007/978-3-642-14673-2>.
- Öchsner, Andreas, Graeme E. Murch, and Marcelo J. S. de Lemos, eds. 2008. *Cellular and Porous Materials: Thermal Properties Simulation and Prediction*. Weinheim: Wiley-VCH.
- Ohwada, T. 1996. "Heat Flow and Temperature and Density Distributions in a Rarefied Gas between Parallel Plates with Different Temperatures. Finite-Difference Analysis of the Nonlinear Boltzmann Equation for Hard-Sphere Molecules." *Physics of Fluids* 8 (8): 2153–60.
- Ordonez-Miranda, J., and J. J. Alvarado-Gil. 2012. "Effect of the Pore Shape on the Thermal Conductivity of Porous Media." *Journal of Materials Science* 47 (18): 6733–40. <https://doi.org/10.1007/s10853-012-6616-7>.
- Pande, R. N., V. Kumar, and D. R. Chaudhary. 1984. "Thermal Conduction in a Homogeneous Two-Phase System." *Pramana - Journal of Physics* 22 (1): 63–70.

- Pardo, N, K Vatopoulos, A Krook-Riekkola, J.A. Moya, and A Perez. 2012. "Heat and Cooling Demand and Market Perspective." <http://publications.jrc.ec.europa.eu/repository/handle/JRC70962>.
- Parthasarathy, P., P. Habisreuther, and N. Zarzalis. 2012. "Identification of Radiative Properties of Reticulated Ceramic Porous Inert Media Using Ray Tracing Technique." *Journal of Quantitative Spectroscopy and Radiative Transfer* 113 (15): 1961–69. <https://doi.org/10.1016/j.jqsrt.2012.05.017>.
- Patel, Vipul M., Miguel A.A. Mendes, Prabal Talukdar, and Subhashis Ray. 2018. "Development of Correlations for Effective Thermal Conductivity of a Tetrakaidecahedra Structure in Presence of Combined Conduction and Radiation Heat Transfer." *International Journal of Heat and Mass Transfer* 127: 843–56. <https://doi.org/10.1016/j.ijheatmasstransfer.2018.07.048>.
- Patel, Vipul M., and Prabal Talukdar. 2016. "Evaluation of Radiative Properties of a Representative Foam Structure Using Blocked-off Region Approach Integrated with Finite Volume Method." *International Journal of Thermal Sciences* 108: 89–99. <https://doi.org/10.1016/j.ijthermalsci.2016.05.003>.
- . 2018. "Determination of Radiative Properties of Representative and Real Open Cell Foam Structures Using the Finite Volume Method." *International Journal of Thermal Sciences* 132 (February): 117–28. <https://doi.org/10.1016/j.ijthermalsci.2018.06.001>.
- Pennec, F, A Alzina, N Tessier-doyen, B. Nait-Ali, N Mati-baouche, H De Baynast, and D S Smith. 2013. "A Combined Finite-Discrete Element Method for Calculating the Effective Thermal Conductivity of Bio-Aggregates Based Materials." *International Journal of Heat and Mass Transfer* 60: 274–83. <https://doi.org/10.1016/j.ijheatmasstransfer.2013.01.002>.
- Petrasch, Jörg, Sophia Haussener, and Wojciech Lipinski. 2011. "Discrete vs. Continuum-Scale Simulation of Radiative Transfer in Semitransparent Two-Phase Media." *Journal of Quantitative Spectroscopy and Radiative Transfer* 112 (9): 1450–59. <https://doi.org/10.1016/j.jqsrt.2011.01.025>.
- Petrasch, Jörg, Birte Schrader, Peter Wyss, and Aldo Steinfeld. 2008. "Tomography-Based Determination of the Effective Thermal Conductivity of Fluid-Saturated Reticulate Porous Ceramics." *Journal of Heat Transfer* 130 (3): 032602. <https://doi.org/10.1115/1.2804932>.
- Petrasch, Jörg, P. Wyss, and A. Steinfeld. 2007. "Tomography-Based Monte Carlo Determination of Radiative Properties of Reticulate Porous Ceramics." *Journal of Quantitative Spectroscopy and Radiative Transfer* 105 (2): 180–97. <https://doi.org/10.1016/j.jqsrt.2006.11.002>.
- Pia, Giorgio, and Ulrico Sanna. 2014. "An Intermingled Fractal Units Model to Evaluate Pore Size Distribution Influence on Thermal Conductivity Values in Porous Materials." *Applied Thermal Engineering* 65 (1–2): 330–36. <https://doi.org/10.1016/j.applthermaleng.2014.01.037>.

- Pittsburgh Corning Europe NV. 2018. "FOAMGLAS® PERINSUL S Product Data Sheet." https://nl.foamglas.com/-/media/files/products/nl/4-pds_pc_perinsul/4-1-1_pds_fg_perinsul_s/5811-pds_fg_perinsul_s_20140425-be-nl.pdf.
- Placido, E., M. C. Arduini-Schuster, and J. Kuhn. 2005. "Thermal Properties Predictive Model for Insulating Foams." *Infrared Physics and Technology* 46 (3): 219–31. <https://doi.org/10.1016/j.infrared.2004.04.001>.
- Pohl, R. O. 2006. "Lattice Vibrations of Glasses." *Journal of Non-Crystalline Solids* 352 (32–35): 3363–67. <https://doi.org/10.1016/j.jnoncrysol.2006.01.102>.
- Prasher, Ravi. 2006. "Transverse Thermal Conductivity of Porous Materials Made from Aligned Nano- and Microcylindrical Pores." *Journal of Applied Physics* 100 (6). <https://doi.org/10.1063/1.2337786>.
- Progelhof, R. C., J. L. Throne, and R. R. Ruetsch. 1976. "Methods for Predicting the Thermal Conductivity of Composite Systems : A Review." *Polymer Engineering & Science* 16 (9): 615–25.
- Rader, D. J., M. A. Gallis, J. R. Torczynski, and W. Wagner. 2006. "Direct Simulation Monte Carlo Convergence Behavior of the Hard-Sphere-Gas Thermal Conductivity for Fourier Heat Flow." *Physics of Fluids* 18 (7). <https://doi.org/10.1063/1.2213640>.
- Raed, Khaled. 2013. "Investigation of Knudsen and Gas-Atmosphere Effects on Effective Thermal Conductivity of Porous Media." Technische Universität Bergakademie Freiberg.
- Ramires, M. L. V., C. A. Nieto de Castro, Y. Nagasaka, A. Nagashima, M. J. Assael, and W. A. Wakeham. 1995. "Standard Reference Data for Thermal Conductivity of Water." *Journal of Physical and Chemical Reference Data*. [https://doi.org/10.1016/S0065-2717\(08\)70119-9](https://doi.org/10.1016/S0065-2717(08)70119-9).
- Randrianalisoa, Jaona, and Dominique Baillis. 2008. "Monte Carlo Simulation of Steady-State Microscale Phonon Heat Transport." *Journal of Heat Transfer* 130 (7): 072404. <https://doi.org/10.1115/1.2897925>.
- . 2010. "Radiative Properties of Densely Packed Spheres in Semitransparent Media: A New Geometric Optics Approach." *Journal of Quantitative Spectroscopy & Radiative Transfer* 111 (10): 1372–88. <https://doi.org/10.1016/j.jqsrt.2010.01.014>.
- . 2014. "Thermal Conductive and Radiative Properties of Solid Foams: Traditional and Recent Advanced Modelling Approaches." *Comptes Rendus Physique* 15 (8–9): 683–95. <https://doi.org/10.1016/j.crhy.2014.09.002>.
- Randrianalisoa, Jaona, Dominique Baillis, Christophe L. Martin, and Rémy Dendievel. 2015. "Microstructure Effects on Thermal Conductivity of Open-Cell Foams Generated from the Laguerre–Voronoi Tessellation Method." *International Journal of Thermal Sciences* 98 (April 2016): 277–86. <https://doi.org/10.1016/j.ijthermalsci.2015.07.016>.

- Randrianalisoa, Jaona, Rémi Coquard, and Dominique Baillis. 2013. "Microscale Direct Calculation of Solid Phase Conductivity of Voronoi's Foams." *Journal of Porous Media* 16 (5): 411–26. <https://doi.org/10.1615/JPorMedia.v16.i5.30>.
- Raut, Ashwin Narendra, and Christy Pathrose Gomez. 2016. "Utilization of Waste as a Constituent Ingredient for Enhancing Thermal Performance of Bricks - A Review Paper." *Indian Journal of Science and Technology* 9 (37). <https://doi.org/10.17485/ijst/2016/v9i37/87082>.
- Recticel. 2019. "Eurofloor 300." 2019. <https://www.recticelinsulation.com/be-nl/eurofloor-300>.
- ROBU Glasfilter-Geraete GmbH. n.d. "Technical Data." Accessed January 27, 2017. <http://www.robuglas.com/en/service/technical-data.html>.
- Rockwool. 2019. "RockFit Mono." 2019. <https://www.rockwool.be/producten/gevel/spouwmuur/rockfit-mono/#Specificaties>.
- Rousseau, Emmanuel, Marine Laroche, and Jean-jacques Greffet. 2009. "Surface-Phonon Polariton Contribution to Nanoscale Radiative Heat Transfer." <http://hal.archives-ouvertes.fr/hal-00428574/>.
- Rousseau, Emmanuel, Alessandro Siria, Guillaume Jourdan, Sebastian Volz, Fabio Comin, Joël Chevrier, and Jean-Jacques Greffet. 2009. "Radiative Heat Transfer at the Nanoscale." *Nature Photonics* 3: 514–17.
- Saadatfar, M., M.A. Knackstedt, C.H. Arns, A. Sakellariou, T.J. Senden, A.P. Sheppard, R.M. Sok, H. Steininger, and W. Schrof. 2004. "Polymeric Foam Properties Derived from 3D Images." *Physica A: Statistical Mechanics and Its Applications* 339 (1–2): 131–36. <https://doi.org/10.1016/j.physa.2004.03.054>.
- Sääskilähti, K., J. Oksanen, J. Tulkki, A. J.H. McGaughey, and S. Volz. 2016. "Vibrational Mean Free Paths and Thermal Conductivity of Amorphous Silicon from Non-Equilibrium Molecular Dynamics Simulations." *AIP Advances* 6 (12): 1–6. <https://doi.org/10.1063/1.4968617>.
- Saaskilähti, K., J. Oksanen, J. Tulkki, A. J H McGaughey, and S. Volz. 2016. "Vibrational Mean Free Paths and Thermal Conductivity of Amorphous Silicon from Non-Equilibrium Molecular Dynamics Simulations." *AIP Advances* 6 (12): 1–9. <https://doi.org/10.1063/1.4968617>.
- Sahba, Nazanin, and Thomas J. Rockett. 1992. "Infrared Absorption Coefficients of Silica Glasses." *Journal of American Ceramic Society* 75 (1): 209–12.
- Salmon, David, and Ron Tye. 2001. "An Inter-Comparison of Guarded Hot Plate and Heat Flow Meter Apparatus within the United Kingdom and Ireland."
- Sanjaya, Christian. 2011. "Pore Size Effect on Heat Transfer through Porous Medium." National University of Singapore.

- Schaedler, Tobias A., and William B. Carter. 2016. "Architected Cellular Materials." *Annual Review of Materials Research* 46 (1): 187–210. <https://doi.org/10.1146/annurev-matsci-070115-031624>.
- Schelling, Patrick K, Simon R Phillpot, and Pawel Keblinski. 2002. "Comparison of Atomic-Level Simulation Methods for Computing Thermal Conductivity" 65: 1–12. <https://doi.org/10.1103/PhysRevB.65.144306>.
- Schiavoni, S., F. D'Alessandro, F. Bianchi, and F. Asdrubali. 2016. "Insulation Materials for the Building Sector: A Review and Comparative Analysis." *Renewable and Sustainable Energy Reviews* 62: 988–1011. <https://doi.org/10.1016/j.rser.2016.05.045>.
- Schmierer, Eric N., and Arsalan Razani. 2006. "Self-Consistent Open-Celled Metal Foam Model for Thermal Applications." *Journal of Heat Transfer* 128 (11): 1194–1203. <https://doi.org/10.1115/1.2352787>.
- SCHOTT. n.d. "BOROFLOAT 33 - Thermal Properties." Jena, Germany. https://www.schott.com/d/borofloat/b89578c1-3509-40a2-aacf-ca3c2371ef7b/1.2/borofloat33_therm_eng_web.pdf.
- Seyf, Hamid Reza, Luke Yates, Thomas L. Bougher, Samuel Graham, Baratunde A. Cola, Theeradetch Detchprohm, Mi Hee Ji, et al. 2017. "Rethinking Phonons: The Issue of Disorder." *Npj Computational Materials* 3 (1). <https://doi.org/10.1038/s41524-017-0052-9>.
- Shan, Xiaodong, and Moran Wang. 2013. "Understanding of Thermal Conductance of Thin Gas Layers." *Advances in Mechanical Engineering* 2013: 1–7. <https://doi.org/10.1155/2013/692842>.
- She, Wei, Yunsheng Zhang, and M.R. Jones. 2014. "Three-Dimensional Numerical Modeling and Simulation of the Thermal Properties of Foamed Concrete." *Construction and Building Materials* 50 (January): 421–31. <https://doi.org/10.1016/j.conbuildmat.2013.09.027>.
- She, Wei, Guotang Zhao, Degou Cai, Jinyang Jiang, and Xiaoyu Cao. 2018. "Numerical Study on the Effect of Pore Shapes on the Thermal Behaviors of Cellular Concrete." *Construction and Building Materials* 163: 113–21. <https://doi.org/10.1016/j.conbuildmat.2017.12.108>.
- Shewchuk, Jonathan Richard. 2003. "Tetrahedral Mesh Generation by Delaunay Refinement," 86–95. <https://doi.org/10.1145/276884.276894>.
- Siegel, Robert, and John R. Howell. 1981. *Thermal Radiation Heat Transfer*. 2nd ed. New York: Hemisphere Publishing Corporation.
- . 1992. "Radiative Properties of Real Materials." In *Thermal Radiation Heat Transfer*, edited by Mary Prescott and Carolyn V. Ormes, 3rd ed., 137–87. Hemisphere Publishing Corporation.

- Singh, Ramvir. 2008. "Thermal Conduction through Porous Systems." In *Cellular and Porous Materials: Thermal Properties Simulation and Prediction*, edited by Andreas Öchsner, Graeme E. Murch, and J. S. de Lemos, 199–238. Weinheim: Wiley-VCH.
- Singh, Ramvir, and H. S. Kasana. 2004. "Computational Aspects of Effective Thermal Conductivity of Highly Porous Metal Foams." *Applied Thermal Engineering* 24 (13): 1841–49. <https://doi.org/10.1016/j.applthermaleng.2003.12.011>.
- Siwińska, A., and H. Garbalińska. 2011. "Thermal Conductivity Coefficient of Cement-Based Mortars as Air Relative Humidity Function." *Heat and Mass Transfer/Waerme- Und Stoffuebertragung* 47 (9): 1077–87. <https://doi.org/10.1007/s00231-011-0772-1>.
- Smith, David S., Arnaud Alzina, Julie Bourret, B. Nait-Ali, Fabienne Pennec, Nicolas Tessier-Doyen, Kodai Otsu, Hideaki Matsubara, Pierre Elser, and Urs T. Gonzenbach. 2013. "Thermal Conductivity of Porous Materials." *Journal of Materials Research* 28 (17): 2260–72. <https://doi.org/10.1557/jmr.2013.179>.
- Solórzano, Eusebio, J. A. Reglero, M. A. Rodríguez-Pérez, D. Lehmhus, M. Wichmann, and J. A. de Saja. 2008. "An Experimental Study on the Thermal Conductivity of Aluminium Foams by Using the Transient Plane Source Method." *International Journal of Heat and Mass Transfer* 51 (25–26): 6259–67. <https://doi.org/10.1016/j.ijheatmasstransfer.2007.11.062>.
- Solórzano, Eusebio, Miguel Angel Rodriguez-Perez, Jaime Lázaro, and José Antonio de Saja. 2009. "Influence of Solid Phase Conductivity and Cellular Structure on the Heat Transfer Mechanisms of Cellular Materials: Diverse Case Studies." *Advanced Engineering Materials* 11 (10): 818–24. <https://doi.org/10.1002/adem.200900138>.
- Sugawara, A., and Y. Yoshizawa. 1962. "An Experimental Investigation on the Thermal Conductivity of Consolidated Porous Materials." *Journal of Applied Physics* 33: 3135.
- Sundarram, Sriharsha S., and Wei Li. 2013. "On Thermal Conductivity of Micro- and Nanocellular Polymer Foams." *Polymer Engineering & Science* 53 (9): 1901–9. <https://doi.org/10.1002/pen>.
- Talukdar, Prabal, Miguel A. A. Mendes, Ritesh Kumar Parida, Dimosthenis Trimis, and Subhashis Ray. 2013. "Modelling of Conduction-Radiation in a Porous Medium with Blocked-off Region Approach." *International Journal of Thermal Sciences* 72: 102–14. <https://doi.org/10.1016/j.ijthermalsci.2013.04.027>.
- Tang, G. H., C. Bi, and B. Fu. 2013. "Thermal Conduction in Nano-Porous Silicon Thin Film." *Journal of Applied Physics* 114 (18). <https://doi.org/10.1063/1.4829913>.
- Tarkhanyan, R. H., and D. G. Niarchos. 2013. "Reduction in Lattice Thermal Conductivity of Porous Materials Due to Inhomogeneous Porosity." *International Journal of Thermal Sciences* 67: 107–12. <https://doi.org/10.1016/j.ijthermalsci.2012.12.008>.
- ToolBox, Engineering. 2004. "Universal and Individual Gas Constants." Engineering ToolBox. 2004. <https://www.engineeringtoolbox.com/individual-universal-gas-constant->

d_588.html.

- Vignoles, Gerard L. 2016. "A Hybrid Random Walk Method for the Simulation of Coupled Conduction and Linearized Radiation Transfer at Local Scale in Porous Media with Opaque Solid Phases." *International Journal of Heat and Mass Transfer* 93: 707–19. <https://doi.org/10.1016/j.ijheatmasstransfer.2015.10.056>.
- Vignoles, Gerard L., and Alberto Ortona. 2016. "Numerical Study of Effective Heat Conductivities of Foams by Coupled Conduction and Radiation." *International Journal of Thermal Sciences* 109: 270–78. <https://doi.org/10.1016/j.applthermaleng.2015.09.094>.
- Volz, Sebastian. 2007. *Microscale and Nanoscale Heat Transfer*. Edited by Sebastian Volz. Vol. 112.
- Walle, Wouter Van De, and Hans Janssen. 2016. "A Thermal Conductivity Prediction Model for Porous Building Blocks." *Bauphysik* 38 (6): 340–47. <https://doi.org/10.1002/bapi.201610037>.
- . 2019a. "Impact of Pore Scale Parameters on the Thermal Conductivity of Porous Building Blocks." In *Proceedings of the 4th Central European Symposium on Building Physics*. Prague.
- . 2019b. "The Heat Flow Meter: Principles, Design & Operation." In *The Art of Thermal Measurements*, edited by Joshua Meyer and Michel de Paepe.
- Wan, Bin, Kai Yue, Lian Cun Zheng, and Xin Xin Zhang. 2011. "The Effective Thermal Conductivity of Composite Materials with Spherical Dispersed Phase." *Advanced Materials Research* 239–242: 1870–74. <https://doi.org/10.4028/www.scientific.net/AMR.239-242.1870>.
- Wang, Fangzhou, and Xianglin Li. 2017. "The Stagnant Thermal Conductivity of Porous Media Predicted by the Random Walk Theory." *International Journal of Heat and Mass Transfer* 107: 520–33. <https://doi.org/10.1016/j.ijheatmasstransfer.2016.11.069>.
- Wang, Guilong, Chongda Wang, Jinchuan Zhao, Guizhen Wang, Chul B. Park, and Guoqun Zhao. 2017. "Modelling of Thermal Transport through a Nanocellular Polymer Foam: Toward the Generation of a New Superinsulating Material." *Nanoscale* 9 (18): 5996–6009. <https://doi.org/10.1039/C7NR00327G>.
- Wang, Guilong, Chongda Wang, Jinchuan Zhao, Guizhen Wang, Chul B Park, Guoqun Zhao, Wouter Van De Walle, and Hans Janssen. 2018. "Correction: Modelling of Thermal Transport through a Nanocellular Polymer Foam: Toward the Generation of a New Superinsulating Material." *Nanoscale* 10 (43): 20469–73. <https://doi.org/10.1039/c7nr00327g>.
- Wang, Guilong, Jinchuan Zhao, Lun Howe Mark, Guizhen Wang, Kejing Yu, Chongda Wang, Chul B. Park, and Guoqun Zhao. 2017. "Ultra-Tough and Super Thermal-Insulation Nanocellular PMMA/TPU." *Chemical Engineering Journal* 325: 632–46. <https://doi.org/10.1016/j.cej.2017.05.116>.

- Wang, Guilong, Jinchuan Zhao, Guizhen Wang, Lun Howe Mark, Chul B. Park, and Guoqun Zhao. 2017. "Low-Density and Structure-Tunable Microcellular PMMA Foams with Improved Thermal-Insulation and Compressive Mechanical Properties." *European Polymer Journal* 95 (May): 382–93. <https://doi.org/10.1016/j.eurpolymj.2017.08.025>.
- Wang, Moran, and Ning Pan. 2008. "Modeling and Prediction of the Effective Thermal Conductivity of Random Open-Cell Porous Foams." *International Journal of Heat and Mass Transfer* 51 (5–6): 1325–31. <https://doi.org/10.1016/j.ijheatmasstransfer.2007.11.031>.
- Wang, Moran, J Wang, N Pan, S Chen, and J He. 2007. "Three-Dimensional Effect on the Effective Thermal Conductivity of Porous Media." *Journal of Physics D: Applied Physics* 40 (1): 260–65. <https://doi.org/10.1088/0022-3727/40/1/024>.
- Wang, Moran, Jinku Wang, Ning Pan, and Shiyi Chen. 2007. "Mesoscopic Predictions of the Effective Thermal Conductivity for Microscale Random Porous Media." *Physical Review E* 75 (3): 036702. <https://doi.org/10.1103/PhysRevE.75.036702>.
- Wang, Zhaojie. 2012. "Thermal Conductivity of Polycrystalline Semiconductors and Ceramics." University of California Riverside.
- Wei, She, Chen Yiqiang, Zhang Yunsheng, and M.R. Jones. 2013. "Characterization and Simulation of Microstructure and Thermal Properties of Foamed Concrete." *Construction and Building Materials* 47 (October): 1278–91. <https://doi.org/10.1016/j.conbuildmat.2013.06.027>.
- Wei, She, Yang Yonggan, Xie Deqing, and Zhang Yunsheng. 2014. "Finite Volume Numerical Analysis of the Thermal Property of Cellular Concrete Based on Two and Three Dimensional X-Ray Computerized Tomography Images," no. July.
- Wevers, Martine, Bart Nicolai, Pieter Verboven, Rudy Swennen, Staf Roels, Els Verstrynge, Stepan Lomov, et al. 2018. "Applications of CT for Non-Destructive Testing and Materials Characterization." In *Industrial X-Ray Computed Tomography*, edited by Simone Carmignato, Wim Dewulf, and Richard Leach, 267–331. Springer International Publishing.
- Wiener, Otto Heinrich. 1904. "Lamellare Doppelbrechung." *Physikalische Zeitschrift* 5: 332–38.
- Wikipedia. n.d. "Evanescent Field." Accessed May 1, 2019. http://www.wikiwand.com/en/Evanescent_field.
- Williams, R. J. J., and C. M. Aldao. 1983. "Thermal Conductivity of Plastic Foams." *Polymer Engineering & Science* 23 (6): 293–98.
- Wingert, Matthew C, Jianlin Zheng, Soonshin Kwon, and Renkun Chen. 2016. "Thermal Transport in Amorphous Materials : A Review."
- Wirjadi, Oliver. 2007. "Survey of 3D Image Segmentation Methods." *Berichte Des Fraunhofer*

- ITWM 123 (123): 1-25. [https://doi.org/http://dx.doi.org/10.1016/S0040-1951\(01\)00065-8](https://doi.org/http://dx.doi.org/10.1016/S0040-1951(01)00065-8).
- Wolf, Jeffrey R., and William C. Strieder. 1994. "Pressure-Dependent Gas Heat Transport in a Spherical Pore." *AIChE Journal* 40 (8): 1287-96.
- Woodside, William, and J. H. Messmer. 1961. "Thermal Conductivity of Porous Media II. Consolidated Rocks." *Journal of Applied Physics* 32 (9): 1699-1706.
- Xu, Jiyuan, Yong Zou, Mingxiu Fan, and Lin Cheng. 2012. "Effect of Pore Parameters on Thermal Conductivity of Sintered LHP Wicks." *International Journal of Heat and Mass Transfer* 55 (9-10): 2702-6. <https://doi.org/10.1016/j.ijheatmasstransfer.2012.01.028>.
- Yang, Xiaohu, Tianjian Lu, and Tongbeum Kim. 2013. "Effective Thermal Conductivity Modelling for Closed-Cell Porous Media with Analytical Shape Factors." *Transport in Porous Media* 100 (2): 211-24. <https://doi.org/10.1007/s11242-013-0212-4>.
- Young, P. G., T. B.H. Beresford-West, S. R.L. Coward, B. Notarberardino, B. Walker, and A. Abdul-Aziz. 2008. "An Efficient Approach to Converting Three-Dimensional Image Data into Highly Accurate Computational Models." *Philosophical Transactions of the Royal Society A: Mathematical, Physical and Engineering Sciences* 366 (1878): 3155-73. <https://doi.org/10.1098/rsta.2008.0090>.
- Yüksel, Numan. 2016. "The Review of Some Commonly Used Methods and Techniques to Measure the Thermal Conductivity of Insulation Materials." In *Insulation Materials in Context of Sustainability*, edited by Amjad Almusaed and Asaad Almsaad, 113-40. Intech Open. <https://doi.org/10.5772/32009>.
- Zeng, S.Q., A. Hunt, and R. Greif. 1995. "Mean Free Path and Apparent Thermal Conductivity of Gas in a Porous Medium." *Journal of Heat Transfer* 117 (3): 758-61.
- Zhang, H.W., Q. Zhou, and Y.G. Zheng. 2011. "A Multi-Scale Method for Thermal Conduction Simulation in Granular Materials." *Computational Materials Science* 50 (10): 2750-58. <https://doi.org/10.1016/j.commatsci.2011.04.019>.
- Zhang, R. J. Z., L. Liu, and X. Wang. 2013. "Numerical Modeling and Experimental Study of Heat Transfer in Ceramic Fiberboard." *Textile Research Journal* 84 (4): 411-21. <https://doi.org/10.1177/0040517513485630>.
- Zhang, Zhuomin M. 2007. *Nano/Microscale Heat Transfer*. The McGraw-Hill Companies, Inc. <https://doi.org/10.1007/s10765-008-0380-6>.
- Zhang, Zuhua, John L. Provis, Andrew Reid, and Hao Wang. 2014. "Geopolymer Foam Concrete: An Emerging Material for Sustainable Construction." *Construction and Building Materials* 56: 113-27. <https://doi.org/10.1016/j.conbuildmat.2014.01.081>.
- Zhao, Jun Jie, Yuan Yuan Duan, Xiao Dong Wang, and Bu Xuan Wang. 2012a. "A 3-D Numerical Heat Transfer Model for Silica Aerogels Based on the Porous Secondary Nanoparticle Aggregate Structure." *Journal of Non-Crystalline Solids* 358 (10): 1287-97.

<https://doi.org/10.1016/j.jnoncrysol.2012.02.035>.

- . 2012b. “Effects of Solid-Gas Coupling and Pore and Particle Microstructures on the Effective Gaseous Thermal Conductivity in Aerogels.” *Journal of Nanoparticle Research* 14 (8). <https://doi.org/10.1007/s11051-012-1024-0>.
- Zhao, Y., G. H. Tang, and M. Du. 2015. “Numerical Study of Radiative Properties of Nanoporous Silica Aerogel.” *International Journal of Thermal Sciences* 89 (March): 110–20. <https://doi.org/10.1016/j.ijthermalsci.2014.10.013>.
- Zhu, Chuan-Yong, Zeng-Yao Li, and Wen-Quan Tao. 2017. “Theoretical and DSMC Studies on Heat Conduction of Gas Confined in a Cuboid Nanopore.” *Journal of Heat Transfer* 139 (5): 052405. <https://doi.org/10.1115/1.4035854>.

FACULTY OF ENGINEERING SCIENCE
DEPARTMENT OF CIVIL ENGINEERING
BUILDING PHYSICS SECTION
Kasteelpark Arenberg 40 - box 2447
B-3001 HEVERLEE, BELGIUM
wouter.vandewalle@kuleuven.be
<https://bwk.kuleuven.be/bwf>

